Flow Past a Circular Cylinder with a Permeable Wake Splitter Plate

Thesis by
Gregory Scott Cardell

In Partial Fulfillment
of the Requirements for the Degree of
Doctor of Philosophy

California Institute of Technology
Pasadena, California

1993

(Submitted March 29, 1993)

Acknowledgments

Thanks are due to my advisor, Anatol Roshko, for all he has done for me over the years, for sharing his knowledge and insight into the mysteries of fluid mechanics, and for the idea for the research. I would especially like to thank Fred Culick, who has not only been a good friend and available for expert advice, but whose progressive attitude towards the use of computers is outstanding, Don Coles, who so far as it is possible to tell knows everything about fluid mechanics, and Mory Gharib for his technical advice at crucial points during the experiments. I have bothered virtually every other member of the GALCIT faculty at some point with questions or requests, and I thank them all collectively.

Most of the staff of GALCIT have, at one point or another, contributed in very significant ways, but particular thanks must go to Jeri Chittum and Florence Kovacic, whose political views are so reasonable; Jerry Landry, who knows where everything is; George Lundgren, who got out before I did; and the guys in the shop who didn't get out at all, but meanwhile gave freely of their time, experience, patience and humor, Joe Haggerty, Phil Wood and Larry Frazier.

Much of what I have learned about experimental techniques and about fluid mechanics was available only from my friends and fellow students, and former fellow students, especially Jay Hammer, Derek Lisoski, and Greg (MIW) Smedley.

For their friendship, support, encouragement and inspiration, I would like to thank Mark Adler, James Cummings, Mike Hoenk, Shouleh Nikzad and Kellie Whittaker. My thanks to my family, who are also my friends, Mary Tevis (mother), John Armstrong, Cathy Cardell, and Jeff Cardell, for their support and their belief in me.

This thesis is much improved by the comments and suggestions provided by Cathleen Jones who, in a truly monumental effort, read the drafts. I would like to express my deep appreciation not only for that contribution, but also for her unwavering support and frequent encouragement, and the perspective which she provided during the times when the thesis was not visible through the data.

This research was supported in part by the Ocean Technology Program of the Office of Naval Research, ONR Grant No. N00014-90-J-1589.

Abstract

Measurements in the near wake region of a circular cylinder in a uniform flow in the Reynolds number range $2.5 \cdot 10^3 \lesssim \mathrm{Re} \lesssim 1.8 \cdot 10^4$ with permeable splitter plates spanning the wake center plane are presented. Permeability is defined by the pressure drop across the plates, and the relationship between permeability and plate solidity is determined for a set of plates constructed from woven wire mesh, permitting unambiguous characterization of the splitter plates by the solidity. The effects of different solidities on the flow in the near wake are investigated using smoke wire flow visualization, hot-wire anemometry, and measurements of the mean pressure at the cylinder surface, and the results are related to cylinder flow without a splitter plate.

Flow visualization results demonstrate that the introduction of low solidity splitter plates does not change the basic near wake structure, and that sufficiently high solidity uncouples the large-scale wake instability from the body, with the primary vortex formation occurring downstream of the separation bubble due to instability of the wake profile. Hot-wire and surface pressure measurements confirm and quantify the flow visualization results, showing that the permeable splitter plates reduce the drag and modify the primary wake frequency. When the solidity is high enough that the wake is convectively unstable, the base pressure is independent of the Reynolds number and solidity. For a wide range of solidities, the same asymptotic value of the Strouhal number is reached at high Reynolds numbers. The relationship between the Strouhal number and the base pressure is discussed.

Detailed measurements in the separating shear layers with splitter plates moderating the primary vortex formation show that in the mean the development of the separating shear layers is similar to that of the plane mixing layer. The presence of the splitter plates enhances shear layer development, and it is found that for all solidities the instability amplifies a broad frequency band without discrete spectral features. Turbulent transition in the shear layer and its role in the pronounced Reynolds number dependency of the flow in this Reynolds number range is discussed. Acoustic excitation of the separated shear layers confirms the broad band frequency response of the shear layer instability, and the effect of the driven shear layers on the near wake is investigated.

Table of contents

Table of contents *(continued)*

Table of contents *(continued)*

Table of contents *(continued)*

List of figures

List of figures *(continued)*

List of figures *(continued)*

List of figures *(continued)*

List of tables

List of symbols

Symbol		Description
AR	–	Cylinder aspect ratio
C_D	–	Cylinder (pressure) drag coefficient
C_{D*}	–	Normalized screen drag coefficient
C_p	–	Surface pressure coefficient
C_{pb}	–	Base pressure coefficient, $C_p(180°)$
D	–	Cylinder diameter
e	–	Voltage signal from the hot-wire anemometer
f_*	–	Non-dimensional frequency, fD/U_∞
f_1	–	Primary wake (vortex formation) frequency
f_2	–	Shear layer instability frequency
f_a	–	Acoustic forcing frequency
f_C	–	Filter cutoff (-3 dB) frequency
f_{*n}	–	'Beat' frequencies between f_1 and f_2 at which peaks appear in Φ
f_N	–	Nyquist frequency
L_f	–	Length of the separation bubble
L_p	–	Downstream distance to the increase in the shear layer growth rate
Nu_w	–	Hot-wire Nusselt number
k	–	Screen pressure drop coefficient
R	–	Shear layer velocity parameter, $\Delta U/2\overline{U}$
Re	–	Cylinder Reynolds number, $U_\infty D/\nu$
Re_*	–	Normalized screen Reynolds number
Re_w	–	Reynolds number based on hot-wire diameter
St	–	Strouhal number, $f_1 D/U_\infty$
u'	–	RMS fluctuating velocity, $\sqrt{\overline{(u(t)-\overline{u})^2}}$.
U_∞	–	Free-stream velocity
U_c	–	Velocity calculated from hot-wire calibration
U_m	–	Velocity measured during hot-wire calibration
ΔU	–	Velocity difference across the shear layer

List of symbols *(continued)*

Symbol		Description
$\overline{U}$	–	Average velocity across the shear layer
x	–	Coordinate in the flow direction, measured from the cylinder axis
y	–	Coordinate transverse to the flow direction, measured from, and normal to, the cylinder axis
y_c	–	Transverse location of the center of the separated shear layer, computed from a fit to the error function profile
y_{01} , y_{99}	–	Transverse locations at which the shear velocity reaches $0.01\Delta U$ and $0.99\Delta U$, respectively
z	–	Coordinate transverse to the flow direction, measured along the cylinder axis
α	–	Pressure tap angle, measured from the forward stagnation point
δ_*	–	Thickness parameter from the fit to the error function profile
δ_ω	–	Vorticity thickness of the separated shear layer
η	–	Normalized transverse shear layer coordinate
θ	–	Momentum thickness of the separated shear layer
θ_0	–	Initial momentum thickness of a shear layer
σ	–	Splitter plate solidity
Φ	–	Power spectral density computed from u'/U_∞
Φ_a	–	Amplitude of Φ at the forcing frequency, $\Phi(f_a)$
Φ_e	–	Power spectral density computed from the fluctuating hot-wire voltage, without conversion to velocity

CHAPTER 1

Introduction

"Before us the thick dark current runs. It talks up to us in a murmur become ceaseless and myriad, the yellow surface dimpled monstrously into fading swirls travelling along the surface for an instant, silent, impermanent and profoundly significant, as though just beneath the surface something huge and alive waked for a moment of lazy alertness out of and into light slumber again."

As I Lay Dying, William Faulkner (1930)

1.1 Cylinder flow

The flow past a circular cylinder in a uniform free stream has come to be regarded as the canonical bluff body flow, and is a frequently cited example of a complex, unsteady, incompressible fluid mechanical system. Despite the simplicity of the geometry the flow is very complicated, exhibiting great diversity in its behavior in the form of a strong dependence on the Reynolds number, as well as a strong sensitivity to small perturbations in the flow. This flow has been the subject of many studies over the past 100 years (for reviews, see Morkovin 1964, Berger and Wille 1972, and Cantwell and Coles 1983), yet despite the large number of experiments our understanding of circular cylinder flow is incomplete. Although the Reynolds number dependent behavior of the flow may be generally characterized, the details are not well determined, as illustrated by the lack of agreement in results from different experiments for which the values of the controlling non-dimensional parameters are the same, so that the flows are theoretically identical.

The scatter in the experimental results may be attributable to the sensitivity of the flow to differences in experimental conditions that are not traditionally well documented, such as the free-stream turbulence level, the cylinder aspect ratio, the blockage, the boundary conditions at the ends of the cylinder, and the effects of three-dimensionality in the nominally two-dimensional flow, many of which have been the subject of independent investigations (Stansby 1974, Apelt and West 1982, Norberg 1988, Szepessy 1991, to cite a few). It is necessary here to distinguish between two types of instability in the flow past a circular cylinder: The flow is unstable at large scales, exhibiting instabilities that lead to reorganization of the flow without necessarily inducing transition to turbulence; and the flow is transitional, exhibiting local or small-scale instabilities that bring about local transition, which may then lead to global modification of the flow. The sensitivity of circular

cylinder flow to such small differences in experimental conditions as were discussed above and the scatter in the experimental results arises from the underlying unstable, transitional nature of the flow.

Since instability and transition are strongly dependent on the Reynolds number, circular cylinder flow exhibits a pronounced dependence on the Reynolds number, so that the flow may be separated into different Reynolds number ranges according to specific phenomena that appear in each (Morkovin 1964, Roshko and Fiszdon 1969, Zdravkovich 1990). The flow is also very sensitive to the many other factors which influence stability and transition, such as those mentioned above, and this sensitivity of the flow makes it difficult to isolate the influence of other disturbances from the Reynolds number dependence. It is therefore necessary to carefully characterize the experimental conditions in order to permit comparison between different experiments, even though the large number of possible sources of disturbance make it an arduous task to fully document the flow environment. The need for such careful control has not often been fully appreciated, even though the fact that such factors have a large effect on the flow has been recognized for some time; for example, the effect of free-stream turbulence on the flow was recognized and documented by Gerrard (1965).

1.1.1 The standard model

A large number of terms have been coined to describe various features of the near wake, and since many of them are specific to flow past the circular cylinder without a splitter plate, it is necessary to be careful about the terminology that will be used to describe the flow both with and without a splitter plate. This will be set forth in the context of what will be referred to here as the "standard model" of the flow, which will be described only for the Reynolds number range $3 \cdot 10^2 \lesssim \mathrm{Re} \lesssim 2 \cdot 10^4$, although much of the general description is applicable to other Reynolds numbers. In this range, the Reynolds number dependence of circular cylinder flow is particularly pronounced, and it is of particular interest here because the experiments presented in this thesis lie entirely within this Reynolds number range.

An illustration of the near wake flow is shown in Fig. 1.1. The basic structure of the flow develops when boundary layers form on the upstream face of the cylinder, encounter an adverse pressure gradient at some point on the cylinder and separate from the cylinder surface, forming free shear layers. The shear layers form the boundaries of the near wake separation bubble, a region of slowly recirculating flow immediately behind the body which is at a considerably lower pressure than the free stream and is responsible for most of the pressure drag on the cylinder. This region is often called the formation or the stagnation region, but for reasons which will become clear later, the term separation bubble is more appropriate here. The separation bubble ends at a downstream closure point that may be

identified heuristically in flow visualizations as the mean location at which the shear layers reach the wake center line and begin to interact, or perhaps more precisely, that point along the wake center line where the mean velocity is zero. For flow past a cylinder without a splitter plate the large-scale vortices form near the end of the separation bubble, and then begin to convect freely downstream, at which point the vortices are described as having been shed from the body. The passage frequency of the large scale vortices is usually referred to as the "shedding frequency"; here it will be referred to as the vortex formation frequency or the primary wake frequency. The end of the near wake is reached when the large-scale vortices are fully formed and separate from the body to convect freely downstream, although this definition is somewhat ambiguous when a splitter plate is present.

The basic concept of the standard model is that the behavior of the near wake varies with Reynolds number due to independent variations of the different near wake processes – boundary layer separation, the state of the free shear layers, vortex formation, the pressure field of the separation bubble – and that the complex, nonlinear interactions between them are the source of the complicated overall behavior of the cylinder wake. However, because of the difficulty of making measurements in the near wake, typical measurements are single point measurements of integrated, or global, values that are indicative of the state of the entire near wake. Measurements of the drag of the cylinder and the primary wake frequency are of this sort, and show the overall Reynolds number dependence of the flow. Closely related to the drag, and more easily measured, is the base pressure, the pressure measured on the surface of the cylinder at the point 180° from the forward stagnation point. Experimental determinations of the values of these parameters as functions of Reynolds number are common, but as has been mentioned, there is wide scatter in the data (Roshko and Fiszdon 1969, Cantwell 1983). The different processes that contribute to the results of such global measurements are interrelated; for example, it is apparent that there is a relationship between the primary wake frequency and the drag, although the precise nature of the relationship is obscured by the scatter in the data, and it is also possible that the details of the relationship are dependent on the Reynolds number. This will be taken up in more detail later.

1.1.2 The role of transition to turbulence

It is now generally accepted that how and where the transition to turbulence occurs in the wake plays a large role in the dynamics of the near wake and that various flow disturbances can contribute to the instability processes leading to transition, which in turn may affect the entire structure of the near wake (Goldstein 1938, Roshko 1953, Roshko and Fiszdon 1969). Much of the Reynolds number dependence of the flow has been attributed to the Reynolds number dependence of the instabilities which lead to transition. In the Reynolds number range of interest here, turbulent transition is observed to occur in the

separated shear layers within the near wake, and the Reynolds number dependence is generally attributed to the upstream movement of the location at which transition occurs as the Reynolds number is increased. Observations by Schiller and Linke (1933), who obtained mean velocity traces across the the separated shear layer, indicate that there is a point at which the growth rate of the shear layer thickness abruptly increases. They identified this point as the point of transition to turbulence and observed that it moves upstream as the Reynolds number is increased. This is an example of a mechanism by which a small flow disturbance may influence the overall wake flow, since a small increase in the free-stream turbulence will promote earlier (*i.e.*, farther upstream) transition in the free shear layers, accompanied by a decrease in the length of the separation bubble and a lower pressure in the separation bubble, which thereby increases the drag (Norberg 1988, see also Appendix A).

Thus, in this Reynolds number range, the stability of the separated shear layers is important to the structure of the near wake, and there have been several investigations that have focused on the state of the separated shear layer, more specifically on the "transition waves" (the terminology is due to Bloor 1964), *i.e.*, quasi-periodic velocity fluctuations in the separated shear layers upstream of the transition point caused by the Kelvin-Helmholtz instability of the shear layer. Inasmuch as shear layer transition has been singled out as one cause of the large Reynolds number dependency of the near wake flow in this Reynolds number range, it is surprising that there are few experiments relating the detailed state of the shear layer to the overall near wake structure. The original measurements of Schiller and Linke are typical; their study of the dependence of the global measurements on the state of the shear layers only observes that as the Reynolds number is increased the location of the point at which there is an increase in the growth rate of the shear layer occurs farther upstream, and, for example, that there is also an increase in the drag; this only demonstrates covariance of the two phenomena, not necessarily interdependence, in the sense that under other conditions the drag may be increased without a change in the location of shear layer transition.

1.2 Circular cylinder flows using splitter plates

Exploration (beyond mere observation) of the relationship between the overall structure of the flow and the Reynolds number dependence of the various elements comprising the near wake may be accomplished through the utilization of some technique for interfering with or varying the near wake interactions and studying the effect on the wake structure, which in turn requires some form of active modification of the wake. Most methods for achieving such modifications utilize interference elements, *i.e.*, some form of solid body introduced into the wake. An interference element technique which has often been used is a wake splitter plate, the introduction of an impermeable barrier into the center plane

of the wake formed by the cylinder axis and the streamwise direction, which splits the wake symmetrically and interferes with communication between the two sides of the wake. Although such splitter plates have been used on bluff bodies other than circular cylinders (*e.g.*, Arie and Rouse 1956, Bearman 1965), it seems that comparable experimental results should be obtained for circular cylinders alone before comparing circular cylinders to other cross-sectional shapes, and so only circular cylinders will be discussed here.

Roshko (1954), using a circular cylinder and working in the present Reynolds number range, discovered that the base pressure was substantially increased by the introduction of a relatively long (five cylinder diameters) solid wake splitter plate and also noted that vortex formation was inhibited. Wake traverses with a static pressure probe indicated that the low pressure point in the wake without the splitter plate is not at the base of the cylinder, but lies downstream. Subsequent measurements with a short ($1.1D$) splitter plate demonstrated that when the leading edge of the short splitter plate was located at downstream positions within about $2.5D$ of the cylinder base, the base pressure and primary frequency varied continuously with the plate position, but that if the splitter plate was moved farther downstream there was a discontinuous change to values close to those measured without the splitter plate present. This indicates that, within limits, it is possible to continuously modify the structure of the near wake with interference elements.

Apelt *et al.* (1973) and Apelt and West (1975) carried out experiments in which the downstream length of the splitter plate was varied, and discovered that a wake instability leading to a primary wake frequency was manifest downstream of long splitter plates, even though increasing the length of the splitter plate had little effect on the base pressure. Furthermore, their results demonstrate that for a long enough splitter plate, the near wake region becomes nearly independent of the downstream wake behavior, in particular, no primary frequency could be detected in the near wake when the splitter plate was sufficiently long ($> 7D$). Their results show that the near wake region may be separated from the large-scale vortex formation through the use of a solid splitter plate, so that the near wake structure may be studied in the absence of primary vortex formation.

Their results also demonstrate the presence of two types of instability that may occur in bluff body wakes. Without a splitter plate the thin, separated shear layers are concentrated into large structures by complex interactions in the near wake and these large structures then separate and convect freely downstream. This form of the wake instability will be referred to as "body-coupled instability" since it develops from that part of the wake structure — the near wake — that depends on the presence of the body. With a long splitter plate the separated shear layers reattach to the splitter plate, and then downstream of the splitter plate a wake profile forms with vorticity smoothly distributed across the wake. Large-scale vortices eventually evolve out of an instability developing in the wake profile, away from the influence of the near wake and the bluff body itself. A similar wake instability was observed

by Cimbala (1984) at lower Reynolds numbers for a wake profile generated by a porous body that does not exhibit the separation bubble or thin vorticity layers characteristic of solid bluff bodies. This type of instability will be referred to as the "wake-profile instability" since it develops from a wake profile which does not necessarily depend on the body generating the wake. The discontinuous change with splitter plate position observed by Roshko (1953) may have been due to a change between the two types of instability.

Igarishi (1982) carried out extensive measurements to determine the effect of splitter plate length on the flow behind a circular cylinder, using a cylinder of aspect ratio $AR \approx 4.4$ and with blockage of about 9%. In these ranges of aspect ratio and tunnel blockage the flow is strongly modified from the flow at higher AR and lower blockage, as has been demonstrated by Apelt and West (1982) (see also Appendix A), and so those data cannot be usefully compared to the results presented here.

Kourta *et al.* (1987) investigated the instability of the shear layer and its relationship to the vortex formation, with and without a splitter plate of moderate length ($4.1D$), and obtained results that appear to indicate an extremely close coupling between the structure of the near wake, the shear layer instability, and the primary vortex formation. They made measurements with a hot wire located in the near wake, and spectra computed from this data show that in their experiments the shear layer instability contained a large amount of energy at several discrete frequencies, and that for certain locations in the wake the magnitude of these spectral peaks exceeded that of the peak at the lower frequency corresponding to the primary vortex formation. They also found that vortex formation still occurred downstream of the splitter plate.

Unal and Rockwell (1988) used a thick plate (with a thickness ratio of $t/D \approx .5$) with a wedge shaped leading edge, which they refer to as a splitter plate, in a fashion similar to that of Roshko. Although they focused on feedback effects using instrumentation in the plate, and although their experimental setup was not geometrically similar to the present experiment or to those discussed before, their work is of interest in that they measured shear layer spectra with characteristics similar to those obtained by Kourta *et al.*, and show spectra from hot-film measurements in the separated shear layers which exhibit spectral peaks at frequencies that are characteristic of the shear layer instability, and that are of the same order of magnitude as the primary formation peak.

1.3 Present research

The experiments that have been discussed using solid splitter plates demonstrate that the introduction of interference elements in the form of splitter plates into the near wake in order to study the near wake interactions is feasible, and that the near wake structure can

be varied to some extent by changing the geometry of the splitter plates (*e.g.*, the location, or downstream length, or both). However, solid splitter plates have drastic effects on the near wake, such as the abrupt changes observed by Roshko (1954) with a short splitter plate, and the removal of the primary vortex formation from the near wake as observed by Apelt and West (1975). Although considerable insight has been gained from the use of solid splitter plates, a technique to make continuous, small changes in the structure of the near wake, thereby inducing small changes in the interaction of the various near wake processes, would help to further elucidate the relationships and dependencies between the various near wake processes.

One method for achieving such a continuous variation in the near wake is a permeable wake splitter plate, constructed from a porous material such as thin perforated metal or a wire-mesh screen. A permeable wake splitter plate (carefully chosen to minimize geometrical effects) will interfere with communication across the wake center plane, and by varying the permeability, it is possible to vary the magnitude of the interference created by the splitter plate. Communication across the center plane of the wake takes two forms, mass transfer due to a transverse velocity component, and changes in the pressure field due to the flow on the different sides of the wake, so it is natural to define the permeability of a plate by the loss in total pressure which it introduces in a flow normal to the plate, and it is reasonable to relate the pressure drop to the free-stream dynamic pressure, which gives the pressure drop coefficient

$$k = \frac{\Delta p}{\frac{1}{2}\rho U_\infty^2}.$$

It is shown in Appendix C that the pressure drop across the plate is a function not only of the velocity normal to plate and the relative solidity σ of the plate, but also depends on the geometry of the perforations that make the plate permeable. However, it is also demonstrated that it is possible to choose a set of splitter plates having similar geometries for which the pressure drop parameter is a continuous, monotonically varying function of the solidity over the velocity range of interest here, so that for plates chosen from that set the solidity uniquely characterizes the plate. The set of such splitter plates described in the appendix – which will be referred to as the "standard plates" – are those primarily used for the experiments shown in this thesis and so splitter plate permeability will be characterized by the solidity, with it always understood that this refers to that specific set of plates.

There are conceptual difficulties using the parameter k alone to characterize the plates; in particular, k is a function of the magnitude of the velocity component normal to the plate and so will vary not only with the magnitude of the free-stream velocity but will be a function of the downstream coordinate x as well, since the transverse component decays as the wake evolves downstream. The results of Appendix C show that the change in k with velocity is particularly important at very low Reynolds numbers (based on the magnitude of the velocity normal to the plate), and therefore, as the transverse velocity decays to

zero, the variation with x will be particularly important. Since the decay of the transverse velocity component is complicated, the variation of k with x will be complicated as well.

A considerable amount of time was spent in the attempt to obtain results which may be compared with other experiments. To this end, the wind tunnel flow is extensively documented in Appendix A. In addition, endplates were used to obtain easily reproducible end conditions on the cylinder and to isolate the flow from the effects of the wind tunnel wall boundary layers. Furthermore, to ensure that the results for splitter plate of different permeabilities are comparable, the free-stream conditions and the experimental geometry, other than that responsible for the splitter plate permeability, were kept constant in the experiments and only the splitter plate solidity was changed. All experiments discussed in this thesis, except for those presented in Appendix A where the changes to the experimental conditions are explicitly discussed, were performed at a fixed aspect ratio of $AR \approx 16.8$ and a free-stream turbulence level of $u'/U_\infty \approx .15\%$.

In the experiments for which results are presented in this thesis, it will be shown that smoothly changing the plate permeability does bring about a smooth change in the near wake behavior. The permeable splitter plates are used to examine the relationship between the primary vortex formation and the base pressure. The permeable splitter plates, which increase the length of the separation bubble and decrease the amplitude of velocity fluctuations in the near wake due to the primary vortex formation, are shown to modify the growth of the shear layer instability and are used to examine the evolution of the separated shear layers and the influence of the shear layers on the flow in the near wake. Results are presented which indicate that, contrary to other reported results, under the present experimental conditions the shear layer instability does not selectively amplify a discrete frequency, but rather amplifies a broad, continuous range of frequencies. Results of experiments using acoustic forcing to produce controlled perturbations at discrete frequencies show that the separated shear layers are very sensitive to small perturbations at frequencies lying within the band of naturally amplified frequencies, and the acoustic forcing technique was used to examine the influence of the forced shear layers on the flow in the near wake.

CHAPTER 2

Experimental apparatus

"The wind tunnel used for most measurements was the small 20-inch square GALCIT 'Correlation' tunnel built many years ago for similar investigations."

Liepmann, Laufer and Liepmann
NACA TN 2473 (1951)

2.1 The wind tunnel

All experiments presented in this dissertation were performed in the GALCIT "Correlation tunnel," a low turbulence open return wind tunnel. The inlet of the tunnel is 1.8 meters square, and contains several turbulence reduction screens (see Fric 1990 and Cimbala 1983 for details), with a two meter long contraction to the test section inlet where the tunnel is 0.51 meters square, for a contraction ratio of 12.5. The test section is 1.8 meters long, and the floor and walls are composed of nine removeable panels machined from 2 cm thick transparent plastic (Lucite), and mounted on four aluminum beams (see Fig. 2.1). The flow quality in the test section is discussed in Appendix A.

The center side panels of the test section were designed to allow the mounting and tensioning of the stainless steel wire mesh screens from which most of the permeable splitter plates were constructed. Figure 2.2 is a diagram of the front center panel, which consists of a fixed piece and a removeable piece. A screen is mounted by folding the edge of the screen over on itself several times to form a raised lip, which is then inserted into a slot in the top edge of the fixed piece of the front panel (Fig. 2.3). The removeable piece is then placed on top of the fixed piece, locking the folded edge into the slot and clamping the edge of the screen in place. The other end of the screen feeds through a slot in the rear center panel of the test section and is clamped along its edge between several short pieces of thin aluminum bar (Fig. 2.4), which are attached in turn to an external frame by turnbuckles. Adjusting the turnbuckles attached at different locations along the edge of the screen permitted the tension to be adjusted until the screen was approximately flat across the center plane of the test section. Tension in the screen is carried by the external frame and by the front center panel of the test section, which is reinforced by vertical struts at the upstream and downstream ends, by the cylinder models themselves, and by a steel shear pin between the fixed and removeable plates. Note that the tension in the splitter

plates was not measured, as it was assumed that if the tension were high enough that the natural frequencies of the splitter plates were not in the range of the wake frequencies there would be no effect. This was only significant for the heaviest splitter plates where it was difficult to achieve sufficiently high tension without threatening the structural integrity of the test section. However, when the tension was not high enough, anamolous points (in that they deviated significantly from most of the data) were visible in the Strouhal number vs. Reynolds number curve, and there was also a clear effect on the corresponding spectra which show the competition between the screen natural frequency and the vortex formation frequency, with "lock-in" to the screen frequency very apparent. This is discussed more fully in Chapter 4.

The test section is followed by a short diffuser section of the same dimensions, which terminates at the entrance to a one meter diameter by one meter long cylindrical pipe which houses the fan. The entrance to the circular pipe is covered by a honeycomb made of masonite arranged in a loose square grid. Flow through the tunnel is provided by a fan constructed of a two-bladed aircraft propeller (trimmed at the blade tips to fit in the tunnel) which is mounted on the drive shaft of a DC shunt motor. The rotation rate is controlled by varying the voltage to the motor and the resistance in the shunt. The fan exhausts into a rectangular plywood enclosure which houses the fan motor, and contains several turning vanes that direct the flow upward out of the enclosure and into the room. Through the use of screens spanning the exit from the test section and louvers installed in the sides of the diffuser section the tunnel velocity may be fine tuned over a small range without changing the fan speed, but during this investigation the louvers were left closed and sealed with wooden covers, so that velocity was controlled only using fan speed and the "downstream screens" resulting in a tunnel velocity range of $2.0 \lesssim U_\infty \lesssim 10.5$ m/s. The downstream screens were only used to obtain the lowest velocities, typically for velocities below 2.5 m/s.

Probe access to the tunnel interior was provided by slots cut through the panels making up the top of the wind tunnel test section. The panels sit on foam or felt sealing strips and are clamped with C-clamps to the top beams of the test section. There are a number of sets of such panels, allowing probes to be positioned and traversed through different locations in the test section.

2.2 Experimental models

2.2.1 Cylinders

The cylinders were constructed of heavy wall aluminum tubing, turned on a lathe and then polished with 600-grit emery cloth. The cylinder diameters were generally accurate

to within 0.3% over the span. Figure 2.5 is a diagram of a typical cylinder (all cylinders were externally the same but some of the end plug details varied). All cylinders were nominally 2.54 cm in diameter and spanned the test section. The ends were sealed with aluminum plugs epoxied in place, and short lengths of 0.32 cm O.D. brass tubing were epoxied into holes through one end of the cylinders, and connected to plastic tubing leading to the pressure sensor. Cylinder wall pressure taps were holes, 0.05 cm in diameter, drilled through the tube wall at center span. With this arrangement the interior volume of the cylinder in combination with the connecting tubing formed a low-pass filter that prevented the measurement of fluctuating pressures on the cylinder surface, so only mean pressure measurements are presented.

2.2.2 Cylinder end plates

Endplates were used for all measurements with permeable splitter plates. Appendix A compares data taken without end plates and discusses the overall effects of changing the boundary conditions at the end of the cylinder. The overall layout of the end plates (Fig. 2.6) was taken from Stansby (1974), as the use of end plates based on that design has become fairly common in circular cylinder measurements. The current end plates were modified with slits parallel to the cylinder wake to allow the introduction of the permeable splitter plates. Measurements of the base pressure and the primary wake frequency were made in the wake of a cylinder fitted with the modified end plates (without a splitter plate) both with and without the slits sealed and, surprisingly, there was no measurable difference. Most of the splitter plates fit very tightly into the slits and so in any case, with the splitter plates in place, leakage through the slits was minimal. The end plates were constructed of 0.53 cm thick transparent plastic, with the leading edges machined to a semicircular cross section. The end plates were mounted to the front and rear tunnel walls using three 0.32 cm diameter circular standoffs, located as shown in Fig. 2.6. Except for some of the measurements presented in Appendix A, the gap between the walls and the end plates was 2.87 cm , well outside the tunnel wall boundary layers that were found to be less than 1.3 cm thick at all Reynolds numbers investigated. Blockage, with the model cylinder and end plates in place and including the end plate standoffs, was 6.3% of the total cross-sectional area. The cylinder model and end plates were removed during the velocity calibration of the tunnel.

2.2.3 Permeable splitter plates

As has been mentioned, most of the permeable splitter plates used in these experiments were constructed of standard industrial grade woven wire mesh. The set of screens was selected on the basis of availability, while attempting to span the solidity range and keep the wire diameters less than about 1% of the cylinder diameter to minimize any secondary

scale effects. This kept the mesh openings to within a small percentage of the cylinder scale as well, but this was not particularly controlled. Appendix C presents the results of detailed measurements of the screens and also discusses the definition of "permeability" and results of measurements of the permeability for the screens, as well as details of the single permeable splitter plate that was not composed of woven wire mesh. Measurements were also made with a solid plate, which consisted of a thin (0.23 mm) sheet of stainless steel fastened over one of the screens. It was intended that all screens be effectively infinitely long in the flow direction, as far as the cylinder near wake flow was concerned, and it was found that a length of approximately 16 diameters met this criterion (see Appendix A), and this length was maintained to a tolerance of 0.25 cylinder diameters.

Screens were tensioned using the method discussed in Sec. 2.1, and the criterion used was that the screen be flat to within a small fraction of the cylinder diameter, typically less than about 2% although the less permeable screens required considerably more tension to achieve this flatness. The screens typically exhibit a sort of "Poisson" effect where tension led to contraction of the screen along a direction normal to the direction of the tension, leading to gaps between the leading edge of the plates and the base of the circular cylinder. Some measurements were made to determine the effect of varying this gap, and it was found that gaps up to 0.13 diameters had no effect on the base pressure or primary wake frequency, but that for gaps of 0.26 diameters a measurable difference appeared, so experiments were performed only for gaps of less than 0.07 diameters (see Appendix A for the actual measurements).

2.3 Instrumentation

2.3.1 Data acquisition system

All data from the hot wires and pressure sensors used in this study were recorded using a computer-controlled analog-to-digital data collection system. The system consists of an Everex 1800 microcomputer (IBM PC-AT compatible) with an RC Electronics ISC-16 analog-to-digital (A/D) converter, consisting of a printed circuit board mounted in the computer bus slots and a connection box at the end of a one meter ribbon cable. The A/D converter has 12-bit resolution over an input range of ± 10 volts, and was calibrated against a voltage standard and found to be highly linear, with a binning error of approximately ± 0.5 bins. Voltage calibrations performed on each channel indicated that all calibrations agreed with each other to within 0.1%, and so the calibration data for all channels were combined and a global calibration was computed and used for all measurements.

The A/D converter has a maximum sample conversion rate of 1 MHz, and can collect up to 16 channels. Multiple channels are collected serially, one sample per channel per microsecond. The board is designed so that at slower collection rates, data may be continuously read off of the board and into the computer memory. This feature was used to collect large amounts of data directly to the disk drive. The input impedance of the A/D converter was 20kΩ, which was too low for some of the measurement instruments used in the experiments, and so it was decided in all cases to condition the signals before they were input to the A/D converter. This was done in a variety of ways, detailed with the description of each instrument. The software provided by the manufacturer was inadequate for these experiments, and so a complete set of computer programs to control the A/D board were written and used to collect all voltage data presented here.

2.3.2 Pressure measurements

Pressure measurements were performed using pressure probes consisting of Pitot-static tubes (United Sensor model PDC-12-G-10-KL), Kiel probes (United Sensor model KDC-12), and wall ports (used only for velocity measurements calibrated against test section dynamic pressure measured using the Pitot-static tube). The probes were mounted so that they were mechanically isolated from the wind tunnel to avoid tunnel vibrations. The Pitot-static tube was mounted in an assembly that allowed the probe-tip yaw angle (rotation around the tube stem) to be changed to allow the tip to be aligned to within $\pm 1°$ of the free-stream direction. Pitch angles were not measured, but the tube stem was mounted to be closely perpendicular to the tunnel top, and the probe tip was measured to be at a right angle to the stem, and it is estimated that pitch alignment was accurate to within $\pm 2°$. The Kiel probes were verified to be insensitive to large deviations – up to $\pm 40°$ – in their alignment with the free-stream direction and so were merely aligned by eye to be approximately perpendicular to the tunnel walls. There were two wall ports used, the first of which was located near the tunnel inlet (well before the beginning of the contraction,) and the second was located approximately 0.5 meters upstream of the entrance to the test section, immediately following the contraction. All measurements involving the two wall ports were measurements of the pressure difference Δp_{12} between them, and were calibrated against the dynamic pressure $q = \frac{1}{2}\rho U_\infty^2$ measured with the test section empty. During the experiments, the calibration of q as a function of Δp_{12} was used as the definition of the test section dynamic pressure. This calibration was found in every case to be linear for $\Delta p_{12} > 5$ Torr, but deviated from a linear fit below this value, so a cubic polynomial fit was used.

For the results reported here, all probe pressures were measured using the two electronic manometer sets detailed in Tab.2.1. The manometers consist of a capacitance bridge sensor and a box containing circuitry for bridge excitation and output conversion and amplification.

The pressure sensors were found to respond to vibration transmitted through the sensor housing, and therefore were mechanically isolated from the wind tunnel so that wind tunnel vibrations would not effect the measurements. Manometer outputs may be read directly on meters built into the front of the amplifiers, and are simultaneously presented to an external connector as a voltage corresponding to the percentage of the full scale voltage range, which was input to the A/D system. Since one of the manometers provided a full scale output of only 1 volt, to improve the dynamic range of the measurements the output was amplified by a (calibrated) gain of 10.0 using a homemade DC amplifier.

Manometer model	Full scale output	Sensor model	Range
1173-B1A-10A1-A1	1 volt	570D-1T-2D1-V1X	1 Torr
1173-B4A-10A1-A1	10 volts	581D-10T-2B1-V3X	10 Torr

TAB. 2.1 Specifications of the Datametrics, Inc. electronic manometers that were used for the pressure measurements.

The manometers were calibrated against each other and two additional manometers from the same manufacturer, and the deviations between the four manometers were found to be less than 0.3% over the measured range. Because of the extremely small dynamic pressures involved, there is a fairly large systematic uncertainty at the lowest pressures since the actual measured pressures were a small fraction of the sensor's range. The systematic uncertainty due to the manometers was computed using the manufacturers specifications.

2.3.3 Hot-wire sensors

Hot-wire measurements were performed using single tungsten hot wires (TSI, Inc., model 1250-T1.5) controlled by constant temperature anemometer circuits built some time ago at GALCIT and known as Matilda Meters (Cantwell 1976, Perry 1982). Overheat ratios were set so that the temperatures of the wires should be approximately 250 C, the manufacturer's recommended operating temperature. The output of the Matilda meter, which consists of the hot-wire bridge voltage (measured at the top of the circuit bridge, not across the hot wire itself), was taken into a locally constructed unity gain op-amp voltage follower for impedance matching and then measured on one channel of the A/D converter. To improve the dynamic range and overcome the limited A/D resolution, the bridge output was also presented as the input to a voltage amplifier (Stanford Research Systems SR560), where it was A/C coupled and the fluctuating signal amplified. The output of the amplifier was sent through either one or two 6-pole 24 dB/decade butterworth filters (Krohn-Hite models 3202 and 3202R) for antialiasing and the output of the filters was sampled using the data collection system. The value of the cutoff frequencies to which the filters were set are given with the data.

Frequency response of the hot-wire circuitry was adjusted according to the square wave test detailed in the manuals for the Matilda meters, and was checked by measuring the turbulent spectrum behind a wire mesh grid at different free-stream velocities. By changing the free-stream velocity and the wire mesh, different spectra could be obtained and compared to spectra taken without the wire mesh. The spectra taken behind the wire mesh exhibited a constant amplitude, several orders of magnitude above the amplitude of spectra taken without the wire mesh, from DC up to some frequency at which the amplitude began to decrease. The rolloff frequency was a function of the free-stream velocity, so by increasing the free-stream velocity the rolloff frequency could be increased to a frequency above those of interest in the present experiments, and the spectra computed from hot-wire data under such conditions showed no distortion of the turbulent spectra. With the hot wire in a uniform free stream, the Matilda meters generate a noise signal in a frequency band from 5 kHz to the maximum value measurable with the existing equipment of about 100 kHz. The total power in this high frequency noise was of the same order of magnitude as the lower frequency signal from the free-stream turbulence, and so the fluctuating hot-wire output was always filtered at or below 5 kHz, which is higher than any significant flow frequencies in the present experiments. The calibration method used to obtain velocity from hot-wire voltage is detailed in Appendix B.

2.3.4 Probe traversing system

Hot-wire probes were usually mounted to a three-axis positioning system (built and described by Fric 1990) mounted on a framework that surrounds the tunnel but is not directly mechanically connected to it, except indirectly through the concrete slab floor. The probes are mounted at the end of a 0.64 cm diameter steel rod with aluminum clamps and set screws. The mounting system with a hot wire installed is visible in Fig. 2.1. The rod holding the sensor extended through slots in the tunnel top, and was sealed by thin neoprene sheeting around the rod, mechanically isolating it from the test section. The steel rod then passed through a stiffening support, which also acted to reduce "lash" when reversing the direction of motion normal to the probe support, and then to a mounting on the Y-traverse. The mounting rod was not streamlined in any way, but even without streamlining, vibration of the probe support was not significant, as can been seen in the power spectrum shown in Fig. A.1, taken with the hot wire mounted at the centerline of the empty test section at the maximum flow velocity. Spectral peaks corresponding to harmonics of the fan rotation speed are visible, but no significant signal is present at frequencies corresponding to shedding or mechanical vibration of the probe mount.

2.3.5 Smoke wire flow visualization

Flow visualization was performed using the smoke wire method, as described in Corke

et al. (1977), Cimbala (1984) and Fric (1990). The smoke wire itself was 0.13 mm diameter stainless steel music wire, and was passed through holes in the test section walls and tensioned externally by small copper weights. The wire was heated by passing approximately one ampere of current through it. Mineral oil was introduced onto the wire by removing a small porthole in the top section of the tunnel and applying it directly onto the wire with a small brush. A timing system was used to turn on the smoke wire current and trigger the camera after a short delay, and both the oil and the timing system were manufactured by Flow Visualization Systems, Inc. Photographs were taken with a Nikon F3 35mm SLR camera, using an f2.8 28–85 mm Vivitar Zoom/Macro lens, and Kodak T-Max 400 black and white print film. A General Radio Model 1540 Strobolume strobelight was used to illuminate the smoke with a flash of 10μs duration, sufficient to freeze the flow at the highest velocities at which the smoke flow visualization could be used. The light was directed along the plane of the smoke sheet, perpendicular to the view direction, which gave the best illumination angle while creating uneven lighting due to the shadow of the splitter plate. The velocity limitation in the flow visualization was the velocity at which the wake of the smoke wire became unstable and commenced vortex shedding, and this turned out to be somewhat greater than 5 m/s (Reynolds number based on wire diameter of ≈ 43). Prints were made on Ilford Multigrade III RC polycontrast paper, and considerable effort was necessary to achieve even print exposures due to attenuation by the splitter plates of the light reaching the top half of the wake.

2.3.6 A note on statistical error

It is normal in measurements of many physical quantities to assume that the central limit theorem applies, and the analysis of uncertainty is therefore based on the assumption that the underlying distribution is Gaussian. The further assumption that the measurements are being made on a random variable leads to the definition of the standard deviation of the mean, $\sigma_{\bar{x}}$, as the standard deviation of the measurements divided by the square root of the number of measurements. However, the assumption that the measured quantity is a random variable is not correct in the case of bluff body wakes, which are modulated by the quasi-periodic phenomena of the primary vortex formation, and so at time scales which are of the order of the period of the vortex formation frequency the randomness affecting the measurements is due to phase and amplitude variations exhibited by the primary vortex formation process. It is therefore necessary to take data over a sufficiently large number of primary frequency cycles to get statistically accurate results. This implies that the number of actual measurements is not the number of recorded data points, but rather the number of vortex shedding events that occurred during the period of the measurement. Thus, when statistical uncertainty was computed for some mean quantity $\bar{x}$ measured in the wake, this

is defined as

$$\sigma_{\bar{x}} = \frac{\sigma_x}{\sqrt{M}}$$

where $M = T_m \cdot f_1$ is an estimate of the number of primary vortex formation cycles which occurred during the measurement period T_m. This is inapplicable in those cases where the primary vortex formation is suppressed, such as when a solid splitter plate is introduced into the wake, but in that case the quasi-periodicity is not imposed on the wake and so the usual formula could have been used. However, in the interest of making reasonable comparisons of the uncertainties with or without vortex formation, when the primary wake frequency could not be detected, the data were collected over intervals which were long compared to the period of the vortex formation without a splitter plate, and the number of cycles was estimated by assuming a value for the Strouhal number of $St = 0.2$, which in this Reynolds number range is close to that for the cylinder without a splitter plate. This is generally an overestimation of the uncertainty, and whether or not a primary frequency could be detected, the smaller of the computed number of cycles and the total number of data points was used.

CHAPTER 3

Flow visualization results

"... I had my staff of highly trained research assistants go over it thoroughly, both visually and by barking at it."

Dave Barry
(Sept. 15, 1991)

3.1 Introduction to the flow visualization

In this chapter, the results of using the smoke wire technique to visualize the changes in the near wake produced by the introduction of permeable splitter plates are presented. Photographs are shown for several different Reynolds numbers and plate permeabilities. The highest cylinder Reynolds number for which photographs were possible (limited by the smoke wire Reynolds number at which the wake of the smoke wire becomes unstable, here $Re \approx 43$ based on wire diameter) was $Re \approx 8600$, and the highest Reynolds number for which photographs are presented here is $Re \approx 8000$.

Figure 3.1 is a diagram of the flow visualization photographs (with smoke lines left out), to help in the interpretation of what is visible in the photographs. The smoke wire is mounted vertically, normal to the cylinder axis and upstream of the cylinder, and is out of the field of view to the left of the photographs. The cylinder projects into the page, and is bounded at either end by end plates. The front end plate is of transparent plastic, but the edges of the front end plate are visible in some of the photographs, while the rear end plate is painted black and is nearly invisible, although the mounting screws holding the end plates were left unpainted and are visible in the photographs. The strobelight illuminates the cylinder from below and the dark band extending from the cylinder towards the upper left of the photographs is the shadow cast by the cylinder on the smoke lines. The bright vertical line extending from near the center of the cylinder to the top of the photographs and the long dark line running horizontally from the bottom of the vertical line are the edges of the removable portion of the front tunnel wall used to clamp the splitter plates in place, and the horizontal edge also marks the edge of the splitter plate, which extends into the page. The out-of-focus short vertical bar that is visible in some of the photographs about 11 diameters downstream of the cylinder is a shear pin used to reinforce the front wall against the tension in the splitter plates. The splitter plates themselves are not visible in the photographs, although the light reflected from the bottom of the splitter plates appears

as a brightly lit band in the smoke on the bottom side of the splitter plate in many of the photographs.

3.2 General observations

It is expected that the main effect of a permeable splitter plate will be to reduce communication across the wake center plane. The interference from a permeable splitter plate, which introduces a pressure drop at the center plane of the wake, will take two forms; the complicated, unsteady pressure field in the near wake will be modified, and mass transfer, and therefore vorticity transfer, across the center plane of the wake will be reduced, which will decrease the mixing of oppositely signed vorticity from the opposite sides of the wake. It is clear in many of the photographs that for high enough permeability the permeable splitter plates only reduce the mass transfer, and smoke lines may be seen that cross the wake center plane (*e.g.*, see Fig. 3.2b).

In general, the first impression received from glancing at the photographs is that the appearance of the wake with a permeable splitter plate is considerably different from that of the wake without one. One obvious difference is that the wake is clearly divided into separate halves by the presence of the splitter plate, and this is apparent since the vortex cores do not cross or overlap the wake center plane. Another obvious difference is that with the permeable splitter plate the vortex cores are substantially more circular in shape, and appear to be less turbulent in the cores, resulting in visually very well-defined vortex structures.

Despite the visual differences, the flow with a permeable splitter plate is structurally very similar to the flow without a permeable splitter plate, at least at low solidity (or for higher solidity, at high Reynolds number). In particular, there is a separation bubble behind the cylinder, at the end of which alternating large-scale vortices form. It is significant that the vortices are alternating in all cases in which they form, indicating that the two sides of the wake are still in communication despite the presence of the permeable splitter plate. The persistence of the alternating vortices is remarkable, and to bring about a change in the basic structure of the near wake it was necessary to go to low Reynolds numbers and high solidity, where it was found that the vortices no longer formed at all within the region of the wake shown in the photographs (as opposed, for example, to vortices continuing to form but without strict alternation).

Reference will be made in several places to the (Re, σ)-parameter space, by which is meant all possible values of the Reynolds number and the plate solidity. It is useful to recall that the plate solidity is being used to unambiguously characterize the permeable splitter plates, but in fact the solidity only labels a particular curve of $k(U)$ as detailed

in Appendix C, and the effective permeability will actually increase as the velocity normal to the plate decreases. Thus it is expected, and the flow visualization confirms, that for a fixed value of the solidity, a permeable splitter plate will be more effective at reducing the communication across the wake center plane and therefore will have a greater effect on the wake at low Reynolds numbers, and so "higher permeability" may be due either to decreased solidity or increased Reynolds number. Also, as was discussed in Chapter 1, the plate permeability k is a complicated function of the downstream distance along the plate, and this will be useful to keep in mind when examining the photographs.

3.3 The effect of changing the plate permeability

Figure 3.2 consists of smoke wire flow visualization photographs of the wake at Re = 7100 with splitter plates of differing permeabilities installed, and serves to illustrate the changes brought about in the wake by the permeable splitter plates. Figure 3.2**a** shows a photograph of the flow without a splitter plate (*i.e.*, solidity $\sigma = 0$), Fig. 3.2**b** shows the flow with a splitter plate of solidity $\sigma = 0.22$, and Fig. 3.2**c** shows the flow with a splitter plate of solidity $\sigma = 0.49$.

As is seen in this figure, the introduction of even the most permeable splitter plate used in these experiments, $\sigma = 0.22$, brings about a significant change in the visualized wake structure. For $\sigma = 0$, the vortices are generally oval in shape, the vortex centers lie very close to the wake center plane, and the bodies of the vortices extend across the wake center plane. In general, smoke lines are not well delineated in the vortex cores, instead the smoke has been dispersed (although not evenly) throughout the cores. In contrast, for $\sigma = 0.22$ the vortices are much more circular in shape, the cores do not cross the wake center plane (although it can be seen that there are smoke lines crossing the center plane and being entrained into vortices on the opposite side) and it is possible to discern some of the original smoke lines inside the vortex cores. The vortices are farther apart, and the length of the separation bubble is increased by the presence of the splitter plate. The vortices are strictly alternating, indicating that at this point in the (Re, σ)-parameter space the permeable splitter plate does not prevent communication between the two separated shear layers. Despite the separation of the wake brought about by the splitter plate, the overall similarities of the wake structures at $\sigma = 0.22$ and $\sigma = 0$ indicate that with the splitter plate present the vortex formation process is similar to that which occurs when no splitter plate is present. Figure 3.2**c** shows that increasing the solidity to $\sigma = 0.49$ results in a near wake structure that is similar to that when $\sigma = 0.22$, but with increased vortex separation distance, a longer separation bubble, and fewer smoke lines crossing the wake center plane. In particular, oppositely signed vortices still form at the end of the separation bubble and alternate across the wake.

With the smoke wire placed upstream of the cylinder very little smoke is entrained into the boundary layers separating from the cylinder, and so in these photographs it is not possible to see any of the internal structure of the separated shear layers. However, in Fig. 3.2**c** it is possible to make out a wavy outline along the boundary of the separation bubble that is suggestive of the vortices that form in the shear layer due to the growth of the Kelvin-Helmholtz instability, and the fully formed primary vortices appear to have "frills" around the outside edges of the cores that may correspond to the evolution of the shear layer instability after the shear layers have been entrained into the primary vortices.

It is possible in each of these three photographs to discern out-of-plane displacement of the smoke lines, indicating that the flow is slightly three-dimensional, particularly in the region where the primary vortices are fully formed.

3.4 The effect of Reynolds number

Since previous experiments (Apelt and West 1975) have shown that a solid wake splitter plate extending downstream to $x/D = 7$ prevents the formation of large-scale vortices in the near wake and changes the character of the wake instability from a body-coupled to a wake-profile instability (see Sec. 1.2), it is likely that if the permeability is low enough, then long permeable splitter plates will also prevent vortex formation. It is of interest to know if there is a region in the (Re, σ)-parameter space (with $\sigma < 1$) inside of which the splitter plates are effectively solid, as indicated by the disappearance of primary vortex formation from the near wake, and if so whether this corresponds to a change to a wake-profile instability, and to determine any other large changes that may occur in the near wake structure due to the presence of the permeable splitter plates. To this end, flow visualization photographs were taken to map a portion of the (Re, σ)-parameter space and these photographs are discussed in this section. For each solidity, photographs were taken across the Reynolds number range at which the smoke wire technique could be used, and those included here were taken at different values of the Reynolds number approximately spanning the Reynolds number range $2500 \lesssim \mathrm{Re} \lesssim 8000$. Although each photograph shown here is a single frozen moment of the dynamic wake formation process, a large number of photographs were taken at each point in the parameter space, and any significant variation in the flow features visible in different photographs at a given flow condition will be discussed. The photographs image the flow from the cylinder to approximately $11D$ downstream.

Figure 3.3 shows the wake of the circular cylinder without a splitter plate at three different Reynolds numbers (specified in the figure caption). In general, an increase in the Reynolds number produces a decrease in the length of the near wake separation bubble and a decrease in the vortex spacing. The vortex cores are most clearly defined at the intermediate Reynolds number shown in Fig. 3.3**b**. In all photographs in this figure, the

boundaries of the vortex cores tend to become more clearly defined, and the cores themselves become more elliptical, as the vortices convect downstream. At the lowest Reynolds number, Fig. 3.3**a**, the vortices form at the end of the separation bubble, but a fully formed circular vortex core is not visible until approximately $8D$ downstream of the cylinder, whereas at the highest Reynolds number, Fig. 3.3**c**, the fully formed circular vortices are apparent by about $4.5D$ downstream. At the lowest Reynolds number, the fully formed vortex cores are more circular in shape, becoming more oval in shape as the Reynolds number is increased, indicating that the vortices are more highly strained by the flow field of adjacent vortices as the Reynolds number is increased. As noted above, the internal structure of the shear layers is not clearly visible, although in Fig. 3.3**c** a wavy outline close to the upper shear layer boundary may be seen at the end of the separation bubble. At all Reynolds numbers, the smoke lines outside the cores remain clearly defined, while the smoke in the vortex cores is mostly diffuse and when smoke lines are discernible in the cores they are highly distorted, possibly indicating that the cores are turbulent.

Figure 3.4 shows the flow with a permeable splitter plate of solidity $\sigma = 0.22$, also at three different Reynolds numbers. At all Reynolds numbers shown, well-defined alternating vortices form at the end of the separation bubble, and the same structural differences noted in the comparison between Fig. 3.2**a** and Fig. 3.2**b** are visible between the flow conditions shown in this figure and those shown in Fig. 3.3, particularly the enhanced circularity of the vortex cores and the fact that vortices of a given sign are confined to one side of the wake. Again, at this solidity it can be seen that the length of the separation bubble decreases with increasing Reynolds number, and by comparing this figure with Fig. 3.3, it can be seen that for all Reynolds numbers the introduction of the splitter plate has substantially lengthened the separation bubble. The smoke in the vortex cores is less diffuse than was the case without the splitter plate, and well-defined smoke lines can be seen in the vortex cores even at the highest Reynolds number. Comparison with Fig. 3.3**c** shows that the smoke in the vortex cores in the two cases is of considerably different appearance, and although in Fig. 3.4**c** diffuse smoke is also visible throughout the cores, much of the diffuse smoke comes from smoke lines that have been entrained from the other side of the wake, and therefore the smoke lines have been altered by their passage through the wire mesh forming the splitter plate. These observations indicate that the vortex cores are somewhat less turbulent with the splitter plate in place, at least in the region immediately after the vortices have formed.

Figure 3.5 shows images of the cylinder flow with a permeable splitter plate of solidity $\sigma = 0.49$. There are five different Reynolds numbers shown in this figure to better show the changes in the wake with Reynolds number at this solidity. In all of these photographs, it appears that the top half of the separation bubble is somewhat larger than the bottom in the direction transverse to the flow, but this is an illusion caused by overexposure of the region near the splitter plate in the bottom half of the image caused by the light reflected from

the dense screen used to make the splitter plate. Figure 3.5**a** shows the wake at Re = 2500, and at this Reynolds number no primary vortex formation is visible, although there is a discernible end to the separation bubble where the shear layers begin directly interacting with the splitter plate. Since large-scale vortices do not form in the imaged region it appears that at this Reynolds number this permeable splitter plate is effectively solid, preventing communication between the two separated shear layers. It is not clear whether the shear layers actually reattach to the splitter plate, although it appears that they might and that the reattachment is unsteady. Data to be presented in Chapter 4 confirm the absence of a near wake primary frequency at these flow conditions.

Figure 3.5**b** shows a slightly higher Reynolds number, Re = 3900, and although the wake structure has changed slightly, it is not actually significantly different than the lower Re case, with no large structures forming at this Reynolds number as well. Although it appears in this photograph that with the increase in the Reynolds number the length of the separation bubble has also increased, this varies considerably between the photographs taken at this Reynolds number, and so this is due to the fact that only a single photograph is shown. In both of the photographs at low Reynolds number the boundary of the separation bubble exhibits wavy outlines, again possibly indicating the presence of shear layer vortices formed due to growth of the Kelvin-Helmholtz instability.

In Fig. 3.5**c**, at Re = 5500, the first indication of the primary large-scale wake instability appears, the wake as a whole taking on a sinuous shape with the two sides of the wake oscillating together, showing that there is communication across the wake center plane even though no circular vortex structures are visible. In Fig. 3.5**d** at Re = 7100 circular structures, with characteristics similar to those discussed for $\sigma = 0.22$, develop at the end of the separation bubble. The vortices that form at the higher Reynolds number shown in Fig. 3.5**e** are slightly more circular in shape and more closely spaced, but otherwise the two photographs in Figs. 3.5**d** and 3.5**e** are quite similar. The waviness in the edges of the separated shear layer edges that was apparent at the lower Reynolds number is almost indiscernible here. Even with the vortex formation, the ends of the separation bubbles are not as clearly defined as in the lower solidity cases, and the vortex separation distance is somewhat larger, although as before it is clear that when the vortex formation occurs at the end of the separation bubble the length of the separation bubble decreases and the vortex separation distance increases as the Reynolds number increases. The development of the sinuous wake at Re = 5500, followed by the appearance of vortex formation at the end of the separation bubble at Re = 7100, indicates that the wake instability with this permeable splitter plate has possibly changed from being a wake-profile instability at the lower value of the Reynolds number to a body-coupled instability at the higher value, although at the lower Reynolds number no circular vortices formed within the imaged region.

Figure 3.6 shows the Reynolds number dependence for a permeable splitter plate of

solidity $\sigma = 0.65$, again for three different Reynolds numbers. As for $\sigma = 0.49$, in Fig. 3.6**a** at Re = 2500 no vortices are observed to form within the imaged region. In Fig. 3.6**b**, Re = 5500, the wake is not markedly different from that at the lower Reynolds number and, in contrast to $\sigma = 0.49$ at this Reynolds number, the wake is not sinuous. In Fig. 3.6**c**, Re = 7900, the wake becomes sinuous immediately after of the separation bubble, and well-defined circular vortices form approximately $9D$ downstream of the cylinder. The presence of the splitter plate at this Reynolds number delayed the formation of large-scale structures until well downstream of the end of the separation bubble, in contrast to the lower solidity cases where the large-scale vortices either did not form in the imaged region, or formed very close to the end of the separation bubble, thus at this point in the (Re, σ)-parameter space the wake does exhibit a wake-profile instability.

3.5 Discussion

The flow visualization results provide support for the hypothesis that the permeable splitter plates can be used to modify the near wake without changing its basic structure. At high enough permeability, with the increased permeability due to either increased Reynolds number or decreased solidity, the basic structure of the wake as described by the standard model for a circular cylinder without a splitter plate is preserved even though the presence of the splitter plates brings about a change in the appearance of the wake. This is most strongly supported by the similarities in the primary vortex formation, in that alternating vortices still form at the end of the separation bubble. The obvious differences – the separation of the wake between the two sides of the splitter plate, the greater circularity of the vortices, and the confinement of the vortex cores on either side of the splitter plate – show that the splitter plates decrease the mixing of oppositely signed vorticity, while still permitting communication across the wake center plane through modification of the pressure field and to a lesser extent, through a decrease in the mass transfer between the two sides of the wake. The greater circularity of the vortices with the splitter plates indicates that they are subjected to a milder strain field than when there is no splitter plate, also consistent with a reduction in communication.

It has been shown that a change in the splitter plate permeability brings about a smooth change in the wake parameters, at least at high permeability (including the completely permeable case of no splitter plate), by the observation from the flow visualization that the length of the separation bubble increases with decreasing Reynolds number and with increasing solidity, which indicates that the length of the separation bubble increases with decreasing permeability. At intermediate and low permeabilities it does not appear from the flow visualization that this is the case, *i.e.*, the mean length of the separation bubble seems to be approximately constant at low permeability. This suggests that it is the

interaction between the vortex formation and the separation bubble that is responsible for the Reynolds number dependence of the length of the separation bubble, at least when the vortex formation occurs immediately downstream of the separation bubble. The change in the length of the separation bubble with changing solidity at constant Reynolds number indicates that the pressure field in the separation bubble is modified by the presence of a splitter plate, but the preceding observations suggest that the mechanism by which this occurs is the modification of the interaction between the separation bubble and the vortex formation process due to the presence of the splitter plate. Thus, the pressure field in the separation bubble is not directly dependent on the pressure drop across the wake center plane within the separation bubble, and therefore is not directly dependent on the value of the splitter plate permeability, but instead depends only indirectly on the permeability through changes in the nature of the wake instability that are brought about by the presence of the splitter plate. This implies that when the wake exhibits a wake-profile instability, with the primary vortex formation process occurring downstream of the separation bubble, the pressure field in the separation bubble will be independent of the splitter plate permeability, and furthermore, will depend on the Reynolds number only through the action of phenomena other than the primary vortex formation, such as the occurrence of transition to turbulence in the separated shear layers. This will be considered in more detail later.

The flow visualization results also indicate that the (Re, σ)-parameter space may be separated into three different regions. At high enough permeability the presence of a permeable splitter plate does not change the basic structure of the near wake; the wake instability remains body coupled (with the primary wake vortices forming at the end of the separation bubble) even though separation of the wake into two halves is apparent (*e.g.*, Fig. 3.4). At lower values of the permeability, the vortex formation is delayed several diameters downstream of the separation bubble, with the wake acquiring a sinuous shape in the region between the end of the separation bubble and the appearance of circular structures (*e.g.*, Figs. 3.5**c** and 3.6**c**), and the wake only exhibits a wake-profile instability. As the permeability is decreased still further, vortex formation does not occur within the region imaged in the photographs, and the wake boundaries show small-scale irregularity with approximately straight mean boundaries, and in particular, the wake boundaries are not sinuous (*e.g.*, Fig. 3.6**a** and **b**). This does not preclude formation of the large-scale vortices downstream of the region imaged, but significantly, when the large-scale vortices form they are always alternating indicating that for the vortex formation to take place, there must be sufficient communication between the opposite sides of the wake, even when the large scale vortices form downstream as a result of the developing wake-profile instability. It is reasonable to expect that for very long splitter plates at a very low value of the permeability the wake profile will decay before the wake-profile instability mechanism leads to formation of the large-scale vortices.

It was intended that the downstream extent of the splitter plate not be an experimental parameter, by the use of splitter plates that were effectively infinite in length. It was found that there was no change in the measured base pressure coefficient between permeable splitter plates of length $20D$ and $16D$, but that a significant change occurred when the plate length was reduced to $12D$ (this is discussed in Appendix A), and so $16D$ plates were used for all experiments as well as for the flow visualization. Note that $12D$ downstream is only slightly beyond the right-hand end of the imaged region, and that large-scale vortex formation is observed to occur at approximately $9D$ in Fig. 3.6**c**. Fig. 3.5**c** shows a sinuous wake downstream of the separation bubble, and it is likely that the growth of the wake-profile instability led to the formation of large-scale vortices at some point past the end of the imaged region, and therefore near to the downstream end of the splitter plate, and thus as far as the wake-profile instability is concerned $16D$ is probably not 'effectively infinite'. It is possible that at low permeability, vortex formation may occur far enough downstream from the near wake that measurements in the near wake are unaffected by the vortex shedding, and so the chosen plate lengths are effectively infinite as far as the structure of near wake is concerned. This will be discussed further in following chapters.

The change to a wake-profile instability at low permeability, with the concomitant shift of the vortex formation process to locations downstream of the separation bubble, is what motivates the avoidance in this thesis of the terms "formation region" and "shedding frequency." The separation bubble has been referred to as the formation region, but this is clearly not correct when vortex formation is delayed to several diameters downstream of the separation bubble, and, in the same circumstances, the vortices cannot be said to have shed from the cylinder when the vortices form far downstream, so that the wake profile has forgotten whether it has formed from the circular cylinder or from some other agency leading to an equivalent profile, such as the porous normal flat plate used by Cimbala (1984).

Modifications in the wake structure due to changes in the Reynolds number (through the effect on the plate-normal transverse velocities in the wake that scale with the free-stream velocity and therefore with the Reynolds number) and in the pressure drop across the plate (through changes in the plate solidity) are related, in that lowering the Reynolds number has an effect that is similar to increasing the solidity and thereby the pressure drop, and it would seem that there is the possibility of combining the two into a single parameter representing the permeability. This concept has already been used informally throughout this chapter, and seems reasonable in light of the results of Appendix C where the scaled drag coefficient of the plate, itself a function of solidity, is related to the plate-normal velocity through the scaled Reynolds number, and is very successful at collapsing the data for different solidities to a single curve. However, it is not obvious that the Reynolds number and the pressure drop coefficient may be combined into a single parameter, due to the complicated interaction of the wake with the splitter plate, the lack of available information

about the transverse velocities in the cylinder wake at these Reynolds numbers, and the complicated way in which the plate pressure drop depends on the downstream location, but informally this concept is useful in describing the wake with a permeable splitter plate.

Finally, in the flow visualization photographs the outlines of what have been conjectured to be vortices that form in the separated shear layers due to the Kelvin-Helmholtz instability are more readily discerned in photographs taken at low values of the permeability. This could be due to the greater length of the separation bubble at low permeabilities, since the instability will then have more time to grow before the shear layers are subsumed into the developing primary wake vortices or become involved in interactions with the splitter plates themselves. Thus, it is expected that growth of the shear layer instability is enhanced by the presence of the splitter plates, and this should be discernible as changes in the power spectral density measured at frequencies that are characteristic of the shear layer instability, which will be considerably higher than the primary wake frequency (as can be seen from the scale of the wavy outlines in the photographs, assuming that the relevant velocity scale is that of the free stream). Furthermore, if the permeable splitter plates do enhance the growth of the shear layer instability, this will also appear as differences in the downstream development of both the shear layer geometry and the power spectral density of the fluctuating velocities measured in the shear layers.

CHAPTER 4

Global measurements

"Through the undergrowth it goes with a plaintive sound, a musing sound; in it the unwinded cane and saplings lean as before a little gale, swaying without reflections as though suspended on invisible wires from the branches overhead. Above the ceaseless surface they stand – trees, cane, vines – rootless, severed from the earth, spectral above a scene of immense yet circumscribed desolation filled with the voice of the waste and mournful water."

William Faulkner, op. cit.

4.1 Introduction to the global measurements

The term "global measurements" is used here to describe measurements of flow quantities that depend on, and are indicative of, the state of the entire near wake. In this chapter, measurements of two such quantities are presented as functions of Reynolds number; the base pressure, which is the pressure measured at a point on the cylinder surface 180 degrees from the forward stagnation point referenced to the pressure in the free stream at infinity, and the primary wake frequency (measured in the near wake) corresponding to the rate at which large structures form in the wake and then convect downstream. It is clear that there is a relationship between these two flow quantities, but the precise nature of this relationship remains obscure (Roshko 1992).

Measurements of the pressure profiles around the cylinder, and the pressure drag on the cylinder obtained from the pressure profiles, are also presented. The drag is closely related to the cylinder base pressure, as the pressure profiles all have similar shapes with only the overall level measured in the base region of the cylinder changing with Reynolds number, so it is expected that the drag will scale with the base pressure.

It is noted in Chapter 2 that the wind tunnel was limited to a velocity range of about 1.5–10.5 m/s, and since all of the cylinders used in this study were of (nominal) diameter 2.54 cm , the accessible Reynolds number range was $2.5 \cdot 10^3 \lesssim \mathrm{Re} \lesssim 1.8 \cdot 10^4$. In this particular Reynolds number range the 'global' values measured in the flow undergo large changes in magnitude with Reynolds number, and as mentioned in Chapter 1 this is usually attributed to a change in the location in the wake at which the separated shear layers undergo transition to turbulence. The measurements presented in this chapter do not by

themselves give definitive answers to questions about the effects of the shear layer structure on the near wake. However, the results do demonstrate that by using permeable splitter plates it is possible to elucidate the Reynolds number dependencies and the interactions of the different elements of the flow in the near wake, and the technique is used here to explore the relationship between the vortex formation and the base pressure on the cylinder. The close relationship between the base pressure and the cylinder drag means that this also gives information about the relationship between the vortex formation and the drag.

4.2 Effects of the permeable splitter plate on global quantities

Figure 4.1 shows both the base pressure coefficient and the non-dimensional primary wake frequency as functions of the Reynolds number. What is plotted is actually the base *suction* coefficient, which is defined as the negative of the base pressure coefficient, defined as

$$C_{pb} = \frac{p_b - p_\infty}{\frac{1}{2}\rho U_\infty^2}.$$

The primary wake frequency is non-dimensionalized as the Strouhal number,

$$St = \frac{f_1 D}{U_\infty},$$

and the two sets of data are plotted on aligned axes to help in visualizing the relationships between them.

Figure 4.1**a** shows the base suction coefficient versus Reynolds number for all of the standard plates, and also includes data for an impermeable ($\sigma = 1$) splitter plate. At all Reynolds numbers, the highest magnitude of the base suction occurs when there is no splitter plate ($\sigma = 0$) and in that case the suction increases with increasing Reynolds number throughout the Reynolds number range. At the opposite extreme of the permeability, the impermeable splitter plate gives (approximately) the lowest value of the base suction, and is practically constant across the Reynolds number range. The value of the base suction for other values of the permeability lie at or between these two extremes, which therefore roughly define an envelope of the possible values of the base suction under these experimental conditions. Although the mean values of the base suction at low Reynolds number were higher for $\sigma = 1$ than for $\sigma = 0.65$ and $\sigma = 0.49$, this may have been caused by misalignment of the impermeable splitter plate (which was constructed by fastening a thin piece of sheet metal on top of one of the permeable splitter plates), which was shown by Apelt and West (1976) to have a significant effect on the value of the base pressure, and is also probably due in part to scatter in the data caused by measuring pressures that were a very small fraction of the full scale range of the pressure sensor. Although the uncertainty in the measurements is greater at low Reynolds numbers, the increase in the uncertainty

is mostly due to the systematic uncertainty contributed by using the sensors at a small fraction of their range, since for Re < 5000 the statistical contribution to the uncertainty is a small fraction (typically less than 10%) of the total uncertainty. In Fig. 4.1, the error bars show the combined systematic and statistical uncertainty.

For the flow with a permeable splitter plate of solidity $\sigma = 0.65$, for Re $\lesssim 9000$ the base suction is constant at approximately the same value as in the impermeable case, and above this Reynolds number the base suction increases linearly with Reynolds number. A similar trend in the base suction with Reynolds number is observed for $\sigma = 0.49$, except that the increase from the $\sigma = 1$ value begins at the lower value of Re ≈ 5000. For $\sigma = 0.22$, $\sigma = 0.35$ and $\sigma = 0.65$, and for $\sigma = 0.49$ at Re $\lesssim 11000$, over the Reynolds number range in which the value of the suction increases with Reynolds number, the increase is approximately linear and the rates of increase are all similar. For flow without a splitter plate ($\sigma = 0$), at low Reynolds number the rate at which the base suction increases is greater than those for nonzero solidity, and above Re ≈ 10000 changes to a value that is slightly less than those for nonzero solidity. This change also seems to occur for $\sigma = 0.49$ at a Reynolds number of Re ≈ 11000, and the new slope is approximately the same as that for $\sigma = 0$. Noting that the scatter for $\sigma = 0.49$ is very low, it is possible that this change in the slope occurs for some other values of the solidity, but is masked by scatter in the data.

In anticipation of the discussion of the Strouhal number below, note particularly that the curves do not converge or intersect as the Reynolds number is increased, unless the curves are extrapolated to much higher Reynolds numbers, *e.g.*, the value of the base suction with $\sigma = 0.22$ will be equal to that with $\sigma = 0$ at a higher Reynolds number than was attainable in this experiment if the slopes of the corresponding curves that are observed at the upper limit of the present Reynolds number range persist to higher values of the Reynolds number.

It is observed in Chapter 3 that the main structural features of the wake were preserved when the highest permeability splitter plate available ($\sigma = 0.22$ in these experiments) was present in the wake. At all Reynolds numbers, when the $\sigma = 0.22$ splitter plate was present there was a large change in the measured values of the base suction from those measured without a splitter plate. Thus, the perturbation produced in the basic flow by the introduction of the the most permeable splitter plate available was not small, but despite the large modification to the base suction caused by the splitter plate, the basic structure of the flow was preserved. It is also observed in Chapter 3 that the size of the separation bubble decreased with increasing permeability, and the base suction shows the opposite trend, *i.e.*, an increase in the permeability led to a higher value of the base suction, so that the length of the separation bubble is inversely correlated with the base suction.

Figure 4.1**b** shows the primary wake frequency in the form of the Strouhal number plotted against Reynolds number for all of the standard plates. For the data shown in the figure, frequencies were obtained from spectra computed from the fluctuating voltage signal measured by a hot wire located at $x/D = 2.5$, $y/D = 1.5$, which is in the potential flow outside of the separation bubble at all relevant Reynolds numbers (see Chapter 5), and therefore only frequencies that were discernible in the near wake region could be measured. The relative amplitudes of the power spectral peaks determined from the spectra at different points in the (Re, σ)-parameter space cannot be meaningfully compared, since the location of the hot wire was fixed in the lab coordinates, but the geometry of the near wake is dependent on both the Reynolds number and the solidity. Details of how the spectra were computed and used to determine the frequencies are given in Appendix D. In general, the data from which the frequencies were derived were collected simultaneously with the base pressure data discussed above and so frequency data were also taken for the impermeable splitter plate, but in that case the discrete frequencies observed in the spectra correspond to vibration of the plate at the second harmonic of the tunnel fan rotation frequency and are of extremely narrow bandwidth and small amplitude, and so it was concluded that no spectral peaks corresponding to vortex formation were observable in the near wake with the impermeable splitter plate.

For low permeability, there is a minimum Reynolds number at which primary frequency peaks were discernible in the spectra, so in this case the Strouhal number is not defined for values of the Reynolds number below that minimum and the corresponding curves, $\sigma = 0.65$ and 0.49, start at higher values of the Reynolds number than the curves for lower values of the solidity. There is some uncertainty in the determination of the value of the minimum Reynolds number, since there is still a discernible, if not clearly defined, "peak" in the power spectra at values of the Reynolds number below the cutoff values, but the lack of a sharp central peak in the spectra was the criterion used (examples of spectra from these low permeability cases are shown in Appendix D). The lack of a discernible primary wake frequency in the near wake does not necessarily indicate that vortex formation no longer occurs, as the location may only have moved downstream far enough that the frequency can no longer be detected at the near wake hot-wire location. That this probably occurs for low permeability flow conditions in the present experiments can be surmised from the flow visualization photograph of the flow with a splitter plate of solidity $\sigma = 0.65$ at Re = 7900, shown in Fig.3.6**c**, where sinuous fluctuations of the wake boundary are seen to evolve into circular vortices, and from the photograph of the flow with a splitter plate of solidity $\sigma = 0.49$ at Re = 5500, shown in Fig.3.5**c**, which is approximately the minimum Reynolds number for that solidity at which the primary wake frequency is discernible, and where sinuous fluctuations of the wake boundary are also visible but do not evolve into vortices. These results give some quantitative points delineating the boundaries in the (Re, σ)-parameter space at which the the wake undergoes a change from a body-coupled to

a wake-profile instability, corresponding to the vortex formation moving downstream away from the separation bubble. For all other solidities ($\sigma \neq 1$), and at the higher Reynolds number for the $\sigma = 0.65$ and 0.49, clearly defined, characteristically shaped sharp peaks were visible in the spectra, examples of which are shown in the appendix.

Four different shapes of the St(Re) curve are seen in Fig. 4.1**b**. For $\sigma = 0$, the Strouhal number gradually decreases with increasing Reynolds number. For $\sigma = 0.22$ the Strouhal number is nearly constant across the Reynolds number range. For $\sigma = 0.35$ and 0.49 at low Reynolds numbers the Strouhal number increases rapidly with Reynolds number, and then quickly levels off to nearly constant values. For $\sigma = 0.65$, the Strouhal number appears to increase linearly above the minimum Reynolds number across the Reynolds number range. For $\sigma \leq 0.65$ all of the curves appear to converge (within the experimental uncertainty) to a common, constant value of St ≈ 0.2. Since the trend of the curve for $\sigma = 0.65$ indicates that it probably would have continued to increase if higher Reynolds numbers had been accessible, it may be that at high enough values of Re this curve would converge to the others as well (although it is possible, or even likely, that other Reynolds number dependent effects would intervene). If it is assumed that the observed curve may be extrapolated to higher Reynolds number, a linear fit to the data points suggests that the Strouhal number for $\sigma = 0.65$ would reach St = 0.2 at Re ≈ 23000. As is the case for the base suction, the Strouhal number varies smoothly with Reynolds number for all plate permeabilities. Note that for $\sigma = 0$ and $\sigma = 0.49$, the approach to a constant value of St at the higher Reynolds numbers corresponds to the decrease in the slope of C_{pb}(Re) at $\sigma = 0$. This is not the case for the other values of σ for which the values of St also approach the same constant without corresponding changes in C_{pb}(Re), in fact, for $\sigma = 0.22$ the value of St is nearly independent of Reynolds number, which is definitely not true for the base suction.

In the curve corresponding to $\sigma = 0.65$, around Re = 15500 there are two data points that do not seem to lie on the same curve as the other data, but instead fall considerably below the other data. Examination of the corresponding spectra, which are the two traces in Fig. 4.2 labeled Re = 15100 and Re = 15800, reveals that the spectral peaks corresponding to these points are considerably narrower than the spectral peaks characteristic of the primary wake frequencies found at Reynolds numbers immediately above and below those at which the anomaly occurs, and increasing the tension in the splitter plates eliminated the anomalous points. This implies that the probable cause of the anomalous results was resonance between the vortex formation frequency and a natural frequency of the plate causing a "lock-in" of the vortex formation frequency to the plate frequency, and increasing the plate tension moved the plate frequency out of the range that could be excited by the flow. As was mentioned in Chapter 2, it was difficult to attain high enough levels of tension in the $\sigma = 0.65$ splitter plate, and this may account for the generally higher scatter observed for the measurements at this solidity. This also demonstrates that the vortex

formation process is sensitive to perturbation frequencies imposed in the wake downstream of the cylinder, and that there is potential for control of the vortex formation by using vibrating elements in the wake. This was not pursued further in the present work.

4.3 Pressure profiles and drag measurements

In this section, the results of mean pressure measurements around the surface of the cylinder are presented in the form of pressure coefficient profiles. The definition of the pressure coefficient is similar to that of the base pressure,

$$C_p(\alpha) = \frac{p(\alpha) - p_\infty}{\frac{1}{2}\rho U_\infty^2}.$$

The rotation angle α is measured from the upstream stagnation point on the cylinder surface, so that the base pressure coefficient as previously defined is given by the value of the surface pressure coefficient measured at $\alpha = \pm 180°$. The profiles were obtained using a cylinder similar to that shown in Fig. 2.5, with the end plugs modified so that thrust bearings could be installed to permit the rotation of the cylinder about its axis when the tunnel walls were under tension from the splitter plates. A shaft led from the plug, through the cylinder mounting hole in the wall of the test section and out of the tunnel, where a protractor was used to determine the rotation angle. With the free-stream velocity constant, the angle of the cylinder was set, and the data were recorded from which the mean pressure was obtained. The cylinder was then rotated to a new angle and a new data point collected.

As is mentioned in the preceding section, Apelt and West (1975), using a circular cylinder and a long, impermeable splitter plate fixed to the cylinder base (so that there was no leakage across the wake centerplane at the base), discovered that base pressure measurements were very sensitive to the orientation of the plate and cylinder, and they found it necessary to carefully adjust the plate angle to obtain pressure profiles that were symmetric for positive and negative angles. The current experimental arrangement is different from that of Apelt and West, in that there is a small gap at the cylinder base, and the plate itself is permeable. To check the symmetry of the profiles, data were taken in every case through a full 360° revolution of the cylinder, and the pressure profiles derived from the data were found in each case to be symmetrical. Figure 4.3 shows the pressure coefficient profile C_p at Re = 9630 for $\sigma = 0.65$, the highest solidity for which pressure profile measurements were made, as a function of the absolute value of the rotation angle α, and shows that the profile is quite closely symmetric. The profiles for other values of the solidity display less discrepancy than that shown in this figure, and so only the data for positive values of α will be discussed.

Figure 4.4 shows pressure coefficient profiles around the surface of the circular cylinder for three solidities (given in the figure caption), at several different Reynolds numbers. The profiles are all very similar, the main difference in the data taken at different Reynolds numbers being displacement of those sections of the profiles corresponding to the base region, *i.e.*, that portion of the cylinder that lies within the separation bubble, with lower base pressures corresponding to higher Reynolds numbers. In all cases the minima of the pressure distributions, which indicate the average location on the cylinder at which the boundary layers separate from the cylinder, appear to be at approximately the same value of $\alpha = (70 \pm 3)°$ from the front stagnation point (the cylinder was usually rotated through 5° and 10° steps).

Using the surface pressure profiles, the pressure drag on the circular cylinder was found by integrating the component of the pressure force exerted on the cylinder surface in the direction of the free-stream velocity, which for symmetric profiles gives

$$C_D = \int_0^{\pi} C_p(\alpha) \cos(\alpha)\, d\alpha .$$

The trapezoidal rule was used to estimate the integral, using the experimental data without smoothing or curve fitting, and the results are plotted in Fig. 4.5 along with classical data for the total drag of a circular cylinder from Wieselsberger (1922) (the difference between the total drag and the pressure drag is the skin friction drag, and is only a few percent of the total drag in this Reynolds number range; see Goldstein 1938). The present values of C_D for $\sigma = 0$ are considerably higher than the classical data at all Reynolds numbers, and this reflects differences in the experiments, most probably the fact that end plates were used in the present case, which are shown in Appendix A to significantly decrease the value of the base pressure. End plates were not used by Wieselsberger, whose data were obtained from cylinders suspended in an open jet wind tunnel, with the drag determined from the deflection of the cylinders from the vertical by the drag forces (see Wieselsberger 1921 for further details). However, the overall shape of the drag curve for $\sigma = 0$ is similar to that of Wieselsberger's over this Reynolds number range.

It can be seen that the drag curves have shapes that are very similar to the base suction curves in Fig. 4.1**a**, suggesting that the drag will scale with the base pressure both with and without a permeable splitter plate present in the wake. Assuming that the drag is proportional to the suction, $C_D = A(-C_{pb})$, and using the value of C_D from this figure and the value of $C_p(180°)$ from the pressure coefficient profiles in Fig. 4.4 the value of A was determined. The results are given in Tab.4.1, and show that although the drag is nearly proportional to the base pressure for a given solidity, the value of A is a function of the solidity.

σ	Re	C_D	$-C_{pb}$	A
0	4800	1.00	0.93	1.1
	7200	1.10	1.08	1.0
	9600	1.18	1.20	0.99
	12300	1.22	1.27	0.96
	15300	1.24	1.30	0.96
.22	4800	0.85	0.75	1.1
	9600	0.93	0.88	1.1
	15300	1.01	1.03	0.98
.65	4800	0.76	0.60	1.3
	9600	0.77	0.61	1.3
	15300	0.81	0.69	1.2

TAB. 4.1 Value of the proportionality factor between the pressure drag coefficient and the base suction.

The profile taken with a permeable splitter plate of solidity $\sigma = 0.65$ at Re = 4800 shown in Fig. 4.4c, which is the profile taken at the lowest permeability, does not follow the same pattern as the other profiles. For most values of α it is nearly coincident with the profile taken at the same solidity and Re = 9600, since even though a primary wake frequency can be detected at Re = 9600, at that Reynolds number the vortex formation does not yet interact strongly with the separation bubble and so the pressure profile is almost unchanged from the lowest Reynolds number. However, there is a small difference between the curves for Re = 4800 and Re = 9600 near the minimum value of the pressure coefficient, which corresponds to the mean location of the boundary layer separation. The minimum occurs at the same value of α, but the value of C_p is lower for the lower Reynolds number, which is the opposite trend than for the flows at higher permeability where the minimum value of C_p decreases when the Reynolds number is increased. Also, the departure from the minimum (as α increases) is more gradual at Re = 4800 in that it reaches the base value somewhat farther around the cylinder. This does not effect the value of the drag since the differences are near $\alpha = 90°$ where the pressure forces do not contribute much to the drag, and the value of the drag coefficient is unchanged between the two Reynolds numbers.

For flow conditions other than $\sigma = 0.65$, Re = 4800, the similarity of the pressure profiles taken under different flow conditions indicates that the structure of the separation bubbles is similar, at least near the cylinder, and that the processes leading to boundary layer separation are similar with and without the permeable splitter plate. The mean separation point is at the same location on the cylinder, and the rise in the pressure from the minimum value to the value in the base region occurs over the same region on the cylinder surface. Thus, except at very low values of the permeability, the process leading to boundary layer separation and the initial formation of the free shear layers, as well as

the pressure field in the separation bubble on the rear of the cylinder, are not substantially altered by the presence of the permeable splitter plates, except for a uniform increase in the value of the pressure.

4.4 Discussion

The observed decrease in the slope of the base suction curve for $\sigma = 0$ beginning around Reynolds number 10^4 is in keeping with the observations of many researchers that for flow past a circular cylinder without a splitter plate at Reynolds numbers in the range $2 \cdot 10^4 \lesssim \mathrm{Re} \lesssim 1.5 \cdot 10^5$ (which will be referred to as the "constant range") the drag coefficient (and hence the base pressure coefficient as discussed in 4.3), and the Strouhal number are approximately constant. The leveling off of the C_{pb} curves is described by the standard model as the penultimate portion of the same process responsible for the large changes with Reynolds number in the present Reynolds number range, *i.e.*, the upstream movement of the location at which the transition to turbulence occurs in the separated shear layers. At the lower end of the present Reynolds number range ($\mathrm{Re} \lesssim 10^4$) turbulent transition in the shear layers occurs in a region which is far enough downstream that the shear layers are relatively unaffected by the presence of the cylinder body and the location of transition is very sensitive to changes in the Reynolds number, as it is for plane mixing layers. However, as the location of transition approaches the cylinder, the presence of a solid boundary in the form of the cylinder itself influences the shear layer instability and slows the upstream movement of the transition point so that the shear layer, and therefore the near wake, is relatively insensitive to changes in the Reynolds number within the constant range. However, the upstream motion of the transition point is only slowed, and ultimately it will move to the point at which separation occurs on the body so that at high enough Reynolds number the boundary layers will be turbulent at or before separation. This places an upper limit on the constant range which is experimentally found to be around $\mathrm{Re} \approx 3 \cdot 10^5$ (Schewe 1986), which corresponds to the so-called critical point in the drag versus Reynolds number curve at which the drag coefficient drops precipitously due to the different behavior of the turbulent boundary layers.

From the data shown in this chapter, it is evident that the process that leads to the leveling of the base pressure curve in the constant range for $\sigma = 0$ is significantly modified by the presence of the permeable splitter plates, since when the permeable splitter plates are present the rate of change in the base pressure with Reynolds number does not always exhibit a decrease as the constant range is approached. This can be accounted for within the standard model if the location at which turbulent transition occurs in the shear layers moves downstream when a permeable splitter plate is present, so that a greater change in the Reynolds number will be required before the transition occurs close to the body, although

this does not explain the change in slope observed for $\sigma = 0.49$. In contrast to this, for most non-zero values of the solidity, the non-dimensional vortex formation frequency does approach a constant value, in some cases much more quickly than for $\sigma = 0$, which has the implication that the mechanism that selects the primary wake frequency is different from that which controls the base pressure.

By comparing Fig. 4.1**a** and **b**, it can be seen that for low permeability the Reynolds number at which the primary wake frequency becomes discernible in the near wake is close to or less than the value of the Reynolds number at which the base suction begins to increase from the value obtained with an impermeable splitter plate. Since the wake frequency was detected by a hot wire located in the potential flow outside of the near wake, it is likely that the potential flow fluctuations in the free-stream velocity caused by the formation and subsequent convection of the large-scale vortices could be detected before the vortex formation had moved far enough upstream to be able to interact with the separation bubble. Conversely, the location of the hot wire makes it improbable that the vortex formation could occur far enough upstream to interact with the separation bubble without the primary wake frequency being detected. These observations indicate that when the permeability is low the deviation of the base suction from a value that is independent of the plate solidity and the Reynolds number occurs at the Reynolds number at which the wake instability changes character from a wake-profile to a body-coupled instability, which occurs when the vortex formation begins to interact with the separation bubble. This supports the prediction made in the last chapter on the basis of the flow visualization results that when the wake instability is not body coupled the base pressure will be independent of the splitter plate solidity, and it also appears that in this case (for the present experimental conditions) the base pressure is independent of the Reynolds number as well.

It follows that there is a baseline contribution to the base pressure that is maintained across the separated shear layers independent of the vortex formation and independent of the Reynolds number, at least in this Reynolds number range. It also follows that if the standard model is correct in explaining the large changes with Reynolds number in this range by the upstream movement of the location of turbulent transition in the shear layer, since there is no effect when vortex formation does not occur in the near wake, this mechanism must act on the base pressure through its effect on the vortex formation process. Still within the context of the standard model, the converse of this is that transition in the shear layers must play a significant role in determining the primary wake frequency.

CHAPTER 5

Effects of permeable splitter plates on the separated shear layers

5.1 Introduction to the shear layer measurements

Details of the relationship between the shear layers separating from a circular cylinder and the overall structure of the near wake have proved elusive because of the sensitive nature of the flow past a circular cylinder and because of the lack of a technique for continuously varying the near wake interactions. It has been shown in previous chapters that varying the communication between the two sides of the wake through the use of permeable splitter plates results in a continuous change in the large-scale vortex formation, making it possible to directly investigate the development of the separated shear layers and their influence on the flow in the near wake. The results of that investigation are presented in this chapter. Detailed measurements of the shear layers that have separated from the circular cylinder are presented, both with and without permeable splitter plates in the wake. The measurements are of mean and fluctuating values of the streamwise velocity component, and were made by moving a calibrated hot wire through the shear layers. Profiles of both the mean and fluctuating velocities were measured, and data were collected with sufficient resolution so that power spectra can be computed from the velocity fluctuations, and these measurements yield information about the Reynolds number dependence of the stability of the separated shear layer.

Measurements were made at three different Reynolds numbers that approximately span the available range, and for three different values of the solidity, for a total of nine different flow conditions. The different solidities were chosen to obtain information about the shear layer under limiting conditions in the near wake: $\sigma = 0$ to provide comparable baseline measurements as well as to explore the structure and development of the "natural" shear layer instability, $\sigma = 0.22$ to examine what happens when the near wake is perturbed, but by the minimum amount possible in the current experiments, and $\sigma = 0.65$ to examine the shear layers when the vortex formation either does not occur or occurs so far downstream that it has little or no effect on the near wake.

When a value for the solidity σ is given, as in the preceding paragraph, it will be understood to indicate that a permeable splitter plate of that solidity is present in the wake.

In this chapter, as in previous chapters, "high permeability" will refer to flow conditions for which the primary wake frequency is discernible in the near wake (*e.g.*, all data taken with $\sigma = 0$ and 0.22) and "low permeability" will characterize the flow for which it is not. Furthermore, throughout this chapter, the shear layers separating from the circular cylinder will be referred to simply as the separated shear layers, and when a distinction needs to be made between the separated shear layers and other experimental geometries that give rise to shear layers (such as plane mixing layers), the difference will be made explicit.

As discussed in Chapter 1, the standard model assumes that the primary cause of the large Reynolds number dependent changes observed in the flow past a circular cylinder in the Reynolds number range $3 \cdot 10^2 \lesssim \mathrm{Re} \lesssim 2.0 \cdot 10^4$ is the upstream movement of the location at which the separated shear layers undergo transition to turbulence (Schiller and Linke 1933, Goldstein 1938, Roshko and Fiszdon 1969). It is reasonable to test this assumption by investigating the stability of the shear layers, the location at which transition occurs in the shear layers, and the relationship between the shear layer instability and the near wake structure. The experiments of Schiller and Linke (1933), which form the basis for this assumption, investigated only the mean properties of the shear layers, and did not explore the development of the shear layer instability. In this chapter, the flow in the shear layer, and the relationship of the near wake structure to the shear layers will be investigated both with and without the permeable splitter plates in the wake. Comparison of the results to other investigations of the separated shear layers will be postponed until the next chapter.

5.1.1 Experimental technique

The quality of the free stream and the basic flow are discussed in Appendix A, and are mentioned here only to point out that although there are several discrete frequencies in the free stream, they are of very low amplitude (see Fig. A.1), and that the free-stream turbulence does not show a broad band turbulent spectrum, but rather the ubiquitous $1/f$-type spectrum that is present in many random processes, upon which small-amplitude discrete frequency peaks are imposed. In particular, the amplitudes of the discrete peaks are several orders of magnitude below that of any frequencies appearing in the flow with the circular cylinder model installed.

The single hot wire was mounted on a three-axis traverse of which only two axes were used during these investigations, and all data were taken at the center of the tunnel in the plane normal to the cylinder axis. The hot wire was calibrated and the hot-wire data were reduced to velocity data according to the technique discussed in Appendix B. For each different case of solidity and Reynolds number, the hot wire was calibrated both before and after the data set was collected. Initially, calibration data points were taken at the completion of each traverse, but all calibrations from a given day were found to

agree to within $\pm 0.5\%$, so only the initial and final calibration data were taken for the rest of the experiments. Therefore, for each day on which data were taken, the initial and final calibration data sets were combined and used to calculate the hot-wire calibration coefficients.

At the inner edges of the shear layers, the minimum velocity encountered was usually somewhat less than the lowest velocity used in the hot-wire calibration, which are limited by the lowest velocity for which the flow could be maintained in the wind tunnel. Similarly, when the free-stream velocity was at the highest values for which data are presented here, the maximum mean velocity measured at the outside edge of the shear layer (which is typically $1.2-1.3\,U_\infty$) as well as the maximum amplitudes of the instantaneous velocity fluctuations were greater than the maximum velocity used in the hot-wire calibration, which was limited by the maximum free-stream velocity attainable in the tunnel with the experiment in place. Under these conditions, conversion of the hot-wire voltage signal to velocity requires extrapolation of the hot-wire calibration, which contributes to the uncertainty in the absolute values of the velocity. The hot-wire calibration method is a good linearizer of the hot-wire voltage signal across this velocity range, so extrapolation of the calibration introduces a proportionality factor that is close to unity. An estimate of the uncertainty in the velocity due to extrapolating the hot-wire calibration in this manner was obtained from a hot-wire calibration using data collected in a jet facility with a higher velocity range. Calibration data were collected over the velocity range $0 < U < 20$ m/s, calibration coefficients were computed using only the data for velocities $U < 11$ m/s, and then the resulting calibration was used to convert the entire data set. The resulting deviation of the fit velocities from the measured velocities, expressed as

$$\delta U_f = \left| \frac{U_f - U_m}{U_m} \right|,$$

was less than 2% at $U \approx 20$ m/s, and decreased with decreasing velocity, falling to 0.5% within the range of the calibration. In any case, the results that are to be presented in this chapter, such as the shear layer boundaries and growth rates, do not depend on absolute values of the velocities and none of the comparisons between different flow conditions are significantly effected by the uncertainty in the absolute values of the measured velocities.

It is important to consider the question of reversed flow for the derivation of the shear layer profiles. In an ideal, completely laminar shear layer with the direction of flow reversed across the layer, there will be a point at which a single hot wire will measure a zero mean velocity. Since the hot wire rectifies velocity directions, away from this point the wire will show a positive velocity magnitude regardless of the direction. If the flow is turbulent but has no net mean velocity, the turbulence still provides a bias velocity (since there will always be some flow past the wire, which only averages to zero if directions are taken into account) and so the measured value of the velocity magnitude will not be zero. However,

across the turbulent shear layer, the actual transverse location of zero mean velocity will be a minimum of the hot-wire derived velocity, and using this it is possible to detect the point at which the hot wire crosses into the reversed flow. If no minimum point is detected, it is probable that the wire has not encountered reversed flow. On the other hand, the flow situation is not necessarily simple in the wake of a bluff body, since the mean flow may not be reversed but the mean direction of the flow may be at some angle to the free stream, and this situation cannot be detected with a single hot wire. Because of this possibility it is not particularly useful to derive specific conclusions about the velocity vectors from data taken with single wires in complicated flows such as bluff body wakes. The non-zero minimum velocity will give a slight bias to the value of the velocity difference across the layer: this will only be significant if the data are compared to other data measured without the bias, since the biased shear layer profiles will scale in the same fashion as the unbiased profiles.

To start a given traverse at a particular downstream location (x/D) the shear layer was first located by doing a "fast" traverse in the y-direction (across the shear layer) that collected only the mean hot-wire voltage without saving the actual sampled data. Usually a second traverse was then performed in which data were collected with low temporal resolution over a long time period to produce a long-time-averaged mean profile. Either this profile, if available, or the profile from the fast traverse was used to locate the outer half of the shear layer and data were then collected at several (four to six) points across the outer half of the shear layer, with sufficient temporal resolution to permit the power spectral density of the fluctuating velocity to be accurately computed. Traverses were made at several downstream locations, until (and usually past) the point at which the profile was observed to take on a wake-like profile, defined as a profile for which the condition $du/dy = 0$ does not occur on the low speed side; an example of a wake-like profile is shown in Fig. 5.1**d**. This technique located the end of the separation bubble under all flow conditions. With a permeable splitter plate installed the hot wire was not moved closer to the permeable splitter plate than $y/D \approx 0.1$.

5.1.2 Data reduction

Each shear layer traverse yielded a table of the mean and fluctuating velocities versus transverse position at each downstream location, corresponding to the shear layer profile. The mean velocity data were then fit to an error function profile according to the formula

$$u_*(\eta) \;=\; \frac{1}{2}\left(1 + \mathrm{erf}(\eta)\right),$$

where

$$u_* \;=\; \frac{(u(\eta) - U_{\min})}{\Delta U},$$

ΔU is the velocity difference across the layer, and

$$\eta \;=\; \frac{y - y_c}{\delta_*}.$$

The fit parameters are y_c and δ_*, and ΔU is taken in all cases as the difference between the maximum velocity $U_{\max}$ and the minimum velocity $U_{\min}$ taken from the data set. Since the profiles become wake-like at some downstream location, as discussed in Sec. 5.1.1, a four-parameter fit was tried by adding ΔU and $U_{\min}$ to the fit parameters. This did not significantly change the results and so only the two-parameter fit was used.

Figure 5.1 shows several example fit profiles with both the mean velocity profile data from which the fits were computed and the mean velocities obtained from the high resolution data superimposed, for several downstream positions in the wake (specified in the figure caption). The data were collected at a Reynolds number of Re = 9300 with a permeable splitter plate of solidity $\sigma = 0.22$ in the wake. The thickness of the profiles and the velocity differences across the layers are considerably different at the different positions. The locations in the shear layer (in normalized coordinates η) at which spectra are available are not identical for each downstream location, but in general they extend to the outer edge of the shear layer (note that for the error function profile, at $\eta = \pm 1.64$ the velocity is within 1% of the free-stream value). Figure 5.1**c** shows the presence of a velocity minimum corresponding to the edge of a region of reversed flow, and Fig. 5.1**d** shows that the two-parameter fit procedure is usually successful at finding a reasonable fit even for wake-like profiles, although in that case it generally underestimates the value of δ_*.

The "momentum thickness"

$$\theta = \int_{-\infty}^{\infty} \frac{u}{\Delta U}\left(1 - \frac{u}{\Delta U}\right) dy ,$$

is estimated from the data using the trapezoidal integration rule, and the vorticity thickness is estimated from the fit profile using

$$\delta_\omega = \frac{\Delta U}{(\partial u/\partial y)_{\max}}$$

$$= \delta_* \sqrt{\pi} \ .$$

The error function profile was chosen over the (also common) hyperbolic tangent profile as the functional form because the values of δ_ω/θ computed solely from the data were in most cases closer to the value of $\delta_\omega/\theta \approx 4.44$ obtained analytically from the error function profile than to $\delta_\omega/\theta \approx 4$, the analytical result for the hyperbolic tangent profile.

The shear layer boundaries, defined as those points y_{01} and y_{99} at which the mean velocity reaches $0.01\Delta U$ and $0.99\Delta U$ respectively, are estimated from the data as the transverse locations of the data points that are closest to the value of y_c but for which the corresponding values of $u(y)$ are outside of the given bounds. This is preferred to using the fit profile because it more clearly identifies the point at which the shear layers intersect the wake centerline.

5.2 Shear layer mean geometry

Figure 5.2 shows the mean shear layer boundaries in terms of y_{01} and y_{99} as defined above, for each of the nine flow conditions. In this figure, as in all subsequent figures containing data for all nine flow conditions, for each solidity the data are shown in order of increasing Reynolds number, first $\sigma = 0$ (Fig. 5.2**a–c**), then $\sigma = 0.22$ (Fig. 5.2**d–f**), then $\sigma = 0.65$ (Fig. 5.2**g–i**) (the solidities and Reynolds numbers are listed in the figure caption). The data are plotted to scale, along with a circle drawn to the same scale as the cylinder diameter.

For each flow condition the data clearly delineate the mean boundaries of the separation bubble and the length of the separation bubble L_f defined as the value of x at which the inner boundaries of the shear layers intersect the wake center plane. When no splitter plate is present, this corresponds to the downstream position at which the profiles become wake-like, and when a splitter plate is present, this corresponds to the minimum value of the mean velocity being at the point of closest approach of the hot wire to the splitter plate. In all cases with $\sigma \neq 0$ this value of $x = L_f$ is also where the profiles became wake-like, with no evidence of a boundary layer forming on the plates downstream of the separation bubble. The value of L_f was taken from Fig. 5.2, and is plotted as L_f/D versus the Reynolds number in Fig. 5.3. Different symbols are used to mark the different solidities and are defined in the caption. Also included in Fig. 5.3 are data taken from a similar shear layer boundary plot for flow past a circular cylinder without a splitter plate reported by Schiller and Linke (1933). The Schiller and Linke data are not strictly comparable to the present data, due to differences in the aspect ratios (and possibly other unreported factors as well), but the trends in the curves are quite similar, although the classical data is somewhat smaller than the present results for all Reynolds numbers.

This definition of L_f parallels, at least in intent, the definition of what is usually called the "formation length" (hence the chosen symbol L_f). Other researchers have defined this in various ways, for example, as the point of the maximum amplitude of the velocity fluctuations along the wake center plane (Bearman 1965, although the term "formation length" was not used there), or as being "marked by the sudden reduction of the low frequency irregularities always observed in the formation region" (Bloor 1964). Such definitions, as well as the name itself, assume that the end of the separation bubble is defined by the region in which the large-scale vortices form, and as was shown in the flow visualization presented in Chapter 3 this is not necessarily the case when a permeable splitter plate is present. In any case, such definitions are difficult to apply since a plot of the (RMS) velocity fluctuations along the wake center plane does not display a sharp peak at the maximum over the Reynolds number range examined here, but rather tends to be broad and flat.

In Fig. 5.3 there is a clear trend of decreasing L_f with increasing Reynolds number except for $\sigma = 0.65$ at Reynolds numbers Re = 4900 and 9400, where — within the large

experimental uncertainty — the value of L_f does not change. The trend is less obvious for $\sigma = 0.65$ where the lowest values of the Reynolds numbers correspond to the low permeability conditions under which the wake exhibits a wake-profile instability, and the primary vortex formation takes place downstream of the end of the separation bubble and has a negligible effect on the structure of the near wake. Thus, the data suggest that for high solidity changes in L_f with Reynolds number occur when the vortex formation region is at the end of the separation bubble. For $\sigma = 0.22$, at low Reynolds numbers L_f is initially considerably larger than for $\sigma = 0$, and at the higher Reynolds numbers the differences in the values of L_f for the two solidities are much less and the curves appear parallel. The values of L_f for $\sigma = 0.65$ are much larger than those for the other solidities. Comparison of Fig. 5.3 and Fig. 4.1a supports the observations from the flow visualization that when the wake exhibits the body-coupled instability, lower base suction coefficients correspond to longer formation lengths and vice versa, and furthermore, when the wake exhibits the wake-profile instability the formation length is constant.

It is not clear from a comparison of Fig. 5.3 and Fig. 4.1 what the relationship is between the vortex formation frequency, the base pressure and the length of the separation bubble when the wake instability is body coupled. For $\sigma = 0$, L_f decreases linearly with Reynolds number, while the base suction coefficient and Strouhal number change in a more complicated fashion, the base suction coefficient generally increasing and the Strouhal number generally decreasing. For $\sigma = 0.22$, L_f initially decreases with increasing Reynolds number while the Strouhal number is constant and the base suction coefficient increases linearly. For $\sigma = 0.65$, in the Reynolds number range where the wake instability is body coupled, L_f decreases with increasing Reynolds number, while the Strouhal number and the base suction coefficient both increase linearly.

5.3 The shear layer instability

5.3.1 Shear layer growth

Figure 5.4 shows the vorticity thickness δ_ω and the momentum thickness θ as functions of downstream distance x/D for all of the nine cases, in the same order as in Fig. 5.2, and Fig. 5.5 shows the shear layer profile data in similarity coordinates $u/\Delta U$ vs. $(y - y_c)/x$ for the same flow conditions, where the value of y_c is obtained from the error function fit to the profile data. Figure 5.5 is presented here because it will be frequently referred to during the discussion of the thickness data shown in Fig. 5.4, and shows that the separated shear layers exhibit self-similarity, an interesting observation in itself. There are at least two different similarity profiles that exist in different regions of the flow, one in the initial growth region and one that develops farther downstream. The initial similarity profile is not

necessarily expected since the initial shear layers are not turbulent, and the similarity scaling is expected to hold only when the turbulent Reynolds stresses are much greater than the viscous, laminar stresses. Furthermore the shear layers derive from separating boundary layer of unknown profile and might reasonably be expected to still be in the process of relaxing to a self similar profile. This will be discussed in more detail in Sec. 5.3.4.

Returning to the thickness data in Fig. 5.4, in each case there is an initial region over which the growth rates $d\delta_\omega/dx$ and $d\theta/dx$ are constant and relatively small, followed by a rapid increase to a higher growth rate, with the new growth rate remaining constant for a short distance farther downstream. Note that in all cases the increased growth rates begin at points $x < L_f$, particularly for $\sigma = 0.65$ where the end of the separation bubble is separated by several cylinder diameters from the point at which the change occurs in the growth rate. This suggests that the increase in the growth rate is independent of the interaction between the shear layers and the processes which occur at the end of the separation bubble.

Farther downstream, past the point at which the increase in the growth rate occurs, the development of the shear layer thickness depends on the solidity of the permeable splitter plate. For $\sigma = 0$, the higher growth rate continues for some distance downstream. At Re = 4800, (Fig. 5.4**a**), the higher growth rate extends downstream to $x = L_f$, at which point the shear layers are presumably being entrained into the primary vortex formation, and the velocity profile is relaxing to a wake profile. This can be seen in the similarity profiles plotted in Fig. 5.5**a**, which show that the shear layer profiles change to a different self-similar shape at $x = L_f$. In this case, the values of δ_ω and θ derived from the profiles at $x \gtrsim L_f$ do not follow the same growth curve but since the shear layer profiles are no longer well defined at this point it is not necessarily expected that they would. At the higher Reynolds numbers Re = 9300 and 15200 (Fig. 5.4**b** and **c**), the growth curves look very similar to those for Re = 4800, but the higher growth rate continues unchanged for $x \gtrsim L_f$. This is not an artifact of the two-parameter fit procedure, since the momentum thickness is computed entirely from the data without using the fit profiles, but the significance of this is unclear. Similarity plots of the shear layer data, shown in Fig. 5.5**b** and **c**, follow the same trend as for Re = 4800 in that the profiles taken at downstream positions $x \gtrsim L_f$, where the profiles are wake-like, conform to a different similarity curve than the shear layer profiles.

For $\sigma = 0.22$ at all Reynolds numbers, the higher growth rate also continues downstream to just beyond $x = L_f$, and then undergoes another change to a lower growth rate (this is more obvious for Re = 9300, which has the least scatter in the data). The similarity profiles Fig. 5.5**d**–**f** show a more gradual change from one self-similar shape to the other than do those for $\sigma = 0$, with changes in the profiles appearing upstream of $x = L_f$. Profiles taken farther downstream show that the profile shape is retained for a considerable distance

beyond the end of the separation bubble, thus the wake profile exhibits self-similarity despite the presence of the splitter plate. This is remarkable since the presence of the splitter plate constitutes an additional boundary condition on the wake, and furthermore, since the pressure drop across the permeable splitter plates is a function of the velocity normal to the plate (see Appendix C) and in the wake of a bluff body this velocity changes as the wake evolves downstream, this boundary condition varies with x. Despite the gradual change between the similarity profiles, the dimensional data show shear layer profiles for all values of $x < L_f$, and assume wake-like shapes for $x > L_f$. The change in the growth rate to a lower value occurs at $x \approx L_f$, so may be related to the interaction of the shear layer with the primary vortex formation, and probably accounts for the increased scatter in the thickness curves for $x \gtrsim L_f$.

For $\sigma = 0.65$, the shear layer curves are similar to those at $\sigma = 0.22$, in that a second change in the the shear layer growth rates is clearly discernible at Reynolds numbers Re = 4900 and 9400, and is somewhat discernible at Re = 15200 at $x/D \approx 1.3$, although it is less clear at this Reynolds number because of the scatter in the data. However, for this solidity the end of the separation bubble at $x = L_f$ occurs far downstream from both the location at which the growth rate first increases and the location farther downstream at which the growth rate decreases. The similarity between the curves for $\sigma = 0.22$ and $\sigma = 0.65$ suggests that a similar process might be responsible for the decrease in the growth rates, but the large separation between the location at which the decrease occurs and the end of the separation bubble in the $\sigma = 0.65$ case supports the assertion that the decrease is not caused by the interaction of the shear layers with the end of the separation bubble. For the lowest Reynolds number, Re = 4900, the similarity profiles (Fig. 5.5**g**) do not clearly exhibit collapse to a single curve. For the other two Reynolds numbers, the shear layer profiles do show collapse to two different profiles, with a gradual change from an initial profile to the final profile. It is also seen that for a permeable splitter plate of solidity $\sigma = 0.22$, the presence of the splitter plate also causes the change in the similarity profiles to take place over an extended region of the wake, so the presence of permeable splitter plates has an effect on the shear layer similarity, with the $\sigma = 0.65$ plate having the most dramatic effect. This will be discussed further in Sec. 5.3.4.

5.3.2 Development of the shear layer instability

In this section, the development of the shear layer velocity fluctuations will be considered as a function of the downstream location x/D, which is roughly representative of the length of time over which the shear layer has developed, and so 'earlier' will be used to refer to a location that is upstream relative to one described by 'later'. Figure 5.6**a–d** show example velocity traces, collected with the hot wire located at the outer, high-speed edge of the shear layer, each for a different value of the Reynolds number and splitter plate

solidity (given in the figure captions). For each flow condition, velocity traces obtained at different values of x/D are shown with x/D increasing from the top of the figure to the bottom. Assuming that the separated shear layers are analogous to plane mixing layers, at least in the region of initial growth, it is plausible that the separated shear layer will scale with some relevant shear layer velocity U and the initial momentum thickness θ_0, so that frequencies that are important in the development of the instability will scale with U/θ_0 and will be higher for higher values of U and smaller values of θ_0. It is clear that the shear layer velocity scale depends on the free-stream velocity, and it is plausible although somewhat less clear that θ_0 will scale in the same fashion as the boundary layer on the front of the cylinder so that $\theta_0/D \sim \mathrm{Re}^{-1/2}$ (with Re based on cylinder diameter) and at higher Reynolds number the wavelengths of the amplified shear layer perturbations will be shorter. Therefore, at high Reynolds number a fixed value of x/D corresponds to a larger number of wavelengths of the disturbances that are amplified by the separated shear layer instability, and at a given x/D the shear layer development will have progressed further than at low Reynolds numbers. This is what is observed, as is seen from a comparison of the traces for $x/D \lesssim 0.9$ shown in Fig. 5.6**a** for $\sigma = 0$ and $\mathrm{Re} = 9800$, with the traces for $x/D \lesssim 0.6$ shown in Fig. 5.6**b** for $\sigma = 0$ and $\mathrm{Re} = 15200$.

In the initial region of the shear layer development (where the growth of the shear layer is small, see Fig. 5.4) the sequence in which the different phenomena associated with the development of the instability appear is similar for all values of the Reynolds number and solidity, and the different phenomena that appear downstream of the initial growth region depend primarily on the splitter plate solidity. This is true even when the splitter plate solidity is high enough to prevent the primary vortex formation from affecting the flow in the near wake, as the differences in the flow due to the velocity fluctuations at the primary wake frequency did not appear to strongly effect the initial development of the instability (however, note that for $\sigma = 0.65$ data were only taken at one location within the initial growth region, $x/D = 0.4$, and by that point considerable growth had already occurred in the shear layer instability). For high enough permeability, so that the primary vortex frequency is discernible in the near wake, the velocity fluctuations at the vortex formation frequency are visible as long wavelength oscillations in the velocity traces, and comparison of Fig. 5.6**a**, **c**, and **d** shows qualitatively that decreasing the permeability by increasing the solidity of the splitter plates progressively reduces the amplitude of the large-scale velocity fluctuations at the primary wake frequency. Furthermore, transverse motion of the shear layer is detectable in the form of noticeable low-velocity excursions in the signal, such as that visible near $t = 0$ at $x/D = 0.5$ in Fig. 5.6**a**, which do not appear when the permeability is low enough that velocity fluctuations at the primary wake frequency are not discernible in the near wake (transverse motion of the shear layers is discussed in more detail in Sec. 5.3.3).

In general, near the cylinder the flow is laminar, whether or not the vortex forma-

tion frequency is discernible, although examination of the velocity traces show that small-amplitude high-frequency velocity perturbations are visible in the shear layer even in this region (Fig. 5.6**c**, $x/D = 0.4$). The small fluctuations grow with downstream distance, with intermittent bursts of high-amplitude high-frequency oscillations beginning to appear (Fig. 5.6**c**, $x/D = 0.7$). These should not necessarily be equated with turbulent bursts as in pipe flow or a boundary layer, as spectral analysis shows that the flow is organized and that the fluctuations show a definite frequency band even though the instability is only intermittently manifested (see Sec. 5.4.2). As the shear layer develops, the bursts become more frequent, and the amplitude of the oscillations in the bursts increases, until the bursts merge and the high-frequency oscillations are continuously present (Fig. 5.6**c**, $x/D = 1.1$). At this point in the development, when oscillations at the primary wake frequency are present as in Fig. 5.6**c**, $x/D = 1.1$, the amplitude of the high-frequency fluctuations is comparable to (and intermittently greater than) that of the fluctuations at the primary wake frequency. In fact, under all flow conditions the maximum peak-to-peak amplitude of the high-frequency oscillations appears to be of order $U_\infty/2$, regardless of whether or not oscillations at the primary wake frequency are discernible.

With the present data it is difficult to determine a precise location at which the velocity fluctuations in the shear layer reach maximum amplitude, not only because the peak at the maximum is broad, but also because of variation in the transverse hot-wire location in the shear layer (in shear layer scaled coordinates), which has a significant effect on the measured amplitudes. However, the approximate downstream locations at which the maximum amplitudes of the high-frequency oscillations were attained roughly correspond to the downstream locations at which the shear layer growth rates underwent the abrupt increase discussed previously (Fig. 5.6**c**, $1.1 \leq x/D \leq 1.3$). After this point, the high-frequency fluctuations begin to diminish, and lower, subharmonic frequencies become apparent in some of the velocity traces (*e.g.*, Fig. 5.6**c**, $x/D = 1.5$). For high enough permeability, the end of the separation bubble followed (more or less) shortly thereafter and the shear layers were entrained by the primary vortex formation, although it is still possible to detect traces of the high-frequency fluctuations or of the subharmonics in all of the velocity traces (and in most of the spectra) as in Fig. 5.6**c**, $x/D \geq 1.5$, for some distance farther downstream.

Figure 5.6**d** shows velocity traces at low permeability, where the primary wake frequency is not visible in the near wake, and the shear layer instability develops in relative isolation from other near wake phenomena. As has been mentioned, the sequence in which the different instability phenomena appear — the occurrence of small-amplitude high-frequency fluctuations, followed by high-amplitude bursts, which increase in frequency until the high-frequency fluctuations are continuous, with subsequent decay of the initial frequencies and the emergence of the subharmonic frequencies — is the same as when the permeability is high. In the low-permeability case, however, the subharmonic is able to

fully develop without the shear layer being involved in any interactions at the end of the separation bubble, either with the splitter plate at the center plane or with the primary vortex formation. This process is visible in Fig. 5.6**d** for $1.4 \leq x/D \leq 3.0$., and the approximate relationship between the high frequency fluctuations and what have been referred to as fluctuations at the subharmonic may be confirmed by counting cycles at $x/D = 1.4$ and $x/D = 3.0$. It is also clear in this figure for this range of x/D that the process through which the subharmonic develops is erratic, which is reflected in the amplitude and phase of the waveforms both before and after the subharmonic develops. By $x/D = 4.0$, which is close to the end of the separation bubble, the fluctuations appear to have lost all coherence and the shear layer appears to have become fully turbulent. In the example velocity traces shown in Fig. 5.6**d** from low permeability flow conditions, the near disappearance of the high frequency component of the fluctuations and its replacement by the development of the subharmonic is completed between $x/D = 2.0$ and $x/D = 3.0$ and this compares well with the value of $x/D \approx 2.4$ where the decrease in the growth rate of the shear layer thickness occurs (Fig. 5.4**g**). The analogy with the plane shear layer suggests that the initial increase in the shear layer growth rate occurs at the point where small scale vortices resulting from the Kelvin-Helmholtz instability of the shear layer are fully developed and begin pairing interactions, leading to their amalgamation into larger vortices. When the permeability is high, the pairing process is not completed before the shear layer is entrained into the primary wake vortices, but as is seen in the Fig. 5.6**d**, when the permeability is low it is possible for the pairing process to reach completion, at which point the shear layer growth rate decreases.

5.3.3 Transverse motion of the shear layers

It has often been remarked that the separated shear layers move in a direction transverse to the free stream under the influence of the oscillations induced by the large-scale vortex formation. In the present data, when the vortex formation is present, near the cylinder the shear layer velocity traces show occasional low-velocity excursions that can be a considerable percentage of the mean, such as the one visible near $t = 0$ at $x/D = 0.5$ in Fig. 5.6**a**. The number of such excursions increases with downstream location until the end of the separation bubble is reached, but they are always aperiodic and intermittent, and in particular, do not occur at the primary wake frequency. Such low-velocity excursions correspond to what has elsewhere been described as "flapping" of the shear layer, *i.e.*, transverse motion of the shear layers due to wake oscillations caused by the primary vortex formation (*e.g.*, Wei and Smith, 1986). The thickness of the separated shear layers is not very large near the cylinder, so a small transverse motion can cause large changes in the measured velocity as the motion of the shear layer causes the hot wire to measure the low-speed flow on the cylinder side of the shear layer. Farther downstream near the end of the separation bubble the low-speed excursions become more frequent as the shear layer boundaries

move over a considerable transverse distance under the influence of the vortex formation, and low-speed fluid from the separation bubble is intermittently entrained into the wake. Downstream of the end of the separation bubble, as the shear layers interact across the center plane and relax to a wake profile, the low-speed excursions disappear entirely or only produce changes that are of the same order of magnitude as those produced by the vortex formation itself and so do not produce a distinct signal in the velocity traces. It can be seen by comparing Fig. 5.6**a**, with no splitter plate at Reynolds number Re = 9500 and Fig. 5.6**b**, with a permeable splitter plate of solidity $\sigma = 0.22$ at Reynolds number Re = 9300, that the introduction of the permeable splitter plate reduces the number of occurrences and the magnitude of the low-velocity excursions.

It may be that the transverse motion of the shear layers is primarily towards the cylinder and back to the original location, in which case the hot wire located at the high-speed edge of the shear layer would experience the flow immediately outside of the shear layer (which has a velocity of $1.2\text{–}1.3\,U_\infty$) and then the flow at the edge of the shear layer again, and this will not show up as clearly in the velocity traces since there is very little difference between the mean velocity at the edge of the shear layer and that farther out (recall that the mean velocity reaches approximately 99% of its maximum value at $\eta \approx 1.64$). Such motion cannot be precluded, although relatively long distance or long duration motion of the shear layer towards the cylinder would show up as a substantial decrease in the amplitude of the velocity fluctuations, since the fluctuation amplitudes decrease rapidly outside of the actual layer. These cannot be reliably separated from the quasi-periodicity of the vortex formation itself (the vortex formation is described here as "quasi-periodic" since even though the vortex formation cycles are all of about the same wavelength, the resulting signal is not a clean sinusoid, as the amplitude and phase of the oscillations tends to vary over time) but for the most part such low amplitude episodes do appear but are fairly rare, and again, are aperiodic, intermittent and do not occur at the primary wake frequency (for example, see Fig. 5.6**b**, $x/D = 0.3$). Note that due to the rectification of velocity directions by the single hot wire, the small transverse velocities involved in the transverse motion of the shear layer do not produce a measurable velocity signal. Thus, in the initial growth region of the shear layer instability the primary effect of the vortex formation on the shear layers is the quasi-periodic increase and decrease of the streamwise component of the velocity at the primary wake frequency.

5.3.4 Shear layer similarity

A straightforward comparison of the turbulent Reynolds stresses to the laminar stresses for a free shear layer using estimates for the RMS streamwise and transverse velocity fluctuations u' and v' of

$$\sqrt{\overline{u'^2}} \sim \sqrt{\overline{v'^2}} \sim \mathcal{O}(0.1\,\Delta U)\,,$$

(taken from Arie and Rouse 1956) so that

$$\overline{u'v'} \sim \mathcal{O}(0.01\,\Delta U^2)$$

giving an estimate for the ratio of the turbulent to laminar stresses of

$$\frac{\rho\overline{u'v'}}{(\mu\,\Delta U)/\delta} \sim 0.01\left(\frac{\rho\,\Delta U\,\delta}{\mu}\right)$$

$$\equiv 0.01\,\mathrm{Re}_\delta\ ,$$

where ρ and μ are the fluid density and viscosity, respectively, and δ is an estimate of the shear layer thickness. Thus the laminar stress will be about 1% of the turbulent stress when $\mathrm{Re}_\delta \sim \mathcal{O}(10^4)$, so for shear layer Reynolds numbers greater than this the laminar stresses may be neglected compared to turbulent stresses and the viscosity μ is no longer a relevant parameter in the flow. It then follows from dimensional analysis that in a turbulent shear layer,

$$\frac{u}{\Delta U} = \mathrm{fn}\left(\frac{y}{x}\right).$$

The Reynolds number range of the present experiments is $2.5 \cdot 10^3 \lesssim \mathrm{Re} \lesssim 1.8 \cdot 10^4$, so that $\mathrm{Re}_\delta \approx 10^4$ when

$$\delta \approx \mathcal{O}(D)\,. \tag{5.1}$$

It can be seen from Figs. 5.2 and 5.4 that this is not satisfied in the initial growth region of the shear layer, so it is not expected from this argument that the shear layer profiles in the intial region would be self-similar. Comparison of Fig. 5.3 with the same two figures also shows that for a cylinder without a splitter plate, the shear layers are entrained into the primary vortex formation before the shear layer thickness satisfies the condition 5.1.

These considerations help to explain the similarity profiles shown in Fig. 5.5. For $\sigma = 0$ at all Reynolds numbers, Fig. 5.5**a**–**c**, the shear layer profiles are initially self-similar in the region $x < L_f$, but this initial similarity profile is not turbulent shear layer similarity as discussed above. When the shear layers reach the end of the separation bubble and begin to interact with the vortex formation, the self-similarity is lost until some distance downstream where the flow has relaxed to a turbulent wake profile (data were not taken far enough downstream to show the wake profile similarity for the low Reynolds numbers, and the data are not compelling in Fig. 5.5**c**, but the data for $\sigma = 0.22$ do support this). For $\sigma = 0.22$, Fig. 5.5**d**–**f**, the situation is analogous, except that due to the longer separation bubble, the development of the shear layer instability progresses further before the shear layers interact with the end of the separation bubble, so that the shear layers begin to evolve to turbulent self-similar shear layer profiles. However, the shear layer profiles do not become fully self-similar before interacting with the end of the separation bubble, at which

point the wake profiles again develop. For $\sigma = 0.65$, Fig. 5.5**g–i**, data were taken at only a very few points downstream of the end of the separation bubble, but within the separation bubble the shear layers clearly exhibit two different similarity profiles. The initial similarity profile is similar to that observed for the other solidities, but a second, turbulent shear layer similiarity profile develops before the end of the separation bubble. Thus, for $\sigma = 0$, the shear layers do not last long enough (as shear layers) to become fully turbulent, but only begin the process; the same is true for $\sigma = 0.22$ but the process proceeds for long enough that significant deviation from the initial profiles occurs; and for $\sigma = 0.65$ the shear layers are able to evolve sufficiently to exhibit self-similar turbulent profiles.

The initial self-similarity of the profiles is unexplained, except that perhaps prior to separation the boundary layers do develop a self-similar profile in the low turbulence flow over the smooth circular cylinder, and proximity of the shear layers to the cylinder after separation prevents more energetic near wake processes from disturbing the resulting profiles during the initial growth of the shear layers. The initial similarity profiles of the shear layers are nearly identical for different Reynolds numbers at a given solidity, and the final similarity profiles, when they develop, are also nearly identical for different Reynolds numbers at a given solidity, but the initial profiles are different for different solidities (this may be observed in Fig. 5.5 by noting that the scales of the axes are different, and comparing the thicknesses, in similarity coordinates, of the profiles). It is observed in Sec. 5.3.2 that the presence of a splitter plate has a significant effect on the amplitude of the velocity fluctuations in the near wake at the primary wake frequency, and since these velocity fluctuations will influence the boundary layer prior to separation, the difference in the initial profiles between different similarities lends support to the suggestion that the initial similarity profiles are remnants from the boundary layer similarity.

5.4 Shear layer velocity spectra

5.4.1 Scaling

Plane mixing layers are usually scaled by the initial momentum thickness θ_0, and the average of the velocities on either side of the mixing layer $\overline{U}$, which in plane mixing layer experiments is usually arranged to be independent of downstream position. However, in the present case the initial momentum thickness is not known, and the velocities on either side of the shear layer are changing with downstream position. With some plausible but rather strong assumptions it is possible to estimate the initial momentum thickness using standard boundary layer scaling, although this probably yields only an order-of-magnitude approximation (and is used for this purpose in Sec. 5.3.2). This boundary layer scaling has been applied in the analysis of the separated shear layers, and the results of using such scaling to interpret experimental results will be discussed in the next chapter.

The initial linear growth of a plane shear layer makes it plausible to extrapolate back to a "virtual origin" at which the shear layer thickness is zero, but without a priori knowledge of the virtual origin, this procedure cannot practically be used to obtain an initial thickness. In the scaling that produced the similarity plots in Fig. 5.5, the origin of the x-coordinate is taken to be at the cylinder axis, and this gives good collapse of the data without the use of a virtual origin for x. This suggests that it is plausible to extrapolate the growth curves back to $x/D = 0$ and use the resulting value of the momentum thickness, but this procedure results in negative values for the initial thickness, and so is of dubious value. The downstream variation in the shear layer boundary conditions suggests that the shear layers might scale by the local values (*i.e.*, those measured at the downstream location at which the shear layer profiles were obtained) of the shear layer thickness and either the average velocity or the velocity difference. The resulting local time scales $\theta/\overline{U}$ and $\theta/\Delta U$ are also functions of x/D, and these scalings had the effect of obscuring the relationship between the spectra measured at different values of x/D, and so were not used either.

Since it is not the development of the shear layer alone that is of primary interest, but rather the relationship of the shear layer behavior to the structure of the near wake, it makes sense to use near wake scaling for the spectra, and so the approach taken here is to scale the spectra with the free-stream velocity U_∞ and the cylinder diameter D, so that non-dimensional frequencies f_* are given in terms of the corresponding dimensional frequencies f by

$$f_* = \frac{fD}{U_\infty}.$$

With this scaling, the non-dimensional frequency corresponding to the primary vortex formation, $f_{1*} = f_1 D/U_\infty$, is equal to the Strouhal number.

As was previously noted, the locations across the shear layer (in normalized coordinates η) at which spectra are available are not identical for each downstream location, but in general spectral features are preserved across the layer but decrease in amplitude by as much as an order of magnitude from the center of the shear layer ($\eta \approx 0$) to the outer, high-speed edge of the layer ($\eta \approx 1.64$), and the amplitudes of the background fluctuations are greater when the spectra are taken deep inside the shear layer and consequently the spectral features are more clearly defined toward the outside edge of the shear layer. This can be seen in the power spectra shown in Fig. 5.7, where the data from which the different spectra were computed were taken at the locations marked by the solid symbols in the profiles shown in Fig. 5.1.

5.4.2 Development of the shear layer instability in the frequency domain

Figure 5.8 shows the downstream evolution of the power spectral distribution $\Phi(f_*)$ in velocity traces taken near the outer edges of the shear layers, for all Reynolds numbers and

solidities for which shear layer data were collected. The procedure for obtaining the data shown in Fig. 5.8 is as described in Sec. 5.1.1, and the spectra were computed as discussed in Appendix D. The data from which spectra could be computed were extensive, and a considerable amount of data is presented in this figure so the data have been consistently organized. For each flow condition (given in the figure caption) several power spectra are shown in the form of power spectral density Φ, computed from the fluctuating velocity signal measured at the outer edge of the shear layer. The bottom graph shown in each part of the figure shows spectra from upstream portions of the shear layer, and the top half shows spectra taken farther downstream, so the evolution of the spectral distribution of the shear layer fluctuations can be seen by reading the parts of the figure from bottom to top. A legend on each graph shows the values of x/D and the shear layer normalized coordinate η at which the corresponding data were taken. The spectra are plotted on semi-log axes, which tends to obscure the relative magnitudes of the spectral features, but which was necessary in this case because of the large differences in the amplitudes of the Φ at the primary wake frequency and the amplitudes at the higher frequencies which develop due to the shear layer instability. It should also be noted that the plotted spectra were computed using a fast Fourier transform of 2048 data points yielding power spectra with 1025 data points, which were rebinned to 128 points when plotted. Except for one flow condition the low plotting resolution does not significantly affect what is shown in the plotted spectra, and the particular case for which it does, $\sigma = 0.22$ and $\mathrm{Re} = 4800$, is shown separately at full resolution. The details of the shear layer, the filter cutoff frequency, and the number of averaged blocks in each spectrum are given in Table 5.1.

Across the different values of Reynolds number and solidity, the spectral evolution of the shear layers shows many common elements. There are general features that are visible in each case, the differences being of degree or definition. These are discussed in general, and then the peculiarities of the different flow conditions will be discussed. For spectra taken at low solidity, here $\sigma = 0$ and 0.22, at all Reynolds numbers well-defined discrete peaks are visible at the non-dimensional frequency f_{1*} corresponding to the primary wake frequency, at that corresponding to the first harmonic at $2f_{1*}$, and in some of the spectra, a peak of much smaller amplitude may be observed at $3f_{1*}$. For $\sigma = 0.65$, or lower permeability, peaks corresponding to primary wake frequencies are not visible at all at low Reynolds number and are only visible near the end of the separation bubble at high Reynolds number. Except for the peaks at f_{1*} and $2f_{1*}$, when they are present, all other discrete frequency peaks visible in the spectra (there are not many) are of relatively low amplitude.

A broad spectral feature, where the magnitude of the power spectral density is increased above the background over a fairly broad frequency band centered at a frequency considerably higher than f_{1*}, appears in all of the spectra taken for low values of x/D,

and for high permeability is generally distinguishable to the end of the separation bubble. Such a feature will be referred to as a "secondary frequency band" or the "secondary frequencies," and the center frequency (which in some cases is not particularly well defined) will be referred to as f_{2*}. The secondary frequency bands are most apparent in the initial growth region of the shear layers and the maximum amplitude of the spectral density in the secondary frequency band increases exponentially with increasing x/D, as does the broad band background, until the secondary frequency band is submerged in the background. Note that when the f_{1*} peak is present, its amplitude is more than an order of magnitude greater than the maximum amplitude in the secondary frequency band. Except for low solidity and the lowest Reynolds numbers for which data were collected, a "subharmonic" band (centered at approximately $f_{2*}/2$) appears some distance downstream in the near wake, grows in magnitude, and then is also eventually submerged by the growth of the turbulent background. The growth of the subharmonic band is more apparent and the subharmonic frequency band is more clearly defined at high Reynolds numbers, and the subharmonic band is more clearly defined at higher solidity.

Generally, at some distance downstream of the point at which the the high frequency fluctuations attain peak amplitude, the spectra subside to a broad-band background with the discrete primary vortex formation peaks visible above the background when the permeability is high enough. The development into a broad band turbulent background occurs both when the shear layers are entrained by the primary vortex formation, and when they are not as in the low permeability cases. When the permeability is low, the development of a turbulent spectrum occurs long before the end of the separation bubble, indicating that the loss of structure in the shear layers occurs before the point at which the shear layers interact with the end of the separation bubble.

Spectra for $\sigma = 0$ are shown Fig. 5.8**a**–**c**, and at all Reynolds numbers it is seen that the secondary frequency bands are poorly defined, *i.e.*, they are broadly distributed in frequency and of low amplitude relative to the background, and the secondary frequency band is more clearly defined in the upstream region in which the shear layer has its initial development. Although in every case a spectral feature is visible that may be identified as a frequency band approximately corresponding to subharmonics of the secondary frequency band, these are only vestigial for Re = 4800 and 9300, and although the subharmonic band is only slightly more defined in the case of Re = 15200, its amplitude rivals that of the secondary frequency band, and it is actually of slightly greater amplitude at $x/D = 0.6$. In general, the development follows that described in the general remarks given above. The only discrete peaks of significant amplitude visible anywhere in the spectra correspond to f_{1*} and its harmonics, with the amplitude at f_{1*} one to two orders of magnitude above the peak amplitudes in the secondary frequency band.

For $\sigma = 0.22$, Fig. 5.8**d**–**f**, at the lowest value of the Reynolds number of Re = 4800

shown in Fig. 5.8**d**, there is a very broad secondary frequency band, and within the band there are several different features visible. When the spectrum is plotted at a higher resolution as in Fig. 5.9, the different features resolve themselves into narrow spectral features for which some harmonic relationships can be discerned. The low-frequency large-amplitude peak visible at all values of x/D corresponds to the primary wake frequency at $f_{1*} \approx 0.2$, and the first harmonic $2f_{1*} \approx 0.4$ is also visible for $x/D \leq 0.9$. The small peak at a frequency slightly higher than f_{1*} at $x/D = 0.7$ corresponds to four times the fan rotation rate of 6.87 revolutions per second and disappears from these spectra by $x/D = 1.3$. Peaks at four times the fan rotation frequencies are also observed at very low amplitude in measurements of the free-stream turbulence. The next peak that survives for all values of x/D for which high resolution spectra are shown is at $f_* \approx 0.64$ and is close to a harmonic of both the primary wake frequency and the fan frequency, and the double peak that shows the highest growth in this range (and continuing farther downstream, see Fig. 5.8d) are at approximately twice this frequency. These peaks are possibly due to the primary vortex formation or the fan frequency driving a natural frequency of the splitter plate, and are amplified because one of the harmonics lies close to the center of the secondary frequency band. The discrete spectral feature at $f_* \approx 2$ is not a harmonic or a beat frequency of the other features but the narrowness of the peak and the fact that it does not survive past the initial region of growth indicates that even if the experimental setup is perturbed somehow at this frequency it is not amplified by the shear layer as are the peaks located close to $f_* \approx 1.2$. The peak at $f_* \approx 0.64$ also does not survive past the initial growth region. The fact that disturbances outside of the secondary frequency band are not amplified but that those lying within the band are suggests that what is being referred to as the secondary frequency band represents a receptive band of frequencies for the shear layer, in the sense that the shear layer amplifies disturbances at frequencies lying in this band and does not amplify those lying outside. In contrast to Re = 4800, in the spectra for Re = 9300 and 15000 shown in Fig. 5.8**e** and **f**, the secondary frequency bands do not exhibit any discrete spectral features. In general, they develop in a fashion that is very similar to that discussed in the general description, and in these cases the growth of the subharmonic band of the secondary frequency band is clearly visible. The maximum amplitude of the subharmonic band eventually reaches a level that is of the same order of magnitude as that of the secondary frequency band, and at the highest Reynolds number grows to dominate the secondary frequency band at $x/D \approx 0.7$, indicating the possibility of pairing interactions between shear layer vortices.

The spectra for $\sigma = 0$ and $\sigma = 0.22$ all show primary vortex formation peaks at $f_{1*} \approx 0.2$, and the growth of the power spectral density at the primary frequency with downstream distance is also clearly visible in these spectra. It is interesting to note that when the permeable splitter plate is present, the amplitude of Φ at the frequency f_{1*} is initially more than an order of magnitude smaller than when the permeable splitter plate

is not present, and then grows rapidly with increasing x/D to an amplitude that is of the same order of magnitude as the peak amplitude without a splitter plate. The decrease in the amplitude of the primary wake fluctuations with a permeable splitter plate present was also seen in the velocity traces. Although measurements made outside the wake (reported in Chapter 4) with $\sigma = 0.65$ at high Reynolds numbers do show the existence of a primary wake frequency, it is not discernible in the spectra for $\sigma = 0.65$ computed from data taken within the shear layers (until x/D is large, not shown in these figures). However, even though the shear layers are not driven by the primary vortex formation, the qualitative development of the spectra with x/D proceeds in much the same manner as when f_1 is present. However, the secondary and subharmonic frequency bands are much more sharply defined and in each case, far enough downstream the secondary frequency band subsides into the background turbulence and the subharmonic band dominates the spectrum for a range of x/D before beginning to subside as well.

5.5 Discussion

5.5.1 Shear layer transition

In the velocity traces shown in Fig. 5.6 it is seen that the downstream location at which the growth rates first increased corresponds to the approximate location at which maximum amplitude is attained by the high-frequency fluctuations resulting from the growth of the shear layer instability. For $\sigma = 0.65$, where the primary vortex formation was not discernible in the near wake, this downstream location was also close to the location at which the value of u'/U_∞ measured at the outer edge of the shear layer reached a maximum, but for high permeability, velocity fluctuations at the primary wake frequency due to the large-scale vortex formation contained most of the energy and so u'/U_∞ vs. x/D simply shows steady growth out to the end of the separation bubble. The growth of the shear layer instability can be resolved by examining the flow in the frequency domain using the power spectral density, and within the resolution in x/D and with the caveat that there are variations in the shear layer normalized location at which the data were collected from which the spectra were computed, the maximum amplitude within the secondary frequency band was found at the same value of x/D. If a velocity trace taken at this location is plotted over a long enough time interval the flow appears to be turbulent, or undergoing transition to turbulence. However, when plotted over short periods of time and at a high enough time resolution, the signal is resolved into short bursts of oscillations and within each burst the oscillations appear to be of the same frequency. This is supported by the spectra, which show that there is a preferred frequency band although the frequency bands are less well defined at higher permeability. The spectra presented in this chapter have

all been the averages of many spectra, taken cumulatively over periods of time that are long compared to any relevant frequencies in the flow and this will average individual wave packets that have slightly different frequencies, resulting in the secondary frequency band.

In analogy with plane mixing layers, it is conjectured that the point at which the increase in the growth rate of the shear layer thickness occurs corresponds to the point at which small scale shear layer vortices, which have developed from the shear layer instability, reach a point of maximum growth and the principal mechanism responsible for the growth of the shear layer thickness changes to pairing interactions among the shear layer vortices. This analogy will be supported and exploited further in following sections. In the standard model based on the data of Schiller and Linke (1933), the point at which the growth rate increases is identified with the point at which the shear layers undergo transition to turbulence, and the distance from the cylinder axis to the origin is referred to as the transition length L_t. To distinguish the present interpretation of this increase in the growth rate, the downstream location at which it occurs will be referred to as the "pairing point" and the downstream distance from the axis of the cylinder to the pairing point will be called the "pairing length" L_p. This point is not clearly defined by any feature on the plots of the shear layer boundaries for high permeability shown in Fig. 5.2**a**–**f**, but is visible at low permeability as in Fig. 5.2**g** and **h**.

The pairing length was obtained from the curves shown in Fig. 5.4, and is plotted in Fig. 5.10. Although the uncertainties in the values of L_p are large due to the coarse resolution in x/D at which the shear layer traverses were made, from this figure it can be seen that in this Reynolds number range the change in the pairing length is smaller for the cylinder without a splitter plate than for the cylinder with either of the permeable splitter plates. At all Reynolds numbers for which the measurements were made, with a splitter plate of solidity $\sigma = 0.22$ in the wake the pairing length is greater than for a cylinder without a splitter plate, although the curves converge as the Reynolds number increases. At the lowest Reynolds number, the estimated values of the pairing length are compatible for $\sigma = 0.22$ and $\sigma = 0.65$, suggesting that even though the primary wake frequency is detectable at all points in the wake for $\sigma = 0.22$, at that Reynolds number the influence of the vortex formation is diminished by the splitter plate to a point at which the shear layer instability is able to develop nearly as though fluctuations at the primary wake frequency were not present, as is the case when $\sigma = 0.65$.

Remarkably, for $\mathrm{Re} \gtrsim 9000$, the pairing length is shorter for the $\sigma = 0.65$ splitter plate than for either $\sigma = 0$ or $\sigma = 0.22$. Although this is approximately the Reynolds number at which the primary wake frequency was first detected in the case of $\sigma = 0.65$ (see Fig. 4.1**b**), this cannot be the cause of the earlier change in the growth rates since both of the higher permeabilities are strongly effected by the vortex formation at these Reynolds numbers, and in any case it can be seen from the spectra in Fig. 5.8**h** and **i** that the primary

vortex formation is not detectable in the velocity fluctuations in the near wake and so are not the cause of the farther upstream location at which pairing begins.

5.5.2 A model for the development of the separated shear layers

The conjecture that the separated shear layers are similar to plane mixing layers in that the instability leads to the development of vortices within the shear layer is supported by flow visualization reported by other researchers (*e.g.*, Wei and Smith 1986), but the development of the shear layer under the present experimental conditions seems to be somewhat different than that reported elsewhere (this is discussed further in the next chapter), and so flow visualization photographs using the smoke wire technique were obtained to confirm the existence of the shear layer vortices in the present experimental setup. For the photographs, a permeable splitter plate of solidity $\sigma = 0.65$ was installed in the wake with a 5 mm gap between the cylinder and the leading edge of the splitter plate, with the smoke wire passing through the gap in a direction normal to the plane of the splitter plate. In the photograph shown in Fig. 5.11, the formation of circular structures is clearly observable downstream of the smoke wire, establishing the existence of the shear layer vortices under these experimental conditions.

The splitter plates have been used to modify the near wake environment in which the separated shear layers develop from the limiting case of flow without a splitter plate, where the separated shear layers are maximally perturbed by the velocity fluctuations due to the vortex formation and do not have much time in which to evolve before being entrained into the large-scale vortex formation, to the other limit of flow with a low-permeability splitter plate where the separated shear layers are not affected by the vortex formation in the region of initial growth and therefore evolve over a considerably longer distance. In combination with results from investigations of plane mixing layers, the present data using permeable splitter plates to modify the interaction between the shear layers separating from the circular cylinder and the primary vortex formation in the wake suggest a model for the development of the separated shear layers.

The model is based on the assumption that the evolution of the separated shear layers in the wake of the circular cylinder may be explained in terms of the development of a plane mixing layer that is modified primarily by two features of the flow in the near wake: Fluctuations in the streamwise velocity that result from the existence of the primary vortex formation, and the early termination of the development of the shear layers through interaction with the processes occurring at the end of the separation bubble (which may be the vortex formation or, when the wake instability is not body coupled, the interaction of the shear layers with either or both of the splitter plate itself and the shear layer from the opposite side of the wake). Several basic features are observed to be common to both the

separated shear layers and plane mixing layers. There is an initial region in which the shear layer thickness grows slowly and in which the shear layer instability develops as a result of the amplification of small perturbations in the free-stream flow, and in this region the mean growth of the RMS amplitude of the velocity perturbations at the instability frequencies is exponential, as predicted by linear stability theory. At the end of the period of initial growth, fully formed shear layer vortices have developed and the mechanism by which the shear layer growth continues changes to pairing between shear layer vortices, resulting in a higher growth rate. In the frequency domain, this corresponds to the appearance and growth of subharmonics of the initial shear layer frequencies (referred to here as the subharmonic band and the secondary frequency band, respectively). Beyond this point, development of the separated shear layers is strongly influenced by the primary wake instability, which in turn depends on the splitter plate permeability.

When the permeability is high, the separation bubble is short relative to the pairing length L_p, and the shear layer development is strongly affected by the interaction of the shear layers with the development of the primary wake vortices. The shear layer thickness data for $\sigma = 0$ in Fig. 5.4**a**–**c** shows that the growth of the shear layer thickness continues unchanged for some distance downstream of $x = L_f$, so that the shear layer growth rate is apparently not immediately affected by the end of the separation bubble, although the data show that the mean profile changes from that of a shear layer to that of a wake (as defined in Sec. 5.1.1). The thickness data for $\sigma = 0.22$ are more ambiguous, as the end of the separation bubble appears to nearly correspond to a second change in the shear layer growth rate although it is also possible that this corresponds to the point at which the pairing process is completed. For $\sigma = 0.65$, *i.e.*, at low permeability, the separation bubble is much longer than for high permeability, and at all Reynolds numbers measured, fluctuations in the transverse velocity at the primary wake frequency are not measurably present in the near wake, so that the environment in which the shear layers develop is more like that for the plane mixing layer. This is supported by the observations indicating that there is greater similarity between the development of the plane mixing layer and the separated shear layers when the permeability is low than when the permeability is high. For $\sigma = 0.65$, far enough downstream the shear layers do appear to develop turbulent self-similarity as is observed in a plane mixing layer at high shear layer Reynolds numbers (based on the shear layer thickness), and the spectral data more clearly show that the decrease in the growth rate corresponds to the point at which the pairing process is substantially completed and the subharmonic frequencies dominate the shear layer fluctuations, and this in turn suggests that this may be what is occurring for $\sigma = 0.22$ at the point where the decrease in the growth rates occurs.

Although both the separated shear layers and plane mixing layers selectively amplify perturbations at particular frequencies, for the separated shear layers a broad amplified

frequency band is observed, in contrast to the somewhat narrower frequency band observed for the plane mixing layer (Browand 1966). The width of the amplified frequency band increases with decreasing plate permeability, in keeping with the previous observation that decreasing the plate permeability makes the environment in which the separated shear layer develops more like that of a typical plane mixing layer experiment. At least two possible explanations for the broad band response of the separated shear layers are suggested by the present results, the limited downstream development of the separated shear layers due to interaction with the end of the separation bubble, and variations in the stability properties of the shear layer due to velocity fluctuations at the primary wake frequency.

It has been suggested by Dimotakis and Brown (1976) that the dynamics of the flow at any point in a shear layer are influenced by the structure downstream of that point, and that this maintains a phase relationship between successive vortex formation cycles. This implies that the downstream structure of the shear layer plays a significant role in the frequency selection process through the presence of perturbations at subharmonics of the shear layer frequencies generated during successive downstream vortex pairings. For the shear layers separated from a circular cylinder, even with a low permeability splitter plate in the wake the downstream extent of the shear layers is limited by interactions at the end of the separation bubble and the subsequent development into a wake-like profile so that only a single vortex pairing occurs. The limited downstream extent of the separated shear layers will modify the feedback process and limit the feedback from subharmonic frequencies, and may also provide an additional source of random perturbations through incoherent fluctuations due to the energetic, possibly turbulent processes occurring at the end of the separation bubble.

The initial development of the instability of the plane mixing layer is well described by linear stability theory, which is discussed in detail in Drazin and Reid (1981). In the following discussion, frequent reference will be made to the concept of a 'mode' of the instability. In linear stability theory, it is assumed that the linearized equations which describe a flow have solutions which can be resolved into a set of functions which may be defined in terms of a wave number and a frequency. These solutions are referred to as the eigenmodes (or just modes) of the instability, and from computations of the rate at which they are amplified by the flow instability, it is possible to identify a particular mode (wave number and frequency) which has the maximum amplification rate, and this particular mode is called the 'most amplified mode.' It is assumed that any small perturbation may be linearly decomposed into such eigenmodes, and since the growth is exponential the mode having the greatest amplification rate will rapidly grow to be the dominant perturbation observed in the flow, until non-linear processes become important.

During the initial growth of a plane mixing layer, with a fixed value of the velocities on the two sides of the shear layer, the growth rate of a sinusoidal perturbation is a function of

the initial thickness θ_0 of the shear layer, the non-dimensional frequency of the perturbation $f\theta_0/\overline{U}$, and the shear layer parameter $R = \Delta U/2\overline{U}$. The growth rate is maximal for a value of the non-dimensional frequency $f\theta_0/\overline{U} \approx 0.032$, which is nearly independent of R (Ho and Huerre 1984), and the frequency selectivity of the plane mixing layer is a result of the exponential growth of perturbations at this preferred, maximally-amplified frequency. For the separated shear layers, when the permeability is low there are large-amplitude fluctuations at the primary wake frequency in the streamwise velocity component outside the separation bubble, whereas within the separation bubble the streamwise velocity is small relative to the free-stream velocity, so that the streamwise velocity fluctuations at the primary wake frequency are, in effect, fluctuations in the value of the non-dimensional frequency that arise from changes in the value of the mean velocity $\overline{U}$. This will have two effects: The dimensional value of the frequency corresponding to the most amplified mode will be changing in time so that instead of a unique most-amplified mode, the amplified modes will be those corresponding to a frequency band, resulting in the observed frequency bands. Furthermore, the amplification rate of any growing perturbations will be changing in time, as the flow conditions pass only momentarily through the point where the value of $f\theta_0/\overline{U}$ corresponding to a particular mode equals the value for the most amplified mode. Thus, the growth rate will decrease during other portions of the vortex formation cycle, and this will tend to increase the pairing length compared to that for a plane mixing layer. However, the pairing length also scales with the wavelength of the most-amplified non-dimensional frequency and therefore scales with $\overline{U}$, and this will tend to increase the pairing length at low free-stream velocities and to decrease it at high velocities.

These considerations help to explain the features of Fig. 5.10. The model predicts that increasing the formation length and decreasing the fluctuations in the value of the non-dimensional frequency through the use of a permeable splitter leads to a decrease in the pairing length due to enhanced growth of the shear layer instability. In competition with this is the observation that when the amplitude of the fluctuations at the primary wake frequency is high, there will be amplification of modes corresponding to additional, higher values of dimensional frequency, leading to a decrease in the predominant wavelengths of the growing shear layer fluctuations, which in turn leads to a decrease in the pairing length. The observed value of the pairing length derived from the present data must therefore correspond to an averaging process of the preferred pairing locations over the band of wavelengths corresponding to the secondary frequency band. Thus, reducing the strength of the fluctuations will tend to enhance the overall growth rate of the shear layer and decrease the pairing length, whereas increasing the strength of the primary wake fluctuations will lead to the growth of shorter wavelength fluctuations and this will also decrease the pairing length. In the present context, this implies that there is competition between the two different mechanisms when the permeability is changed. From Fig. 5.10 it appears that at low Reynolds numbers the growth of shorter perturbation wavelengths dominates, since in

that case the pairing length is smallest at $\sigma = 0$, whereas at higher Reynolds numbers the effect of the increased growth rate arising from increased frequency selectivity dominates, since in that case the pairing length is smallest at $\sigma = 0.65$. Solidity $\sigma = 0.22$ seems to be a hybrid case, similar to the low permeability case at low Reynolds numbers (in keeping with the increase in the value of the screen pressure drop coefficient at low screen-normal Reynolds numbers) whereas it is similar to the $\sigma = 0$ case at high Reynolds numbers (the decreasing importance of the screen pressure drop at high Reynolds number is also shown by the convergence of the Strouhal number for $\sigma = 0$ and $\sigma = 0.22$ at high Reynolds numbers).

The present observation that the instability in the shear layers separating from the circular cylinder amplifies a broad frequency band is in direct contrast with the results from several other investigations that have found discrete secondary frequency peaks in the separated shear layer with power spectral amplitudes that rival the amplitude of the primary wake frequency (Kourta *et al.* 1982, Wei and Smith 1986, Unal and Rockwell 1988). The question then arises as to what causes the difference between the present results and those observed elsewhere, and a possible solution is suggested by the model. Plane mixing layers are fairly sensitive to forcing of the flow at or near to the most amplified shear layer frequency (Ho and Huerre 1984), and therefore it is expected that if the analogy on which the model is based is reasonable, then the separated shear layers should share this sensitivity to forcing of the shear layer. However, since the separated shear layers are receptive to a wide frequency band, they should show a strong response to a wide band of perturbation frequencies. Furthermore, plane mixing layer experiments usually take place in a uniform pressure field. This is not the case for the separated shear layers, as the pressure in the separation bubble is considerably lower than that in the uniform flow at infinity and is varying both in space and in time, and so the shear layers behind the cylinder may show a greater sensitivity to perturbations due to pressure fluctuations in the flow, such as those introduced by acoustic forcing. This will be taken up in the next chapter.

5.5.3 A comment on the standard model

The present results suggest that the standard model hypothesis that movement of the location of transition to turbulence in the shear layers is responsible for the large changes to the flow over this Reynolds number range requires reconsideration. Although the flow is highly perturbed by the growing shear layer instability at $x = L_p$, which is also the location of the maximum value of the $\rho\overline{u'u'}$ component of the Reynolds stress, the flow is organized on time scales that are not short compared to that of the fluctuations at the primary wake frequency, and only exhibits a broad-band spectrum in the mean. Therefore, for flow behind a circular cylinder without a splitter plate, in this Reynolds number range the shear layers do not become fully turbulent before being entrained by the formation of the

large-scale vortices, so it is not accurate to speak of the upstream movement of the location of transition. This has implications for models of the flow in the near wake, since the structure of a fully turbulent shear layer is considerably different than that of the separated shear layers, and so any model must take into account such differences. Furthermore, the trends in the data shown in Fig. 4.1 and Fig. 5.10 do not support the hypothesis that the Reynolds number dependent changes are caused by changes in the pairing length. For both $\sigma = 0$ and $\sigma = 0.22$, an increase in the base suction coefficient corresponds to a decrease in the pairing length, but for $\sigma = 0.65$ at low Reynolds numbers the base pressure coefficient is constant despite a large change in the pairing length. Similarly, for $\sigma = 0$ a decrease in the Strouhal number corresponds to a decrease in the pairing length, but for $\sigma = 0.22$ the Strouhal number is approximately constant despite a large change in the pairing length. As an alternative hypothesis, it seems plausible that for a quiet free-stream flow the base pressure and primary wake frequency are unaffected by the natural development of the shear layer instability, whereas the development of the shear layer instability depends strongly on the length of the formation region and the amplitude in the near wake of the velocity fluctuations at the primary wake frequency, both of which are strongly affected by the interaction of the vortex formation with the separation bubble when the wake instability is body coupled. This hypothesis is supported by the observation that any change in the length of the separation bubble is small when the primary wake instability is a wake-profile instability, and the observation from the data shown in Chapter 4 that changes in the base pressure only occur for the body-coupled instability.

Fig.	U_∞	x/D	y/D	η	y_c/D	δ_*/D	f_C	f_N	K	$\overline{U}$	R
5.8a	3.06	0.40	0.66	1.73	0.62	0.0261	100	200	64	2.23	0.886
	3.06	0.50	0.67	1.65	0.62	0.0278	100	200	64	2.22	0.876
	3.06	0.60	0.68	1.76	0.63	0.0323	400	601	64	2.25	0.867
	3.03	0.70	0.69	1.57	0.63	0.0358	300	601	64	2.22	0.859
	3.02	0.80	0.70	1.79	0.64	0.0367	300	601	64	2.23	0.838
	3.02	1.01	0.73	2.20	0.64	0.0415	300	601	64	2.32	0.782
	3.03	1.21	0.73	1.81	0.64	0.0524	300	601	64	2.47	0.672
	3.03	1.41	0.72	1.75	0.61	0.0658	300	601	64	2.62	0.557
	3.02	1.61	0.72	1.76	0.58	0.0815	400	801	128	2.78	0.390
	3.01	1.81	0.85	1.33	0.52	0.2510	400	801	128	3.31	0.366
	3.00	2.01	0.95	—	—	—	400	801	128	2.71	0.274
5.8b	5.99	0.40	0.66	1.61	0.60	0.0330	1500	1503	64	4.65	0.818
	6.00	0.50	0.67	1.61	0.61	0.0407	1500	1503	64	4.67	0.804
	6.01	0.60	0.68	1.47	0.61	0.0491	1000	1503	64	4.81	0.759
	6.00	0.70	0.69	1.46	0.61	0.0590	1000	1503	64	4.87	0.730
	5.99	0.90	0.72	1.75	0.59	0.0740	1000	1503	64	5.24	0.580
	5.99	1.11	0.75	1.63	0.58	0.1100	1000	1503	64	5.81	0.391
	6.00	1.31	0.75	1.32	0.55	0.1570	1000	1503	128	5.94	0.246
	5.99	1.51	0.87	1.69	0.55	0.1930	1000	1503	128	5.94	0.177
	6.00	1.61	0.95	1.49	0.50	0.3000	1000	1503	128	5.75	0.193
5.8c	9.64	0.30	0.60	2.05	0.54	0.0306	2000	2997	128	7.45	0.836
	9.65	0.40	0.63	2.17	0.54	0.0386	2000	2997	128	7.61	0.783
	9.64	0.50	0.63	1.83	0.55	0.0487	2000	2997	128	7.72	0.751
	9.64	0.60	0.65	1.82	0.54	0.0611	2000	2997	128	7.94	0.703
	9.64	0.70	0.66	1.65	0.54	0.0761	2000	2997	128	8.16	0.637
	9.64	0.80	0.68	1.77	0.53	0.0869	2000	2997	128	8.52	0.551
	9.64	0.90	0.72	1.95	0.52	0.1040	2000	2997	128	8.96	0.444
	9.64	1.01	0.74	1.89	0.51	0.1240	2000	2997	128	9.30	0.355

TAB. 5.1 Information pertaining to the spectra shown in Fig. 5.8a–i . Lines containing a '—' indicate that the fit procedure gave unreasonable results for the corresponding profile. Frequencies f_C and f_N are in Hertz, velocities U_∞ and $\overline{U}$ are in meters per second, and K is the number of 2048-point power spectra averaged to obtain the power spectra shown in Fig. 5.8.

Fig.	U_∞	x/D	y/D	η	y_c/D	δ_*/D	f_C	f_N	K	$\overline{U}$	R
5.8d	3.09	15.70	26.80	2.19	24.50	1.0500	250	500	64	2.11	0.909
	3.08	19.70	27.40	2.36	24.80	1.1000	300	400	64	2.10	0.904
	3.08	27.60	28.40	2.07	25.50	1.4000	300	400	64	2.10	0.898
	3.07	35.40	28.80	1.88	26.10	1.4300	300	400	64	2.12	0.882
	3.08	51.20	29.20	2.06	25.90	1.5900	300	400	64	2.22	0.794
	3.07	66.90	29.50	1.53	24.80	3.0700	300	400	64	2.38	0.662
	3.10	82.70	31.50	1.77	22.80	4.9600	300	400	64	2.63	0.500
	3.08	98.40	33.50	1.68	19.80	8.1500	400	400	64	2.61	0.364
	3.10	110.00	39.40	2.01	18.10	10.6000	300	400	64	2.57	0.358
5.8e	5.95	0.40	0.65	2.00	0.61	0.0197	700	1001	128	4.16	0.905
	5.95	0.50	0.67	2.04	0.62	0.0225	700	1001	128	4.23	0.892
	5.95	0.70	0.69	2.06	0.64	0.0273	700	1001	128	4.30	0.854
	5.96	0.90	0.71	1.96	0.64	0.0375	700	1001	128	4.46	0.790
	5.95	1.11	0.73	1.91	0.63	0.0538	700	1001	128	4.70	0.698
	5.96	1.31	0.76	2.11	0.61	0.0717	700	1001	128	5.05	0.573
	5.95	1.51	0.78	1.91	0.59	0.0995	700	1001	128	5.37	0.436
	5.95	1.61	0.81	1.81	0.57	0.1310	700	1001	128	5.42	0.383
	5.96	1.71	0.85	1.78	0.55	0.1700	700	1001	128	5.47	0.336
	5.95	1.91	0.90	1.60	0.52	0.2390	700	1001	128	5.36	0.299
5.8f	9.60	0.40	0.62	1.88	0.57	0.0260	2000	2502	128	7.11	0.854
	9.59	0.50	0.64	2.01	0.58	0.0313	2000	2502	128	7.16	0.828
	9.58	0.60	0.66	2.00	0.58	0.0393	2000	2502	128	7.29	0.794
	9.59	0.70	0.67	1.98	0.58	0.0460	2000	2502	128	7.44	0.757
	9.60	0.90	0.70	1.92	0.58	0.0662	2000	2502	128	7.85	0.659
	9.60	1.11	0.74	2.03	0.56	0.0896	2000	2502	128	8.64	0.477
	9.59	1.31	0.77	1.43	0.54	0.1550	2000	2502	128	9.39	0.291
	9.59	1.41	0.81	1.30	0.51	0.2290	2000	2502	128	9.08	0.277
	9.58	1.61	0.95	1.49	0.50	0.3030	2000	2502	128	8.82	0.250

TAB. 5.1 *cont.*

Fig.	U_∞	x/D	y/D	η	y_c/D	δ_*/D	f_C	f_N	K	$\overline{U}$	R
5.8g	3.05	0.40	0.68	2.02	0.62	0.0316	300	500	64	2.01	0.887
	3.04	0.60	0.69	1.37	0.65	0.0327	300	500	64	2.03	0.876
	3.03	0.80	0.74	2.00	0.67	0.0373	300	500	64	2.02	0.862
	3.03	1.01	0.75	1.32	0.69	0.0447	300	500	64	2.05	0.846
	3.04	1.41	0.82	1.70	0.73	0.0542	300	500	64	2.15	0.761
	3.05	2.01	0.95	1.74	0.75	0.1200	300	500	64	2.27	0.691
	3.05	3.02	1.15	1.94	0.74	0.2110	300	500	64	2.36	0.610
	3.06	4.02	1.13	1.57	0.69	0.2780	300	500	64	2.26	0.600
	3.06	5.03	1.26	1.71	0.59	0.3860	300	500	64	2.04	0.671
5.8h	6.00	0.40	0.66	2.08	0.62	0.0195	1000	1251	64	4.80	0.887
	5.99	0.60	0.69	2.01	0.65	0.0215	1700	2002	64	4.85	0.874
	5.98	0.80	0.74	2.01	0.68	0.0307	1750	2002	64	4.96	0.826
	5.98	1.01	0.77	1.85	0.69	0.0438	1750	2002	64	5.02	0.792
	5.97	1.21	0.81	1.61	0.71	0.0657	1750	2002	64	5.17	0.742
	5.96	1.41	0.86	1.62	0.72	0.0904	1750	2002	64	5.08	0.746
5.8i	9.52	0.40	0.64	1.37	0.62	0.0159	2500	2997	64	7.78	0.889
	9.48	0.60	0.67	1.68	0.64	0.0225	2500	2997	64	7.91	0.844
	9.51	0.80	0.71	1.54	0.65	0.0416	2500	2997	64	8.10	0.790
	9.51	1.01	0.76	1.42	0.67	0.0696	2500	2997	64	8.25	0.768
	9.52	1.21	0.80	1.44	0.67	0.0902	2500	2997	64	8.31	0.756
	9.52	1.41	0.85	1.52	0.68	0.1120	2500	2997	64	8.37	0.737

TAB. 5.1 *cont.*

CHAPTER 6

Effects of forcing on the shear layer instability

6.1 Introduction

The exploration of the near wake structure using the permeable splitter plates, presented in Chapter 5, indicates that the instability in the shear layers separating from a circular cylinder does not selectively amplify a particular perturbation frequency, but instead amplifies perturbations that lie in a fairly broad frequency band. In particular, the power spectral density computed from the velocity fluctuations do not have sharply defined, discrete peaks dominating the secondary frequency bands, and furthermore the highest amplitudes in the secondary frequency bands do not compare in order of magnitude with the amplitude at the primary wake frequency. These results are substantially different from those of other investigations, where dominant frequencies f_2 are observed in the shear layer fluctuations, and the question then arises as to the cause of the different results obtained in the present experiment.

It is conceivable that the structure of the separated shear layers is substantially perturbed in the present experiment from that investigated elsewhere, perhaps due to some unreported experimental condition that prevents the instability from developing naturally, but it is difficult to imagine conditions for which this would be the case without there being a significant signature in the measurements that have been reported elsewhere in this thesis. In particular, the smoke wire flow visualization shows that the smoke lines remain sharply defined and unperturbed and without significant out-of-plane distortion whenever they do not significantly interact with the cylinder wake, implying that the free-stream flow is quiet and two-dimensional in the plane of the measurements. Furthermore, power spectra computed from measurements of the free-stream turbulent velocity fluctuations show a $1/f$ spectral distribution on which low-amplitude discrete peaks (mostly related to the fan frequency) are superimposed (see Fig. A.1), but these discrete peaks are not generally amplified by the shear layer instability although they may fall in the secondary frequency band (see Fig. 5.9). Strong support for the hypothesis that the current results reflect the natural development of the separated shear layers, unperturbed except by the inevitable low-amplitude incoherent fluctuations of the free-stream turbulence, would be shown if the introduction into the flow of coherent, harmonic perturbations results in the appearance of

sharp spectral peaks in the power spectra computed from the velocity fluctuations in the shear layer. The results of such an investigation using acoustic forcing will be presented here, and show that the shear layers exhibit a very sharp spectral response to harmonic excitation over a broad range of frequencies.

6.1.1 Previous investigations of the separated shear layer instability

A review of several other investigations of the shear layer behind the circular cylinder will help to clarify some of the issues associated with definitions of the secondary frequency, and will elucidate possible causes of the differences between the present results and those of other investigations.

There have been several experimental investigations of the stability of the shear layers separating from a circular cylinder in the last 30 years, and of particular note are the reported observations of the presence in power spectra computed from the velocity fluctuations measured in the separated shear layer of discrete frequencies centered at substantially higher frequencies than the primary wake frequency. These correspond to what is referred to in Chapter 5 as the secondary frequency f_2. Such discrete secondary frequencies have been interpreted as the frequency of the most amplified mode (see Sec. 5.5.2) of the Kelvin-Helmholtz instability of the shear layer, and the growth of the instability is what results in the development of vortices within the shear layer, now often referred to as "Bloor-Gerrard vortices." A simple dimensional argument (Bloor 1964), assuming that the shear layer frequencies scale like $f_2\theta_0/U_\infty$, that the self-similar Blasius boundary layer scaling of the initial shear layer thickness holds, and using the Strouhal number scaling for the primary vortex formation frequency, leads to the conclusion that the ratio of the secondary frequency f_2 to the primary vortex formation frequency f_1 should follow a power law of the form

$$\frac{f_2}{f_1} = C\,\mathrm{Re}^n\,, \tag{6.1}$$

where $n = 1/2$ if the scaling is correct. The assumption that the separating boundary layers scale like a self-similar laminar boundary layer is suspect, because the boundary layers near separation are highly perturbed by the velocity and pressure fluctuations from the primary vortex formation, and so Eqn. 6.1 is only a zeroth-order approximation, subject to experimental verification. In general, it has been concluded in most of the investigations discussed here that this scaling is verified by the experimental results.

Bloor (1964) made extensive hot-wire measurements of the flow in the near wake of a circular cylinder in the Reynolds number range $2 \cdot 10^2 \lesssim \mathrm{Re} \lesssim 5 \cdot 10^4$, with particular emphasis on the shear layer instability, and this seems to be the first systematic examination of the stability of the separated shear layers and of the Reynolds number dependence of the location in the near wake at which the shear layers undergo transition to turbulence. In

Bloor's experiments, the measurements were made in a single wind tunnel using cylinders of varying diameters and with no end plates, so that blockage, aspect ratio and end effects were not controlled, although it is stated that the free-stream turbulence intensity in the wind tunnel was measured to be 0.03%. Bloor also made measurements to determine the validity of Eqn. 6.1. In the experiment, a hot wire was at the same fixed position of $(x/D, y/D) = (0.6, 0.6)$ for all measurements, which in the present experiments is found to lie within the shear layer or the separation bubble at all Reynolds numbers. Frequencies were obtained by counting cycles on photographs of oscilloscope traces of the hot-wire output. This procedure inherently gives a single number for the frequency; only by statistically significant sampling can the actual center frequency be determined, and even then the present results indicate that the center is not well defined. No statistics are available for Bloor's data, so no estimate is available of the uncertainty in the center frequency or of the broadness of the frequency distribution in the separated shear layers. The data are plotted according to Eqn. 6.1, and a fit is shown for one cylinder diameter. Data obtained using a cylinder with a different diameter are plotted on the same axes, and it appears that for this data, different values of n and C would be appropriate, a discrepancy which was also noted by Bloor.

Wei and Smith (1986) made observations similar to Bloor's in the Reynolds number range $1.2 \cdot 10^3 \lesssim \mathrm{Re} \lesssim 1.1 \cdot 10^4$ using different measurement techniques. Using hydrogen bubble flow visualization and a video camera, fully developed shear layer vortices were visualized and then counted frame by frame, and from the known framing rate a passage frequency was computed. They then repeated the experiments using hot-wire anemometry and digital data collection, and analyzed the data using Fourier transform techniques. Unfortunately, few details of the analysis are given and no example spectra are shown. In these experiments the hot wire was located at the same fixed location of $(x/D, y/D) = (0.6, 0.6)$ as in the experiments by Bloor. Their experiments were performed in a water channel with a free-stream turbulence level of 0.4% using several cylinders of different diameters and without end plates. The data obtained from the two different techniques each separately fit a power law relationship like Eqn. 6.1 but the data obtained from each technique and cylinder diameter require different values of C and n. They conjecture that the lack of agreement in the results is due to the hot wire results being affected by the primary vortex shedding moving the shear layer closer to and then farther from the hot wire, causing the f_2 frequency to only be observed part of the time and thus shifting the apparent peaks to lower frequencies. The issue of the transverse motion of the shear layer is discussed in Sec. 5.3.3, and is found to not be important in the present experiments, and in any case when Fourier analysis techniques are used the transverse motion of the shear layer would not effect the center frequencies of the spectral peaks, so the explanation for the differences must lie elsewhere.

Kourta *et al.* (1987) in an extensive set of experiments in the Reynolds number range $2 \cdot 10^3 \lesssim \mathrm{Re} \lesssim 6 \cdot 10^4$ also observed secondary frequencies using hot-wire anemometry and digital measurement and analysis techniques. They used end plates of the Stansby (1974) design and a fixed aspect ratio of $13D$, and report a free-stream turbulence level of 0.1%. They present some interesting flow visualization photographs that show completely formed shear layer vortices less than $0.5D$ downstream of the cylinder at Re = 4800. Example power spectra are presented that show signal spectra at fixed y/D and three different values of x/D. Discrete, high-amplitude peaks corresponding to a secondary frequency are clearly visible at $x/D = 0.125$ and $x/D = 1.375$, and at the latter position the peak is of greater amplitude than that at the primary frequency. They conclude that $n = 1/2$ gives reasonable agreement with their data, and find a best fit to Eqn. 6.1 that they say agrees with the data from Bloor (although Bloor gives two sets of data which do not agree with each other), using $C = 0.0095$ and $n = 1/2$. It is significant that the spectra that are shown are from data taken at fixed y/D, while only x/D was varied. The present results show that sampling the data at fixed y/D and varying the downstream position will place the hot wire at a different point in the shear layer, or even entirely within the separation bubble, which makes it impossible to meaningfully compare the amplitudes of the velocity fluctuations. However, at a fixed value of x/D this probably leaves the frequencies at which different spectral features appear relatively unaffected, although it is seen in the present results (see Fig. 5.8) that the center frequency of the secondary frequency band will slowly move to lower values with increasing x/D, probably due to changes in the value of the velocity difference across the shear layer. They also used a solid wake splitter plate to modify the primary vortex shedding and study the effect on the secondary frequencies. The plate was not long enough to eliminate fluctuations at the primary wake frequency from the near wake, but the amplitude of the fluctuations were reduced and found to be independent of the Reynolds number. Spectra are also shown for the flow with the splitter plate, and a secondary frequency peak is still observed. The absolute amplitudes of the peaks identified as being at the shear layer frequency are three orders of magnitude greater than the amplitudes observed without a splitter plate. Here again, the significance of the relative amplitudes is difficult to determine. All else being the same, and if their spectra can be directly compared with each other, this supports the results of the present experiments using low permeability splitter plates that show that the presence of a low permeability or an impermeable splitter plate enhances the development of the shear layer instability and hence enhances the definition and amplitude of the secondary frequency band.

Unal and Rockwell (1988) made similar measurements of the shear layer instability using hot-film anemometry in a low-turbulence (0.06%) water channel in the Reynolds number range $4.4 \cdot 10^2 \lesssim \mathrm{Re} \lesssim 5 \cdot 10^3$, but they were primarily concerned with the effect of feedback from a downstream body on the shear layer growth rates and were not particularly interested in the frequency dependence of the separated shear layers. However, they also show

spectra taken at differing transverse locations across the shear layer, and these exhibit discrete peaks at the primary wake frequency and high-amplitude discrete peaks at frequencies considerably higher than that of the primary wake frequency. Few details of the spectral analysis are given, so it is not possible to make quantitative comparisons with the amplitudes of their published spectral data. However, qualitatively it may be seen that at certain locations in the shear layer, if the relative scales of the spectra shown are accurate and unaffected by antialiasing filtering or smoothing, the amplitude of the discrete secondary frequency peak is higher than that of the peak at the primary wake frequency. They mention in passing that measurements of the growth of the shear layer momentum thickness give results that do not fit the boundary layer scaling used in the Bloor model, so they assume that equation Eqn. 6.1 should not hold, and therefore do not plot the secondary frequencies against Re. The interference element that they used to modify the near wake interactions, described as a wake splitter plate, was actually an afterbody with a wedge-shaped leading edge of thickness that was large compared to the cylinder diameter ($t/D \simeq 0.53$, estimated from one of the published flow visualization video frames), and thus there were probably additional modifications to the near wake structure from the downstream boundary condition created by the thick afterbody, which complicates the interpretation of their data in the present context.

6.1.2 Discussion of previous results

Except for observing the existence of a well-defined secondary frequency, the results of other investigations are not in particularly close agreement. Bloor's results show that a single correlation does not fit data for cylinders of differing diameters, and Wei and Smith used four cylinders of different diameters to obtain their data (different sets of three cylinders were used with each technique). Furthermore, only one cylinder diameter (2.54 cm) is common between the experiments of Bloor and those of Wei and Smith. This suggests that there is another parameter, related to the cylinder diameter, which affects the scaling of the shear layer vortices, and one possible candidate is the free-stream turbulence, which will introduce length scales independent of the cylinder diameter. Data on the spectral distribution of the free-stream turbulence in the present experiments are shown in Appendix A, but no information is available on the frequency content of the free-stream flow for the other investigations that have been discussed.

Another possible source of the differing results may be differences that arise from the two different experimental definitions of f_2: It has been defined as the average number of high-frequency oscillations per unit time measured at a single point in the flow, and also has been defined as the frequency at which the discrete peak having the maximum amplitude is observed in a power spectrum computed from the shear layer velocity fluctuations. The definition used by Bloor based on visually counting flow oscillations, and the similar defini-

tion used by Wei and Smith of counting the shear layer vortices passing a point, will always result in a single value of f_2. If the frequencies are distributed over a broad band, then the number that is obtained is an estimate of the center frequency of the secondary frequency band. This number is subject to statistical uncertainties, but if the standard deviation of the measurements is computed and reported, this procedure gives information about how well the center frequency is known as well as an estimate for the width of the secondary frequency band. The computation of power spectra gives a large amount of information about the instability, particularly the frequency distribution of the amplified frequencies as well as information about perturbations at related frequencies such as harmonics and subharmonics, but also raises the possibility of ambiguity about the correct value of f_2 if multiple discrete peaks are present, or if the "peak" is broadly distributed and of low amplitude relative to the background (as is observed in the present experiments, see Sec. 5.4.2).

In the analysis leading to Eqn. 6.1, there is the a priori assumption of the existence of a well-defined frequency in the shear layer. This assumption arises from the theory of hydrodynamic stability, which predicts that the shear layer instability will select the particular most unstable mode (corresponding to a particular instability frequency) and selectively amplify it, so that this particular mode experiences exponential growth and a single frequency and its harmonics quickly dominate the fluctuations in the shear layer (Drazin and Reid 1981). For the plane mixing layer, this has been experimentally investigated and confirmed in some detail (Browand 1966, Brown and Roshko 1974, Winant and Browand 1974, Ho and Huerre 1984). However, as discussed in Sec. 5.5.2, the shear layers separating from a circular cylinder are in a different flow environment than that which is usually arranged in plane mixing layer experiments, so the development of the instability may be expected to be somewhat different than, although related to, that of the plane mixing layer. The data shown in Chapter 5 demonstrates that the assumption of the existence of a uniquely defined most amplified mode of the instability may not be correct.

The differences between Bloor's results and those of Wei and Smith suggest that there is an unidentified factor related to the cylinder diameter that may be responsible for the different results obtained by different investigations. Furthermore, the discrete secondary frequency peaks observed by those investigations that used spectral methods to determine the frequency distribution combined with the lack of frequency selectivity demonstrated in the present experiments indicate that some external influence is responsible for the frequency selectivity observed in other investigations, which is not a factor in the current experiments. It was noted in Chapter 5 that the wide-band frequency response of the separated shear layers and the model presented there for the shear layer development suggest that the shear layers should be sensitive to a band of perturbation frequencies, and that artificially exciting the shear layer with perturbations in the sensitive band could lead to enhanced growth at the excitation frequency. These results suggest that a possible cause of the different results

is the introduction of length scales by perturbations in the free stream which are close to the important shear layer length scales and which are independent of the cylinder diameter. If the perturbations occur at sufficiently well-defined discrete frequencies lying within the frequency bands to which the shear layers are receptive, they may cause the discrete spectral response of the shear layers observed by other researchers.

This provides the motivation to impose perturbations having a narrow frequency bandwidth into the present experimental setup. The results of measurements on the shear layers in the presence of such excitation are reported in the rest of this chapter. The method that was used for introducing such narrow bandwidth perturbations (hereafter referred to as "harmonic perturbations") was acoustic forcing, using a loudspeaker driven by a function generator (the details are discussed in Sec. 6.2.1). Three types of measurements were made with the acoustic forcing; smoke wire flow visualization of the near wake and the shear layers that establishes that the forcing technique has an effect on both the overall structure of the near wake and on the development of the shear layers; single point measurements that show that the shear layers do respond to forcing in a receptive frequency band, and also help to delineate the receptive frequency bands; and a hot-wire survey of the near wake similar to those presented in Chapter 5 but with the acoustic forcing present.

6.1.3 Flow visualization of the effects of the acoustic forcing

Figure 6.1 shows three smoke wire flow visualization photographs of the flow past a circular cylinder with a splitter plate of solidity $\sigma = 0.65$ at $\mathrm{Re} = 4900$. The smoke wire flow visualization technique is discussed in Chapter 3. Figure 6.1**a** was taken with the acoustic forcing turned off, (but with the speaker in place), Figure 6.1**b** shows the flow with acoustic forcing at $f_{a*} = 1.14$, and Figure 6.1**c** shows the flow with acoustic forcing at $f_{a*} = 1.18$. These two frequencies are near the frequency at which the flow shows the greatest response to the acoustic forcing, as discussed in Sec. 6.2.3, but although the two different photographs shown in Fig. 6.1**b** and Fig. 6.1**c** are taken at slightly different forcing frequencies, the variation between the two photographs is not particularly significant since equivalent variations occur even at the same forcing frequency. The two show here were selected to give an idea of the range of variation.

The photographs show that with the forcing the waviness that is visible in the smoke lines delineating the edge of the separation bubble, which corresponds to the developing shear layer instability (see Chapter 3) is more pronounced, and appears upstream of the location at which it appears in the unforced case. The length of the separation bubble appears to be decreased by the forcing although at this permeability, for which the wake instability is not body coupled, the end of the separation bubble is not as clearly delineated as it is when the primary vortex formation occurs at the end of the separation bubble. In

Fig. 6.1**b** the wake has sinusoidal boundaries downstream of the separation bubble, resulting from the development of the wake-profile instability and indicating that large-scale vortices probably develop farther downstream, although no large-scale vortices are seen to form within the imaged regions.

A smoke wire flow visualization photograph of the shear layers was shown in Fig. 5.11 for the flow with a permeable splitter plate of solidity $\sigma = 0.65$ without forcing. Using the same technique and locating the smoke wire in the same place as detailed in the discussion in Sec. 5.5.2, photographs showing the effect of the forcing on the shear layers were obtained. Figure 6.2**a** shows a photograph of the shear layer without a splitter plate ($\sigma = 0$) at Re = 5200 without forcing, and Fig. 6.2**b** shows the same flow with acoustic forcing at $f_{a*} = 1.68$. It can be seen that with the forcing the shear layer vortices are very regular and appear very close to the cylinder, whereas without the forcing the shear layer vortices develop irregularly, and fully formed vortices do not appear for some distance downstream of the cylinder. The same results are seen with a permeable splitter plate of solidity $\sigma = 0.65$ at Re = 5600, shown in Fig. 6.2**c** without forcing and in Fig. 6.2**d** with acoustic forcing at $f_{a*} = 1.39$, except that without the forcing the fully formed shear layer vortices first develop farther downstream than for $\sigma = 0$.

6.2 Single point measurements of the forced shear layer

The results presented in this section are from simultaneous measurements of the velocity fluctuations at a single point in the shear layer and of the cylinder base pressure while acoustic forcing is applied to the flow. From the measurements of the velocity fluctuations it is possible to compute the spectral power density, and thereby to determine the effect of the forcing on the primary vortex formation frequency as well.

6.2.1 Experimental method

Acoustic forcing was provided by a commercially available low frequency speaker (Radio Shack model 40-1024) mounted to a piece of 3/4″-thick plywood faced up against a circular hole having the same diameter as the speaker cone, and the plywood was in turn mounted to a stand using C-clamps and placed against the honeycomb at the inlet to the wind tunnel. The speaker was driven by one channel of a stereo power amplifier (Scientific Audio Electronics model 2200) with the amplifier input in turn driven by a function generator (Krohn-Hite model 5100A) set to produce sine waves. The location of the speaker in the tunnel inlet did produce some flow interference, which had a significant effect on the measured base pressure (with the forcing off) only at the lowest Reynolds number and solidities $\sigma = 0$ and 0.22 where the base suction coefficient increased by approximately

10% and 5%, respectively. Since the goal was to measure the effects of the forcing on the flow, this should not affect the conclusions presented here. The speaker response was specified by the manufacturer to be flat from 0.03–3 kHz, but this was not checked. Instead, the acoustic power was monitored by a calibrated microphone system (B&K Instruments microphone model 4138 and power supply model 2801) mounted through a hole in the test section top located at the cylinder station and 1/4 of the tunnel width from the front wall. With this setup, the microphone not only measured the acoustic power output from the speaker, but also experienced pressure fluctuations due to the oscillations in the flow. The microphone output was amplified and filtered by a preamplifier (Stanford Research SR560), and then collected using the digital data collection system described in Chapter 2. The manufacturer's calibration was used to convert from the microphone voltage to pressure fluctuations. The hot-wire system, pressure sensors and the test section setup were as described in Chapter 2.

The hot wire was located at $x/D = .6$ during the collection of all data presented in this section, and the transverse location of the hot wire was determined for each flow condition by moving the the hot wire to the streamwise position, doing a fast traverse of the shear layer (as described in Sec. 5.1.1) with the acoustic forcing off, using the results of the fast traverse to locate the outer edge of the shear layer, and then positioning the hot wire at the outer edge. The hot wire was calibrated to determine actual velocities, but even though the actual velocity signal is computed and the data are presented as either $u(t)/U_\infty$ or as velocity spectra in terms of the power spectral density computed from u'/U_∞, the data were collected at the same actual streamwise position for all flow conditions, and not quite at identical transverse location (in terms of normalized shear layer coordinates η) and therefore the hot wire was not at geometrically similar positions for the different flow conditions. Thus, the amplitudes of the spectral features should only be compared semi-quantitatively between different flow conditions, in the sense that order of magnitude differences are significant, whereas differences of only a few percent are not. The results of the last chapter show that changes in the frequencies at which spectral features appear (see Fig. 5.8) with increasing x/D are small, at least within the initial growth region of the shear layer, and so the locations of the spectral features may be quantitatively compared. For each flow condition, data were first collected with the acoustic forcing turned off, and then the acoustic forcing was turned on and the frequency varied. Once positioned, the hot wire was not moved during the frequency sweeps, and since the forcing affects the shear layer development (as will be shown in a later section), it is likely that this also produced a small change in the position of the hot wire relative to the shear layer.

The precise amplitude of the acoustic waves present at the cylinder location was not controlled, but was measured to obtain the forcing frequency, which was determined from the discrete peak with the highest amplitude appearing in the power spectral density computed

from the microphone output, which in all cases corresponded to within about 1% of the value selected using the dial on the frequency generator. At several frequencies, harmonics of the forcing frequency appeared in the acoustic spectra, but these were always at least an order of magnitude lower than the peak at the selected forcing frequency. Determining the relationship between the strength of the forcing and the amplitude of the shear layer response would be interesting, but it is not of primary concern here, where the intent is to demonstrate the frequency receptivity of the shear layers and to examine the effect on the near wake of forcing the separating shear layers, and so it will be assumed that the amplitude of the acoustic forcing was high enough in all cases to overwhelm the natural perturbations in the flow and that only the frequency dependence is important. Actually controlling the acoustic power driving the flow is difficult without carefully designed wind tunnels and acoustic sources (see Peterka and Richardson 1969), so the acoustic power was merely obtained from the microphone measurements. The results of the microphone measurements are given in Appendix E in the form of the amplitude of the acoustic power spectral density at the forcing frequency, and do not show any clear correlation with the response of the near wake although the acoustic power is not particularly constant with forcing frequency.

6.2.2 Effects of forcing on the shear layer velocity fluctuations

It is seen in the flow visualization shown in Sec. 6.1.2 that the shear layers and the near wake as a whole do respond to the acoustic forcing, and it remains to be established that the response is frequency dependent. Figure 6.3 shows example velocity traces for $\sigma = 0.22$ and $\mathrm{Re} = 4900$, for several values of the forcing frequency. Figure 6.3**a** is a velocity trace without any forcing, and shows the features that were generally described in Sec. 5.3.2, *i.e.*, large-scale velocity fluctutations at the primary wake frequency, small-scale low-amplitude fluctuations at a higher frequency. Figure 6.3**b** shows a velocity trace with the forcing turned on, but at a frequency that is considerably lower than any frequencies that exhibit a peak response (as will be discussed in Sec. 6.2.3. Figure 6.3**c** shows a velocity trace with the forcing frequency set to a value that corresponds to a local maximum in the amplitude of the power spectral density measured at the forcing frequency when plotted against the forcing frequency. Figure 6.3**d** shows a velocity trace with the forcing frequency set to the value that corresponds to the maximum amplitude of the power spectral density measured at the forcing frequency. Figure 6.3**e** shows a velocity trace with the forcing frequency set to a value near the high frequency limit of the frequency band to which the shear layer responds, and Fig. 6.3**f** shows a velocity trace with the forcing far higher than the upper limit of the frequency band to which the shear layer responds. It is fairly clear from these velocity traces that for this solidity and Reynolds number, the shear layer does respond to the acoustic forcing and that the magnitude of the response depends on the frequency of the forcing.

6.2.3 Response of the global measurements to the acoustic forcing

Figure 6.4 shows the response of the shear layer to the acoustic forcing as a function of the forcing frequency, as indicated by several measured values that will be collectively referred to as the "near wake parameters." The figure is organized into vertical columns, each corresponding to a different value of the solidity and the Reynolds number, and within each column, each row has the results of a different measurement plotted against the non-dimensional acoustic forcing frequency $f_{a*} = f_a D/U_\infty$. Each column is alphabetically labeled at the top, which indexes the flow conditions given in the figure caption. The top row shows the amplitude of the power spectral density at the forcing frequency, $\Phi_a \equiv \Phi(f_{a*})$; the second row shows the root mean square (RMS) value of the velocity fluctuations defined using

$$u' = \sqrt{\overline{\left(u(t) - \overline{u}\right)^2}},$$

normalized as u'/U_∞ and estimated from the data; the third row shows the base suction coefficient $-C_{pb}$ and the bottom row shows the Strouhal number, both defined as in Chapter 4. The values shown for $f_{a*} = 0$ were measured without any forcing, and the zero values for St shown in Fig. 6.4**g**–**i** indicate that no primary wake frequency was detected. It is clear from the data shown in this figure that acoustically forcing the flow has an effect on all of the measured values, and that the magnitude of the effect depends on the forcing frequency.

In general the response to the forcing shows similarities across the range of solidities and Reynolds numbers for which the measurements were made. Many of the near-wake parameters show peaks responses at two or more different values of the forcing frequency, and for a given flow condition, the two different frequencies at which a peak response is obtained are not harmonically related (*e.g.*, Fig. 6.4**c**). Two cases are exceptional, $\sigma = 0$, Re = 9300, (Fig. 6.4**c**), and $\sigma = 0.22$, Re = 15300, (Fig. 6.4**f**), in that they are both very similar (to each other), both only show peak responses at a single frequency, and both show baseline values of u'/U_∞ that are significantly higher than for the other flow conditions. Furthermore, the response for which the maximal value of Φ_a occurs at a lower frequency than that at which the other near wake parameters reach their peak response in both cases. This will be discussed further in Sec. 6.4

It is plausible to expect that at very high frequencies the forcing should have no effect, in particular when the frequencies lie outside the shear layer receptive frequency band. However, this is not the case for Re < 10000 when the wake exhibits the body-coupled instability, corresponding to Fig. 6.4**a**, **b**, **d**, and **e**, where the values of u'/U_∞ and $-C_{pb}$ are depressed at high frequencies from the values without forcing, while for $\sigma = 0$ the value of St increases at high forcing frequency. It is possible that the decreased values at high f_{a*} are caused by the high frequency perturbations overwhelming the natural perturbations at

the most amplified frequency and thereby damping the shear layer response. The damped shear layer response then leads to the observed variations in the near wake parameters, generally a decrease in the base pressure, a decrease in the velocity fluctuations, and an increase in the primary wake frequency.

The value of Φ_a represents the response of the shear layer only at the forcing frequency, in some sense separated from other effects such as the excitation at harmonics of the forcing frequency, and in general it may be noted that a peak in Φ_a corresponds to peaks in the other near wake parameters, although the converse is not true, since peaks appear in the other near wake parameters do not correspond to peaks in Φ_a. Notable examples of this are the two exceptional, single response peak cases shown in Fig. 6.4**b** and Fig. 6.4**f**, where in both cases the maximum in Φ_a occurs at a somewhat lower frequency than that at which the other near wake parameters reach their maximum values. Note that the relationship between the frequency corresponding to the maximum in Φ_a and the frequency corresponding to the maxima in the other near wake parameters are not harmonically related. With the splitter plates in the wake, the peaks in the value of Φ_a are an order of magnitude greater with than without a splitter plate at the same Reynolds numbers. The increase in solidity from $\sigma = 0.22$ to $\sigma = 0.65$ also increases the peak values of Φ_a but the increase is not an order of magnitude, except at the highest Reynolds number. Also, the peak values of Φ_a decrease with increasing Reynolds number at $\sigma = 0$ and $\sigma = 0.22$, and increase with increasing Reynolds number at $\sigma = 0.65$.

The velocity fluctuations and the base suction seem to be more closely related than the other wake parameters, in that at forcing frequencies for which there are peaks in the base suction coefficient $-C_{pb}$, there are corresponding peaks in u'/U_∞, although the relative sizes of the peaks are not necessarily the same, *i.e.*, the highest peak in the base suction may not be at the highest peak of u'/U_∞ (see Fig. 6.4**d**). Furthermore, the base suction increases with the amplitude of the shear stresses (as indicated by u') in all cases, while the situation for the Strouhal number is not so clear except that it generally decreases. The response of the Strouhal number to the forcing frequency is related to the response of the rest of the near wake parameters in most cases, and the relationship is usually inverse, *i.e.*, the Strouhal number is smaller when $-C_{pb}$ and u'/U_∞ are large. These general comments do not hold true for all flow conditions and forcing frequencies, however; for example, for $\sigma = 0$ and $\mathrm{Re} = 4900$, there is a peak in all near wake parameters except Φ_a at $f_{a*} \approx 1.2$. For $\sigma = 0$ and $\mathrm{Re} = 9500$, there is a frequency range for which a large response occurs in all near wake parameters except St, and in this range St is constant, rising as the forcing frequency is increased out of this band and the values of the other parameters decrease. For $\sigma = 0.22$ $\mathrm{Re} = 4900$ there is a peak at $f_{a*} \approx 0.8$ in both $-C_{pb}$ and St that does not appear in either u'/U_∞ or Φ_a. Note, however, that higher base suction corresponds to lower Strouhal number in nearly all cases for which St is defined. No vortex formation frequency

is observed in the near wake for $\sigma = 0.65$ at any Reynolds number, indicating that the presence of the forcing does not change the character of the wake from a wake-profile to a body-coupled instability.

There are fairly well-defined bands of forcing frequencies for which the near wake shows a large response, and as in the last chapter these bands will be referred to as the secondary frequency bands. There is some difference in the usage here, in that with the forcing the sensitive bands appear to encompass what was previously referred to as the subharmonic band. At a given Reynolds number the shapes and the band widths of the secondary frequency bands are similar at all solidities, although the details of the response within the frequency bands vary considerably. For low Reynolds numbers the frequency bands are narrow, and show narrower features, and the widths of the frequency bands increase as the Reynolds number increases. The frequencies at which maximum response of the shear layer is observed (in terms of maximal or minimal values of the near wake parameters) also increase as the Reynolds number increases.

6.2.4 Effects of the acoustic forcing on the shear layer power spectra

Figure 6.5 shows example power spectra, computed from the same data from which Fig. 6.4 was derived, which show how the forcing effects the power spectral density. The power spectra are computed as in Appendix D. Each page of the figure corresponds to a different flow condition arranged in order of increasing Reynolds number, with $\sigma = 0$ first, (Fig. 6.5**a**–**c**), $\sigma = 0.22$, (Fig. 6.5**d**–**f**), and $\sigma = 0.65$, (Fig. 6.5**g**–**i**). The spectra have been arranged to be read left to right, top to bottom with the forcing frequency increasing commensurately.

As was the case for the presentation of the data in Fig. 6.4, it can also be seen from the spectra that the shear layers respond strongly to forcing within the secondary frequency band and, in terms of changes in peak amplitudes and the number of harmonics that appear, the response is much greater as the solidity is increased. This can be seen in almost every set of spectra, although the secondary frequency band is most clearly defined for $\sigma = 0$ and $\sigma = 0.22$ (for which the wake exhibits the body-coupled instability) in the sense that the greatest response occurs when the forcing frequency is in the secondary frequency band, and the response is not nearly so great when the forcing frequency lies outside this band (*e.g.*, see Fig. 6.5**a**, $1.44 \leq f_{a*} \leq 2.50$ compared to $f_{a*} = 0$, all of Fig. 6.5**d**, and Fig. 6.5**e**, $2.06 \leq f_{a*} \leq 3.40$). When $\sigma = 0.65$, the overall response of the shear layers to the forcing is much greater than at lower solidities, and so although the forcing in the secondary frequency band still gives the greatest response, the shear layers are sensitive to forcing at nearly all frequencies across most of the forcing frequency range, and the response only begins to diminish when the frequency is very high relative to the secondary frequency

band (Fig. 6.5g–i). Also, at this solidity non-linear effects are exhibited in that peaks appear at $(n+1)f_{a*}/4$, rather than just at the subharmonics and harmonics (Fig. 6.5h, $2.15 \leq f_{a*} \leq 3.36$ and i, $1.95 \leq f_{a*} \leq 2.95$). Note that for all flow conditions, forcing in the secondary frequency band raises the overall level of the power spectral density, not just at the discrete peaks but throughout the frequency range. This effect is most apparent at low Reynolds number (Fig. 6.5a, comparing $f_{a*} = 0$ with $f_{a*} = 2.08$).

For $\sigma = 0$, forcing in the secondary frequency band brings about a large response, but does not seem to excite subharmonics of the forcing frequency. Conversely, forcing in the subharmonic band does not bring about much response at either the forcing frequency f_{a*} or at the harmonic $2f_{a*}$ lying within in the secondary frequency band. With a permeable splitter plate, when the forcing frequency lies in the subharmonic band so that $2f_{a*}$ lies within the secondary frequency band, strong peaks appear at both f_{a*} and $2f_{a*}$, showing that the presence of a subharmonic of one of the most amplified frequencies is able to excite the shear layer instability, although the increase in the amplitude is not as large as when the forcing frequency actually lies within the secondary frequency band. When the forcing frequency lies within the secondary frequency band, the subharmonic response, in terms of amplitude and definition of the peaks at $f_{a*}/2$, is pronounced. Note that the forcing frequency, not the center frequency of the unforced subharmonic band, determines the subharmonic frequency (*e.g.*, Fig. 6.5f, $f_{a*} = 3.40$). However, the shear layers do not generally respond strongly to forcing at frequencies that are greater than the upper limit of the secondary frequency band, *i.e.*, if the subharmonic of the forcing frequency lies within the secondary frequency band, there is not much effect at $f_{a*}/2$, although there may be a pronounced feature in the spectrum at f_{a*} (*e.g.*, Fig. 6.5a, $f_{a*} = 2.91$, Fig. 6.5b, $f_{a*} = 5.41$ Fig. 6.5f, $f_{a*} = 6.54$ Fig. 6.5g, $f_{a*} = 2.10$). This is not to say that there is no effect at $f_{a*}/2$; under these conditions the secondary frequency band may have a slightly higher amplitude and become more defined (*e.g.*, Fig. 6.5c, $f_{a*} = 3.43$).

For $\sigma = 0$ and 0.22, the presence of velocity fluctuations due to the primary vortex formation leads to a splitting of the spectral response to the forcing into frequencies $f_{*n} = f_{a*} + nf_{1*}$, where n is a small (positive or negative) integer. This is visible in all spectra for these solidities, Fig. 6.5a–f. A related observation is that for those frequencies within the secondary frequency band, the value of Φ_a is not necessarily the maximum amplitude of $\Phi(f_*)$, even over those frequencies within the secondary frequency band. There are two causes of this, the frequency splitting, and the response at the first harmonic. Due to the frequency splitting, when f_{*n} is closer to the center frequency of the sensitive band for some n, that frequency is then the most amplified and so $\Phi(f_{*n})$ is the maximum (*e.g.*, Fig. 6.5c, for $f_{a*} = 3.15$). When the forcing frequency is below those frequencies to which the shear layer responds directly, in several of the spectra it is clear that the maximal response occurs at the first harmonic $2f_{a*}$, *i.e.*, the forcing is at the subharmonic of a frequency to which

the shear layer is sensitive (*e.g.*, Fig. 6.5**d**, for $0 < f_{a*} \leq 0.88$).

For certain flow conditions and certain values of the forcing frequency, the spectra do not show spectral peaks at any frequency, including at the forcing frequency itself. In these cases, the forcing frequency lies either between the subharmonic band and the secondary frequency band, as in Fig. 6.5**c** for $f_{a*} = 2.09$ and 2.37, or is much higher than the upper limit of the secondary frequency band as in Fig. 6.5**a**, $f_{a*} = 4.07$. The frequency selectivity of the separated shear layers in the former case can be very specifically divided into secondary and subharmonic frequency bands, with a band of frequencies between them to which the shear layers do not respond. With the acoustic driver that was used, it was not possible to force the flow at frequencies below the lower limit of the subharmonic band.

6.3 Detailed measurements of a forced, separated shear layer

To investigate the relationship between the various flow elements in the wake, extensive shear layer traverses, similar to those described in Chapter 5, were made at a single Reynolds number with a permeable splitter plate of solidity $\sigma = 0.65$, with acoustic forcing near the frequency for which a maximal response was observed. It may be seen by examination of Fig. 5.8 in Chapter 5 that the most well-defined secondary frequency band occurs for the highest solidity at the intermediate value of the measured Reynolds numbers. It was decided instead to use the same high solidity, but to make the measurements at the lower Reynolds number for which the unforced shear layer exhibited less frequency selectivity to demonstrate that the less responsive shear layer at these flow conditions would strongly respond to the shear layer forcing. The wake exhibits the wake-profile instability in this case, and evidence from the single point measurements indicates that the presence of the forcing did not cause a change from the wake-profile to the body-coupled instability, and flow visualization showed that although in the presence of forcing the wake-profile instability was intermittently visible near the end of the separation bubble, large-scale circular vortices did not form at the end of the separation bubble.

The data collection technique, and the type of data collected were the same as for the shear layer traverses without forcing discussed in Chapter 5. Flow conditions are the same as those shown in the flow visualization photographs shown in Fig. 6.1**a-c** and Fig. 6.2**d** (except that the forcing frequency $f_{a*} = 1.25$ is slightly different), and the flow conditions are also comparable to one case of the unforced shear layer traverse data presented in Chapter 5. The same microphone arrangement as was discussed in Sec. 6.2 was used to monitor the acoustic power levels and frequency, and the microphone output was collected on another channel of the data collection system simultaneously with the other data.

Figure 6.6 shows the shear layer boundaries y_{01} and y_{99}, defined as in Sec. 5.1.2 but with the acoustic forcing, and plotted with the same physical scaling as in Fig. 5.2. Comparing

this figure with Fig. 5.2**g** shows that the acoustic forcing has a considerable effect on the mean geometry of the shear layers. The length of the separation bubble has decreased significantly, and this may also be seen in Fig. 5.3 where L_f taken from Fig. 6.6 is plotted with the data taken Fig. 5.2. This is also suggested by comparison of the flow visualization of the forced wake with the unforced wake in Fig. 6.1 . There is only a suggestion of an initial thin region of slow growth, whereas in the unforced case the shear layer exhibits a thin region of slow growth extending for nearly $1.5\,D$ downstream. With the forcing the shear layer is much thicker at all downstream positions and the boundaries are more irregular.

Figure 6.7 shows the vorticity thickness δ_ω and the momentum thickness θ of the acoustically forced shear layer, defined as in Sec. 5.1.2, as functions of downstream distance x/D. Comparing this figure with Figs. 5.4**g** and **i** shows that at Re = 4800 with the forcing present the growth of the shear layer thickness is much more similar to that observed without forcing at the higher Reynolds number of Re = 15200 (Figs. 5.4**i**) than to that observed without forcing at the same Reynolds number (Figs. 5.4**g**). This is reflected in the pairing length as well, taken from this figure and plotted in Fig. 5.10, which is clearly less than that for Re = 4800 without the forcing and may be less than that for $\sigma = 0.65$ and Re = 15200 without forcing, although the large experimental uncertainty makes this less certain.

Figure 6.8 shows velocity traces illustrating the development of the shear layer fluctuations with x/D in the presence of forcing. Other than being somewhat more rapid, the sequence in which the development proceeds is similar to that without the forcing (see Sec. 5.3.2 and Fig. 5.6). The initial instability appears to have a single frequency and is larger than is observed without forcing, but the growth proceeds in a similar fashion, through bursts of higher amplitude against a smaller amplitude background, with the bursts becoming more frequent or the background amplitude increasing until the high frequency instability fluctuations are continuously present. The high frequency fluctuations then decay and are replaced by lower frequency fluctuations that appear to be approximately subharmonics of the forcing frequency. Eventually the harmonic high frequency fluctuations disappear entirely, the lower frequency fluctuations start to become irregular, and intermittent, high amplitude, incoherent turbulent bursts begin to appear (Fig. 6.3, $x/D = 2.4$). Following this, the maximum amplitude of the fluctuations and of the bursts decrease steadily. Note that for this solidity and Reynolds number, even with the forcing the primary vortex formation is not detectable in the near wake.

Power spectra of the velocity fluctuations measured at different x/D are shown in Fig. 6.10 (the details of the computation of the power spectra and the corresponding shear layer are given at the end of this chapter in Table 6.1). In Fig. 6.5**g**, the maximum amplitude of Φ_a occurs at a forcing frequency of $f_{a*} = 1.15$, and this can be seen to be somewhat lower than the maximum amplitude of Φ in the secondary frequency band without forcing,

which lies closer to $f_{a*} = 1.6$. This is also visible in Fig.6.10, where the peak at the forcing frequency initially lies to one side of the spectral feature representing the secondary frequency band ($x/D = .4$). However, by the next measurement location ($x/D = .6$) the natural secondary frequency band has been overwhelmed by the growth of the fluctuations at the forcing frequency and only the peak at f_{a*} remains within the range of the secondary frequency band. At this point a harmonic of f_{a*} is visible, and a feature is beginning to appear at the subharmonic. By $x/D = 1.0$ the subharmonic is well-established, and note also that this is the measurement location at which Φ_a reaches its maximum value. For $x/D > 1.0$, the peak at the forcing frequency decays, and by $x/D = 2.0$ is of lower amplitude than the subharmonic peaks. Both peaks continue to decay, with the peak at $f_{a*}/2$ still visible at $x/D = 4.0$ although the peak at f_{a*} has disappeared. The flow at the farthest downstream measurement location appears to be fully turbulent, or at least completely disorganized, both in the spectrum and in the velocity traces shown in Fig.6.3.

When the profile data are plotted in the similarity coordinates $u/\Delta U$ vs. $(y - y_c)/x$, as in Fig.6.9, the data show a limiting envelope, and appear to have developed a nearly self-similar profile by $x/D = 2.4$. It is more difficult to determine whether or not the profile is initially self-similar, as only the three profiles for $x/D \leq 0.8$ might qualify, and show considerable scatter. However, the transition to the final profile appears to be more rapid than in the unforced case shown in Fig.5.5g.

6.4 Discussion of the forced shear layer experiments

The experiments using the acoustic forcing confirm that the separated shear layers amplify a large range of frequencies. For high Reynolds numbers, this range of frequencies may be separated into two bands, which roughly correspond to as the secondary frequency band and the subharmonic frequency band appearing in the development of the unforced shear layers. The distinction between the secondary and subharmonic bands does not seem to be important at the lowest Reynolds number Re = 4900 for which the experiments were performed, regardless of the splitter plate solidity, although the subharmonic frequency band does appear at $\sigma = 0.65$ when the flow is forced. At this Reynolds number, for $\sigma = 0$ and 0.22 where the primary vortex formation influences the near wake, the lower limit of the secondary frequency band is only about five times the primary wake frequency, and evidence that in this case there are interactions between the primary vortex formation and the forced shear layer instability can be seen in the peaks that appear in the plots of $-C_{pb}$ and St for $\sigma = 0$ at $f_{a*} \approx .8$ and for $\sigma = 0.22$ at $f_{a*} \approx 1.2$, without corresponding peaks appearing in Φ_a. At Reynolds numbers Re > 9000, where the response of the subharmonic band is clearly visible in the power spectra, there are two forcing frequencies corresponding to the two bands that induce maximal response in the shear layer and the near wake parameters.

One frequency, defined as the frequency that produces the maximum amplitude of Φ_a, is identified with the unforced secondary frequency band, although it is not necessarily the center frequency. The other frequency, $f_3 > f_2$, is that which for $\sigma = 0$ and 0.22 brings about the peak response in the subharmonic frequency band. The frequency f_3 does not itself lie within the subharmonic band, but instead is the harmonic of the frequency that shows the maximum amplitude of Φ within the subharmonic band. This relationship is not surprising since the subharmonic response is due to pairing interactions of the initially developing shear layer vortices, and so forcing at f_3 promotes the development of shear layer vortices at the scale that is most conducive to pairing interactions in the near wake. For Re $\geq$ 9000 it is seen that forcing at f_3 produces the greatest response from the near wake parameters, thus the development of the subharmonic in the shear layer has a greater effect on the near wake than the initial development of the instability at the secondary frequency. This in turn suggests that the shear layers have a greater effect on the near wake when the pairing interaction is able to proceed further, either through forcing or through the increased length of the separation bubble brought about by the introduction of splitter plates. This has implications for the flow past a circular cylinder without a splitter plate, as it was shown in Chapter 5 that the pairing process does not progress very far in this Reynolds number range before the shear layers are entrained by the developing primary wake vortices.

Beat frequencies $f_{*n} = f_{a*} + nf_{1*}$ between the primary wake frequency and the forcing frequency are seen in the shear layer spectral response for $\sigma = 0$ and $\sigma = 0.22$ (*i.e.*, when fluctuations at the primary wake frequency are present in the near wake). It can be seen that the resulting discrete frequencies for $n \neq 0$ can have a significant effect on the shear layer development, depending on the relationship between the beat frequencies, the forcing frequency, and the secondary frequency bands, and that when a beat frequency f_{*n} more closely corresponds to the most amplified mode of the shear layer, the highest amplitude of $\Phi(f_*)$ can lie at the beat frequency (*e.g.*, Fig. 6.5**b**, $f_{a*} = 2.47$, where the highest amplitude of Φ_a occurs at $f_{*n} = 2.22$ for $n = 1$).

Similar beat frequencies may also be seen in the results of Kourta *et al.* (1987) at a lower Reynolds number of Re = 2660 for a very similar experimental setup, in power spectra computed from hot-wire velocity measurements (shown here as Fig. 6.11**b**). Their spectra appear to be steeply high-pass filtered with a cutoff frequency that is close to the primary wake frequency f_1, and this may explain why the amplitude of the corresponding peak is reduced relative to the value of the highest peak seen in the secondary frequency band. It is not possible to make quantitative comparisons in the amplitudes of the peaks in the power spectral density, since no details of the computation of the spectra are given and the data are presented in arbitrary units. However, this does not effect the relative location of the peaks and a qualitative comparison may be made. Figure 6.11**a** shows a

similar spectrum from the present data, but at the higher Reynolds number used in the forcing experiments. The beat frequencies are labeled on the plot, and the corresponding unforced spectrum is also shown. The figure corresponds to flow without a permeable splitter plate forced at $f_{a*} \approx 2.08$, which is within the secondary frequency band but is above the point of peak response in Φ_a, which occurs at $f_{a*} \approx 1.64$. The similarities between the distribution of beat frequencies in Fig. 6.11**a** and **b**, coupled with the results of Chapter 5 and the flow visualization of the shear layers shown in Sec. 6.1.2, suggest that the discrete secondary frequency peaks detected by other researchers may have their origin in undetected forcing in the flow. Note that acoustic forcing will not show up in hot-wire velocity measurements made in the free stream, since at the relatively low frequencies (and therefore long wavelengths) that are of significance in the present experiments, acoustic pressure fluctuations appear as small fluctuations in the ambient pressure level, but do not cause measurable variation in the free-stream velocity.

If forcing is responsible for the appearance of the discrete frequencies in other experimental investigations, it remains to explain the correlation to Eqn. 6.1 with $n = 1/2$ found by Bloor and Kourta *et al.*. One possible explanation is suggested by the large number of peaks in Φ that appear due to the beat frequencies $f_{a*} + nf_{1*}$. Although the flow corresponding to Fig. 6.11**a** is forced at a single frequency, three peaks at beat frequencies appear, one of which is of comparable amplitude to the peak at the forcing frequency. It is observed earlier in this section that it is possible for a peak at a beat frequency to be of greater amplitude than the peak at the forcing frequency. If there are additional perturbation frequencies, it is likely that even more beat frequencies will appear, and thus it is more likely that there will be a frequency close to that at which the shear layer shows the greatest response in Φ. This leads to the possibility of ambiguity in the selection of the secondary frequency since the peak with the highest amplitude is most likely to be chosen for f_2, unless the forcing frequency is measured as well.

The present results also suggest a slightly different interpretation of the scaling suggested in Eqn. 6.1. The perturbation wave number that is most amplified by the shear layer scales with the initial momentum thickness: Using the boundary layer scaling for the initial momentum thickness, and the additional assumption that the relevant shear layer velocity scale in the separated shear layers is proportional to U_∞(as is observed), it follows that the most amplified frequency in the steady flow would be related to the Reynolds number by

$$f_2 \sim \frac{U_\infty}{D} \mathrm{Re}^{1/2} .$$

Noting that the variation of the Strouhal number in this Reynolds number range is small (although non-zero), to a good approximation the primary wake frequency is proportional to the free-stream velocity, and for fixed cylinder diameter and fluid viscosity,

$$f_1 \sim \frac{U_\infty}{D} ,$$

and Eqn. 6.1 follows. It is observed that when the forcing perturbation is near the center of the secondary frequency band, which is defined as the band of frequencies to which the shear layer is receptive (corresponding to a stability diagram similar to that shown in Ho and Huerre 1984, figure 2(a), but not precisely the same since here the flow may be driven by the primary wake frequency), the dominant frequency will be the beat frequency that is closest to the most amplified frequency. Since the separated shear layer is receptive to a band of frequencies, if the forcing frequency is proportional to the free-stream velocity (as is the case for perturbations introduced by the fan blades in a typical fan-driven wind tunnel) the induced perturbation frequency may remain within the secondary frequency band and therefore a frequency close to the most amplified frequency will always be available for amplification by the shear layer. Note that if the analogy with the plain shear layer is correct and linear stability theory describes the initial growth of the separated shear layers, the amplitude of the perturbation at the forcing frequency is not important. This leads to the hypothesis that in the presence of low-amplitude forcing at frequencies related to the free-stream velocity, the highest amplitude spectral peak lying within the secondary frequency band will always follow Eqn. 6.1.

In the velocities relevant to the present experiments, it is observed that the wind tunnel fan rotation frequencies ranged over $6 < f_{\text{fan}} < 24$ Hz, and that there are small but detectable peaks at harmonics of f_{fan} in the free-stream turbulence; the low values of f_{fan} have the potential to make a large number of closely spaced harmonic frequencies available. Evidently the amplitude of the perturbations was usually too low to excite the shear layer frequencies, although in the discussion in Sec. 5.4.2 of Fig. 5.9, measurements are presented for which it is possible that harmonics of the fan frequencies were amplified by the shear layer and detected in the power spectra. This suggests that the forcing scenario is plausible in typical wind tunnels.

The results of Bloor (1964) and of Wei and Smith (1986) indicate that the cylinder diameter has an effect on the scaling of the shear layer instability. This would be the case when perturbations in the free stream that depend on the value of the free-stream velocity force the shear layer instability, since the perturbation frequencies, and therefore the perturbation wavelengths, will be a characteristic of the free-stream velocity and therefore independent of the cylinder diameter. Thus changing the cylinder diameter changes the relationship between the frequency content of the free-stream perturbations and the frequency bands to which the shear layer is receptive and this will change the observed relationship between f_1 and f_2.

It is reasonable to expect that at very high forcing frequencies the forcing should have no effect, in particular when the frequencies lie outside the shear layer receptive frequency band. However, this was not the case for $\sigma = 0$ at $\text{Re} < 10000$, corresponding to Fig. 6.4**a** and **b**, where the values of u'/U_∞ and $-\text{C}_{\text{pb}}$ are depressed at high frequencies from the val-

ues without forcing, while the value of St increases at high values of the forcing frequency. It is possible that the decreased values at high f_{a*} are caused by the high frequency perturbations overwhelming the natural perturbations at the most amplified frequency and thereby damping the shear layer response. The damped shear layer response then leads to the observed variations in the near wake parameters, generally a decrease in the base pressure, a decrease in the velocity fluctuations, and an increase in the primary wake frequency. This observation is in accord with the observed trends in the base suction coefficient and the Strouhal number in the Reynolds number range of the present experiments, where at low Reynolds number the drag is low and the Strouhal number is high, but as the Reynolds number is increased the drag increases and the Strouhal number decreases.

It is strongly indicated by the results of the forcing experiments that in the present experimental setup the separated shear layers are not forced at discrete frequencies by perturbations in the free-stream flow. This in turn implies that the natural, unforced development of the shear layers results in broad, flat, low-amplitude secondary frequency bands and does not lead to the development of the high amplitude discrete peaks in power spectra computed from the velocity fluctuations in the shear layers that have been reported by other researchers. It has been clearly shown that forcing the shear layers produces a large effect on the shear layer development and on the measured values of the near wake parameters. It is therefore possible that an additional source of the large scatter in the measurements of the flow around a circular cylinder is unrecognized, accidental forcing of the separated shear layers.

Fig.	U_∞	x/D	y/D	η	y_c/D	δ_*/D	f_C	f_N	K	$\overline{U}$	R
6.10	3.10	0.40	0.68	2.37	0.63	0.0241	300	601	64	2.20	0.824
	3.11	0.60	0.72	1.67	0.66	0.0352	300	601	64	2.26	0.765
	3.10	1.01	0.82	1.52	0.71	0.0777	300	601	64	2.35	0.692
	3.10	1.61	1.01	2.02	0.73	0.1360	300	601	64	2.42	0.652
	3.10	2.01	1.11	1.65	0.77	0.2060	300	601	64	2.44	0.631
	3.09	2.81	1.26	1.86	0.78	0.2540	300	601	64	2.45	0.592
	3.08	4.02	1.26	1.48	0.74	0.3480	300	601	64	2.22	0.635

TAB. 6.1 Information pertaining to the spectra shown in Fig. 6.10 . Frequencies f_C and f_N are in Hertz, velocities U_∞ and $\overline{U}$ are in meters per second, and K is the number of 2048-point power spectra averaged to obtain the power spectra shown in Fig. 5.8.

CHAPTER 7

Discussion and Summary

The work described here shows that the introduction of a permeable splitter plate into the wake center plane does make possible a continuous variation of the communication between the two sides of the wake, resulting in a continuous variation of the near wake interactions. The presence of a sufficiently permeable splitter plate does not change the basic structure of the near wake, with the primary wake vortices forming at the end of a separation bubble, which is itself located immediately behind the cylinder, but it is seen in the flow visualization that the wake is separated into two halves, and that across the permeable splitter plate the mass transfer and mixing of oppositely signed vorticity are reduced. When the permeability is sufficiently reduced, either by increasing the solidity or decreasing the Reynolds number, the character of the large-scale wake instability is modified from a body-coupled instability to a wake-profile instability, with the formation of large-scale vortices delayed until some distance downstream of the end of the separation bubble.

The ability of permeable splitter plates to modify the communication across the wake center plane has been exploited in the experiments reported in this thesis to explore the interactions between the various elements of the flow in the near wake by modifying the intensity of the interactions. For example, it is observed that the introduction of a highly permeable splitter plate does reduce the intensity in the near wake of the velocity fluctuations at the primary wake frequency, and therefore reduces the effects of the associated forcing on the development of the separated shear layers. The technique has been used to elucidate the relationship between the base pressure and the primary wake frequency, and between the global state of the near wake and the detailed state of the separated shear layers.

The following discussion of the results refers only to the present experiments on flow past a circular cylinder in the Reynolds number range $2.5 \cdot 10^3 \lesssim \mathrm{Re} \lesssim 1.8 \cdot 10^4$. The phrase "low Reynolds number" refers to values of $\mathrm{Re} \lesssim 10^4$ and "high Reynolds number" refers to $\mathrm{Re} \gtrsim 10^4$.

7.1 The near wake structure

7.1.1 The effect on the global measurements

Although the introduction of the permeable splitter plates preserves the large-scale structure of the near wake, they significantly affect the value of the global parameters $-C_{pb}$ and St, and the permeable splitter plates were used to explore the relationship between the base pressure and the primary wake frequency.

When the splitter plate permeability is high enough (including the highest possible permeability, *i.e.*, no splitter plate), the formation of the large-scale vortices occurs at the end of the separation bubble and interacts strongly with the flow in the near wake, and this is referred to as body-coupled instability. When the permeability is very low, as for low Reynolds numbers and high values of the splitter plate solidity, large-scale vortices do not form at the end of the separation bubble, but appear farther downstream as a consequence of the development of the instability of the wake profile, and this is referred to as wake-profile instability. Through modifications of the splitter plate permeability from changes in both the solidity and the Reynolds number, the effect of the change between the two forms of wake stability on the base pressure and the vortex shedding was investigated. It is found that when the wake instability is not body coupled, the base suction coefficient is constant and does not depend on the Reynolds number or the splitter plate solidity. When the permeability is high enough that the wake instability is body coupled (except for solidity $\sigma = 0$), the base suction increases approximately linearly with Reynolds number, and the rate at which the suction increases is nearly the same for all solidities. When there is no splitter plate ($\sigma = 0$), the initial increase in $-C_{pb}$ with Reynolds number is linear but at a somewhat higher rate than is observed for other solidities, and decreases at $Re \approx 10^4$ to a value that is close to the common value observed for $\sigma \neq 0$.

The Strouhal number, which is the non-dimensional value of the frequency of the primary vortex formation, shows a more complicated dependence on the Reynolds number. For $\sigma = 0$, the Strouhal number decreases with increasing Reynolds number, for $\sigma = 0.22$, the Strouhal number is nearly constant at all Reynolds numbers, and for $\sigma < 0.22$ the Strouhal number increases with increasing Reynolds number. However, for $\sigma > 0.65$, the Strouhal numbers appear to approach a common, constant value at the high end of the Reynolds number range. It is possible that if higher Reynolds numbers could have been attained in the current experiment, this common value might have been approached for $\sigma = 0.65$ as well.

7.1.2 The state of the shear layers

The detailed measurements of the shear layers presented in Chapter 5 also reveal infor-

mation about changes in other global parameters of the near wake, *e.g.*, the length of the separation bubble. The length of separation bubble L_f determined from the shear layer measurements for different solidities shows that the general trends in L_f with Reynolds number are similar to those observed for the base suction. The results suggest that the length of the separation bubble is approximately constant when the wake instability is not body-coupled, although this cannot be said with a great degree of certainty since for these flow conditions the experimental uncertainty was large. However, it is clear that L_f decreases with Reynolds number when the wake instability is body coupled.

It is a hypothesis of the standard model of cylinder flow that the detailed structure of the shear layers separating from the circular cylinder has a large effect on the global structure of the near wake. For a cylinder without a splitter plate, it is possible to study the effect of the shear layer structure on the near wake by modifying the shear layers through the use of boundary layer trips, increased free-stream turbulence or similar methods. However, these modify the natural development of the shear layers and can introduce unwanted perturbations into the other components of the near wake. The introduction of permeable splitter plates allows the natural development of the separated shear layers to be studied in a modified near wake environment by reducing the influence of other components of the near wake, for example by reducing, without eliminating, the influence of the primary vortex formation on the development of the shear layers. It is also possible to use the technique to approach the development of the shear layer instability behind the cylinder without a splitter plate as a limiting case of the development of the plain mixing layer subjected to the near wake environment, with changes in the solidity determining the similarity of the environment in which the separated shear layer develops to that usually arranged for a plane mixing layer.

Measurements of the shear layer velocity fluctuations as a function of solidity, Reynolds number, and downstream position show that the introduction of the permeable splitter plates, by decreasing the amplitude of the velocity fluctuations at the primary wake frequency and by increasing the length of the separation bubble, does lead to downstream development of the separated shear layers that is more similar to that of the plane mixing layer. In particular, the development of subharmonic frequencies, such as those observed in plane mixing layers and attributed to the mechanism of vortex pairing, is enhanced by the presence of the permeable splitter plate, particularly for high values of the solidity. The shear layer instability is found to amplify a broadly distributed band of frequencies, referred to as the secondary frequency band, and similarly, a subharmonic frequency band appears broadly distributed about a center frequency that is approximately half the center frequency of the secondary frequency band. The development of the subharmonic frequency band, in terms of the maximum amplitude in the power spectral density within the subharmonic frequency band, is observed to be greater at high Reynolds numbers. Time traces

of the fluctuating velocity in the shear layer show that the shear layer instability is still organized on time scales that are long compared with the primary wake frequency, and power spectra computed from the velocity fluctuations in the shear layer show that the shear layer displays frequency selectivity at all Reynolds numbers and at all downstream positions $x < L_f$. The secondary frequency band and the subharmonic bands become more apparent at high Reynolds numbers, indicating that increasing the Reynolds numbers results in greater organization in terms of frequency specificity within the separated shear layers. When the solidity is high the separated shear layers are able to complete the pairing process and lose the frequency selectivity and coherence in the fluctuations and perhaps do undergo transition to turbulence. It is also observed that in the absence of shear layer forcing, the shear layer instability does not develop the discrete, high-amplitude, well-defined spectral peaks observed by other researchers.

7.2 The effect of forcing the separated shear layers

Since the separated shear layers are able to amplify bands of frequencies, acoustic forcing of the shear layers was used to determine the sensitivity of the near wake structure to the artificially driven shear layer instability. As suggested, the shear layers are found to be very responsive to the acoustic forcing across a large band of frequencies, and the forced shear layer structure is clearly different from that of the unforced shear layers. This is seen in both time traces of the velocities measured in the shear layer, and in power spectra computed from the shear layer velocity fluctuations. This indicates that the shear layer data presented in this thesis that were collected without the acoustic forcing are not significantly perturbed by undetected harmonic perturbations in the free stream.

It is found that forcing the shear layers has a large effect on the near wake structure as indicated by measurements of u'/U_∞, $-C_{pb}$, and St. Two observations seem to be of particular consequence for the flow past a circular cylinder; the greatest change in the value of $-C_{pb}$ is observed when the shear layer is forced at a frequency that brings the greatest response from the subharmonic frequency band, implying that the base suction is more affected by the development of the pairing interactions than by the initial growth of the instability; and a large effect on the value of St is observed when the shear layer is forced at or very close to a harmonic of the primary wake frequency, *i.e.*, when $f_a = nf_1$ where n is a small integer, even when this particular forcing frequency does not produce a large response in the amplitude of the spectrum at the forcing frequency. This suggests that the primary wake frequency is generally decoupled from the shear layer instability, and that the significant changes in St that occur at other values of the forcing frequency may have been caused more indirectly, such as by the changes to the base pressure induced by the forcing. Hot-wire traverses of the shear layer for Re = 4900 and $\sigma = 0.65$, for which the

wake instability is not body coupled in the unforced case, taken at downstream positions spanning the separation bubble also give information about the effect of the forcing on the near wake structure. It is found that in this case the forcing reduces the length of the separation bubble, and since a primary wake frequency was not detected at any value of x/D, it is concluded that the forcing did not change the large-scale wake instability from a wake-profile to a body-coupled instability. Time traces of the velocity fluctuations from data taken at the edge of the shear layers at different downstream positions, and the corresponding power spectra, show that despite the high amplitude, narrow bandwidth frequency response at the forcing frequency that is apparent in the initial development of the shear layer, the development of the shear layer instability is very similar to that without the forcing. Specifically, the fundamental (in this case at the forcing frequency) grows to a maximum amplitude, after which the subharmonic begins to grow and eventually dominates the spectrum while the peak at the forcing frequency decays. The subharmonic then begins to decay, and the velocity fluctuations become disorganized, with the fundamental and the subharmonic eventually disappearing altogether near the end of the separation bubble. The similarities between the development of the acoustically forced shear layer and that of the unforced shear layer, particularly the growth of the subharmonic and the eventual disappearance of the spectral peaks corresponding to the initially amplified frequency and the subharmonic, indicate that excitation of the shear layer instability modes by the the perturbations induced by the acoustic forcing and their amplification by the shear layer instability is what gives rise to the observed frequency response.

7.3 Implications for the standard model

The differing results found for the base suction coefficient and the primary wake frequency suggest that the primary vortex formation process is not adequately characterized by the vortex formation frequency alone. It is clear that the value of the base suction is related to the primary vortex formation process from the observation that when the permeability is low enough, so that the wake instability is not body coupled and the vortex formation does not interact with the end of the separation bubble, the base pressure is a constant independent of the Reynolds number and the plate solidity. Furthermore, when the wake exhibits the body-coupled instability, so that the primary vortex formation strongly intereacts with the separation bubble, the base suction increases uniformly with Reynolds number and the rate of increase is very similar for different values of the solidity. However, depending on the value of the solidity, differing trends are exhibited in the Strouhal number dependence on Reynolds number, and furthermore for values of the solidity $\sigma > 0.65$ the Strouhal number for different solidities converges to the same limiting value at higher values of the Reynolds number. Since the same value of the Strouhal number is observed for most solidities at high Reynolds number, while the values of the base suction vary with

solidity at all Reynolds numbers when the wake instability is body coupled, it is clear that the mechanism that determines the base pressure is not identical to the mechanism that determines the primary wake frequency.

The experiments on the forced shear layers and associated discussion indicate that accidental forcing of the shear layer is probably a large factor in the observed large scatter in cylinder flow measurements. All conclusions about circular cylinder flow have to be modified in the presence of shear layer forcing, since the structure of the near wake (C_{pb}, St, u'/U_∞, L_f, L_p, *etc.*) is modified in a fashion that depends upon the forcing frequency. The shear layer forcing frequency is an additional parameter on the flow with effects that are comparable to the effect of changing the Reynolds number. The effects of the amplitude of the acoustic forcing and the possibilities of different forcing mechanisms remain to be explored. This leads to the possibility that data might be more reliably compared if the measurements were performed in a "standard turbulent field," which might be produced by a standardized arrangement of turbulence generating screens. If many flow facilities do in fact introduce perturbations having discrete frequencies or a narrow frequency distribution, it is plausible that by adding perturbations that are distributed over a broad frequency band and have amplitudes similar to those of the harmonic perturbations, the shear layer would be free to amplify the full band of frequencies to which it is naturally sensitive. Although this is a different flow than the ideal quiet, uniform free stream, such experiments may show less scatter than the 'quiet' flows that have been reported in the past.

Several observations from the present experiments are relevant to the hypothesis that the upstream movement of the location of shear layer transition is responsible for the large changes in the near wake parameters in this Reynolds number range. The most important observation is that when the permeability is high enough for the wake instability to be body coupled, the evidence indicates that the shear layers do not undergo transition to turbulence before the end of the separation bubble. Time traces of the fluctuating velocity in the shear layer show that the shear layer instability is still organized over time scales that are long compared with the primary wake frequency, and power spectra computed from the velocity fluctuations in the shear layer show that the shear layer does display frequency selectivity at all Reynolds numbers and at all downstream positions $x < L_f$. The secondary frequency band and the subharmonic bands become more apparent at high Reynolds numbers, indicating that increasing the Reynolds number apparently results in greater organization in terms of frequency specificity within the separated shear layers. At low Reynolds numbers, smoke wire flow visualization of the shear layers shows that smoke lines that are involved in the shear layer instability are sharply defined and are not significantly distorted other than by the developing shear layer vortices, both in the unforced and forced shear layers. A large change is observed to appear in the unperturbed values of the near wake parameters in response to the artificial coupling of the shear layer

instability and the primary wake frequency by excitation of the shear layers at a harmonic of the primary wake frequency, without a corresponding peak in the response of the shear layers at the excitation frequency as defined by Φ_a. This gives some indication that in the absence of artificial excitation, in this Reynolds number range the naturally developing shear layer instability is not strongly coupled to the primary vortex formation frequency. Thus it appears that the hypothesis that upstream movement of the point at which the shear layers undergo transition to turbulence is responsible for the observed large changes in the near wake with increasing Reynolds number is not supported by the present data.

There is some indication that there is a relationship between the observed Reynolds number dependence of the base pressure coefficient and the development of the subharmonic in the shear layer velocity fluctuations. In the experiments with acoustically forced shear layers, it is observed that the maximum change in the base pressure occurs when the forcing is at the frequency f_3 that brings about the maximum subharmonic response from the shear layer. It is also observed that the development of the subharmonic is not as apparent at low Reynolds numbers as it is at high Reynolds number. In the unforced shear layer, the amplitude of the subharmonic frequency band develops to approximately the same amplitude as the secondary frequency band at $\mathrm{Re} \approx 10^4$, and for higher Reynolds number the amplitude of the subharmonic frequency band is greater than that of the secondary frequency band. When $\sigma \neq 0$, at Reynolds number $\mathrm{Re} \gtrsim 9500$ the subharmonic band is pronounced and is more apparent than that for $\sigma = 0$. Furthermore, for $\sigma = 0$ a change in the rate at which the base suction increases with Reynolds number is seen at a Reynolds number of $\mathrm{Re} \approx 10^4$, and the final slope of the curve of $-C_{pb}(\mathrm{Re})$ is about the same as that for $\sigma \neq 0$. Thus, for $\sigma = 0$ the subharmonic frequency band becomes relatively important in the shear layer instability at about the same Reynolds number at which the slope in the base suction decreases, and the new, decreased value of the slope is about the same as that observed at all Reynolds number (for which the wake instability is body coupled) for $\sigma \neq 0$. $\mathrm{Re} = 10^4$ does not seem to be particularly significant to the Strouhal number. These observations suggest that at this value of the Reynolds number, the shear layer instability develops to a point where it begins to make a significant contribution to the base pressure.

This further suggests that there is a shear layer length scale λ that is important in the development of the instability and depends on Reynolds number in such a way that $(L_f - L_p)/\lambda$ increases with Reynolds numbers (where L_f and L_p are the length of the separation bubble and the pairing length, respectively, defined in Chapter 5). Thus the development of the shear layer instability is able to progress to a later stage at higher Reynolds numbers. The process is limited by the presence of the cylinder body, since L_p and L_f are observed to be continually decreasing with Reynolds number, and this is compatible with the observation by other researchers that in the Reynolds number range $2.0 \cdot 10^4 \lesssim \mathrm{Re} \lesssim 1.5 \cdot 10^5$ the value of the base pressure is approximately constant. However,

it does not offer any explanation of why the primary vortex frequency is approximately constant beginning at $\mathrm{Re} \approx 1.5 \cdot 10^4$ but does add weight to the suggestion that the primary wake frequency alone is insufficient to characterize the vortex formation process. Recall that the value of L_p defined here roughly corresponds to what other researchers have reported as the downstream distance to the point of shear layer transition, and that the standard model explains the large changes in the near wake across this Reynolds number range as being caused by the upstream movement of this point. The preceding discussion suggests that it is not the decrease in the value of L_p alone that is important to the near wake flow in this Reynolds number range, but rather the relative change in L_p with respect to the length of the separation bubble L_f that is important.

The technique of modifying the communication across the center plane of the wake behind a circular cylinder through the use of permeable splitter plates provides the means to modify the interactions between the complicated flow phenomena in the near wake in a continuous and controllable fashion. The efficacy of the technique for unraveling the details of the near wake flow has been demonstrated, and has been successfully used to obtain new information about the flow in this Reynolds number range, suggesting some new interpretations of the observed flow phenomena and some different explanations for the Reynolds number dependence of the near wake. It would be useful and informative to apply the technique to the investigation of circular cylinder flow at Reynolds numbers outside the range that was accessible in the present investigation. The application of the technique is not limited to circular cylinders, and can be applied to investigations of the flow past bluff bodies of other cross-sectional shapes as well.

7.4 Summary of results

The flow past a circular cylinder with a permeable wake splitter plate has been generally characterized through flow visualization and global measurements in the near wake. Furthermore, the technique of introducing permeable splitter plates as a means of modifying the near wake interactions has provided new information about the structure of the near wake in the Reynolds number range $2.5 \cdot 10^3 \lesssim \mathrm{Re} \lesssim 1.8 \cdot 10^4$.

7.4.1 Results from the global measurements

The experiments have shown that gradual changes in the splitter plate permeability bring about gradual changes in the near wake. When the permeability is high, the basic structure of the near wake is preserved, and the primary wake instability leading to the formation of the large-scale vorticies is very similar to that when no splitter plate is present. When the instability is body coupled, the large-scale vortex formation occurs at the end

of, and strongly interacts with, the separation bubble and has a large influence on the near wake. When the permeability is low, the near wake becomes largely independent of the large-scale vortex formation, and the large-scale vortices develop downstream of the end of the separation bubble from an instability of the wake profile. Under these flow conditions and in this Reynolds numbers range, no fluctuations at the primary wake frequency are discernible in the near wake and the base suction is approximately constant with respect to both Reynolds number and plate solidity. This result and the results from the detailed measurements of the shear layers indicate that any contribution from the development of the shear layer instability to the large changes in the base pressure observed in this Reynolds number range must proceed indirectly, by modifying the primary vortex formation. The different Reynolds number dependencies of the base suction coefficient, the Strouhal number, and the length of the separation bubble indicate that although the Reynolds number dependency of the changes in the base suction and the formation length are directly related to the occurrence of large-scale vortex formation at the end of the separation bubble, changes in the large-scale vortex formation do not appear to depend strongly upon the base suction. The large-scale vortex formation is not well-characterized by the Strouhal number alone, as shown by the different trends in St(Re) observed for different permeabilities.

7.4.2 Results from the shear layer measurements

Contrary to previous results, the naturally developing instability of the separated shear layer did not result in discrete spectral peaks, but rather a band of amplified frequencies was observed. When the permeability is high enough that the wake instability is body-coupled, the shear layers do not completely transition, to fully developed turbulence, before they are involved in the large-scale vortex formation at the end of the separation bubble. At high permeability and low Reynolds numbers, the development of the shear layer instability does not proceed far enough for subharmonics of the initially amplified frequencies to be detected, but at higher Reynolds number the subharmonic bands become clearly defined. For low permeability splitter plates, the wake instability is not body-coupled, the large-scale vortex formation does not significantly influence the near wake, the length L_f of the separation bubble is considerably increased, and the shear layer develops well-defined subharmonic bands at all Reynolds numbers. In this case, the shear layer fluctuations do eventually become incoherent. The results suggest that it is not the classical "transition length" alone (referred to here as the pairing length L_p) which is important to the development of the shear layers, but rather the difference between the length of the separation bubble and the pairing length in terms of the relevant shear layer length scale.

Acoustic excitation of harmonic perturbations at frequencies within the secondary frequency band shows that the shear layers are receptive to and strongly amplify harmonic

perturbations lying within the secondary frequency band. Acoustic excitation of the shear layer within the receptive band has a large effect on the structure of the near wake, and there is little or no change in the near wake when the excitation lies outside the receptive band. The shear layer response to the excitation is complex, exhibiting numerous beat frequencies between the excitation frequency and the primary wake frequency, a complex harmonic and subharmonic structure, and a complex interaction between the shear layer excitation frequencies and the near wake structure. Comparison of the development of the natural shear layers, the acoustically excited shear layers and other reported results suggest that a possible, additional cause of the observed scatter in cylinder wake measurements arises from inadvertent, undetected shear layer excitation.

APPENDIX A

Flow documentation

A.1 Introduction

As is discussed in Chapter 1, it is clear that many different aspects of the experimental setup and conditions can affect measurements made on a circular cylinder. Although many causes of the observed scatter in the measurements have been identified and investigated, the mechanisms are still poorly understood and it is not clear under what conditions the nominally two-dimensional experimental flow most closely approaches the ideal flow. Thus it is not possible to select a best possible experimental setup, and the best that can be done is to carefully document as many aspects of the flow as possible. This appendix presents such flow documentation. Since the goal of the research is to examine the effects of the permeable splitter plates, it is of primary concern to characterize the flow in the present experimental setup without a splitter plate installed, since this is the basic flow to be perturbed by the introduction of the splitter plates.

A.2 Velocity definition and calibration

It is probable that some of the scatter in the results for flow past a circular cylinder arises from the use of definitions of the free-stream velocity which are not identical. There are many different ways in which the free-stream velocity is measured in wind tunnels, two common ways being calibration of the pressure difference between the flow before and after the contraction section against the dynamic pressure measured in the empty test section (Rae and Pope 1984), and by directly measuring the velocity in the test section with the experimental models installed, using a pressure probe (such as a Pitot-Static tube) located far from the model. Due to the effect of the experimental models on the flow in the tunnel, the two different methods usually give results which differ by a few percent. It was decided to use the latter method for the present experiments, as it does not depend on the model geometry or the blockage as much as directly measuring the flow in the test section with the model installed.

A.3 Flow quality in the wind tunnel

A.3.1 Free-stream turbulence level and power spectral distribution

Figure A.1 shows power spectra from velocity traces measured in the empty wind tunnel test section with the hot wire in the center of the test section at the downstream location at which the cylinder models were mounted. Different parts of the figure correspond to different free-stream velocities. Various discrete peaks show up in the spectra, particularly at frequencies $f \geq 400$ Hz, and these frequencies are within the range of the frequencies corresponding to the most-amplified modes of the shear layer instability. It can be seen that the frequencies at which these discrete peaks are located do not change when the tunnel fan speed and free-stream velocity are changed. This behavior is characteristic of electrical noise, and since no evidence of forcing in this frequency range was found in the flow, it is concluded that the disturbances are not fluid mechanical in nature.

Part	f_{Fan} (Hz)	U_∞ (m/s)	u'/U_∞
a	6.5	3.0	0.0011
b	10.6	5.0	0.0014
c	15.4	7.3	0.0010
d	19.1	9.1	0.0016
e	23.0	10.9	0.0015

TAB. A.1 Flow conditions corresponding to the spectra shown in Fig. A.1 .

For the discrete peaks found at lower frequencies, it is possible to identify several of the corresponding frequencies as harmonics of the wind tunnel fan rotation rate at either $2f_{\mathrm{Fan}}$ or $4f_{\mathrm{Fan}}$, and higher harmonics of the fan frequency do not appear in the free-stream turbulence (see Table A.1). The range of frequencies at which the the fan frequency harmonics appear does overlap both the primary wake frequencies and the secondary shear layer frequencies that are observed in the present experiments, but there is only one flow condition for which frequencies corresponding to harmonics of the fan frequency appeared to actively force the flow and this is discussed in detail in Sec. 5.4.2. It was therefore concluded that flow perturbations due to the wind tunnel fan did not have a significant effect on the experimental results, other than the one case identified.

A.3.2 Flow uniformity

To determine the flow uniformity and the boundary layer thickness in the wind tunnel test section, the hot wire was traversed across the center of the wind tunnel in the z-direction (*i.e.*, parallel to the cylinder axis), at the streamwise cylinder location but without the cylinder installed. At all values of U_∞, the flow was uniform to within $\pm 0.01 U_\infty$ across the

test section except for the region within 3.3 cm of the front and rear walls, where the effect of the wall boundary layers was significant. The velocity fluctuations in the boundary layers, as indicated by the RMS values of u'/U_∞, were found to be less than 2% for $U_\infty = 4.1$ m/s and approximately 8% for $U_\infty = 7.1$ and 9.1 m/s.

In addition, a circular cylinder of the same nominal diameter as the cylinder used in the experiments with the permeable splitter plates was constructed with base pressure taps located at 5.1 cm intervals from the center span. This was used to determine the base pressure coefficient as a function of spanwise position with the end plates installed. The data are shown in Fig. A.3 as $-C_{pb}(z)$, and show that the pressure distribution was uniform to within $\pm 1.3\%$ across the span.

A.4 The effects of splitter plate geometry

For these experiments it was intended that the gross plate geometry (the streamwise length and position of the plate) not be a parameter in the experiments, and long splitter plates were used in an attempt to make the splitter plate length infinite as far as the flow in the near wake was concerned. All of the splitter plates for which data are reported in this thesis (other than in this section) were nominally $16D$ in length. To check whether this was effectively infinite or not, measurements of the base pressure and primary wake frequency were made on a permeable splitter plate of $\sigma = 0.49$, using plates of lengths $16D$, $12D$ and $8D$, and the results are shown in Fig. A.4**a** and **b**. It can be seen that for splitter plates of length $12D$ and $16D$ the results are very similar for both $-C_{pb}$ and St, and although the results for $8D$ are compatible, they show a systematic bias to higher values in both cases.

When the wire mesh screen used to form the high solidity splitter plates was installed in the tunnel and placed under tension, the shape of the leading edge of the plate would change from the tension, resulting in a gap between the leading edge and the base of the cylinder. The gap was very small near the ends of the cylinder, and increased in size to a maximum value at the center of the cylinder span of approximately $.06D$. To investigate the possible effect of such a gap, a permeable splitter plate of solidity $\sigma = 0.49$ and $8D$ in length was installed and measurements of $-C_{pb}$ and St were made for different gap sizes. The results are shown in Fig. A.4**c** and **d**. It is seen that there was little effect of changing the nominal gap from 0 to $0.25D$, and that increasing the gap to $0.75D$ resulted in a systematic increase in the measured values of $-C_{pb}$ and St at high Reynolds numbers. It was concluded that the small gap introduced by tensioning the screen had a negligible effect.

A.5 The effects of changing the experimental conditions

It is discussed in Chapter 1 that the flow past a circular cylinder is very sensitive to external effects. Experimental factors which have been identified as having a large effect on measured values are the free stream turbulence level, the cylinder aspect ratio, the blockage due to the experimental model, boundary conditions at the ends of the cylinder, and three-dimensionality. The mechanisms by which these various factors modify the flow and possible effects due to interactions between them are not well understood, although there have been several investigations of various aspects of the problem (a partial list is Gerrard 1965, Stansby 1974, Fox and West 1990, Apelt and West 1982, Kurosaka *et al.* 1988, and Norberg 1988). Measurements of the effects of changing the end plates, the turbulence level, and the apect ratio in the present experimental setup are discussed.

The basic cylinder geometry in the present case is a circular cylinder fitted with square end plates and spanning a test section with a square cross section. The blockage with the cylinder and end plates installed is slightly less than 6%. The results of Apelt and West (1982) indicate a blockage level above this value modifies the pressure distribution on the cylinder surface. The lack of agreement between different investigations of the efficacy of blockage corrections suggest that current methods are not necessarily valid, or at least of limited applicability, and so no blockage corrections were applied to the present data (Apelt and West 1982). The blockage was constant for all experiments presented in this thesis.

Figure A.5 is a compendium of base suction (Fig. A.5**a**) and Strouhal number (Fig. A.5**b**) data taken under varying experimental conditions in the current experimental setup. The figure shows data taken with and without end plates, data taken at two different turbulence levels, and data taken at two different aspect ratios. Also shown are data from Norberg (1988) for similar end plate geometry, an aspect ratio of 8, and a free-stream turbulence level of .1%. This figure illustrates the large scatter in circular cylinder flow measurements that can be caused by variations in the experimental conditions. The effects of the different modifications are discussed individually in the following sections. The flow conditions which were used for all of the permeable splitter plate experiments will be referred to as the basic flow, and it is shown in the figure by the solid triangular symbols. The basic flow is with the cylinder end plates installed, the "natural" turbulence level in the test section (*i.e.*, without turbulence generating screens) which was approximately 0.15% at all velocities, and the maximum possible aspect ratio for the single cylinder diamter used of $AR \approx 17$, which was determined by the distance of the end plates from the walls, which was in turn determined by the requirement that the end plates be outside the tunnel wall boundary layer at all flow velocities.

A.5.1 The use of end plates

The use of end plates was not motivated by a belief that the flow around the cylinder

with end plates is somehow closer to the ideal two-dimensional uniform infinite flow than that around a cylinder without end plates, as this is not clear from currently available results. As this was not the focus of the present experiments, end plate design and effects were not investigated in detail. The use of the end plate design due to Stansby (1974) is common, and so the same basic design was used here (with slight modifications necessary for accommodating the permeable splitter plates) with the intention that the data might be comparable with other published results.

The base pressure coefficient and the primary wake frequency were measured with and without the end plates, and in common with other investigations, it was found that the use of end plates modified the flow. The open square symbols (□) in Fig. A.5**a** and **b** show the flow without the end plates. The end plates used in the present experiments had a slit in the rear portion along the intersection with the wake centerline to accommodate the splitter plates, but as is noted in Chapter 2, whether or not the slit was sealed had no measurable effect on the base suction or the Strouhal number. As found by other researchers (*e.g.*, Stansby 1974), the base suction is found to be increased by about 30% at $\mathrm{Re} = 10^4$ when the end plates are present, and the curves are seen to have slightly different shapes, although the trends in the curves are the same. Without end plates the rate at which the base suction increases does not vary much across the measured Reynolds number range, while for the basic flow (with the end plates) $-C_{pb}$ initially increases at a higher rate than that for the flow without, and then decreases at a lower rate for $\mathrm{Re} > 10^4$. The absolute change across the Reynolds number range is approximately the same, although the percent change is somewhat higher for the flow without the end plates.

The use of end plates also significantly changed the the Strouhal number from that for the basic flow (Fig. A.5**b**, symbol (□)). For the basic flow, the Strouhal number decreases uniformly from $\mathrm{St} \approx .215$ to $\mathrm{St} \approx 0.198$ as the Reynolds number is increased, and the total decrease is about 8%. Without the end plates, the Strouhal number is nearly constant at 0.207 for $\mathrm{Re} < 1.2 \cdot 10^4$ and then rapidly decreases to nearly the same final value as is measured for the basic flow.

A.5.2 Measurements at different free-stream turbulence levels

The turbulence level in the current tunnel was found to be relatively low across the velocity range and to be free of high-amplitude harmonic perturbations (those which give rise to discrete frequency peaks in the power spectrum, see Fig. A.1 and Table A.1), and the results of the experiments presented in the main body of the thesis indicate that the flow is not strongly driven by any of the detectable frequencies. The effects of increasing the turbulence level were investigated in the present experimental setup through the use of turbulence generating screens. Due to the distance from the fixture for mounting the turbulence generating screens to the cylinder station, only one of the available screens generated

a significant turbulence level across the entire velocity range, and this screen produced a turbulence level of 0.6%, which is about four times the 'natural' tunnel turbulence. Figure A.2 shows a typical power spectrum computed from the velocity fluctuations due to the generated turbulence, measured at the cylinder station without the cylinder in place but with the end plates installed. Other spectra for different velocities varied only in the decay rates, with the decay being faster at lower velocities, and there are no discrete peaks visible in any of the spectra.

At low Reynolds number, the higher turbulence level leads to a faster growth rate in the base suction with increasing Reynolds number (Fig. A.5**a**, symbol ($\triangle$)), which then changes at high Reynolds number to a growth rate that is nearly the same as that for the basic flow, and is also at the same level as for the basic flow. Thus the measured base suction at the lower Reynolds numbers and the higher Reynolds numbers is nearly the same for both turbulence levels, but is considerably increased at the intermediate Reynolds numbers at the higher turbulence. For the Strouhal number the effect of the increased turbulence level is to significantly lower the value of the Strouhal number overall, but in contrast to the flow without end plates, the shape of the curve is very similar to that of the basic flow. (Fig. A.5**a**, ($\diamond$)).

A.5.3 Measurements at different aspect ratios

The aspect ratio could be changed by using different length standoffs for the splitter plates, and in this way measurements were made at an aspect ratio of $\mathcal{AR} = 8$. The turbulence generating screen was then installed for this aspect ratio and the measurements repeated. Overall, it can be seen in Fig. A.5**a** (low turbulence marked by ($\diamond$) and high turbulence by (o)) that decreasing the aspect ratio to $\mathcal{AR} = 8$ led to base suction curves which are shaped very similarly to that for the base suction curve at high aspect ratio and high turbulence. However, the base suction for the $\mathcal{AR} = 8$ aspect ratio at low turbulence was only slightly elevated above that of the basic flow, while the two high turbulence curves are nearly the same for $\mathrm{Re} < 10^4$, and at higher Reynolds number the curve for $\mathcal{AR} = 8$ continues to increase while the curve for $\mathcal{AR} = 17$ levels off and approaches that for the basic flow.

Similarly, for $\mathcal{AR} = 8$ and low turbulence the Strouhal number is only changed by a small amount Fig. A.5**b** (low turbulence again marked by ($\diamond$) and high turbulence by (o)) while increasing the turbulence level at $\mathcal{AR} = 8$ significantly decreases the Strouhal number overall, although the decrease from the low turbulence flow is not as great as that caused by increasing the turbulence at $\mathcal{AR} = 17$.

APPENDIX B

Hot-wire calibration

B.1 Introduction

The method used for hot-wire calibration is based on one developed by Cimbala and Park (1990), and uses a version of King's law which retains a dependence on the ambient temperature. The calibration requires initial hot-wire calibration taken over the range of temperatures of interest that are used to derive a set of calibration coefficients for the hot wire. The resulting calibration coefficients are sufficient to linearize subsequent hot wire measurements at different ambient temperatures, and only a linear calibration need be performed to compute the velocity data.

The method was originally developed for calibrating hot wires when the flow temperature varied substantially during the course of an experiment, but the experiments presented in this thesis were carried out in a facility where the temperature is typically constant to within about 0.1 K per hour, and under these circumstances it is simpler to compute the calibration coefficients using calibration data taken before and after each experiment, rather than attempting to use a single set of coefficients obtained from a large quantity of data. The accuracy of the method when the temperature is controlled is always better than that found for data taken under varying temperature conditions, although the deviations are similar when the calibration data comes from combined data taken before and after particularly long experiments.

B.2 Development of the equations

The starting point is the following form of King's Law:

$$\mathrm{Nu}_w = a + b\mathrm{Re}_w^n \tag{B.1}$$

where Nu_w is the Nusselt number and Re_w is the Reynolds number based on wire diameter and the local flow velocity U normal to the wire. Following Blackwelder (1981) and modeling the hot wire as a circular cylinder, the Nusselt number is defined by

$$\mathrm{Nu}_w = \frac{q}{\pi l_w k(T_w - T_a)}$$

where q is the convective heat loss from the wire, l_w is the hot-wire length, $k = k(T)$ is the thermal conductivity and T_w and T_a are the wire operating temperature and the ambient temperature, respectively. Assuming that the heat loss is equal to the power dissipated in the wire,

$$q = \frac{{e_w}^2}{R_w}$$

where e_w is the voltage across the hot wire and R_w is the (nominally fixed) hot-wire resistance. This gives

$$\mathrm{Nu}_w = \frac{{e_w}^2}{\pi R_w l_w k(T_w - T_a)} . \tag{B.2}$$

As in Cimbala and Park, k and the kinematic viscosity ν are evaluated at $T = \frac{1}{2}(T_w + T_a)$ (Sutherland's law) and at the ambient pressure.

Substituting Equation B.2 into Equation B.1 provides the desired explicit dependence on the ambient temperature.

If the equation is evaluated directly in the form given here, Nu_w and Re_w are of order 1 and minimization of

$$\chi^2 = \sum (\mathrm{Nu}_w(U_i, T_{ai} \; ; \; a, b, n, T_w) - \mathrm{Nu}_{wi})^2$$

is straightforward, giving the values of the fit parameters (a, b, n, T_w) for use in calibrating the hot wire. Although T_w is a dimensional value of order 100 K, and is used as one of the fit parameters, this does not affect the minimization scheme since it is combined into Nu_w which is of order 1. The expression for Nu_w gives $e_w(U, T_a)$ and is directly invertible, so $U(e_w, T_a)$ is easily calculated once the values of the fit parameters are known.

B.3 Example hot-wire calibrations

To verify the efficacy of the method, a large quantity of data was taken in air with the hot-wire anemometers described in Chapter 2 at several different temperatures in the range 18–30 C. The physical properties of air, k and ν, were computed by interpolation from the tables published in Hilsenrath (1955). Values of the fit parameters were determined using a simplex method (Press *et al.*, 1988) to search for a multi-dimensional minimum of χ^2 in the (a, b, n, T_w) parameter space, which works by moving the vertices of a multidimensional polygon around in the parameter space. The simplex method requires a set of initial vertices for the polygons, and in the present case, a single initial point is provided, and the other points are determined by moving 15% of the initial value along each axis in the parameter space. The criterion used in the computation to define when a minimum has been found is that all of the vertices must be within a given "distance" of the others (evaluated as the

Euclidean distance between vertices), and it was found that setting this distance to $1 \cdot 10^{-12}$ gives accurate results. The method was found to be very tolerant of the choice of the initial guess, and for the example data always converged to the same values of the parameters. The fit parameters found from the example data are listed in Table B.1. The value of T_w in Table B.1 which minimizes χ^2 should reflect the actual hot-wire temperature, which is selected to be of approximately 550 K by a setting in the hot-wire anemometer, and it can be seen from the table that the value of T_w found by the method using the example data is considerably smaller. It was found during the course of the research that the value of T_w estimated by the calibration procedure is always considerably smaller than the actual value, but since the method results in a accurate calibration this anomaly was not investigated further.

Parameter	Best fit value
a	0.2318
b	0.3171
n	0.4225
T_w	381.0 K

TAB. B.1 Example hot-wire calibration parametersfrom a best-fit to the data shown in Fig. B.1

Figure B.1 is a plot of the example data in the form of Nu_w vs. Re_w, and also shown is the curve defined by Equation B.1 and the coefficients in Table B.1. Figure B.2a shows a plot of the same data in the form of the velocity U_c computed by applying the calibration to the measured hot-wire voltages versus the corresponding measured values of the velocity U_m, and Fig. B.2b shows a plot of the absolute deviations of the computed velocities from the measured velocities plotted against the measured velocity, defined by

$$\Delta U_c = \frac{U_c - U_m}{U_m}.$$

The average deviation of the fit velocities from the measured values is 0.06 m/s, which is typical of the the hot-wire calibrations determined using this method. It can be seen that the relative deviation increases for low velocities.

Further calibration data for the same hot wire was collected on a different day from the previous data, and the results of processing these data using Equation B.1 and the coefficients in Table B.1 are shown in Fig. B.3, and the hot-wire drift is apparent as deviation of the linearized data from the line of slope one. A linear fit calculated from the linearized data may then be applied as a correction, and the result is also shown in the figure. After the linear correction is applied the relative deviations (not shown) were all less than 1% for $U > 2$ m/s, with an average deviation of 0.04 m/s, demonstrating that Equation B.1 is a good linearizer of the data, and the results is then linearly corrected to obtain the velocity.

The data shown in Fig. B.4 were collected in the facility used for the experiments described in this thesis, and has been presented in the same way as the data in Fig. B.2 without applying a linear correction. Although the data shown in the figures are a combination of two data sets taken approximately nine hours apart, it can be seen that the deviations are all considerably less than 1%, even at the lowest velocities, and this is typical of calibration data taken in this facility and is attributed to the constancy of the temperature.

From an examination of the figures, it appears that there might be a small curvature in the "linearized" data sets. In an attempt to correct for this a quadratic term was added to Equation B.1 resulting in the form

$$\mathrm{Nu}_w = a + b\mathrm{Re}_w^n + c\mathrm{Re}_w^{2n},$$

which is also invertible in closed form. The additional term can be thought of as the next term in a power series for $\mathrm{Nu}_w(\mathrm{Re}_w^n)$, and so is not entirely without foundation. Using the data set of Fig. B.1, and the simplex method described above, the value of c was computed, and was found to be 5 orders of magnitude less than a and b, and the magnitude of the deviations ΔU_c was not reduced.

B.4 Summary

The temperature dependent King's law given in Equation B.1 and Equation B.2, combined with a linear correction, provides an effective means for making hot-wire measurements in facilities where variations in ambient temperature make the more traditional method impractical or impossible to use, and is also quite accurate when the temperature variation is small. Because the values of the variables and coefficients are all of order one, minimizing χ^2 to find the values of the fit coefficients has proven to be both simple, and fairly robust, in the sense that the method is not highly sensitive to the value of the initial guess. This form of King's law, while not particularly complicated, is also philosophically satisfying since all variables and coefficients are non-dimensional. Treating this form of King's law as a truncated power series for $\mathrm{Nu}_w(\mathrm{Re}_w^n)$ and adding the next term in the series was shown to have no significant effect on the quality of the fit to the data. The method is also seen to give good results for calibration of hot wire when the temperature is controlled.

APPENDIX C

Pressure drop coefficients of the permeable splitter plates

C.1 Introduction

This appendix presents the results of measurements of the "permeability" of the splitter plates used in these experiments. The results of the flow visualization presented in Chapter 3 indicate that there is very little mass transfer across the plates, and therefore it is reasonable to assume that the main communication between the two separated shear layers is through the pressure field. The permeability will then be determined by the pressure drop Δp_s across the permeable plate, and so measurements were made to determine the dependence of Δp_s on the normal velocity U_∞, the plate solidity σ, and the effect of the detailed geometry, which in the case of wire mesh is represented by the wire diameter and the mesh count.

Most of the measurements on the cylinder with the permeable splitter plate were carried out using splitter plates made from commercially available stainless steel woven-wire screens. Those screens which had nominal wire diameters in the range 0.019 – 0.025 mm (0.0075 to 0.010 inches) with nominal mesh counts varying from 5.5 – 15.7 meshes per cm (14 to 40 meshes per inch) will be referred to in this appendix as the "standard plates." One other woven wire screen was used, which was not part of the standard plates due to the fact that its geometrical characteristics – a (nominal) wire diameter of 0.025 mm (0.001 inches) and mesh count of 39 meshes per cm (100 meshes per inch) – were different in order of magnitude, and this turned out to have a significant effect on the properties of the screen. A more rigorous definition of the "standard plates" based on the results of the measurements will be given below. Measurements were also made using a permeable splitter plate made from 0.48 mm thick aluminum plate perforated by a regular array of circular holes, and measurements of the pressure drop across this plate are also presented in this appendix.

nominal		measured				
mesh	d_w	mesh	d_w	mesh	d_w	σ
100	0.001	—	0.0010	—	0.0010	0.19
14	0.009	14	0.0080	14	0.0087	0.22
18	0.009	18	0.0089	18	0.0088	0.29
26	0.0075	25.5	0.0076	24.5	0.0077	0.35
30	0.0095	30	0.0090	31	0.0095	0.49
40	0.010	40	0.0105	40	0.0095	0.65
perforated plate						0.65

TAB. C.1 Screen nominal and measured parameters. d_w is the screen wire diameter, and is given in inches. The two measured values of mesh and d_w represent the two different directions on the screen.

The values of the wire diameters and mesh counts for the woven wire screens are detailed in Tab.C.1 and a diagram of the perforation pattern on the aluminum plate is given in Fig. C.1. Values listed under "actual" are the measured values (meshes were counted under a magnifying glass using a steel rule for reference, and wire diameter was measured using a calibrated micrometer accurate to $\pm 0.5 \cdot 10^{-4}$ inches), those under "nominal" are quoted from the manufacturer. Nominally, all of the meshes are square, but this was not true for several of the screens so the value of the mesh and wire diameters in both directions are listed. Specific screens will be referred to by the nominal meshes per inch and wire diameter in inches, as in 100M/0.001 for the 100 meshes per inch, 0.001 inch wire diameter screen. For undistorted circular wires, it is easy to work out the formula for the solidity given the mesh count and wire diameter:

$$\sigma = (1 - M_x d_x)(1 - M_y d_y)$$

where M_x, M_y are the meshes per linear unit in the x and y directions, and d_x and d_y are the corresponding wire diameters. The screens and the plate will be referred to generically as "plates."

C.2 Experimental arrangement

The pressure drop across each plate was measured in the low speed open-return wind tunnel described in Chapter 2, which has a maximum velocity with no experiment installed of about 11 m/s. Located 0.56 and 0.25 m upstream of the entrance to the test section are slots into which may be inserted square frames designed for the introduction of turbulence generating screens. An existing frame, which is normally placed in one of the slots and has its inner surface flush with the tunnel walls, had a hole through one side and a corresponding groove through which a pressure probe and tubing could be led. An adapter was built to

hold a Kiel probe in the hole, which was in turn connected to plastic tubing led through the groove and out of the tunnel, and the frame replaced in the farthest upstream slot. Another frame, similar in dimensions to the first but designed to hold a plate in tension spanning the test section, was used to hold each plate, and was placed in the slot closest to the test section. The plate then completely spanned the settling chamber, normal to the flow and just upstream of the entrance to the test section. A carefully aligned pitot-static tube was placed in the otherwise empty test section. Total pressure upstream of the plate was obtained from the Kiel probe, and total pressure downstream was obtained from the Pitot-static tube. Test section dynamic pressure was also obtained using the Pitot-static tube. The manometers described in Chapter 2 were used to measure the test section dynamic pressure q, as well as the difference between the total pressure upstream of the screen and the total pressure downstream (which gives directly the pressure drop Δp_s across the screen, ignoring losses from wall boundary layers which are negligible over such a short distance). With the exception of one data point which will be discussed in detail, the maximum uncertainty over all of the data was 0.4% in k, and 0.3% in U_∞. All pressure were obtained using the personal computer based digital data acquisition system described previously, and were sampled for time periods that were long compared with any relevant flow time scales.

C.3 Screen-normalized scaling

It is plausible that the pressure drop will scale with the dynamic pressure of the flow, which results in a non-dimensional pressure drop coefficient of

$$k = \frac{\Delta p_s}{q}.$$

Since all of the screens present a decrease in area to the oncoming flow, continuity implies that the velocity, which is necessarily measured far from the screen, be scaled by the ratio of the open area of the screen to the total area (the open area ratio). If the solidity is σ, then the open area ratio is given by $1-\sigma$, so

$$U_* = \frac{U_\infty}{(1-\sigma)}$$

and the effective Reynolds number is

$$\mathrm{Re}_* = \frac{U_\infty d_{\mathrm{wire}}}{\nu(1-\sigma)}.$$

The normal drag force is given by the pressure drop times the area, so the appropriately scaled drag coefficient for a screen is

$$\mathrm{C_{D*}} = \frac{(1-\sigma)^2}{\sigma} k$$

(since $q_* = \frac{1}{2}\rho U_*^2$, q must be scaled by two factors of $(1-\sigma)$).

C.4 Results

Measurements were made on all screens in Tab.C.1, over all velocities that were attainable in the tunnel with each particular screen in place (the limits on tunnel velocities of course varied, depending on which screen was installed). The data are plotted in Fig. C.2 as screen pressure drop coefficient k versus free-stream velocity U_∞. It can be immediately seen from Fig. C.2 that the values of k do not scale directly with the screen solidity. The perforated plate with $\sigma = 0.65$ has a much higher value of k than the 40M/0.010 screen for which $\sigma = 0.65$, and the 100M/0.001 screen with $\sigma = 0.19$ has nearly the same k as the 26M/0.0075 screen for which $\sigma = 0.29$.

Figure C.3 is a plot of C_{D*} against Re_* for the wire mesh screens listed in Tab.C.1 using logarithmic scales (there seems to be no reasonable equivalent of Re_* for the perforated plate, so it is not plotted). Also shown are data derived from Schubauer and Spangenberg (1949) figure 5, taken from Coles (1988). The solid line is low Reynolds number drag data for long circular cylinders, from Wieselsberger (1921). It can be seen that the shape of the curve in Fig. C.3 is similar to that for the circular cylinder at low Reynolds number, although the slopes are somewhat different, with the screen drag rising faster as the Reynolds number is decreased. The data from Schubauer and Spangenberg do not appear to follow the same trend as the data from the present experiments, and this may be due to a lack of uniformity in the screens available to them. In the present case, it proved necessary to be careful about measuring the actual screen parameters, as opposed to those quoted by the manufacturers, in order to obtain the collapse of Fig. C.3. The apparently anomalous point at $Re_* \approx 20$ is at the lower velocity limit of the experimental apparatus, and the pressure drop was measured with the manometer range setting at the highest gain (this is the only data point for which this setting was used) and therefore its validity is regarded as suspect.

C.5 Summary

It can be seen from Fig. C.2 that the value of the pressure drop is not a function of the solidity alone, but also depends on the screen geometry. Furthermore, this figure shows the reason for selecting a "standard" set of plates, which is that for the standard plates, the pressure drop coefficient varies monotonically with the solidity at all velocities, and so a splitter plate made from a standard plate is unambiguously described by its solidity alone, and varying the solidity by selecting a different screen from this set varies the pressure drop coefficient in a predictable fashion. This is significant when using permeable splitter plates since the amplitude of the transverse velocity fluctuation varies with downstream location, and since the pressure drop varies with the velocity normal to the permeable plate, and this will cause variations in the relevant value of k with downstream location. The data presented in this figure for plates which are not in the standard set also show clearly that

it is not generally true that the pressure drop coefficient varies smoothly with the solidity alone.

Figure C.3 shows that the geometric scaling presented in this appendix is reasonable, in that it brings about a good collapse of the data for those screens of similar local geometry (*i.e.*, those made of woven wire mesh). The resulting curve is similar in shape to that of the drag curve for circular cylinders at low Reynolds numbers, but the curve for the screen has a different slope than that for the circular cylinder at all Reynolds numbers measured here. This seems reasonable, since the screens are constructed of wire of a nominally circular cross section, but the local boundary conditions for each short segment in the screen are different than those for a long circular cylinder in a uniform flow, and the boundary conditions have a large effect on the flow of a circular cylinder at low Reynolds numbers.

APPENDIX D

Calculation of power spectra and determination of wake frequencies

D.1 Computation and interpretation of power spectra

Power spectra presented in this thesis are computed according to the methods described in Chapter 12 of Press *et al.* (1988) using digital Fourier transform techniques. Power spectra were computed to obtain to determine the power spectral density of the fluctuating velocity signals, the primary wake frequency, and to determine the acoustic power during the forcing experiments. It is typical to show power spectra computed from fluid mechanical measurements in terms of "arbitrary units," but this makes it difficult to compare the amplitudes of the power spectra between different experiments (or even within a single experiment). If some care is taken in the computation it is possible to assign physical meaning to the amplitude of the power spectral density, and since this is intended here the computation of the power spectra will be described in some detail.

For each time segment over which data were continually collected, the resulting voltage samples from the A/D converter were saved to a file on the computer system, so that each data file represents continuous periodic sampling from some initial time to some final time. For hot-wire measurements for which the actual velocity spectra were desired (such as the shear layer measurements presented in Chapter 5) each voltage sample was then converted into a velocity sample using the method described in Appendix B and then normalized by the free-stream velocity. For hot-wire measurements used to determine only the primary wake frequency, no conversion was performed on the samples, since determination of the amplitude of the velocity fluctuations from data taken with the hot wire situated in the potential flow outside the near wake itself were not necessary for the determination of the frequency, and are also difficult to compare between different flow conditions. The nonlinearity of the relationship between hot-wire voltage and velocity has no effect on the frequencies at which the relevant spectral features are observed (*e.g.*, the peak at the primary wake frequency) and in any case the fluctuations at the measurement location were extremely small and the relationship is approximately linear, in which case the location of spectral features and their relative amplitudes are the same whether or not the velocity conversion is performed. Also, for measurements to determine the frequency distribution

and power spectral density of the acoustic forcing, no conversion was performed on the signal as the microphone output voltage was arranged to be proportional to the strength of acoustic pressure fluctuations. Any of the continuous time signals will be referred to as $x(t)$, and the result of sampling this continuous signal are the $\{x_i\}$. To compute the power spectra, each data file was broken up into $2K$ blocks of length $M/2$ samples, which were then combined into K longer blocks each composed of two contiguous blocks (the last long block is wrapped around to the beginning of the data). Actually, at this point the conversion to velocity, if necessary, was performed. The mean of the resulting M data samples, as x, was removed and the digital Fourier transform computed according to

$$\phi \approx \mathrm{FFT}\left(W \cdot x^2\right),$$

where W is the Welch windowing function (described in Press *et al.*) used to reduce the "leakage" between adjacent frequency bins. FFT in this expression stands for the computation of the digital Fourier transform using the fast Fourier transform algorithm, and the details are completely documented in, *e.g.*, Press *et al.* (1988) or Brigham (1974). The resulting $M+1$ values ϕ_i are averaged at each value of i to produce the $M+1$ estimates of ϕ_i. As discussed in Press *et al.*, this results in a percent uncertainty in the value of ϕ_i of $1/\sqrt{MK}$, and this is what is reported.

Note that ϕ is not the power spectral density, but is the estimated total power in the Fourier modes of the signal in the i^{th} frequency bin of width Δf. What is shown in the figures is the estimated power spectral density $\Phi_i = \phi_i/\Delta f$, which is an estimate of the continuous power spectral density normalized so that

$$\int_0^{f_N} \Phi(f)\, df \;\simeq\; \frac{1}{T}\int_0^T x^2(t)\, dt\,. \tag{D.1}$$

Here again $x(t)$ stands either for the velocity fluctuations $u'(t)/U_\infty$ or the voltage fluctuations $e'(t)$ from the hot wire or the microphone. This normalization of Φ means that the amplitude is independent of the size of the frequency bins, and therefore is independent of the sampling rate of the original data. The relationship D.1 is only approximate due to the use of windowing, since the contribution of the window function cannot be precisely normalized out unless the window is a square window. In the digital representation, the integrals are approximated by discrete sums, and so the relationship becomes

$$\sum_{i=0}^{N/2} \Phi_i\, \Delta f \;\simeq\; \frac{1}{T}\sum_{i=0}^{N} x_i^2\,.$$

The value of the sum on the right-hand side is the variance of the sampled, zero-mean signal. The computation of the power spectra using the FFT insures that this relationship is an equality for a square window and a single block of data (within the precision of the computation) but all of the power spectra shown are averages of typically 32 or more blocks of sampled data to reduce the variance in the power spectra, and are windowed with non-square windows and and thus this relationship is only exact in the statistical limit.

Equation D.1 indicates the physical interpretation of the power spectral density. If the signal is the velocity trace $u'(t)/U_\infty$, the right-hand side is equal to the average total energy in the velocity fluctuations normalized by the energy of the free stream flow. Thus, the amplitude of the power spectral density represents the contribution of the Fourier component of the fluctuations at a single frequency to the total energy. Note that the right-hand side is also the variance of the velocity signal, and is therefore the square of the turbulence level, defined as the RMS (root mean square) of the velocity fluctuations.

D.2 Determination of the primary wake frequency

For measurements intended only to determine the primary frequency a hot wire was introduced into the flow at the location $(x/D, y/D) = (2.0, 1.5)$, which is outside of the wake for all cases measured but close enough so that a distinct signal could be obtained. The hot-wire bridge output (from the Matilda meters – see Chapter 2) was connected to a preamplifier (Stanford Research Systems SR560) and filtered by two stages of a dual 24-pole butterworth filter (Krohn-Hite 3202). The filter cutoff (-3dB) point was set to approximately three times the expected primary wake frequency, estimated using $f_1 D/U_\infty \approx 0.2$. The base pressure and free-stream velocity were measured as described in Sec. 2.3. During the collection of a data point, the data collection system simultaneously sampled the fluctuating hot wire voltage at the filter output, the output from the manometer measuring Δp_{12}, the output of the manometer measuring Δp_b (the pressure at the cylinder base, referenced to the free stream), and the output of a pulse generator triggered by a sensor on the fan shaft. The primary wake frequency was determined by computing the power spectral density $\Phi_e(f)$ of the fluctuating hotwire voltage signal using the method described in Sec. D.1 and then determining the location of the peak corresponding to the primary wake frequency. The peaks were typically of such high amplitude above the background that it was sufficient to determine the frequency corresponding to the maximum amplitude of Φ_e, and this procedure was performed by a computer program. Under certain circumstances, it was necessary to limit the search for the maximum to a range of frequencies which were then scanned by the program to determine the location of the peak. In extreme cases, such as for spectra taken with high solidity permeable splitter plates at low Reynolds number, it was necessary to examine the data individually to determine the location of the peaks, or even if such a peak existed.

Figure D.1**a-d** show example power spectra for a cylinder without a splitter plate at different Reynolds numbers which span the attainable range. The amplitudes are comparable among the different spectra because they are not normalized or converted to a common physical variable. It can be seen in this figure that the peaks at the primary wake frequency were sharply defined and assume approximately the same characteristic shape for

all Reynolds numbers. Also, peaks at the harmonic $2f_1$ are visible in all spectra, probably due to the effects of the vortex formation on the opposite side of the wake. Peaks having such a characteristic shape and large amplitudes relative to the background appeared in all spectra except for flow conditions with a high solidity permeable splitter plate and low Reynolds number. Figure D.2**a**–**d** show example power spectra for the flow past the cylinder with a permeable splitter plate of solidity $\sigma = 0.65$ for several Reynolds number that span the range at which a primary wake frequency could be detected in this case. It is assumed that the discrete spectral feature at $f_{a*} \approx 0.21$ which is visible in all of the spectra is not fluid mechanical in origin since it does not change with Reynolds number. At high Reynolds numbers, the primary wake frequency is clearly defined, but as the Reynolds number decreases, initially the amplitude decreases, eventually decreasing below that of the noise peak in the spectrum (necessitating the limitation of the search for the peak to a small frequency band), and eventually the peak disappears into the background. In Fig. D.2**d** two spectra are shown one above the limiting Reynolds number at which no primary frequency is said to be detected, and one below. This is a fairly heuristic definition, but it can be seen from Fig. D.2**d** that it gives results which are as precise as the resolution in Reynolds number for which data were taken.

APPENDIX E

Acoustic forcing power measurements

Figure E.1 shows the measured acoustic power spectral density at the selected forcing frequency. What is shown is the value of the peak of the power spectrum computed from a calibrated, linear, instrument quality microphone (B&K Instruments microphone model 4138 and power supply model 2801) that is inserted through the tunnel top into the flow at the cylinder location (the cylinder is positioned horizontally).

There are several reasons why the values shown in the figure may not be representative of the forcing power that is available to the flow at the cylinder. Most of the problems are experimental: The speaker itself has a rather non-linear frequency response (both because the design is not particularly good, and because the speaker was mounted by securing it with wood screws over a circular hole in a $3/4''$ thick piece of plywood, and then using C-clamps to mount the resulting assembly onto a thin steel frame). The tunnel frequency response is important as well, since the speaker was placed at the tunnel inlet facing downstream, and so the acoustic waves had to traverse the tunnel contraction and part of the test section, and no effort was made to compensate for any absorption or distortion due to tunnel acoustics. But in addition to problems due to the acoustics of the experimental setup, the microphone was placed so that there were two possible additional sources of acoustic power. One source is the pressure waves generated by the wake fluctuations at the forcing frequency, which are enhanced when the forcing frequency is in the shear layer sensitive band, and the other is the tunnel wall boundary layer, which may be excited at the forcing frequency due to the acoustic input as well as due to any vibrations of the tunnel in response to the forcing.

To control all of these additional effects would have required greater effort than would have been justified by the immediate goals of showing that the shear layer is highly responsive to coherent perturbations at frequencies lying in the corresponding sensitive band, and study the effect of the forced shear layer on the near wake structure. The development of the shear layer instability in the presence of forcing shown in Fig. 6.8 and Fig. 6.10 does indicate that the main influence of the forcing is the initial excitation of a single eigenmode of the shear layer instability, which is then amplified and develops without significant further influence from the acoustic forcing.

References

APELT, C. J., WEST, G. S., AND SZEWCZYK, A. A. 1973 The effects of wake splitter plates on the flow past a circular cylinder in the range $10^4 < R < 5 \times 10^4$. *J. Fluid Mech.* **61**, 187–198.

APELT, C. J., AND WEST, G. S. 1975 The effects of wake splitter plates on the flow past a circular cylinder in the range $10^4 < R < 5 \times 10^4$. Part 2. *J. Fluid Mech.* **71**, 145–160.

APELT, C. J., AND WEST, G. S. 1982 The effects of tunnel blockage and aspect ratio on the mean flow past a circular cylinder with Reynolds numbers between 10^4 and 10^5. *J. Fluid Mech.* **114**, 361–377.

ARIE, A., AND ROUSE, H. 1982 Experiments on two-dimensional flow over a normal wall. *J. Fluid Mech.* **1**, 129-141.

BEARMAN, P. W. 1965 Investigation of the flow behind a two-dimensional model with a blunt trailing edge and fitted with splitter plates. *J. Fluid Mech.* **21**, 241–255.

BERGER, E., AND WILLE, R. 1972 Periodic flow phenomena. *Ann. Rev. Fluid Mech.* **4**, 313–340.

BLACKWELDER, R. F. 1981 Hot-wire and hot-film anemometers. *Methods Exp. Physics* **18**, 259–314.

BLOOR, S. M. 1964 The transition to turbulence in the wake of a circular cylinder. *J. Fluid Mech.* **19**, 290–304.

BRIGHAM, O. 1974 *The Fast Fourier Transform.* Englewood Cliffs: Prentice-Hall.

BROWAND, F. K. 1966 An experimental investigation of the instability of an incompressible, separated shear layer. *J. Fluid Mech.* **26**, 281–307.

CANTWELL, B., AND COLES, D. 1983 An experimental study of entrainment and transport in the turbulent near wake of a circular cylinder. *J. Fluid Mech.* **136**, 321–374.

CANTWELL, B. 1976 *Manual for Matilda Meter Constant Temperature Anemometers.* Pasadena: GALCIT (unpublished).

CIMBALA, J. M., AND PARK, W. J. 1990 A direct hot-wire calibration technique to account for ambient temperature drift in incompressible flow. *Exp. Fluids* **8**, 299–300.

CIMBALA, J. M. 1984 Large structure in the far wakes of two-dimensional bluff bodies. Ph.D. Thesis, California Institute of Technology.

CIMBALA, J. M., NAGIB, H. M., AND ROSHKO, A. 1988 Large structure in the far wakes of two-dimensional bluff bodies. *J. Fluid Mech.* **190**, 265–298.

COLES, D. 1988 *private communication.*

CORKE, T., KOGA, D., DRUBKA, R., AND NAGIB, H. 1977 A new technique for introducing controlled sheets of streaklines in wind tunnels. *IEEE publication* 77-CH1251-8 AES.

DRAZIN, P. G., AND REID, W. H. 1981 *Hydrodynamic stability.* Cambridge: Cambridge University Press.

DIMOTAKIS, P. E., AND BROWN, G. L. 1976 The mixing layer at high Reynolds number: large-structure dynamics and entrainment. *J. Fluid Mech.* **78**, 535–570.

FOX, T. A., AND WEST, G. S. 1990 On the use of end plates with circular cylinders. *Exp. Fluids* **9**, 237–239.

FRIC, T. F. 1990 Structure in the near field of the transverse jet. Ph.D. Thesis, California Institute of Technology.

GERRARD, J. H. 1965 A disturbance-sensitive Reynolds number range of the flow past a circular cylinder. *J. Fluid Mech.* **22**, 187–196.

GOLDSTEIN, S., ED. 1938 *Modern Developments in Fluid Dynamics.* Oxford: Clarendon Press.

HILSENRATH, J. *et al.* 1955 *Tables of Thermal Properties of Gases.* National Bureau of Standards Circular 564. Washington D.C.: U.S. Dept of Commerce.

HO, C., AND HUERRE, P. 1984 Perturbed free shear layers. *Ann. Rev. Fluid Mech.* **16**, 365–424.

IGARISHI, T. 1982 Investigation on the flow behind a circular cylinder with a wake splitter plate. *Bull. JSME* **25**, 528-535.

KOURTA, A., BOISSON, H. C., CHASSAING, P., AND HA MINH, H. 1987 Nonlinear interaction and the transition to turbulence in the wake of a circular cylinder. *J. Fluid Mech.* **181**, 141–161.

KUROSAKA, M., CHRISTIANSEN, W. H., GOODMAN, J. R., TIRRES, L., AND WOHLMAN, R. A. 1988 Crossflow transport induced by vortices. *AIAA J.* **26**, 1403–1405.

MORKOVIN, M. 1964 Flow around circular cylinder — a kaleidoscope of challenging fluid phenomena. *ASME Symposium on Fully Separated Flows* , 102–118.

NORBERG, C. 1988 Turbulence and Reynolds number effects on the flow and fluid forces on a single cylinder in cross flow. *J. Fluids Struct.* **1**, 337–357.

PERRY, A. E. 1982 *Hot-wire Anemometry.* Oxford: Clarendon Press.

PETERKA, J. A., AND RICHARDSON, P. D. 1969 Effects of sound on separated flows. *J. Fluid Mech.* **37**, 607–616.

PRESS, W. H., FLANNERY, B. P., TEUKOLSKY, S. A., AND VETTERLING, W. T. 1988 *Numerical Recipes in C.* Cambridge: Cambridge University Press.

RAE, W. H., AND POPE, A. 1984 *Low-Speed Wind Tunnel Testing.* New York: John Wiley & Sons.

ROSHKO, A. 1953 On the development of turbulent wakes from vortex streets. *NACA TN 2193.*

ROSHKO, A. 1954 On the drag and shedding frequency of two-dimensional bluff bodies. *NACA TN 3169.*

ROSHKO, A., AND FISZDON, W. 1969 On the persistence of transition in the near wake. *Problems of Hydrodynamics and Continuum Mechanics,* pp. 606-616. Soc. Industrial and Appl Math: Philadelphia.

ROSHKO, A. 1992 Perspectives on bluff body aerodynamics. Second International Colloquium on Bluff Body Aerodynamics and Applications, Melbourne, Australia.

SCHEWE, G. 1986 Sensitivity of transition phenomena to small perturbations in flow round a circular cylinder. *J. Fluid Mech.* **172**, 33–46.

SCHILLER, L., AND LINKE, W. 1933 Pressure and frictional resistance of a cylinder at Reynolds numbers 5,000 to 40,000. *NACA TM 715.*

SCHUBAUER, G. B., AND SPANGENBERG, W. G. 1949 Effect of screens in wide-angle diffusers. *NACA TR 949.*

STANSBY, P. K. 1974 The effects of end plates on the base pressure coefficient of a circular cylinder. *Aero. J.* **78**, 36–37.

SZEPESSY, S. 1991 On the three-dimensionality of vortex shedding from a circular cylinder. Ph.D. Thesis, Chalmers University of Technology.

UNAL, M. F., AND ROCKWELL, D. 1988 On vortex formation from a cylinder: Part 1. The initial instability, Part 2. Control by slitter-plate interference. *J. Fluid Mech.* **190**, 491–529.

WEI, T., AND SMITH, C. R. 1986 Secondary vortices in the wake of circular cylinders. *J. Fluid Mech.* **169**, 513–533.

WEST, G. S., AND APELT, C. J. 1983 The effects of tunnel blockage and aspect ratio on the mean flow past a circular cylinder with Reynolds numbers between 10^4 and 10^5. *J. Fluid Mech.* **71**, 145–160.

WIESELSBERGER, C. 1922 New data on the laws of fluid resistance. *NACA TN 84.*

ZDRAVKOVICH, M. M. 1990 Conceptual overview of laminar and turbulent flows past smooth and rough circular cylinders. *J. Wind Eng. Ind. Aero.* **33**, 53–62.

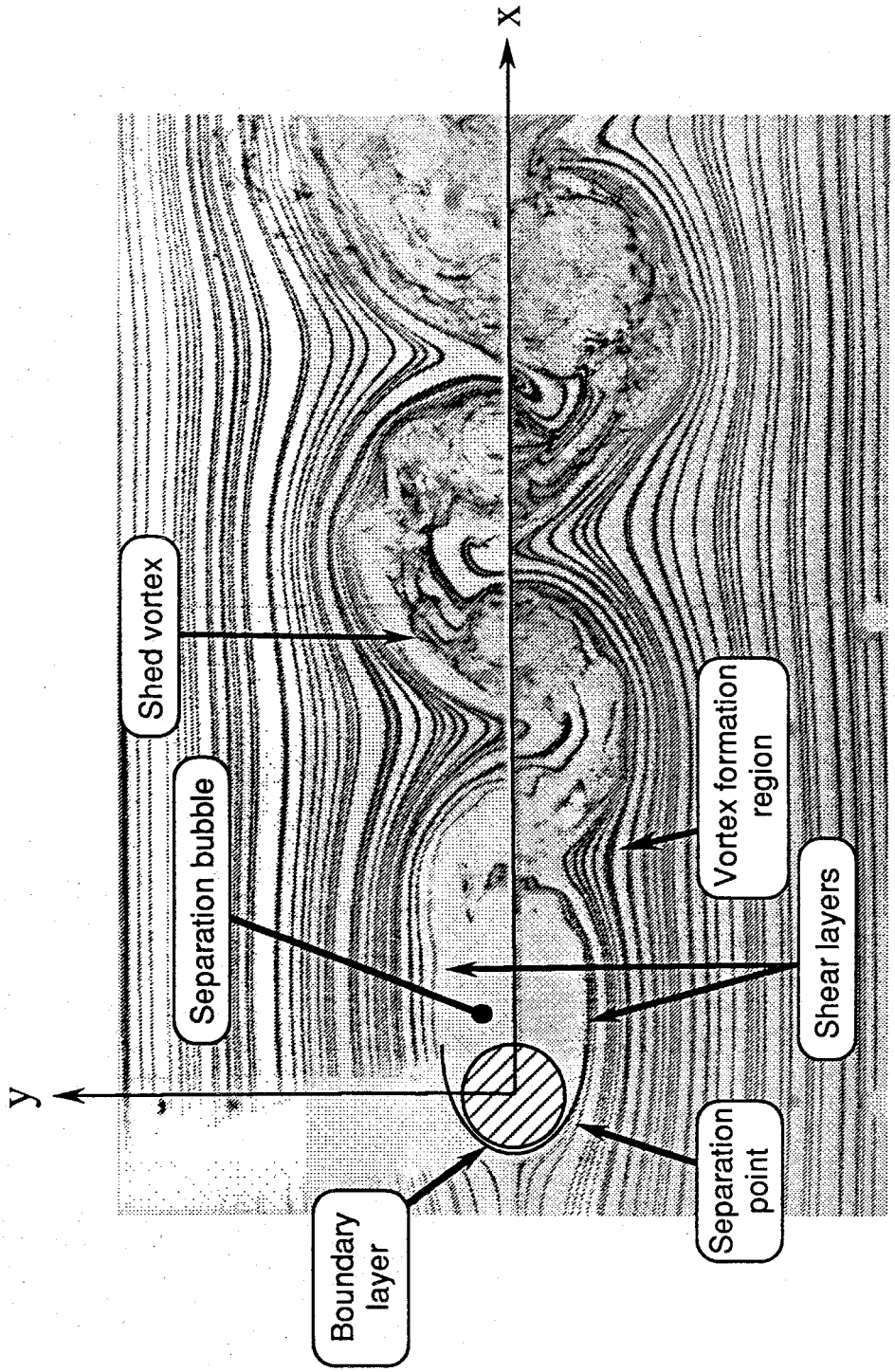

FIG.1.1 Schematic diagram of the basic structure of the near wake. The image is derived from a smoke wire flow visualization photograph of the flow past a circular cylinder without a splitter plate at $Re = 5500$.

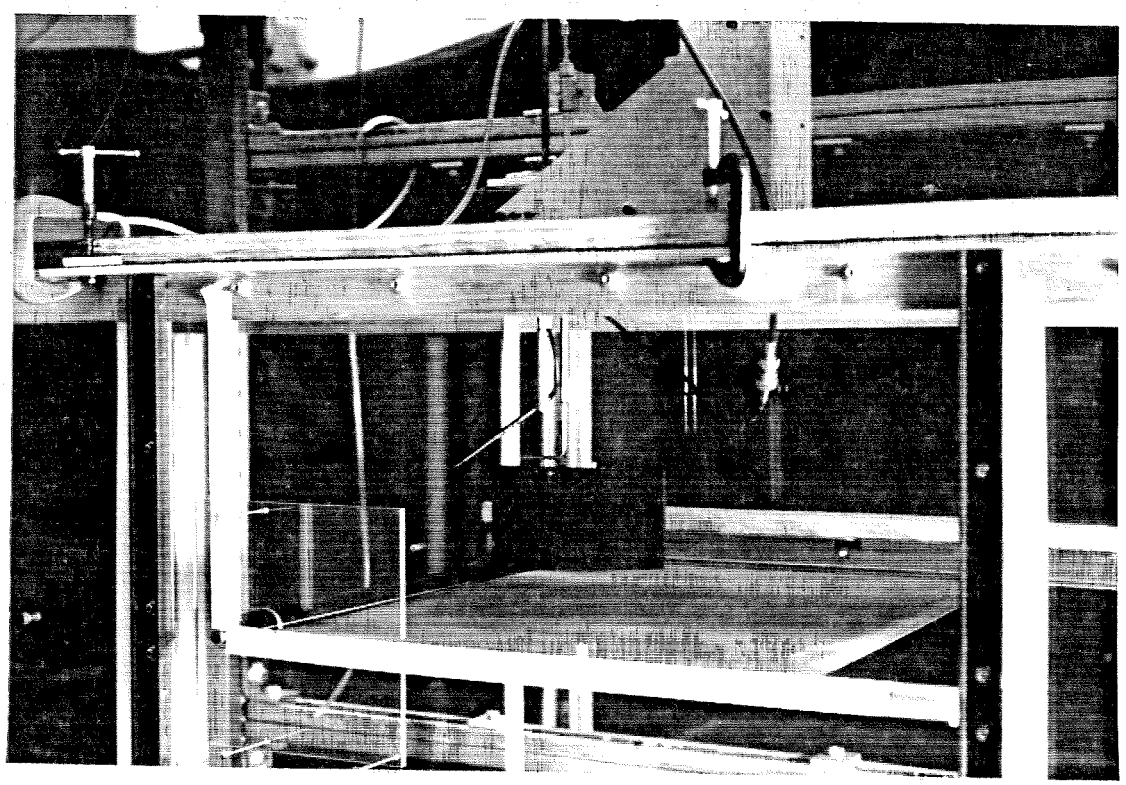

(a)

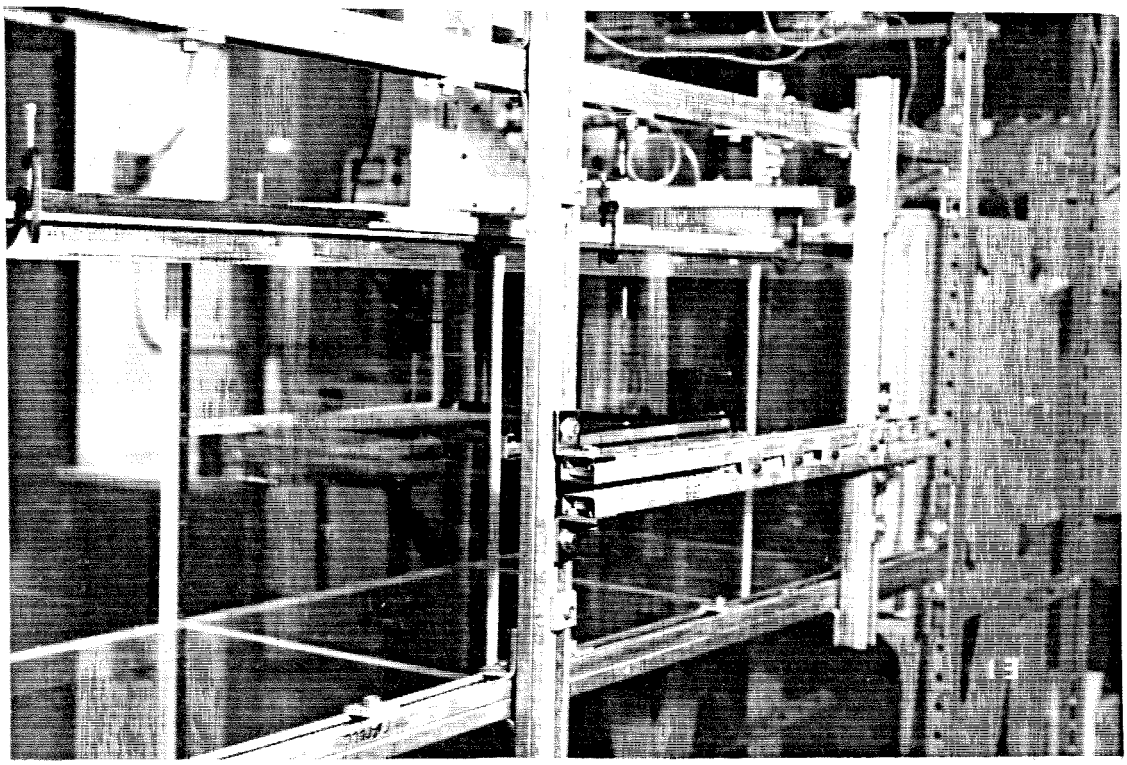

(b)

FIG. 2.1 Photos of the assembled test section with the cylinder, endplates, and a permeable splitter plate installed. (a) Front view, (b) Rear view showing the frame used for tensioning the permeable splitter plates.

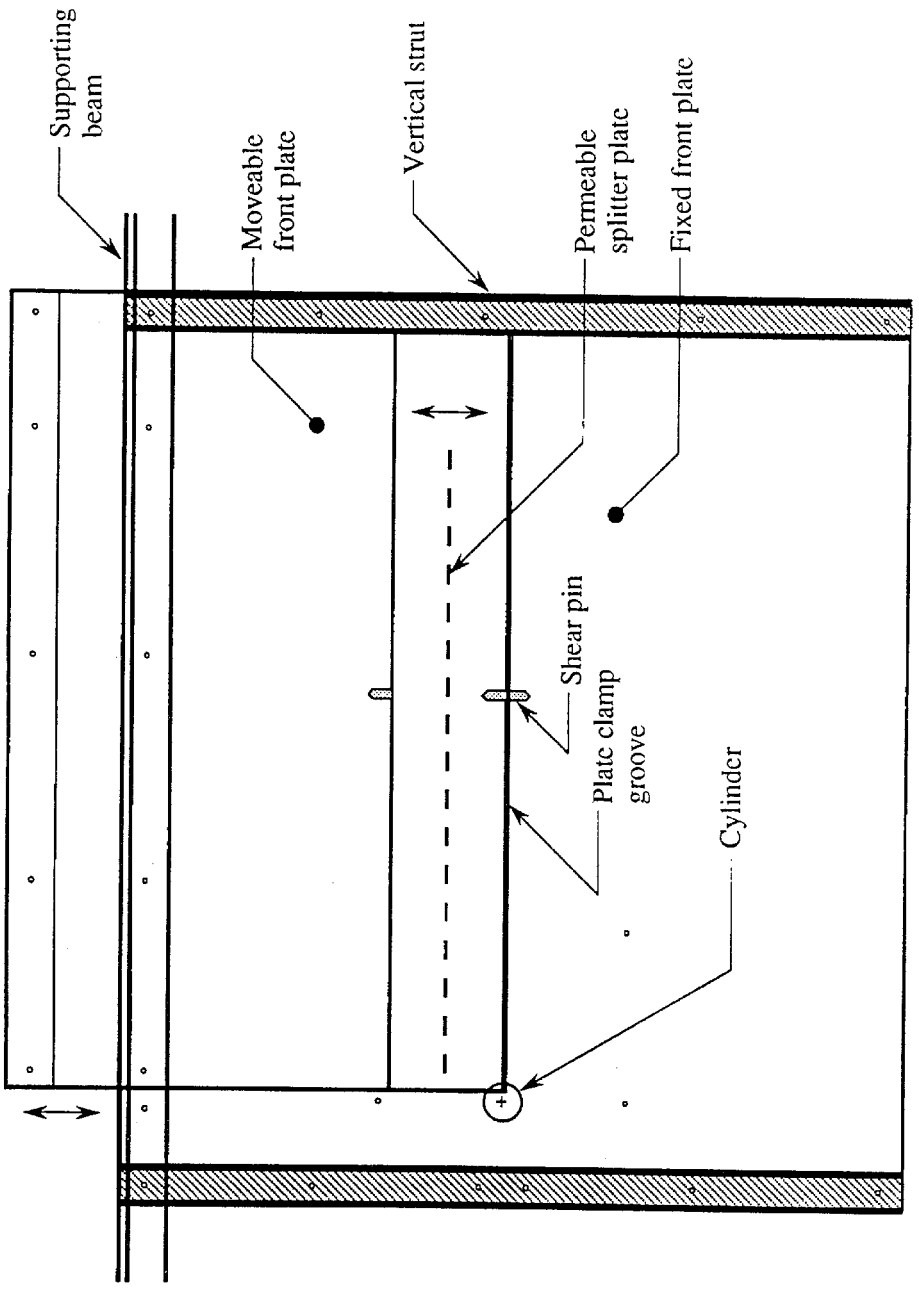

FIG. 2.2 Sketch of the test section front center panel, showing the fixed plate, the removeable plate, the vertical reinforcing struts, and the shear pin.

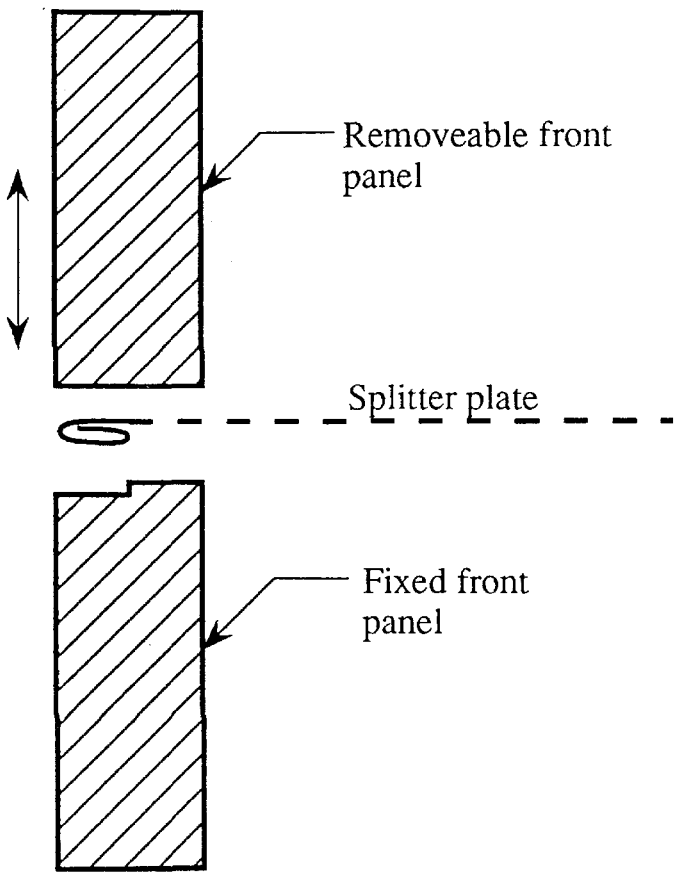

FIG. 2.3 Sketch showing how splitter plates are clamped in the front wall of the test section.

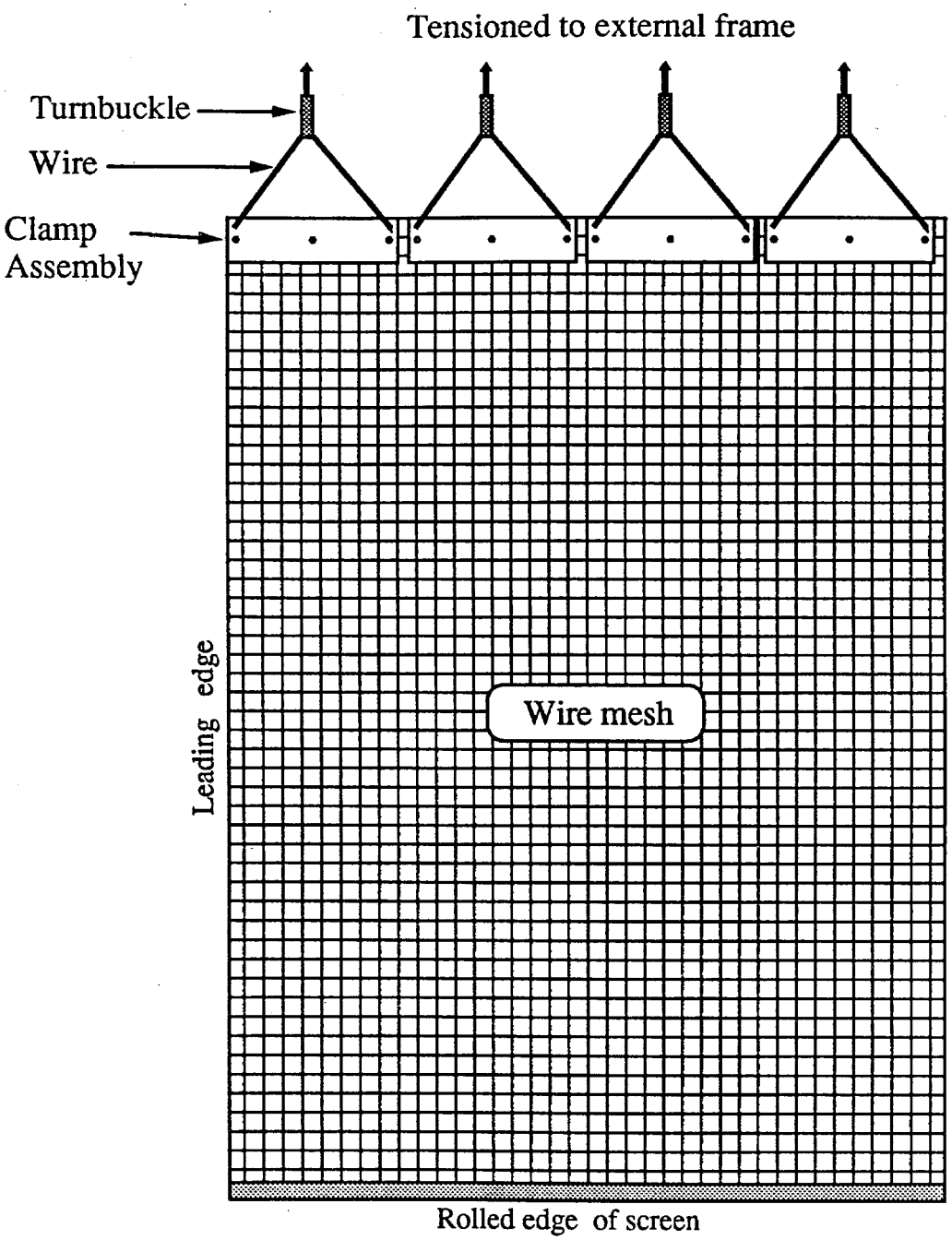

FIG. 2.4 Top view sketch of an assembled splitter plate showing the layout of the aluminum clamps used for tensioning the splitter plates.

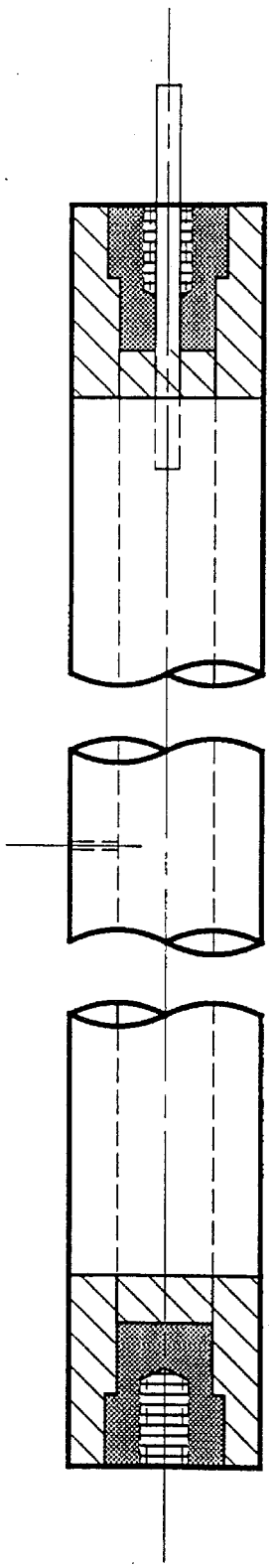

FIG.2.5 Sketch of a cylinder model, with cross-sectional views of the cylinder end plugs.

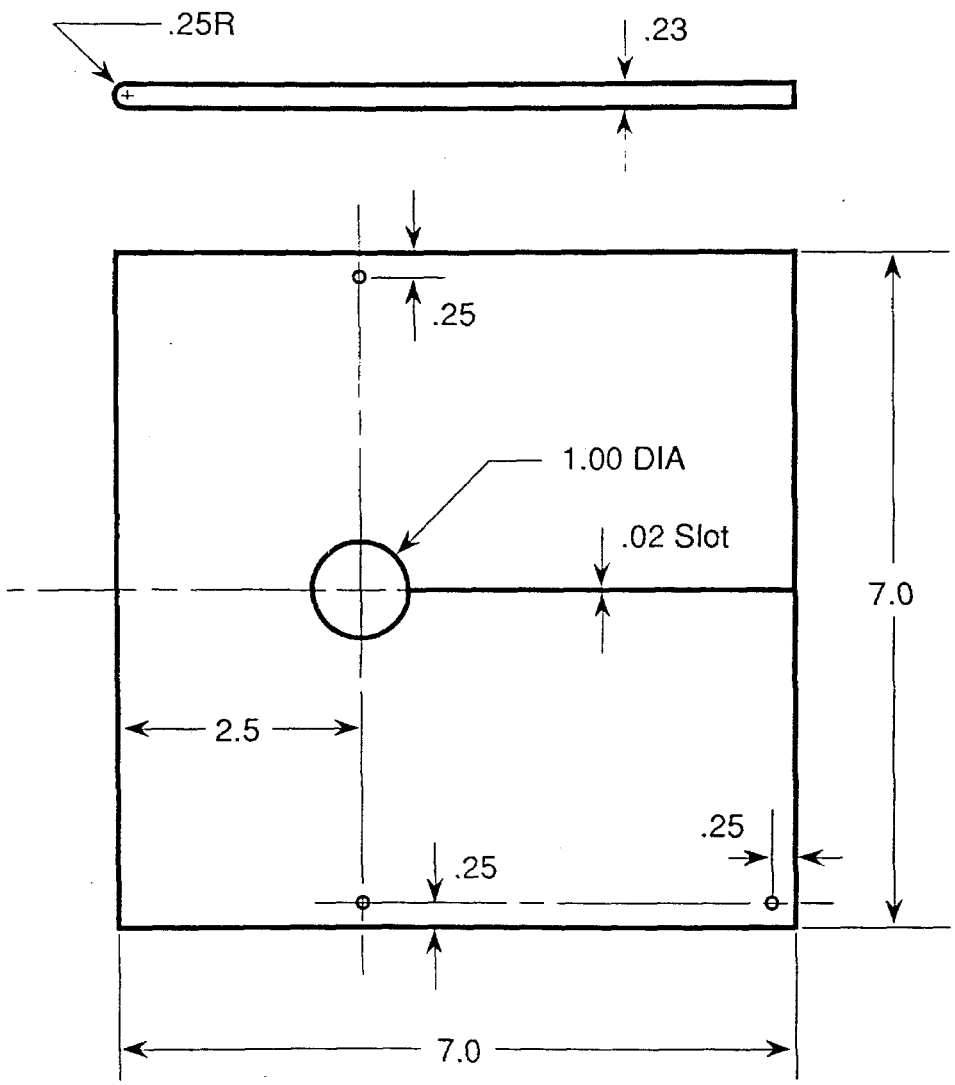

FIG. 2.6 Sketch of end plate layout and the end plate leading edge profile. Dimensions are in cylinder diameters.

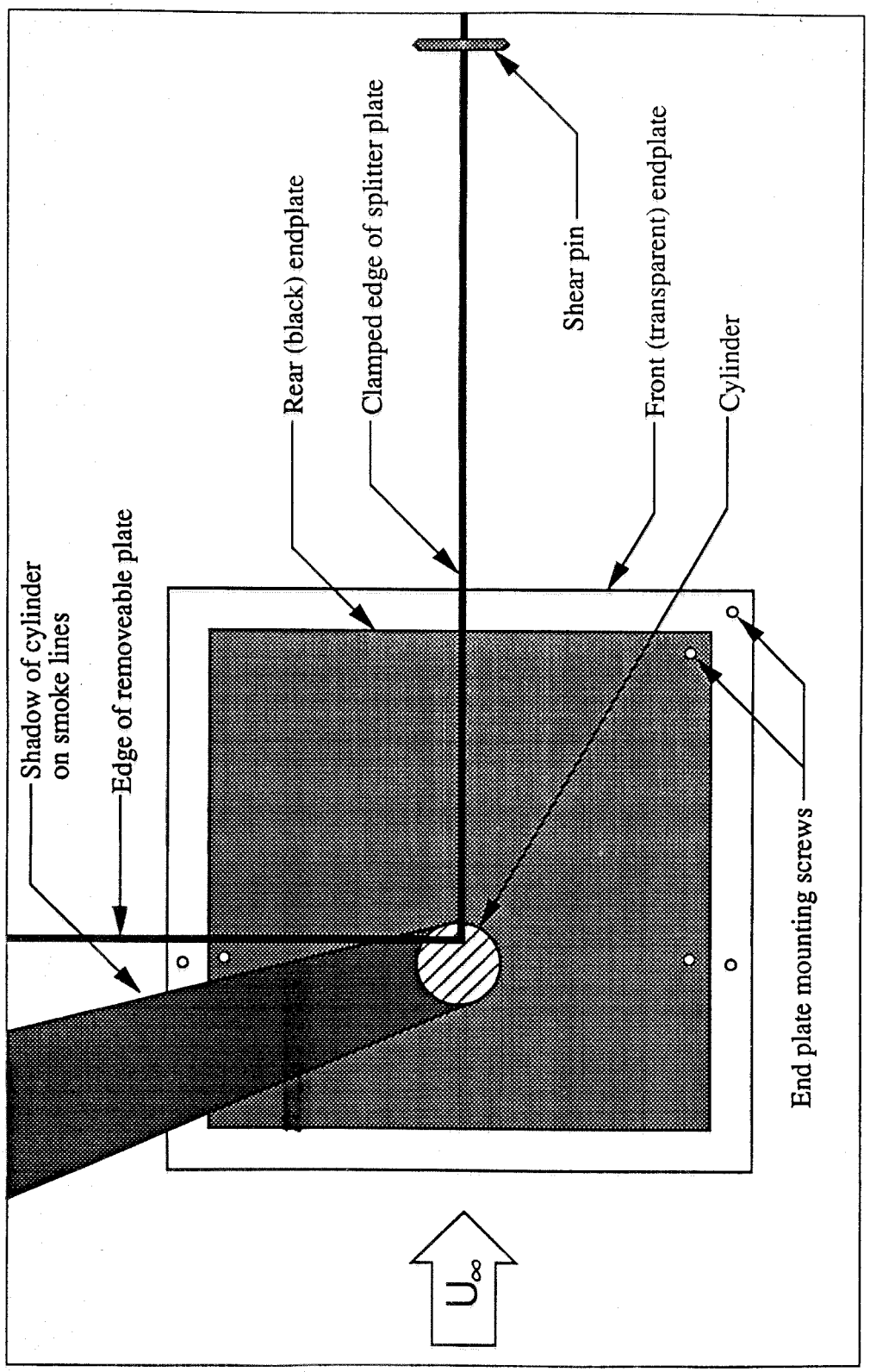

FIG. 3.1 Diagram of the flow-visualization photographs showing the location of the cylinder, cylinder end plates, and the splitter plate. The smoke wire itself is not visible in any of the photographs, and the cylinder is mounted so that it is seen in cross-section. The black region at the upper left is the shadow cast by the cylinder on the smoke lines.

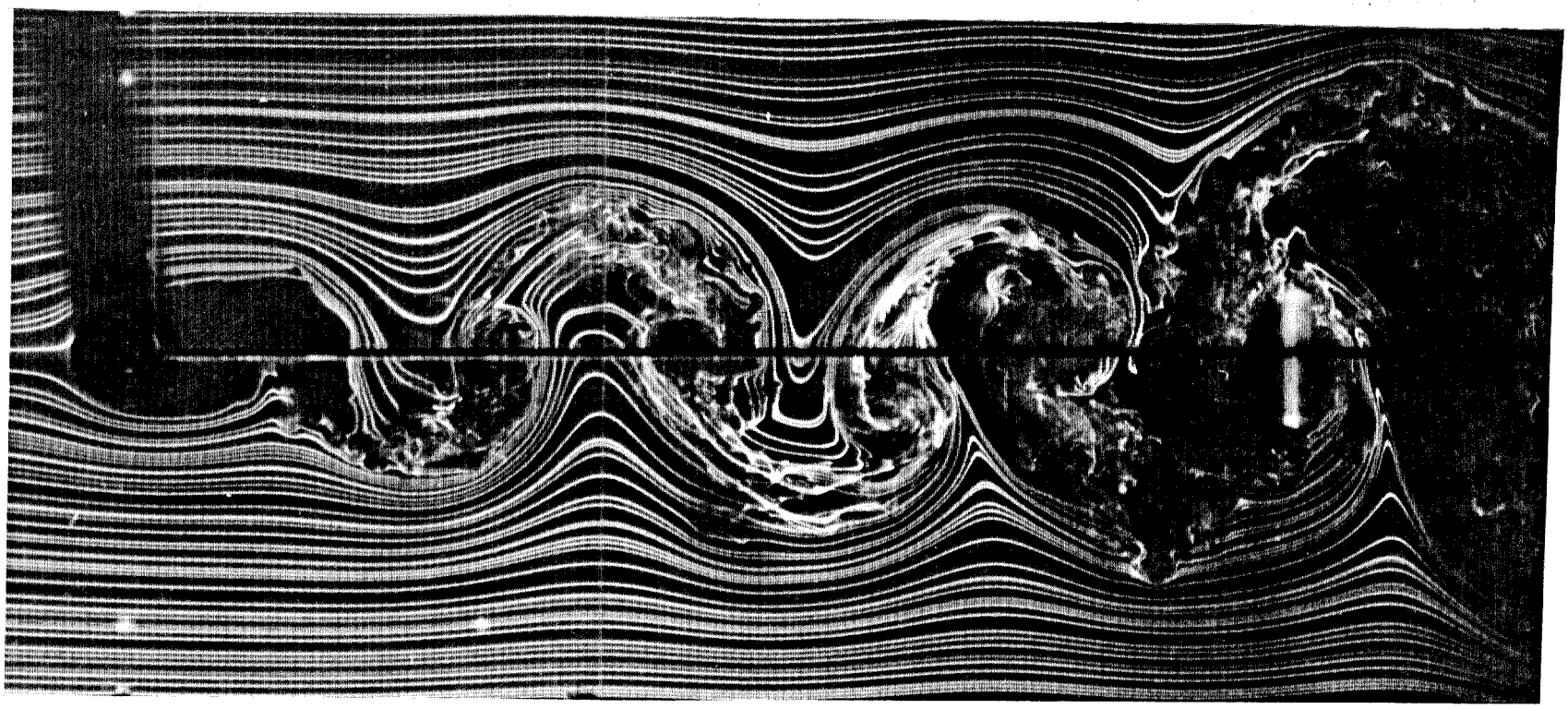

(a) $\sigma = 0$

FIG.3.2 Comparison of the flow past a circular cylinder fitted with different permeable splitter plates, Re = 7100, smoke wire flow visualization *(figure continues on next page)*.

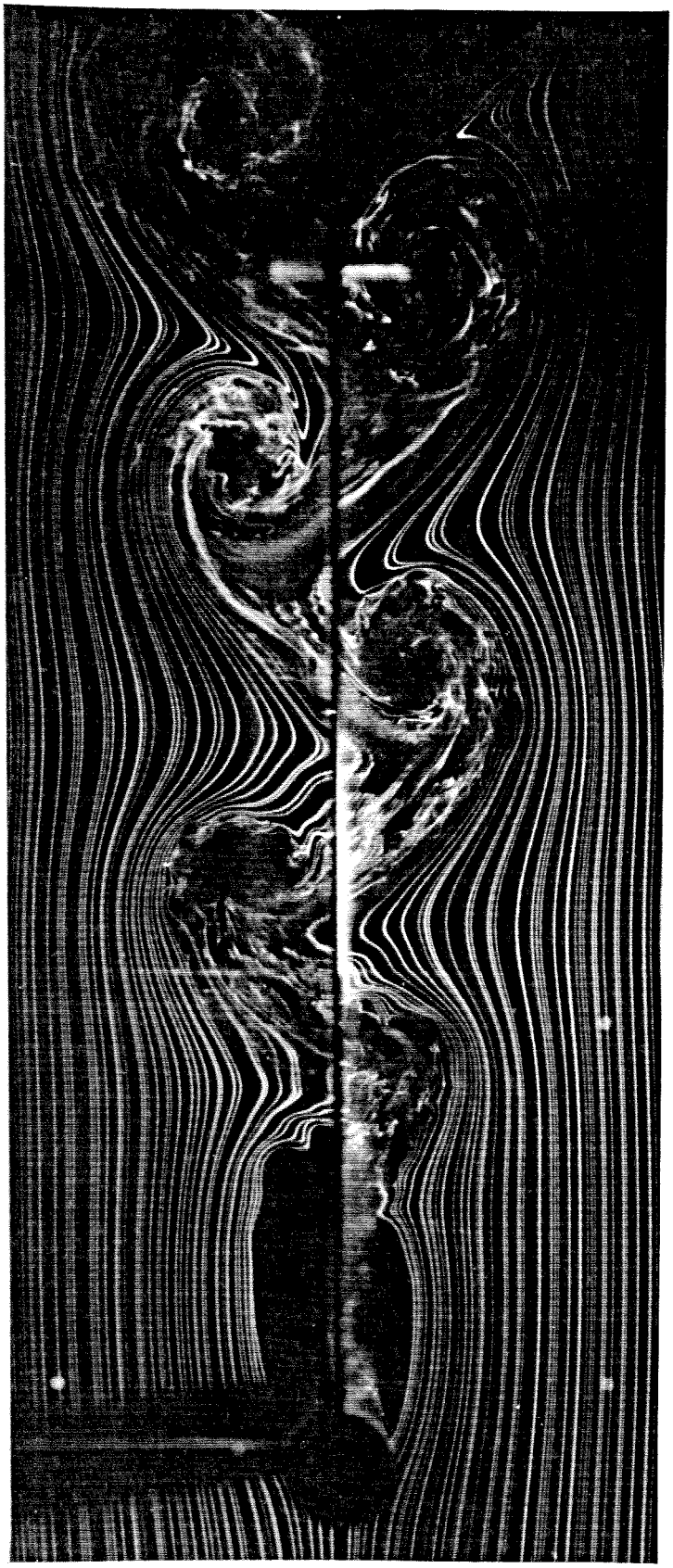

FIG.3.2b $\sigma = 0.22$, $\mathrm{Re} = 7100$ *(figure continues on next page).*

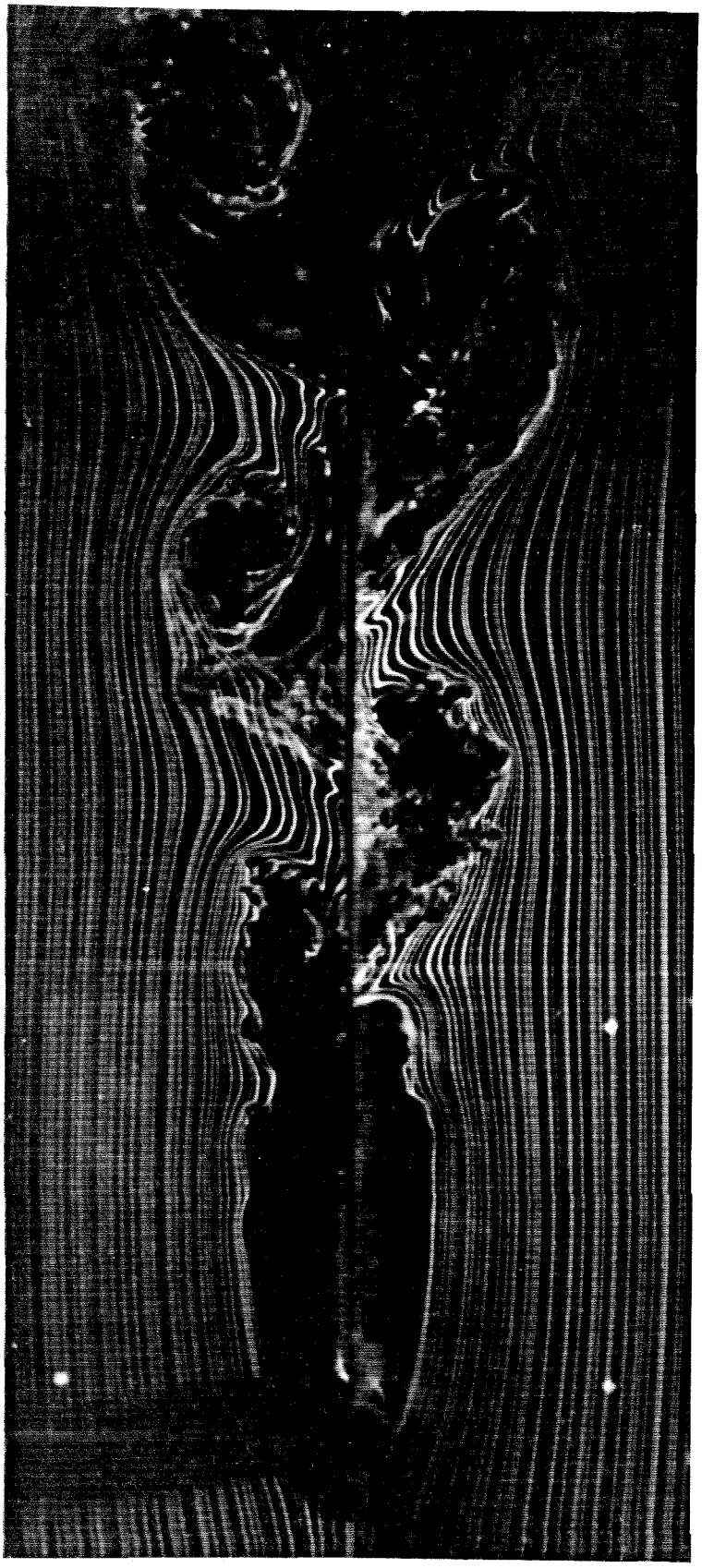

FIG. 3.2c $\sigma = 0.49$, $\mathrm{Re} = 7100$.

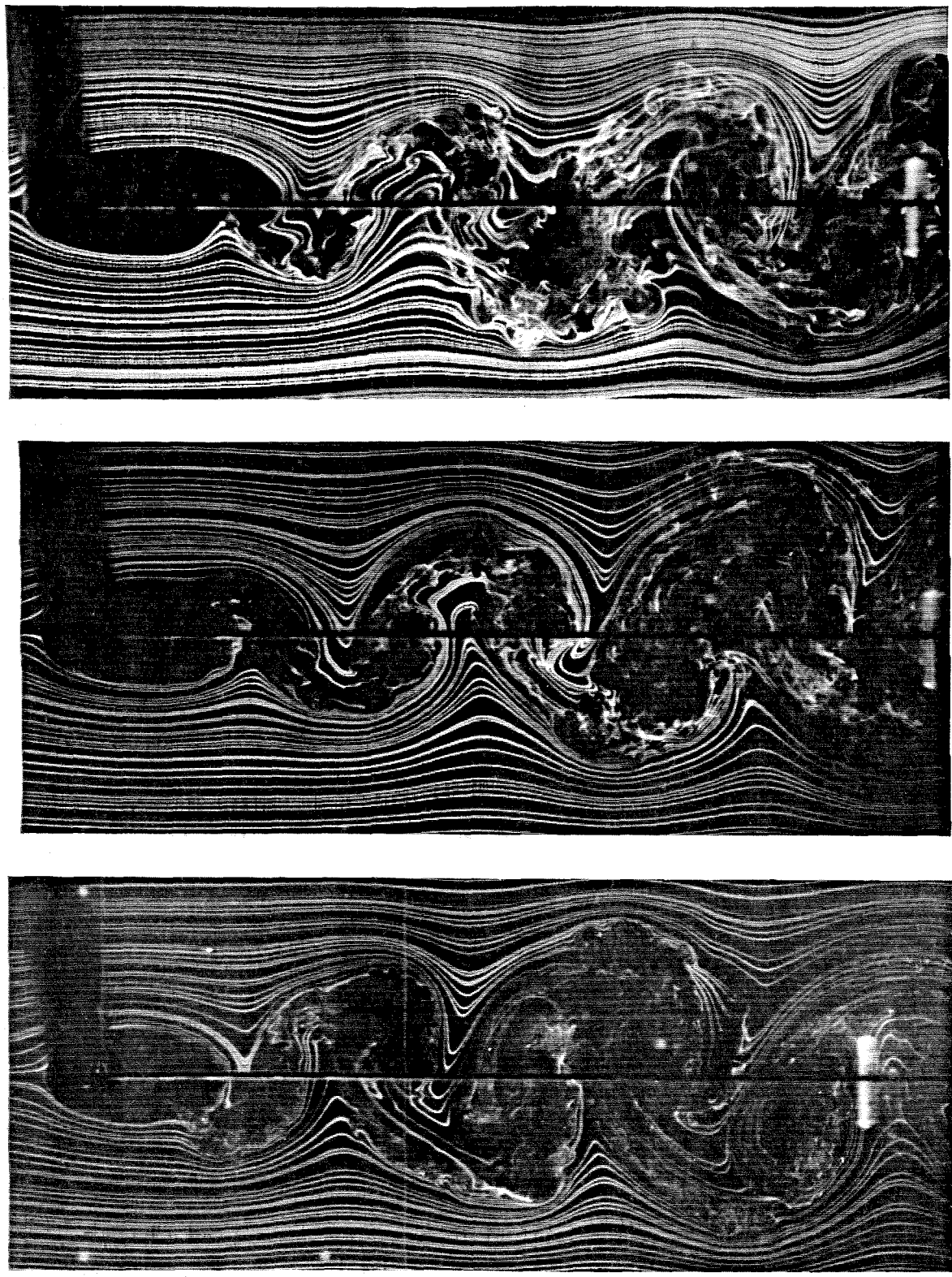

FIG. 3.3 Smoke wire visualization of the flow past a circular cylinder with no wake splitter plate, $\sigma = 0$: (a) Re = 2600, (b) Re = 5500, (c) Re = 8000.

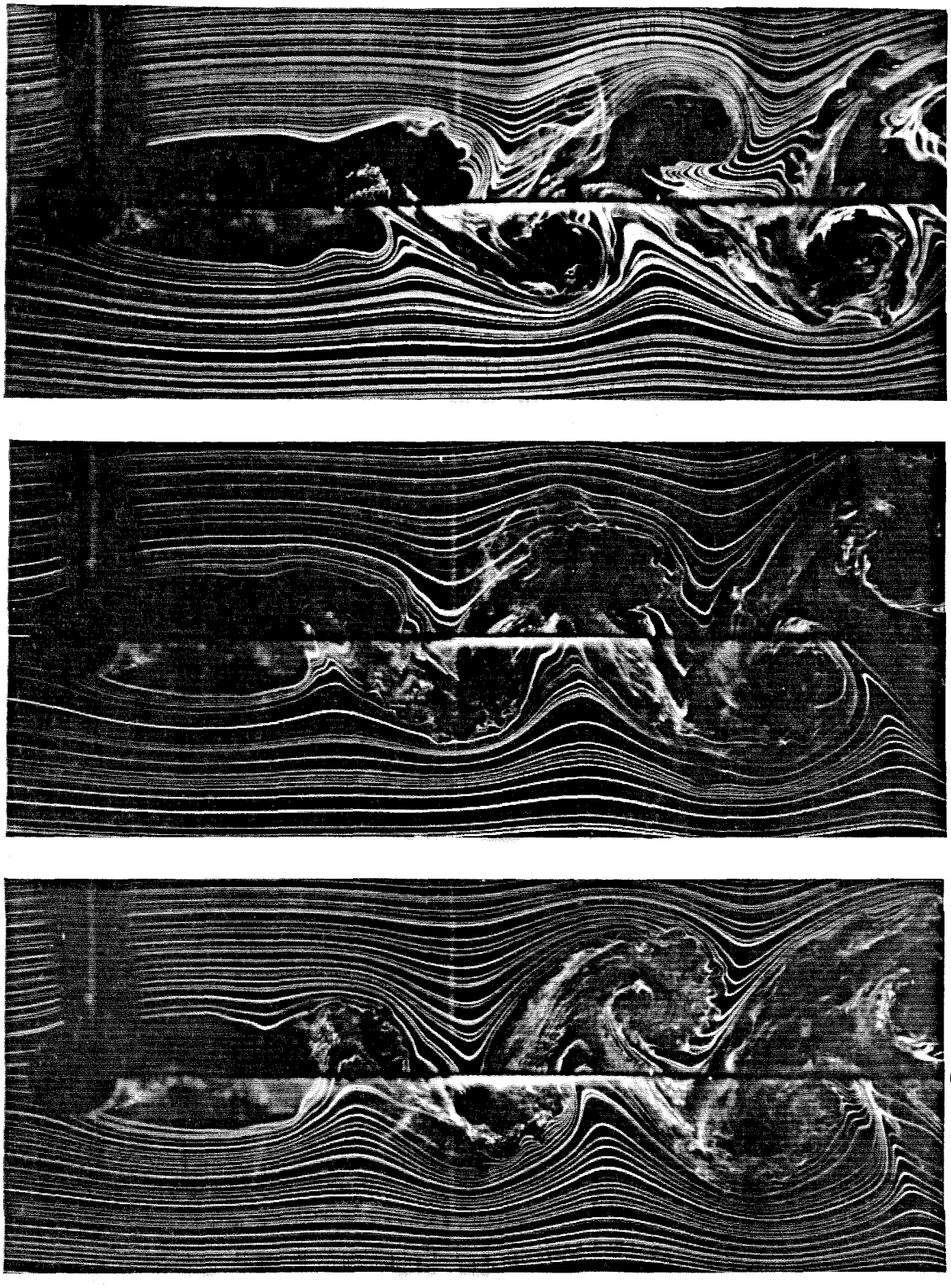

FIG. 3.4 Smoke wire visualization of the flow past a circular cylinder with a permeable splitter plate, $\sigma = 0.22$: (**a**) Re = 2500, (**b**) Re = 5500, (**c**) Re = 8000.

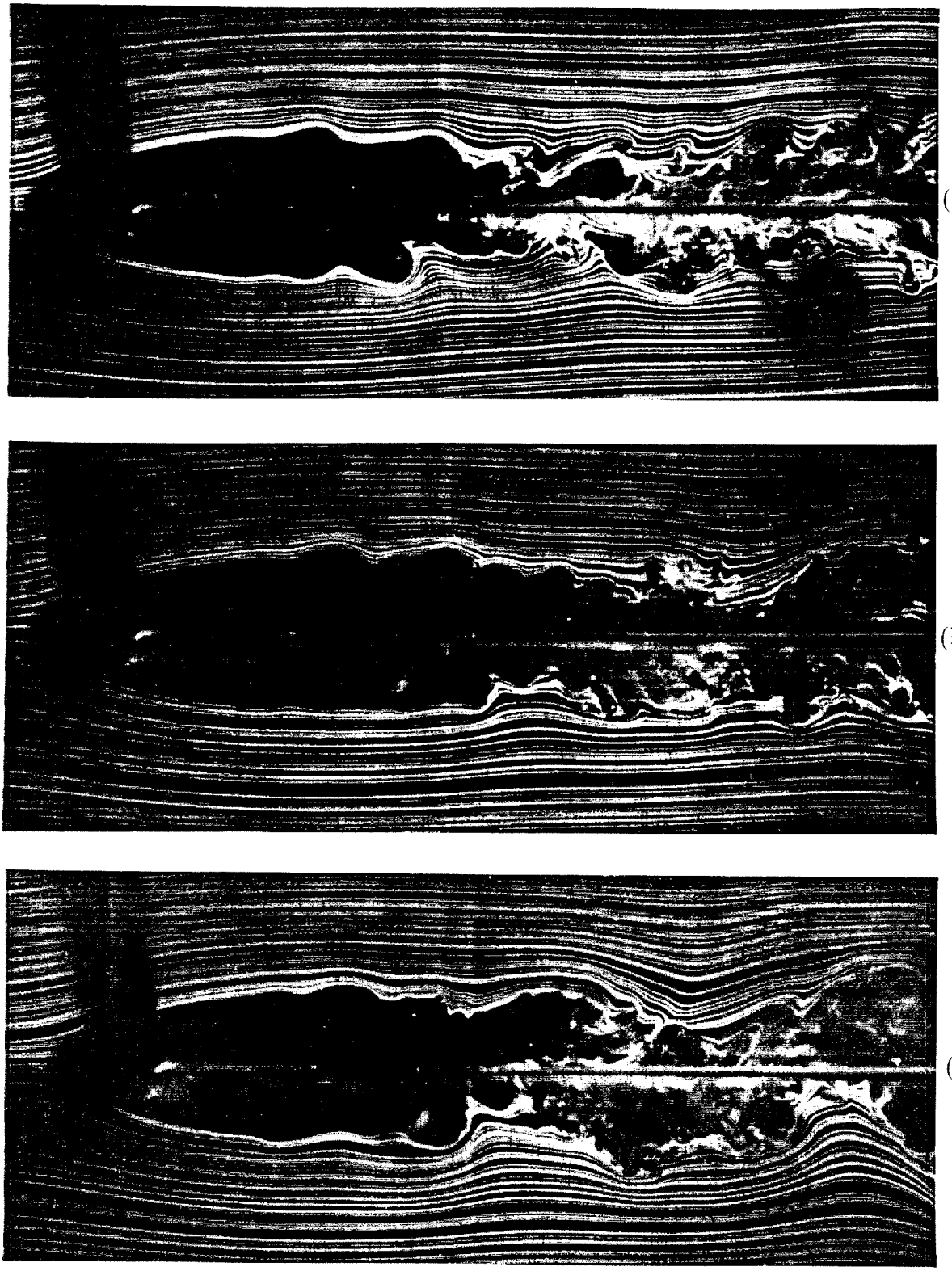

FIG. 3.5 Smoke wire visualization of the flow past a circular cylinder with a permeable splitter plate, $\sigma = 0.49$: (**a**) Re = 2500, (**b**) Re = 3900, (**c**) Re = 5600 *(figure continues on next page).*

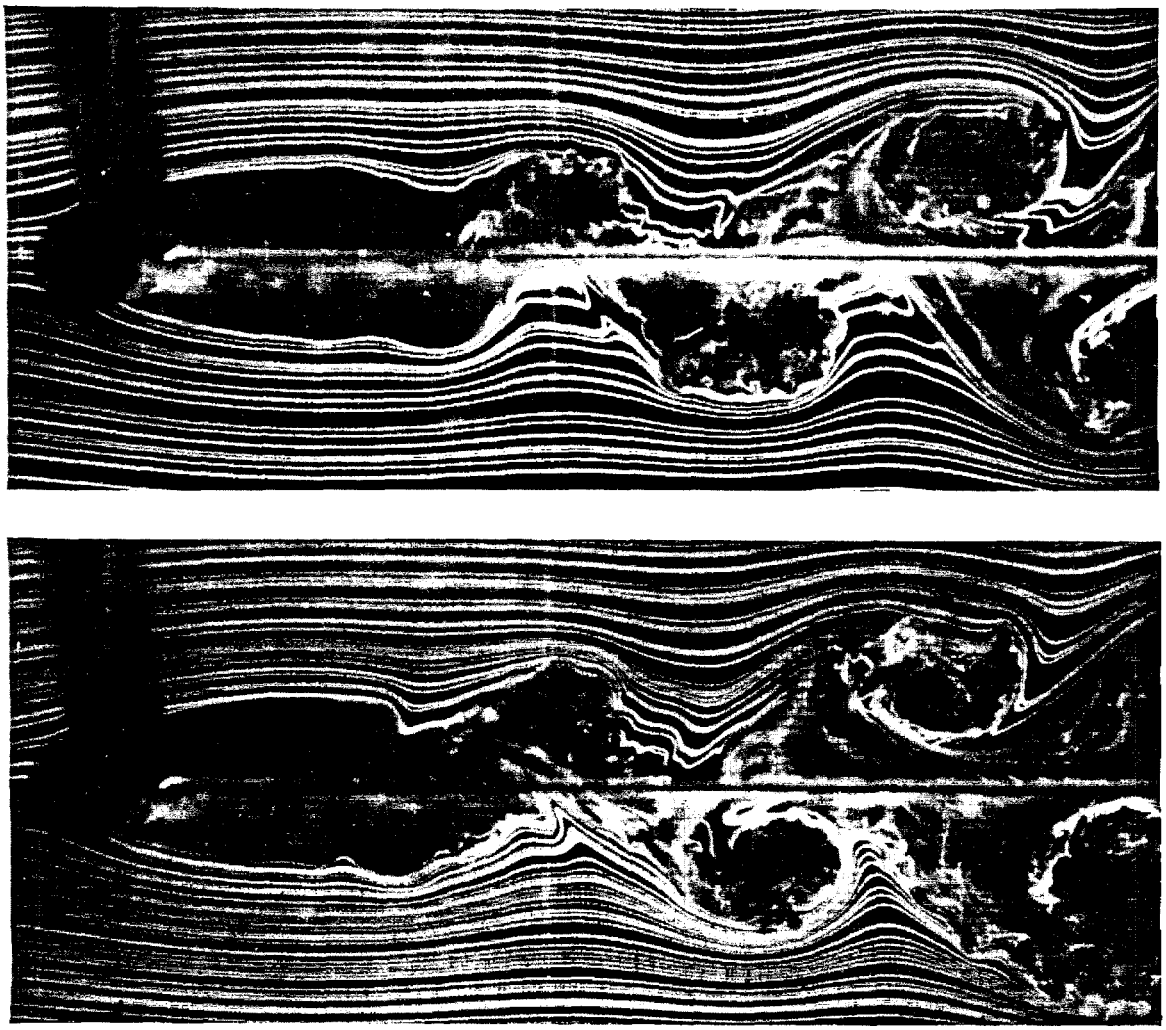

FIG. 3.5 *cont.* (**d**) Re = 7100, (**e**) Re = 7900.

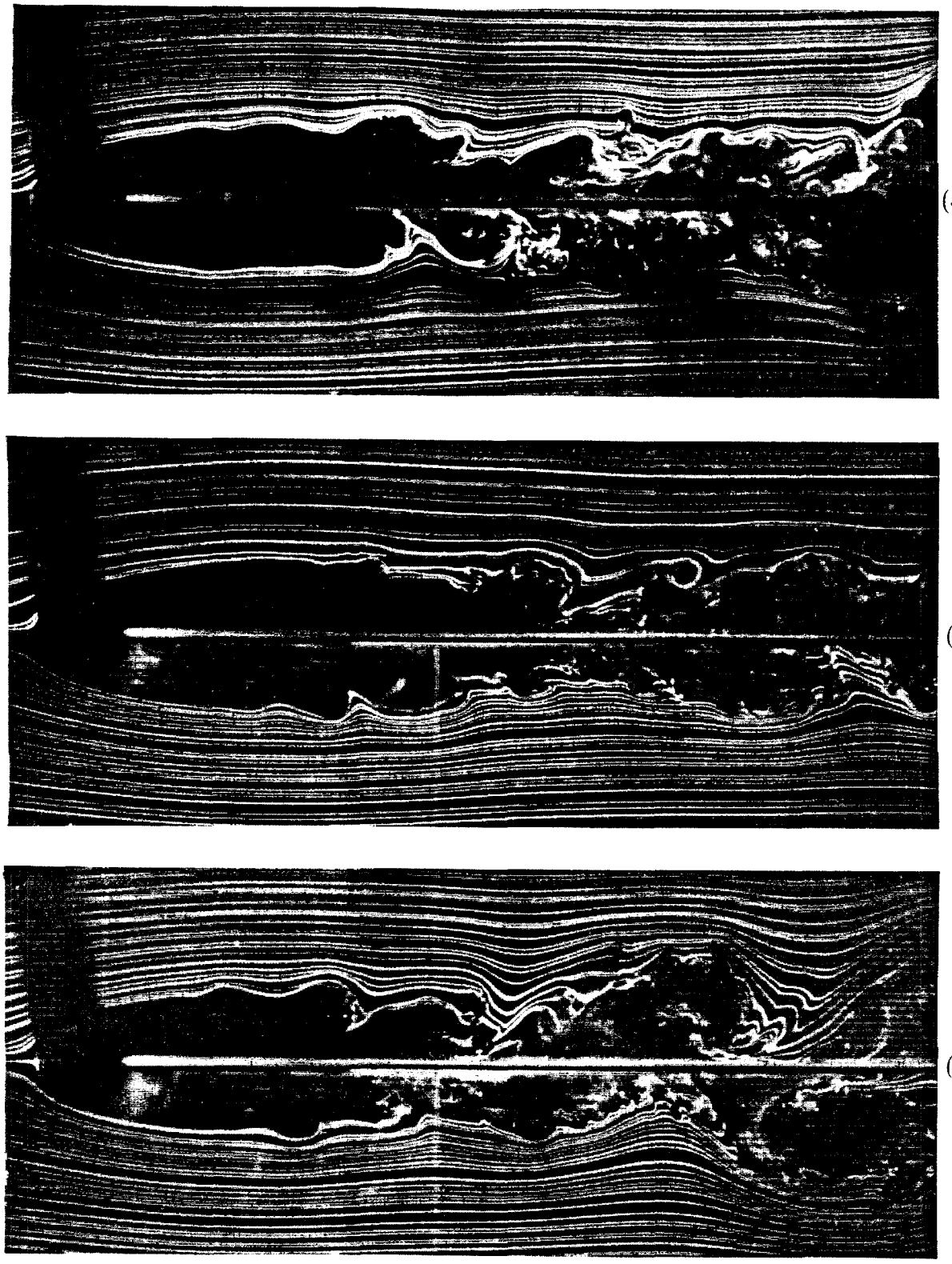

FIG. 3.6 Smoke wire visualization of the flow past a circular cylinder with a permeable splitter plate, $\sigma = 0.65$: (**a**) Re = 2600, (**b**) Re = 5500, (**c**) Re = 7900.

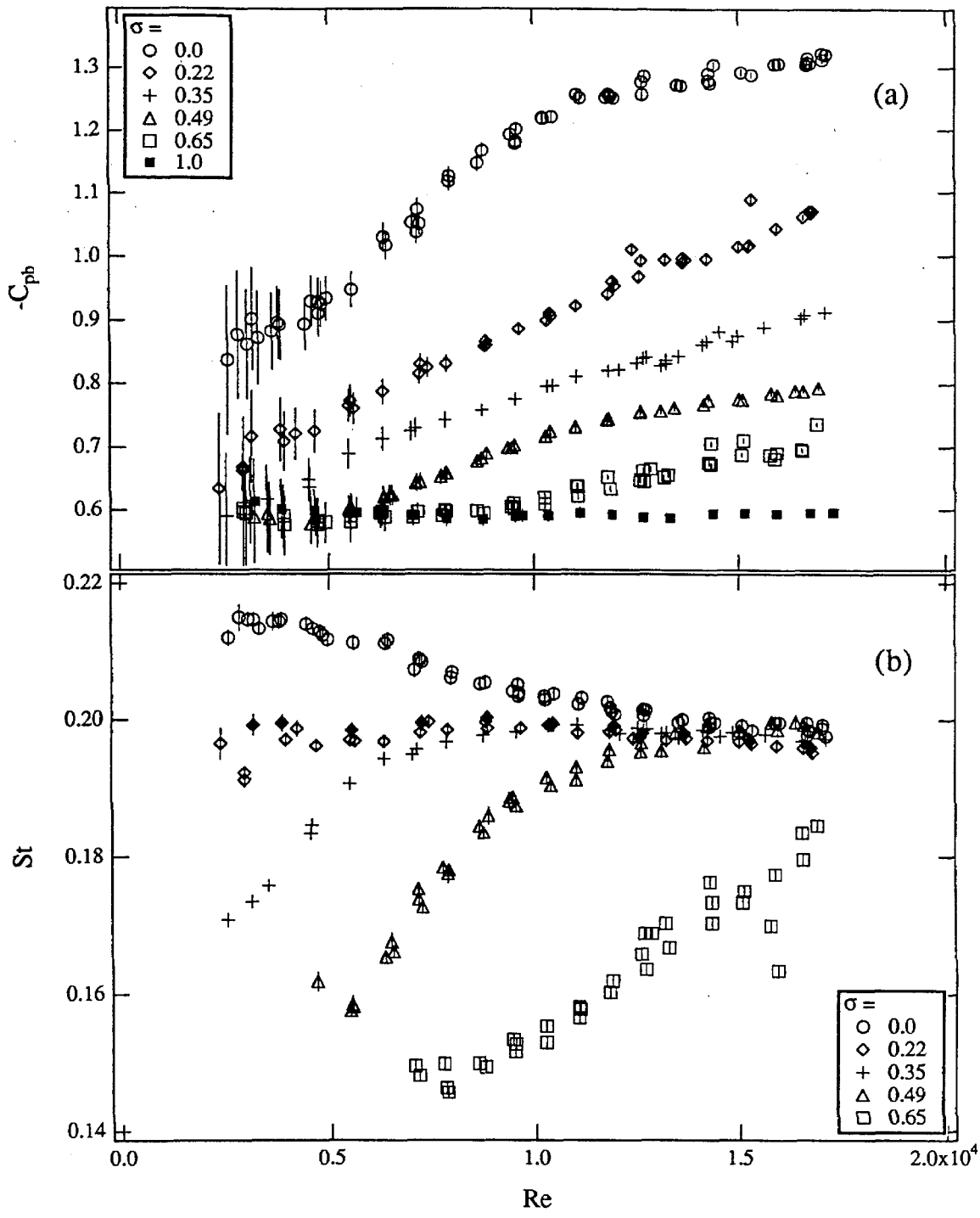

FIG. 4.1 Global near wake parameters as functions of Reynolds number for all of the 'standard' splitter plates; (**a**) Base suction coefficient $-C_{pb}$, (**b**) Strouhal number St.

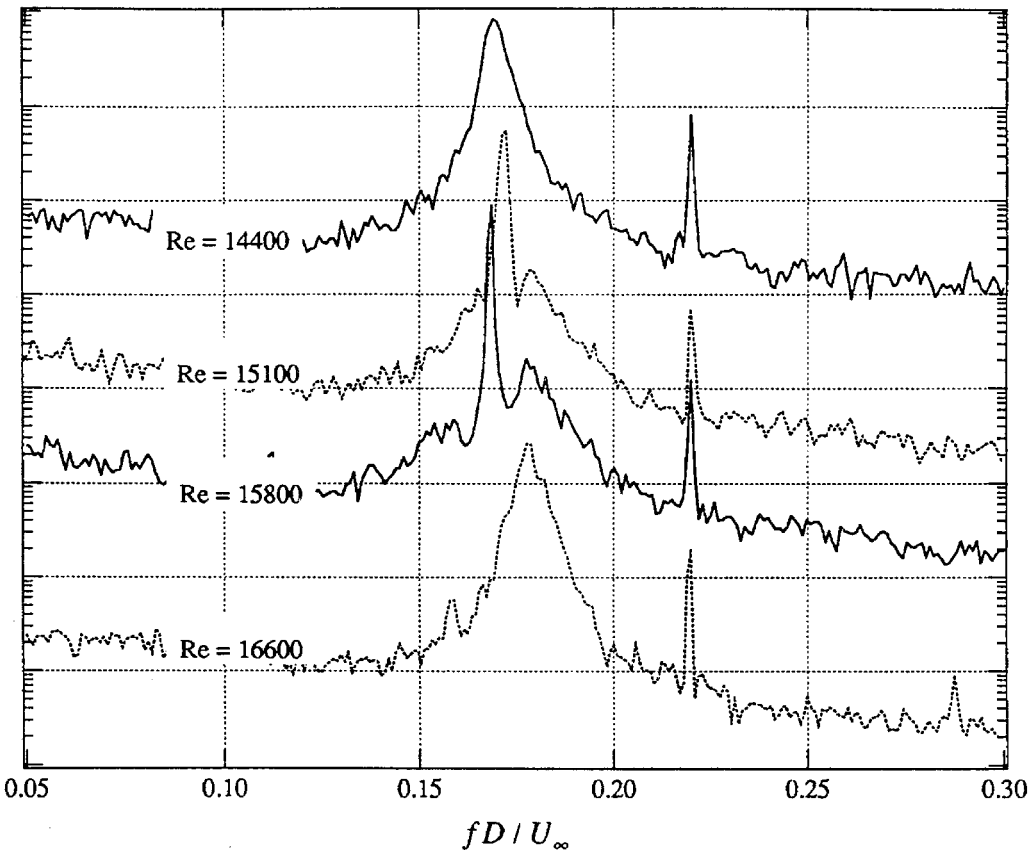

FIG. 4.2 Power spectra corresponding to the anomalous values of St measured with a permeable splitter plate of solidity $\sigma = 0.65$ in the wake, computed from the hot-wire voltage signal. The two spectra marked Re = 15100 and 15800 correspond to the anomalous St values, and exhibit much narrower peaks at the primary wake frequencies than the other spectra taken at Re = 14400 and 16600. Spectra are offset vertically by varying amounts to allow the separate spectra to be distinguished.

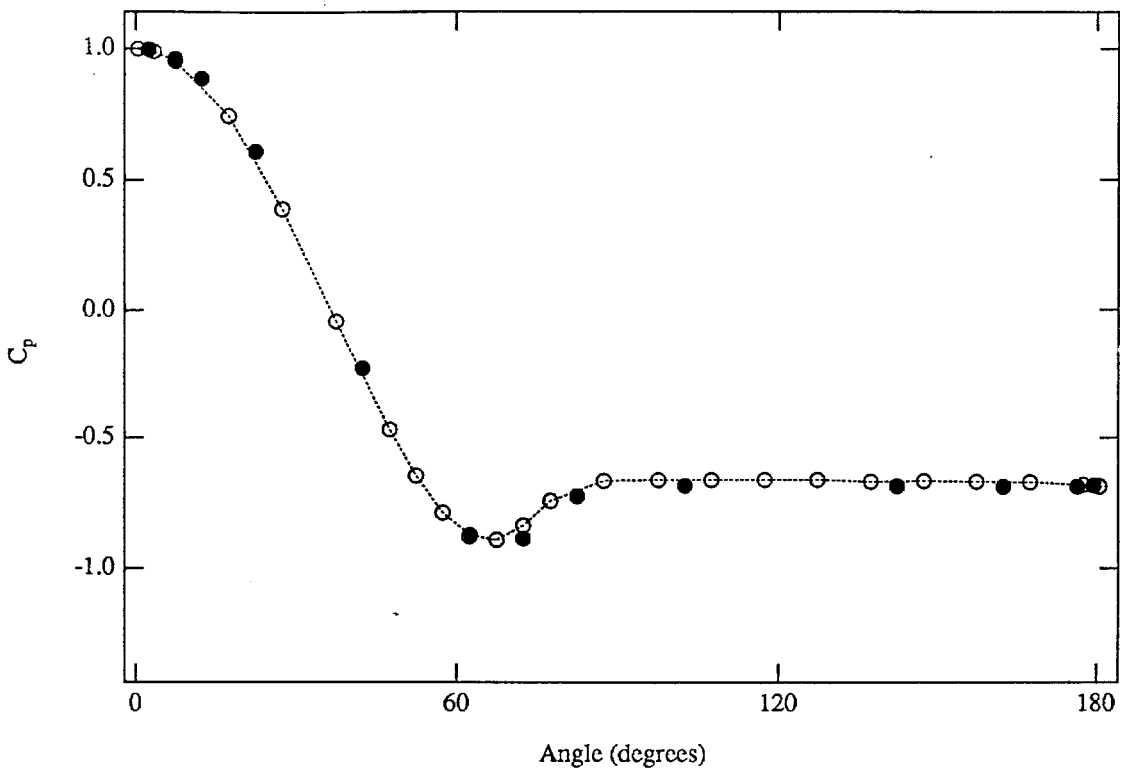

FIG. 4.3 Pressure coefficient profile, $\sigma = 0.65$, Re = 9600, with values for $-180 < \alpha < 0$ folded onto positive values, showing the symmetry of the profile. Solid symbols are for $\alpha < 0$.

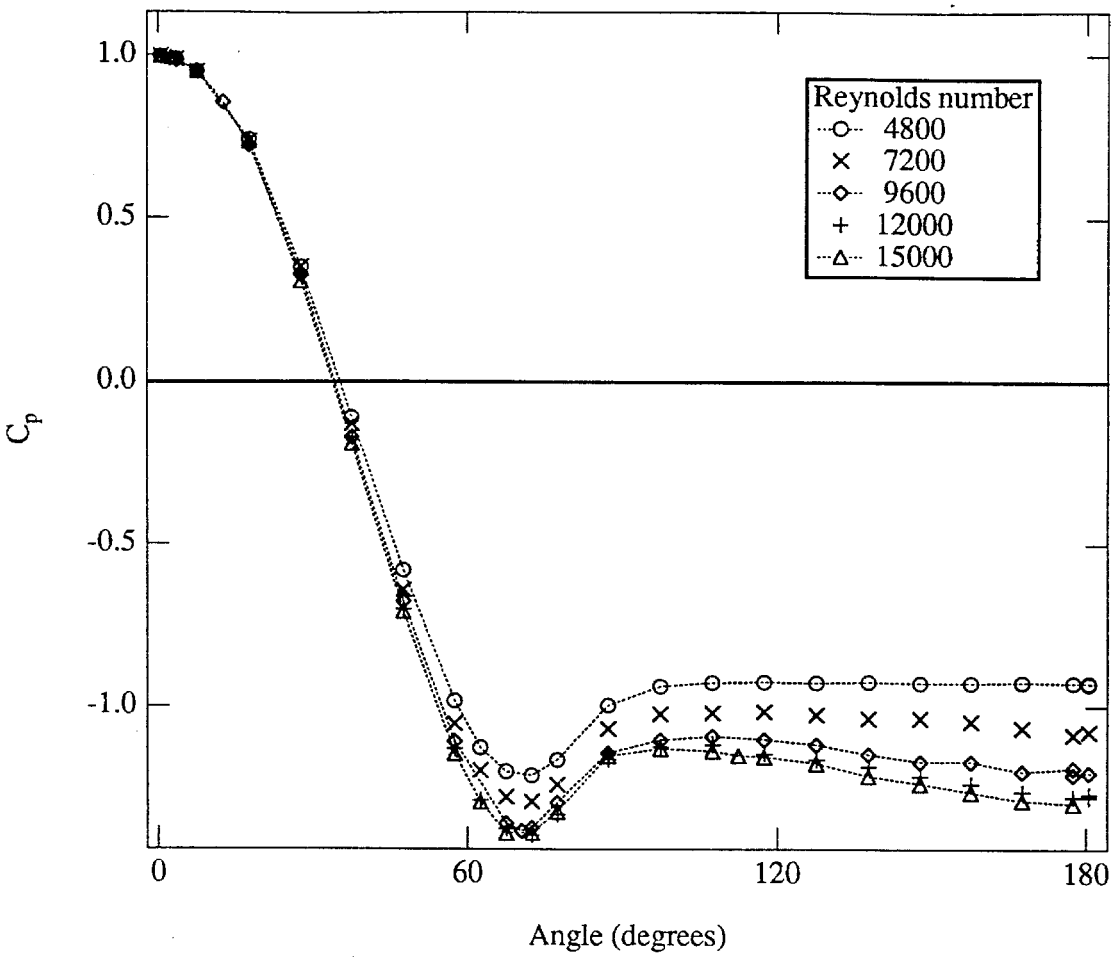

(a) $\sigma = 0$

FIG. 4.4 Surface pressure coefficient profiles $C_p(\alpha)$ *(figure continues on next page).*

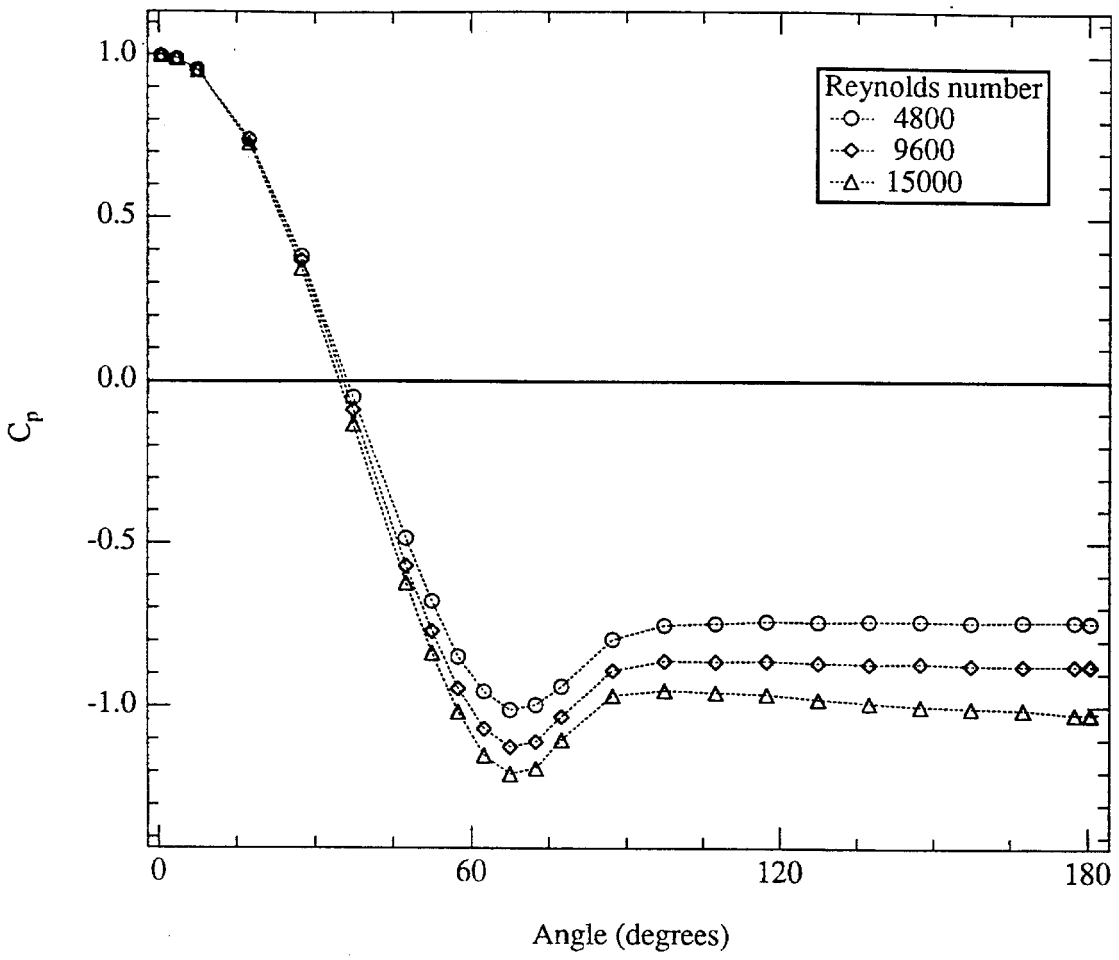

FIG. 4.4b $\sigma = 0.22$ *(figure continues on next page).*

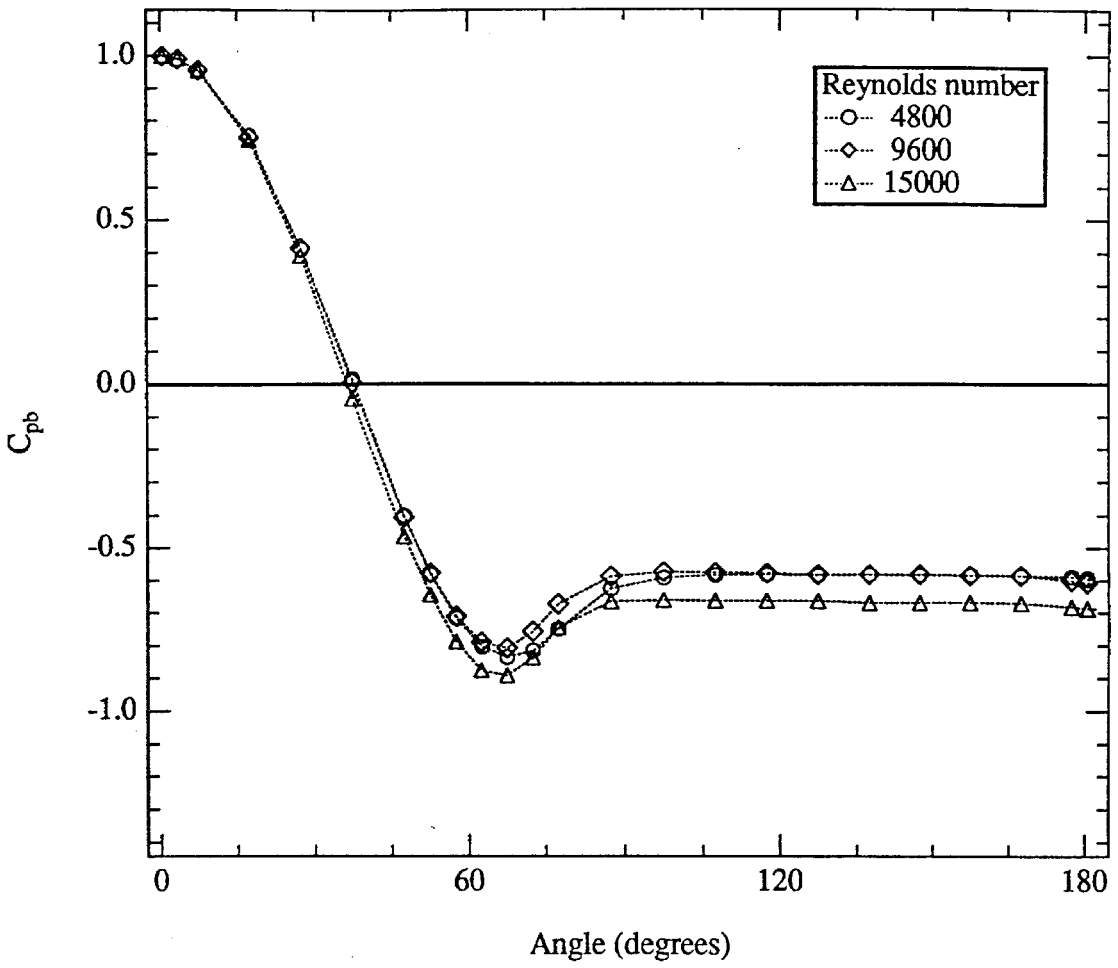

FIG. 4.4c $\sigma = 0.65$.

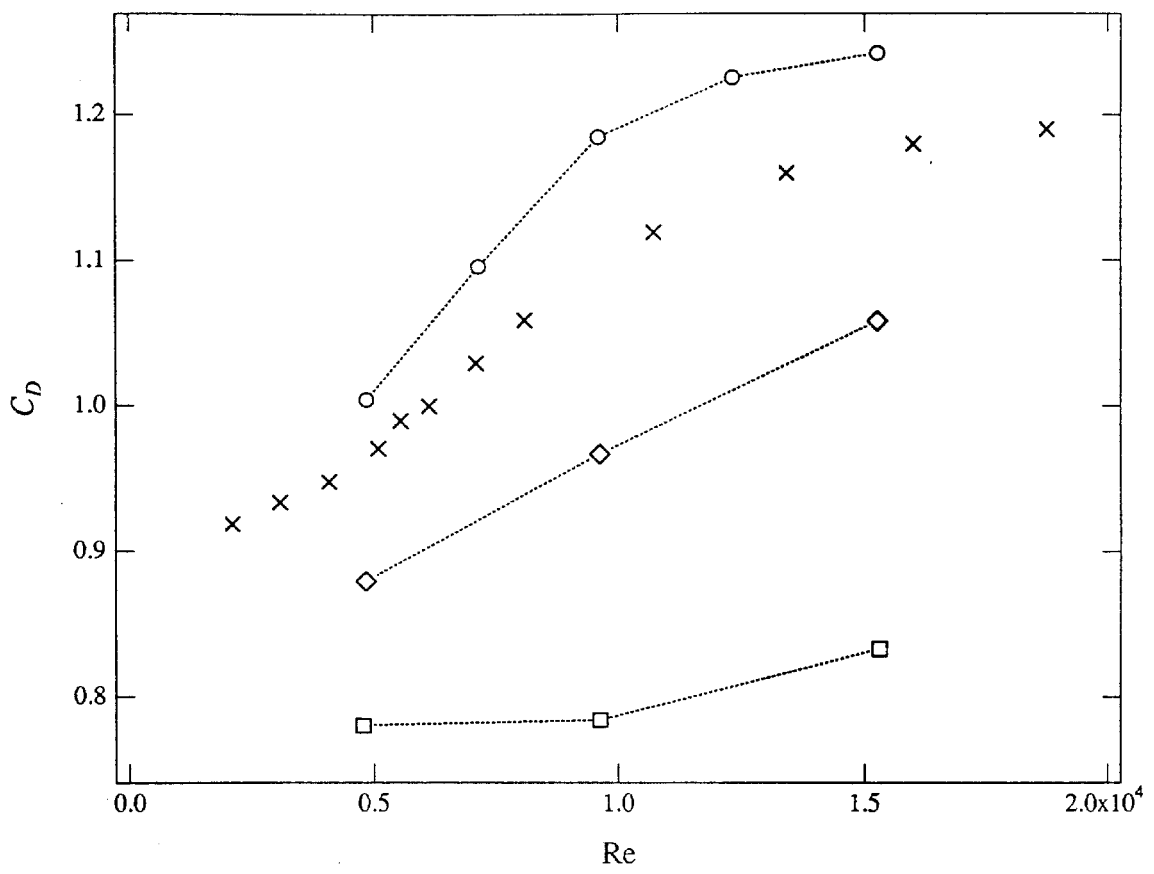

FIG. 4.5 Pressure drag coefficients versus Reynolds number, computed from cylinder surface pressure profiles: (o) $\sigma = 0$, ($\diamond$) $\sigma = 0.22$, ($\square$) $\sigma = 0.65$, ($\times$) Classical data from Wieselsberger (1922).

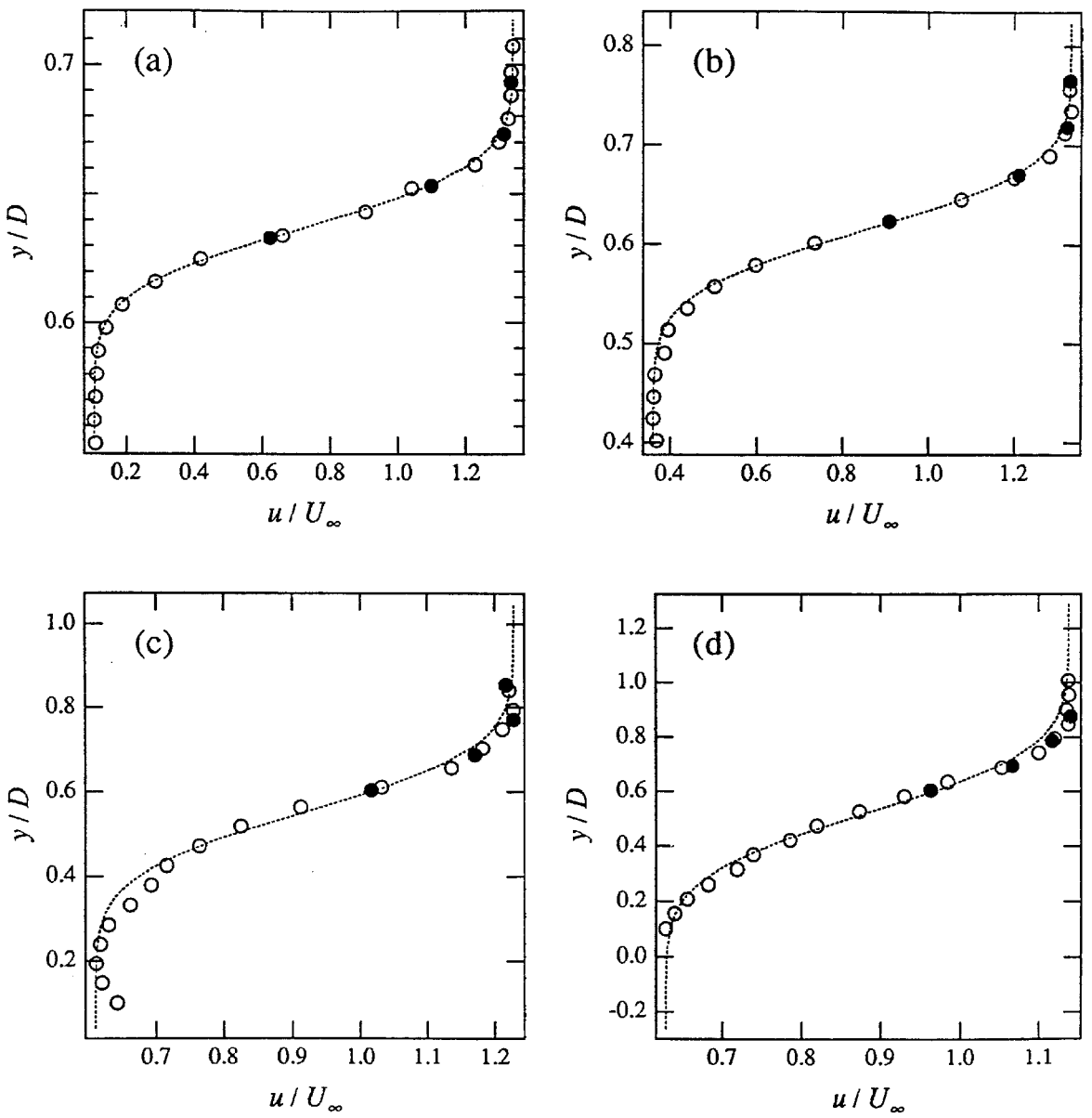

FIG. 5.1 Example Shear layer profiles, $\sigma = 0.22$, Re = 9300. Symbols are; (○) mean velocities from data collected to obtain the mean shear layer profile; (●) mean velocities from high-resolution data collected for computations of power spectra; (· · ·) fit profile computed from the mean shear layer profile. The different parts of the figure show data from different downstream positions: (**a**) $x/D = 0.7$, (**b**) $x/D = 1.3$, (**c**) $x/D = 1.7$, (**d**) $x/D = 2.0$.

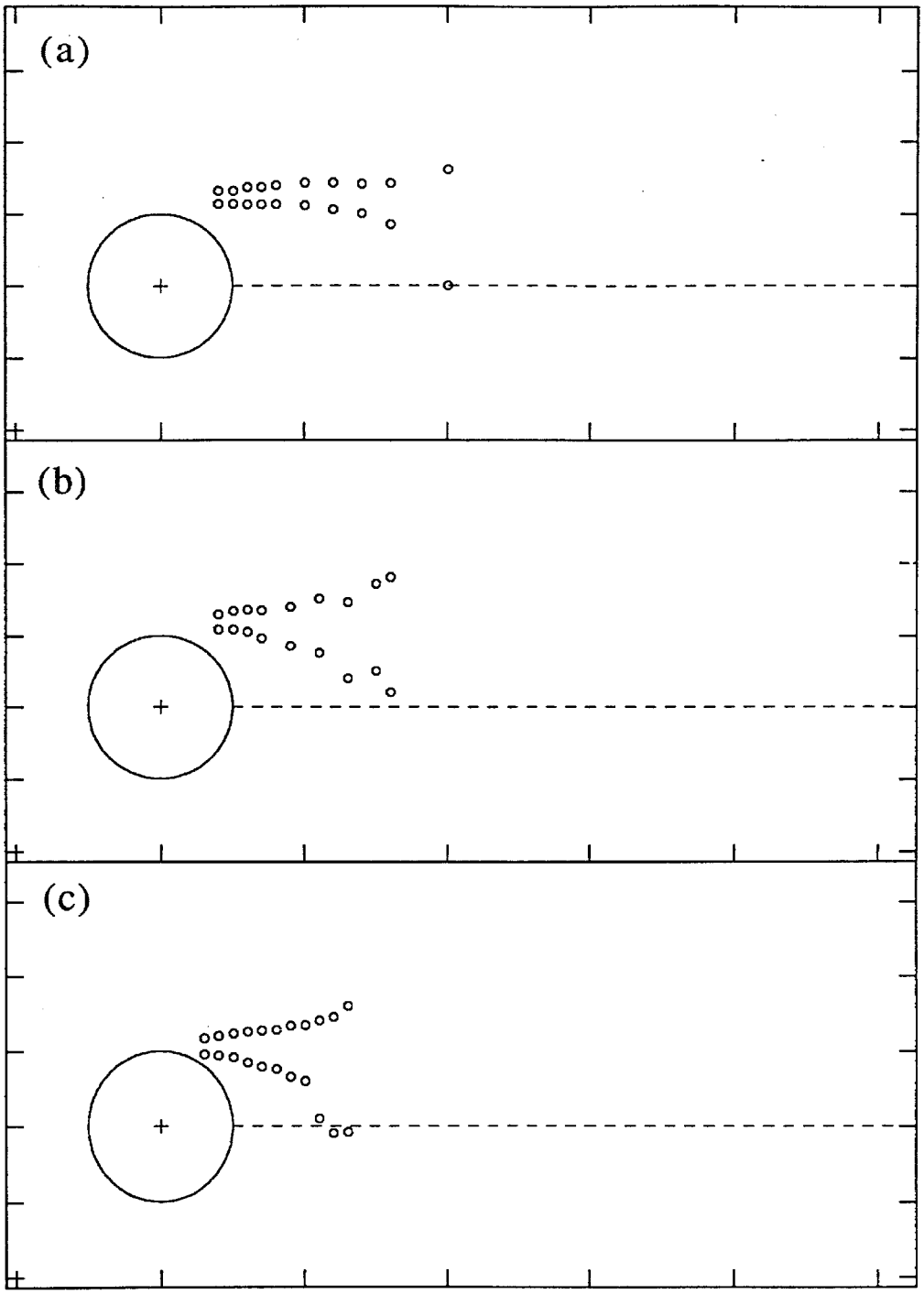

FIG. 5.2 Approximate locations in the shear layers where the velocity reaches 1% and 99% of the local velocity difference across the layers, plotted to scale: (**a**) $\sigma = 0$, Re = 4800, (**b**) $\sigma = 0$, Re = 9500, (**c**) $\sigma = 0$, Re = 15200 *(figure continues on next page).*

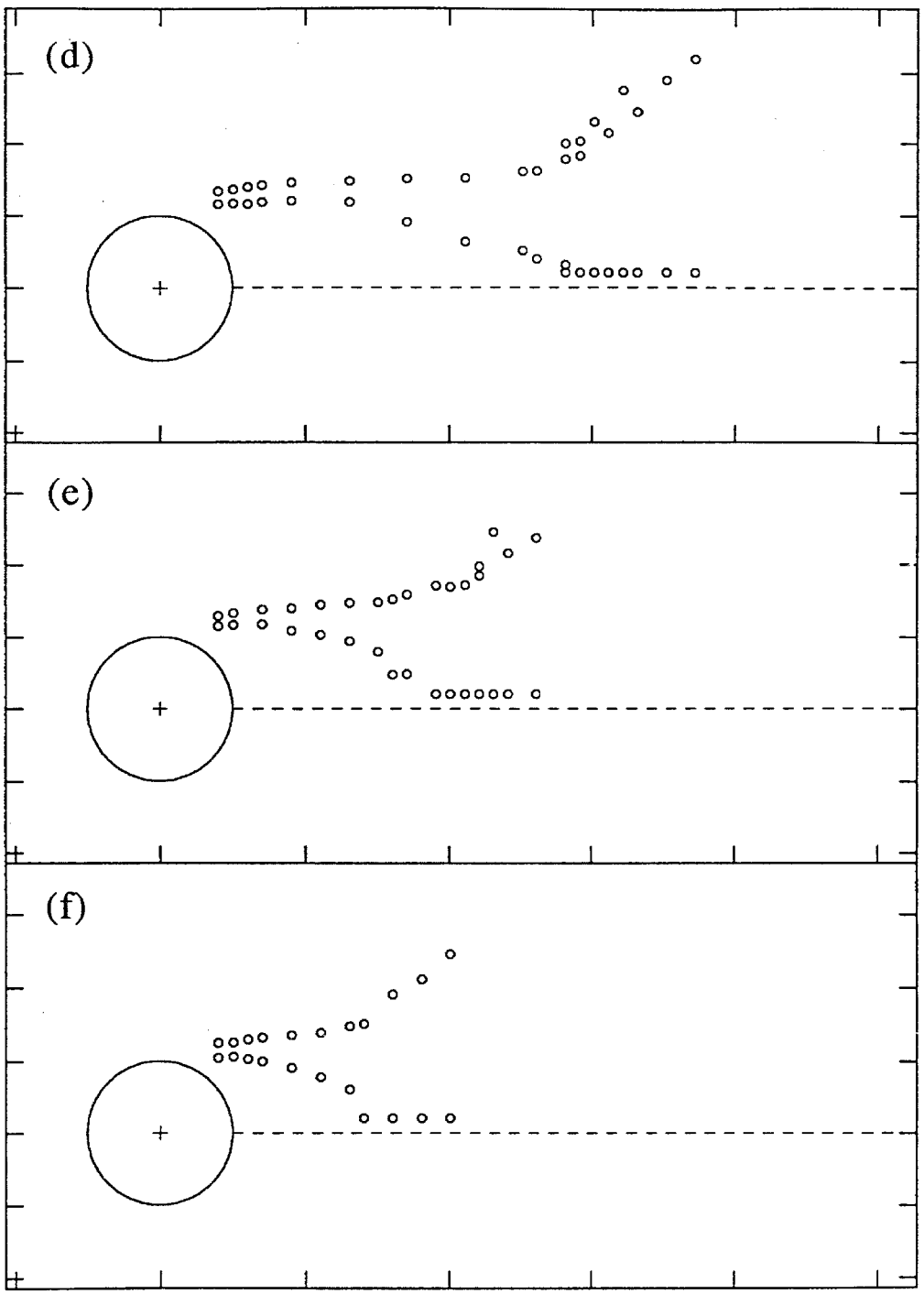

FIG. 5.2 *cont.* (**d**) $\sigma = 0.22$, Re = 4800, (**e**) $\sigma = 0.22$, Re = 9300, (**f**) $\sigma = 0.22$, Re = 15000 *(figure continues on next page).*

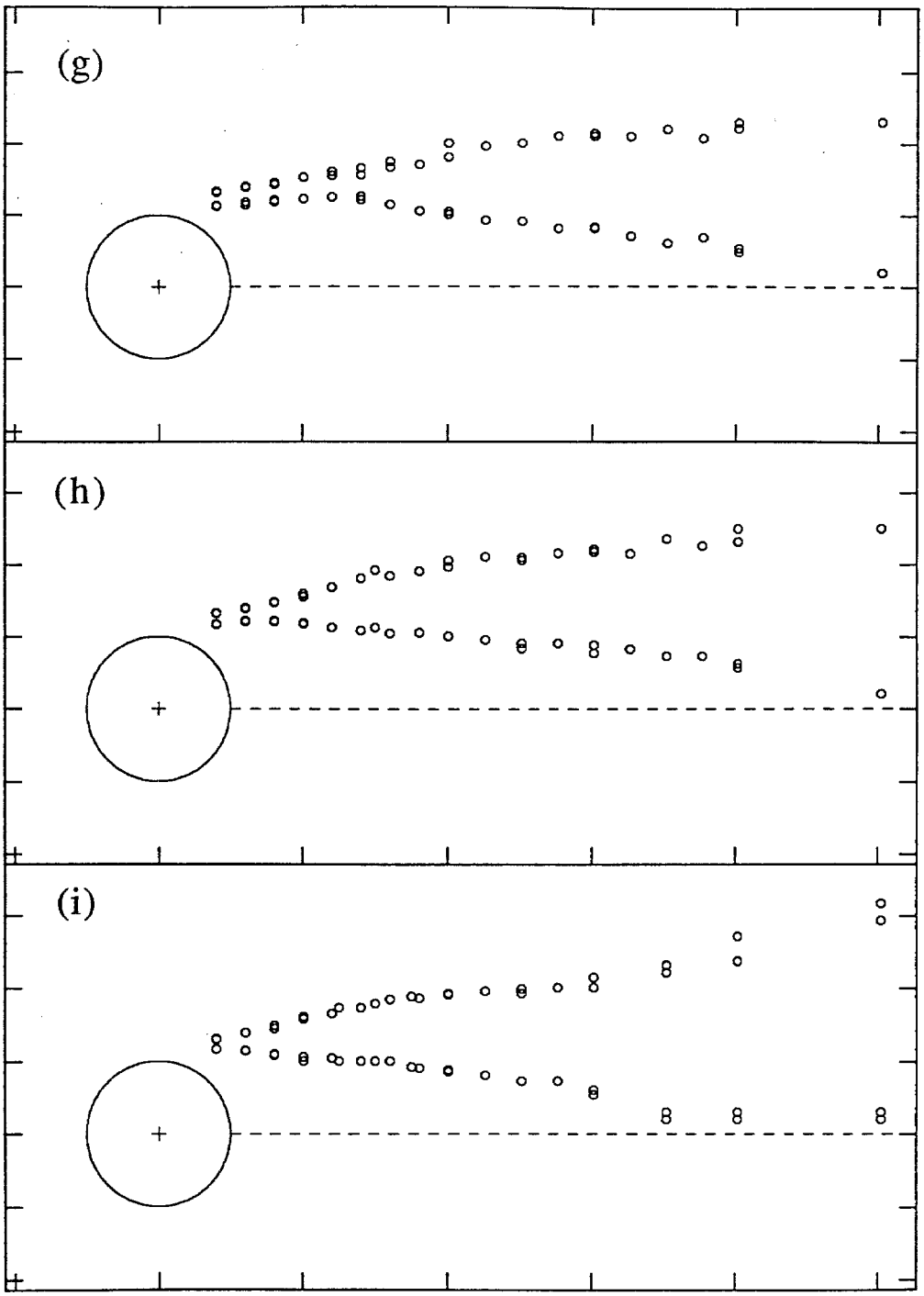

FIG. 5.2 *cont.* (g) $\sigma = 0.65$, Re = 4900, (h) $\sigma = 0.65$, Re = 9400, (i) $\sigma = 0.65$, Re = 15200.

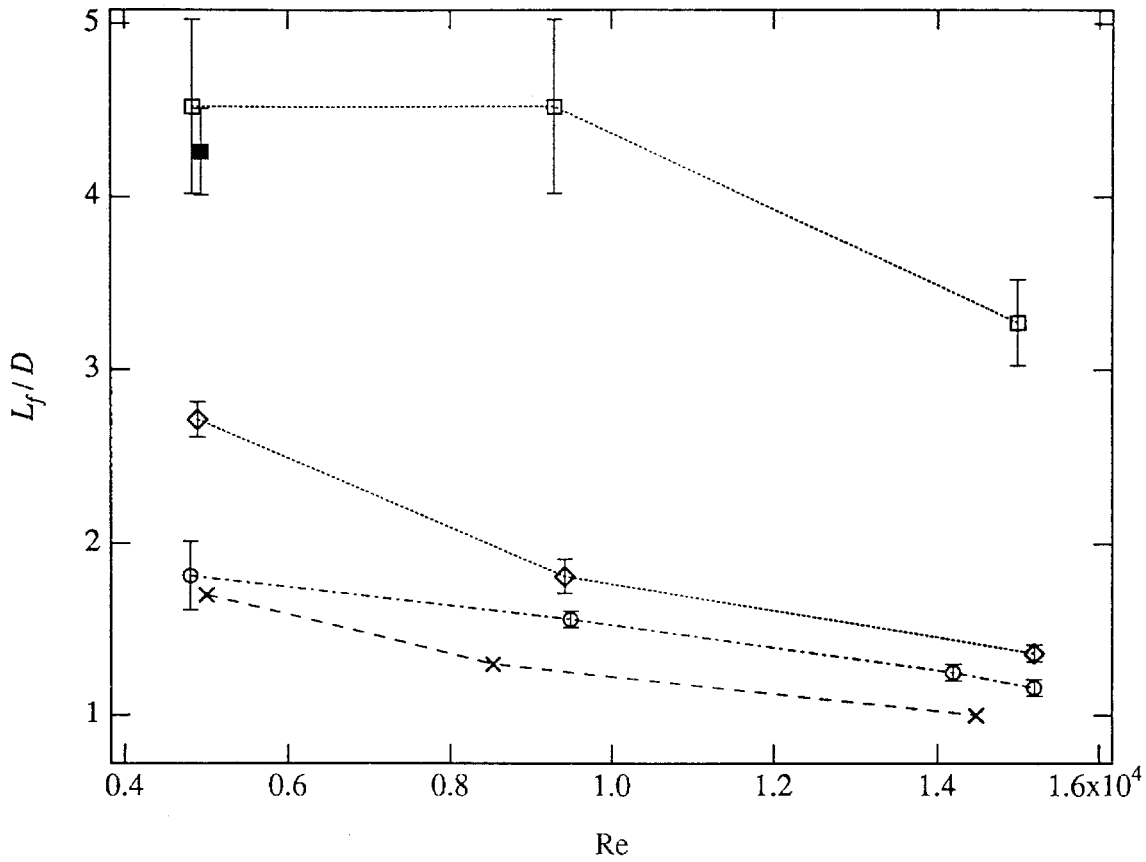

FIG. 5.3 Plot of formation length L_f/D vs. Reynolds number . Symbols are: (○) $\sigma = 0$; (◇) $\sigma = 0.22$; (□) $\sigma = 0.65$; (■) $\sigma = 0.65$, with acoustic excitation of the separated shear layers (see Chapter 6); (×) data taken from Schiller and Linke (1933).

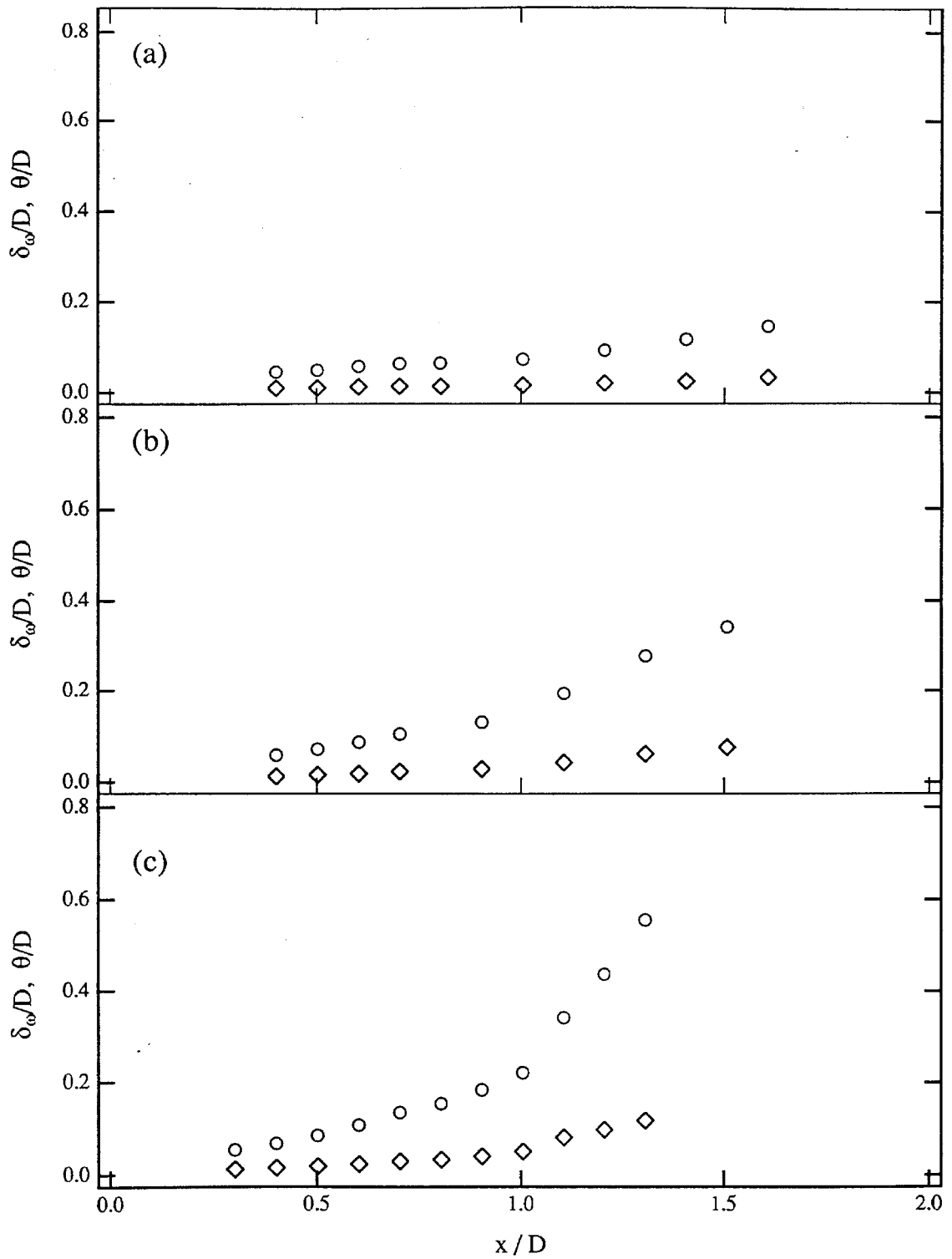

FIG. 5.4 Vorticity and momentum thickness, for all (Re, σ) cases. Note that the scales are different on the x/D-axes for the different solidities. Symbols are; ($\diamond$) θ; ($\circ$) δ_ω: (**a**) $\sigma = 0$, $\mathrm{Re} = 4800$, (**b**) $\sigma = 0$, $\mathrm{Re} = 9500$, (**c**) $\sigma = 0$, $\mathrm{Re} = 15200$ *(figure continues on next page).*

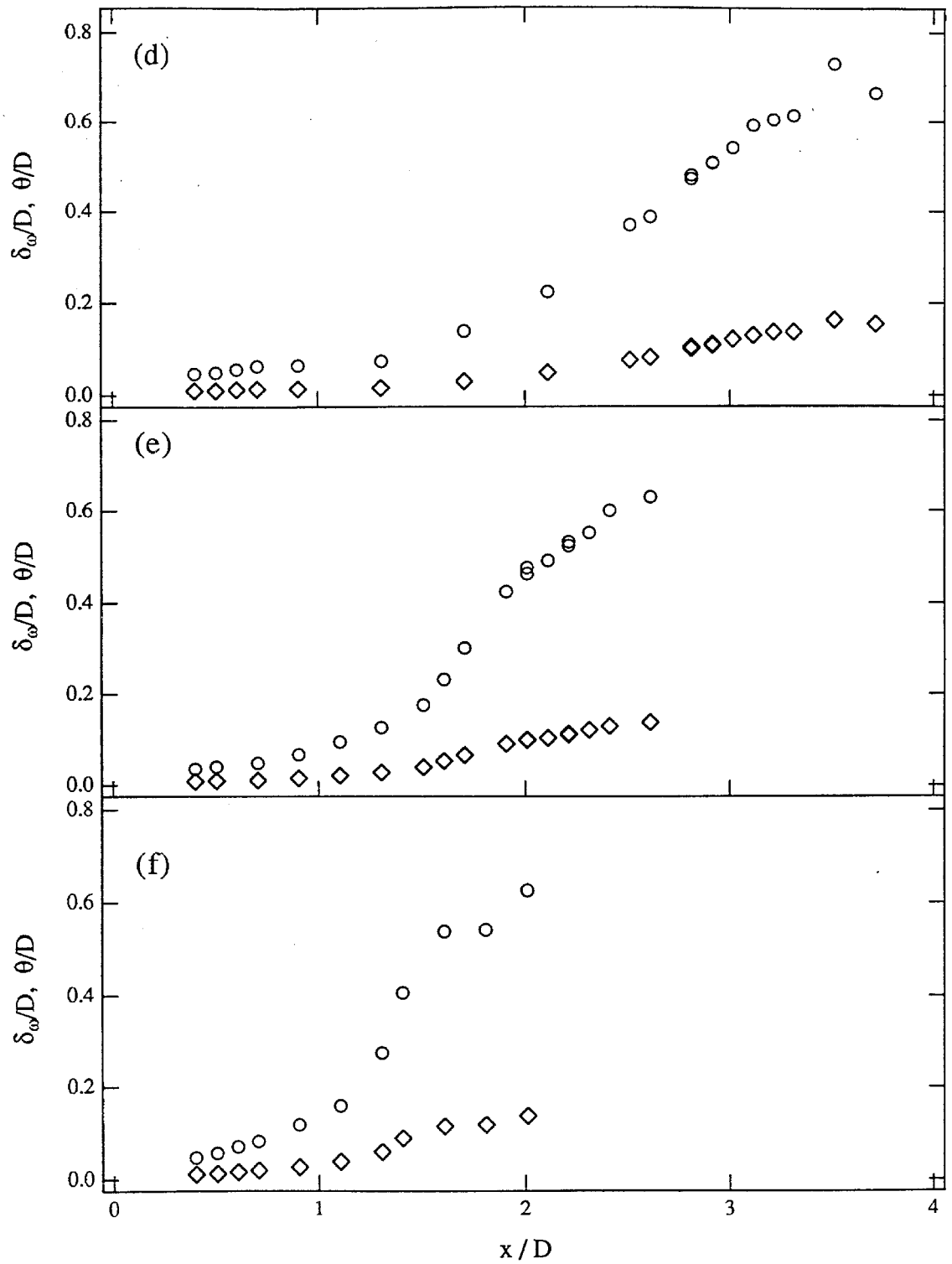

FIG. 5.4 *cont.* (**d**) $\sigma = 0.22$, Re = 4800, (**e**) $\sigma = 0.22$, Re = 9300, (**f**) $\sigma = 0.22$, Re = 15000 *(figure continues on next page).*

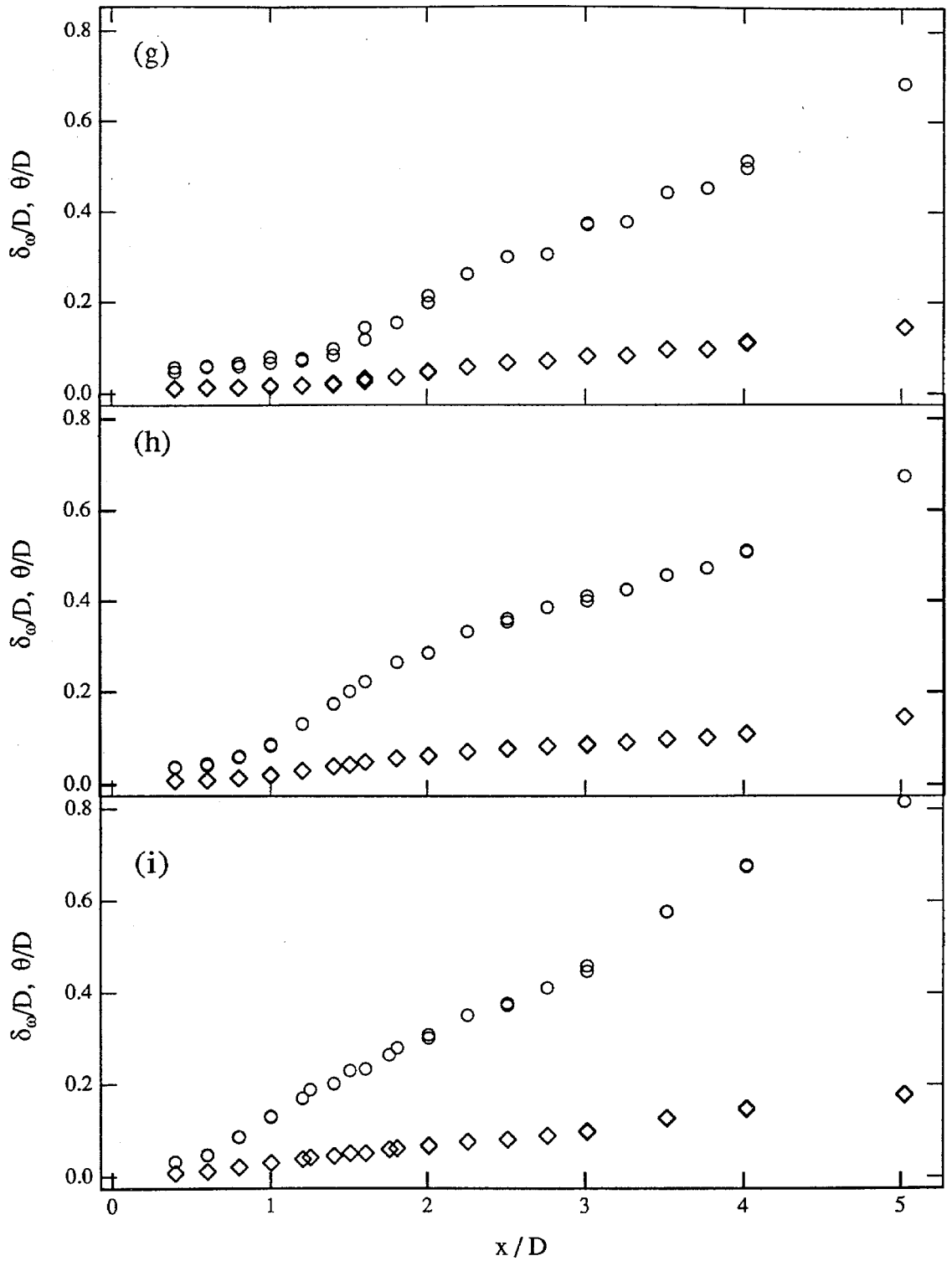

FIG. 5.4 *cont.* (g) $\sigma = 0.65$, Re = 4900, (h) $\sigma = 0.65$, Re = 9400, (i) $\sigma = 0.65$, Re = 15200.

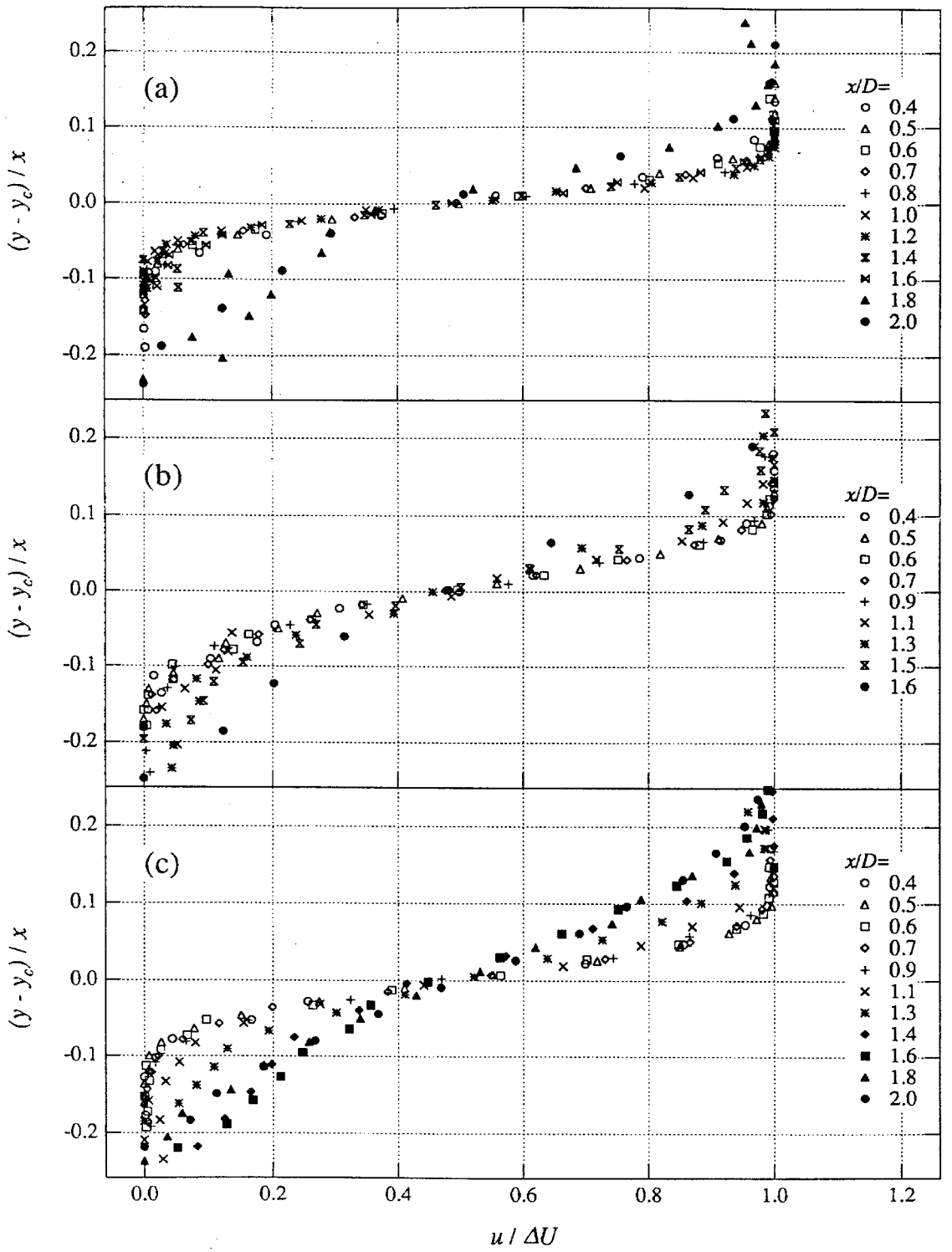

FIG. 5.5 Shear layer profile data plotted using similarity coordinates $u/\Delta U$ versus $(y - y_c)/x$; (**a**) $\sigma = 0$, Re = 4800, (**b**) $\sigma = 0$, Re = 9500, (**c**) $\sigma = 0$, Re = 15200 *(figure continues on next page).*

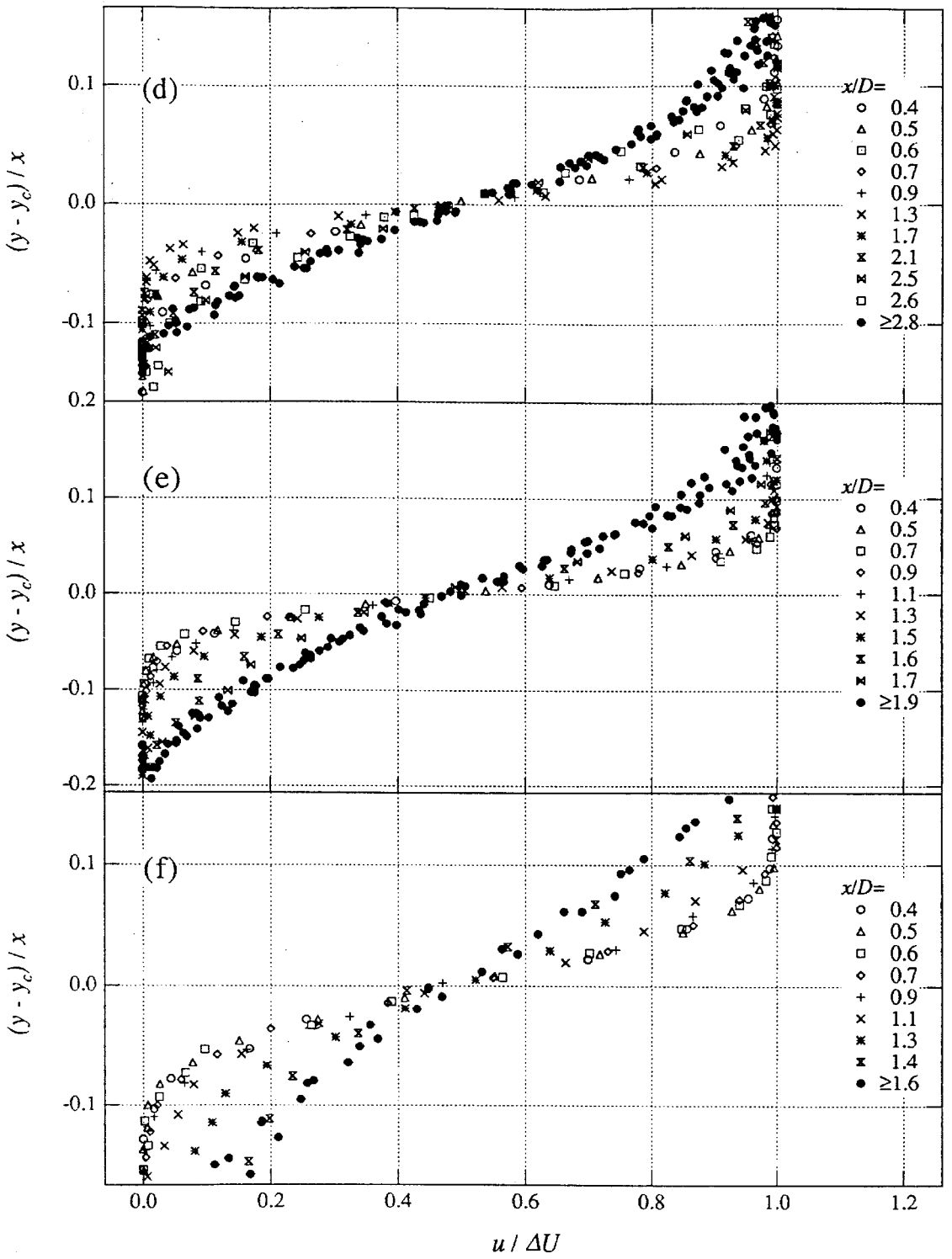

FIG. 5.5 *cont.* (**d**) $\sigma = 0.22$, Re = 4800, (**e**) $\sigma = 0.22$, Re = 9300, (**f**) $\sigma = 0.22$, Re = 15000 *(figure continues on next page).*

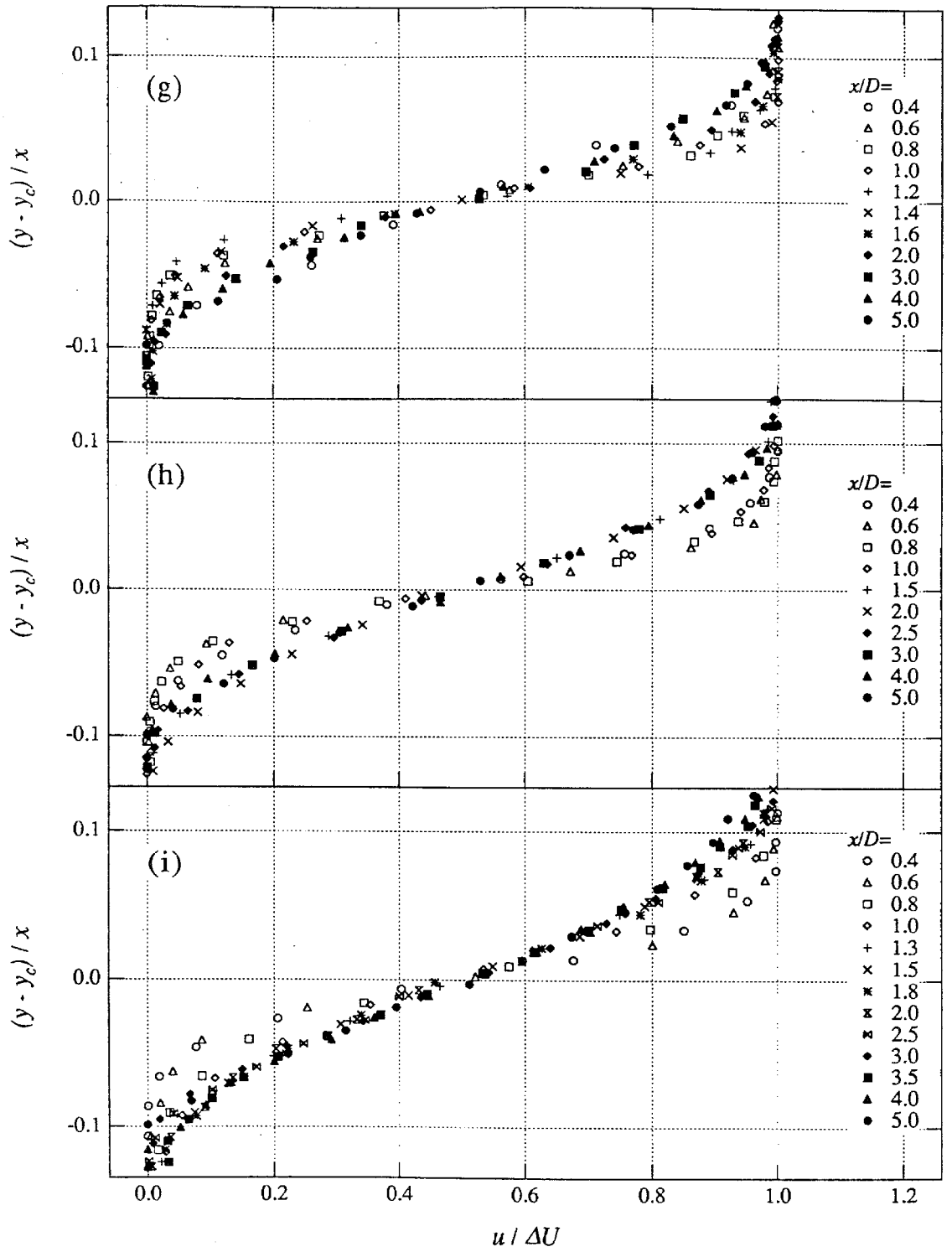

FIG. 5.5 *cont.* (g) $\sigma = 0.65$, Re = 4900, (h) $\sigma = 0.65$, Re = 9400, (i) $\sigma = 0.65$, Re = 15200.

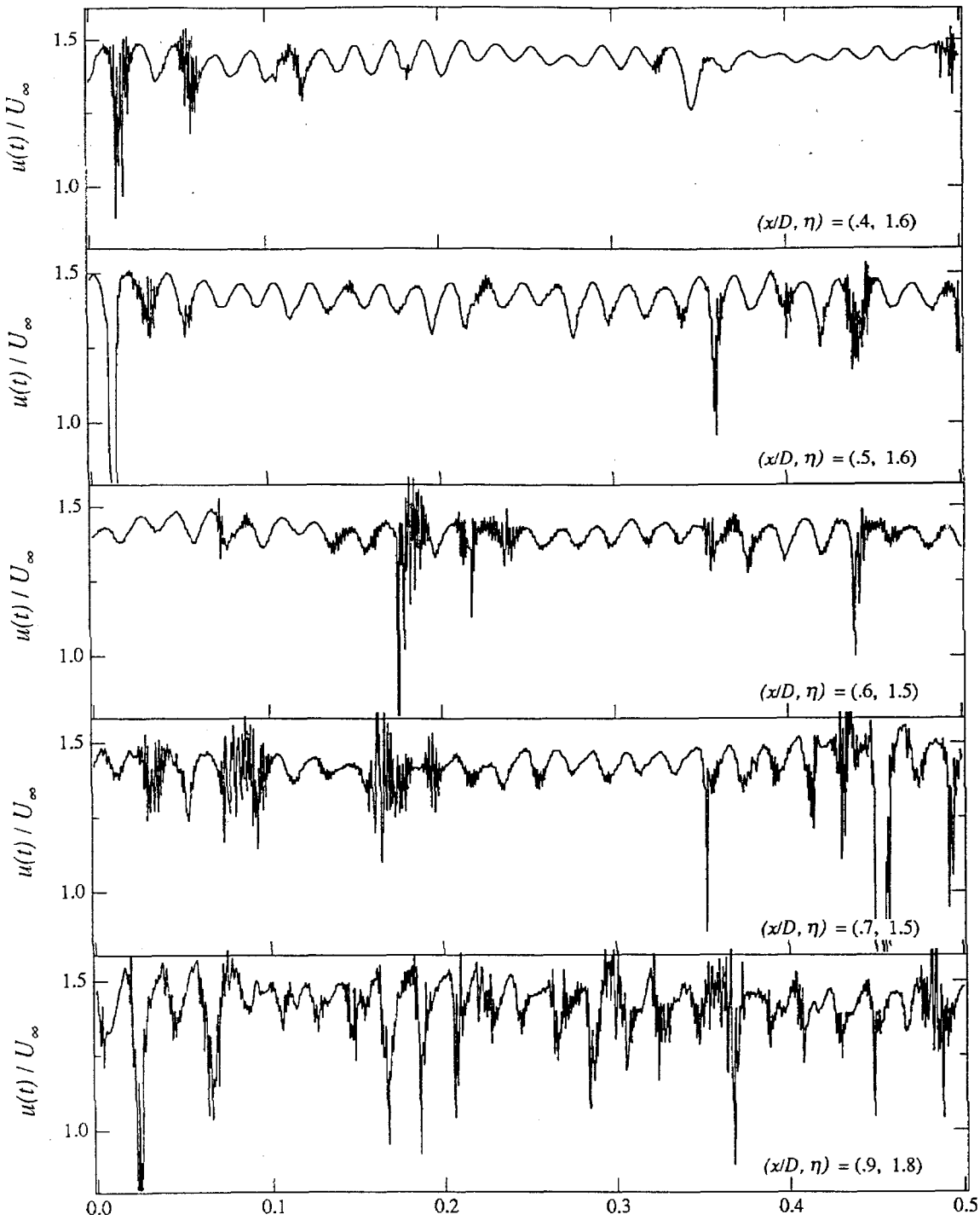

(a) $\sigma = 0$, Re = 9500.

FIG. 5.6 Shear layer velocity traces showing the evolution of the shear layer instability with downstream position. Each trace in the figure corresponds to a different downstream location. Downstream location x/D and normalized transverse shear layer coordinate η are shown on each trace *(figure continues on next page).*

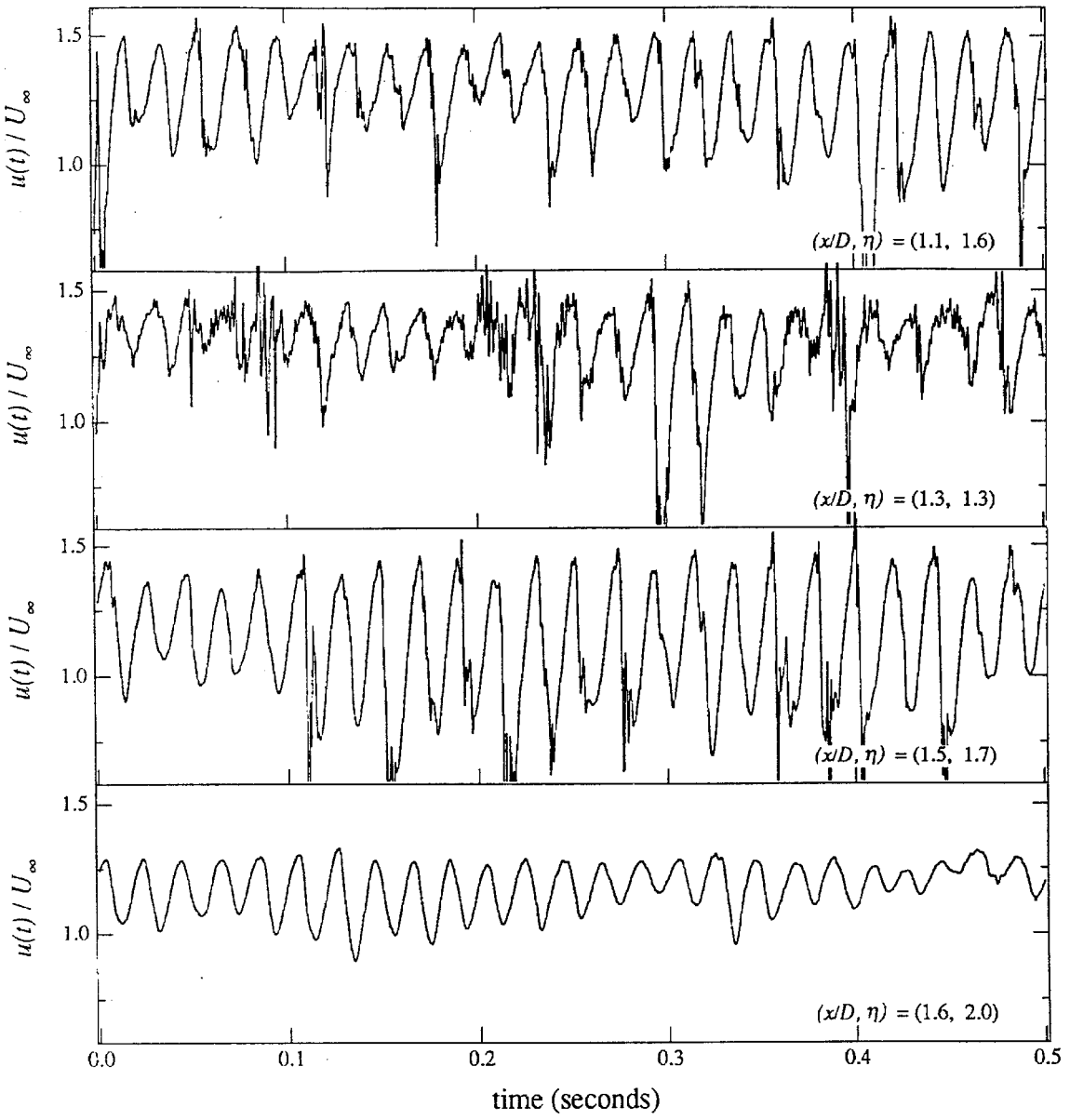

FIG. 5.6 Continuation of part **a** *(figure continues on next page).*

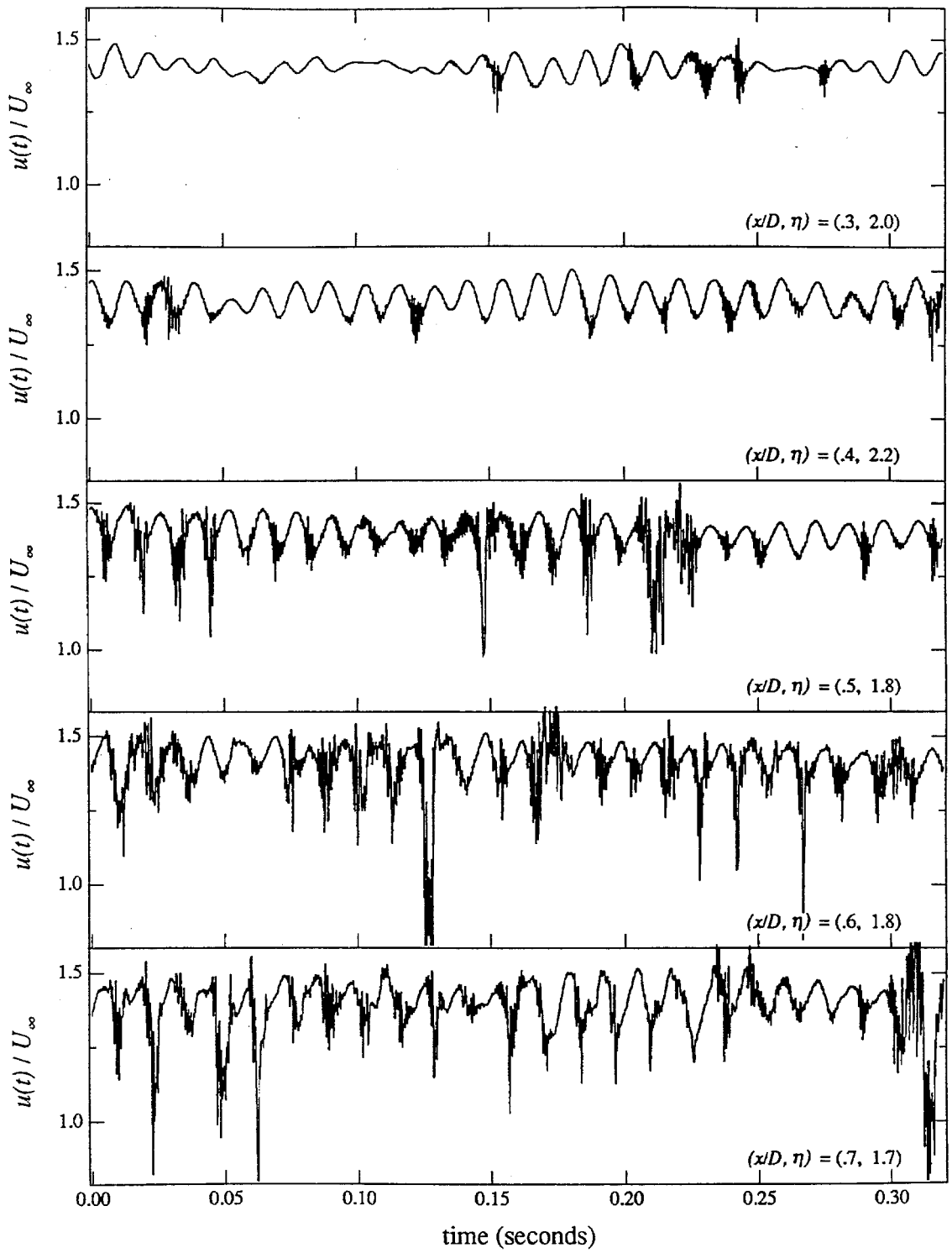

FIG. 5.6b $\sigma = 0$, Re = 15000 *(figure continues on next page).*

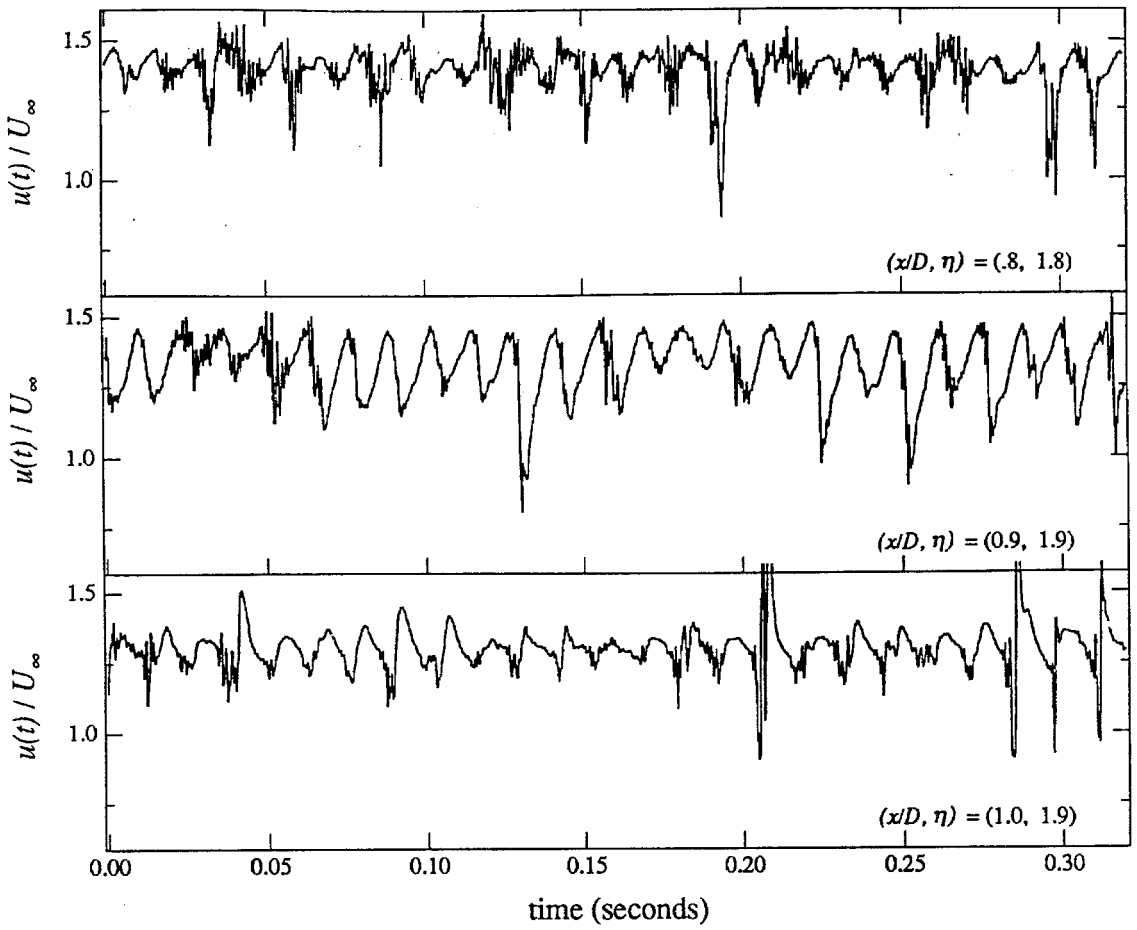

FIG. 5.6 Continuation of part **b** *(figure continues on next page).*

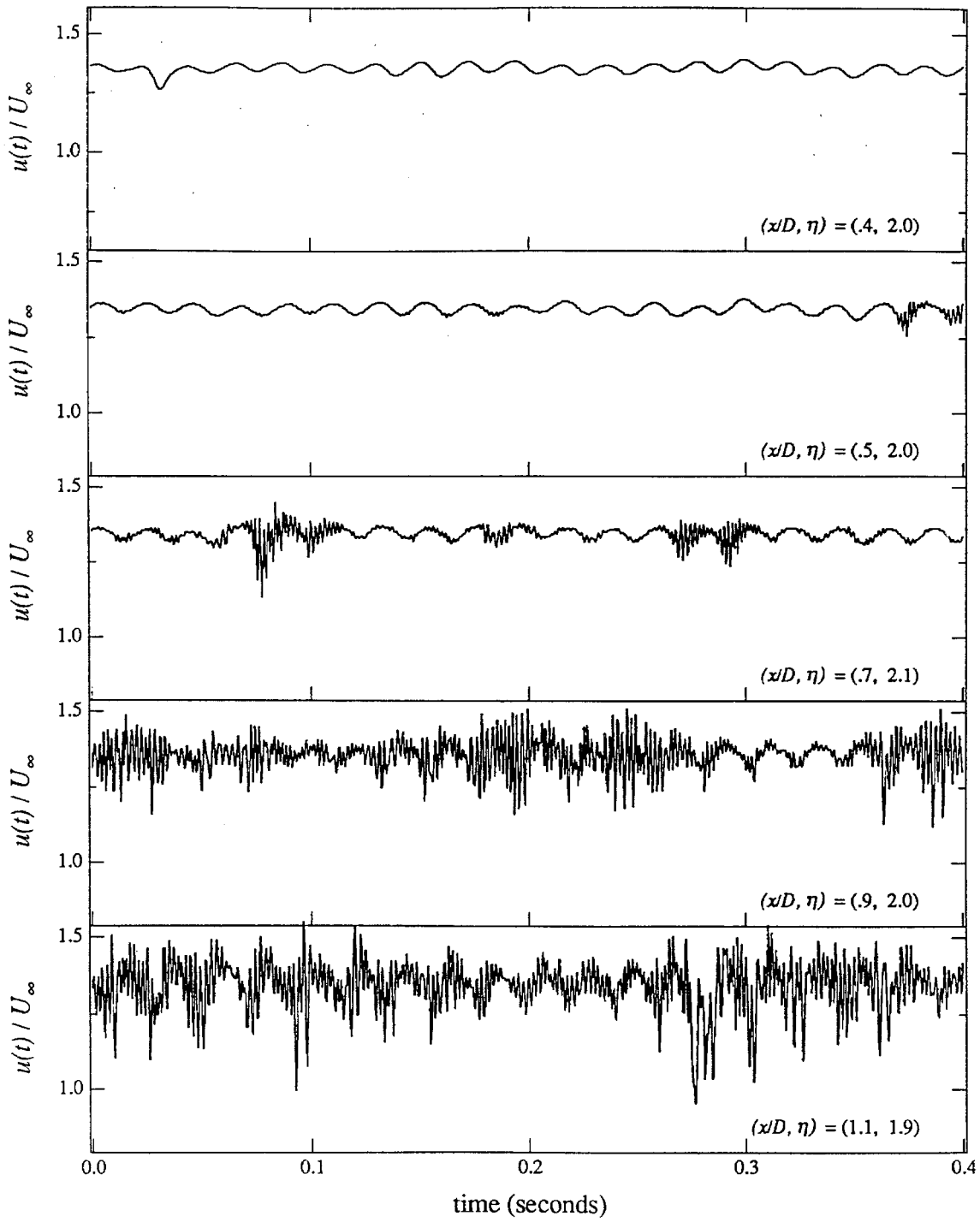

FIG. 5.6c $\sigma = 0.22$, Re = 9800 *(figure continues on next page).*

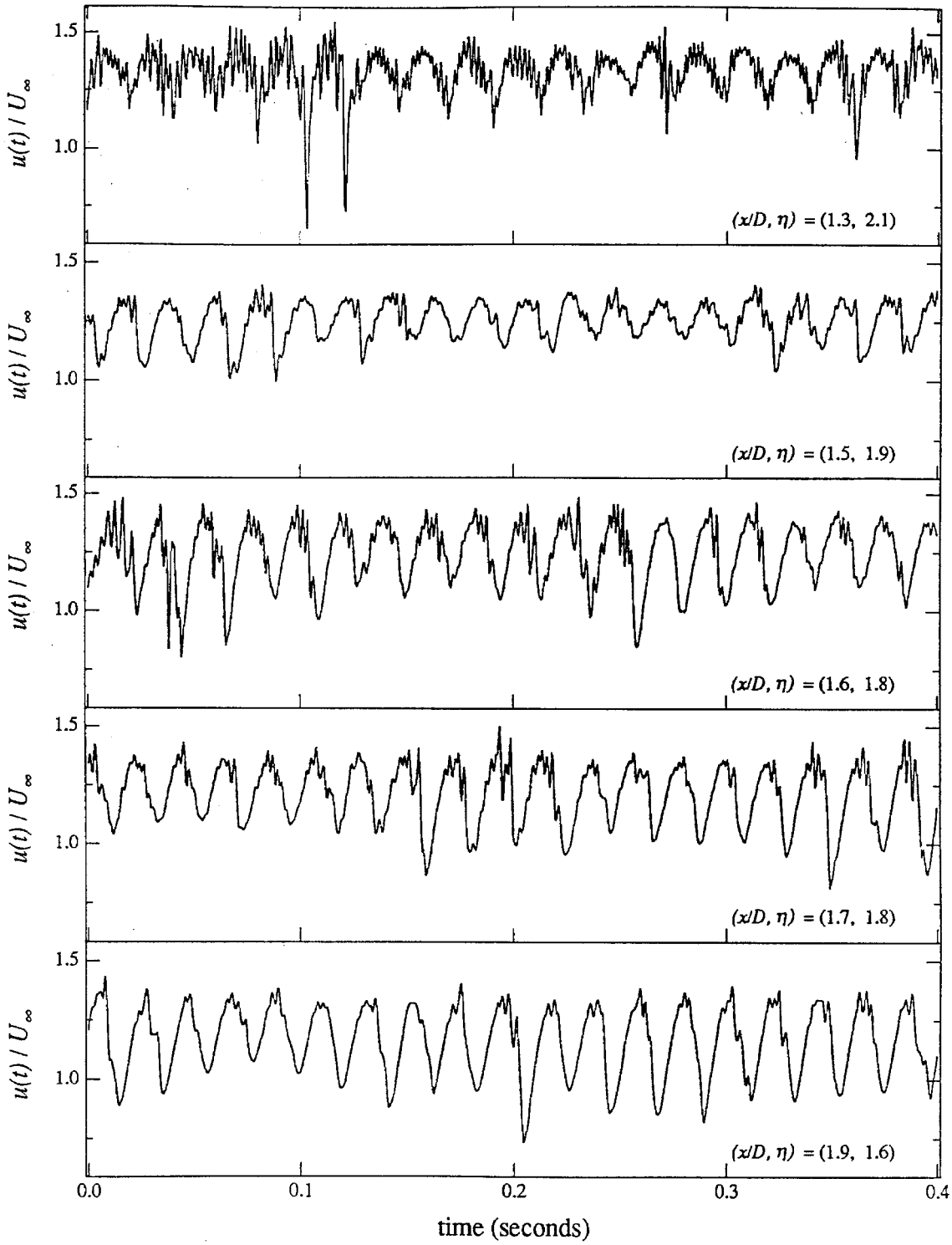

FIG. 5.6 Continuation of part **c** *(figure continues on next page).*

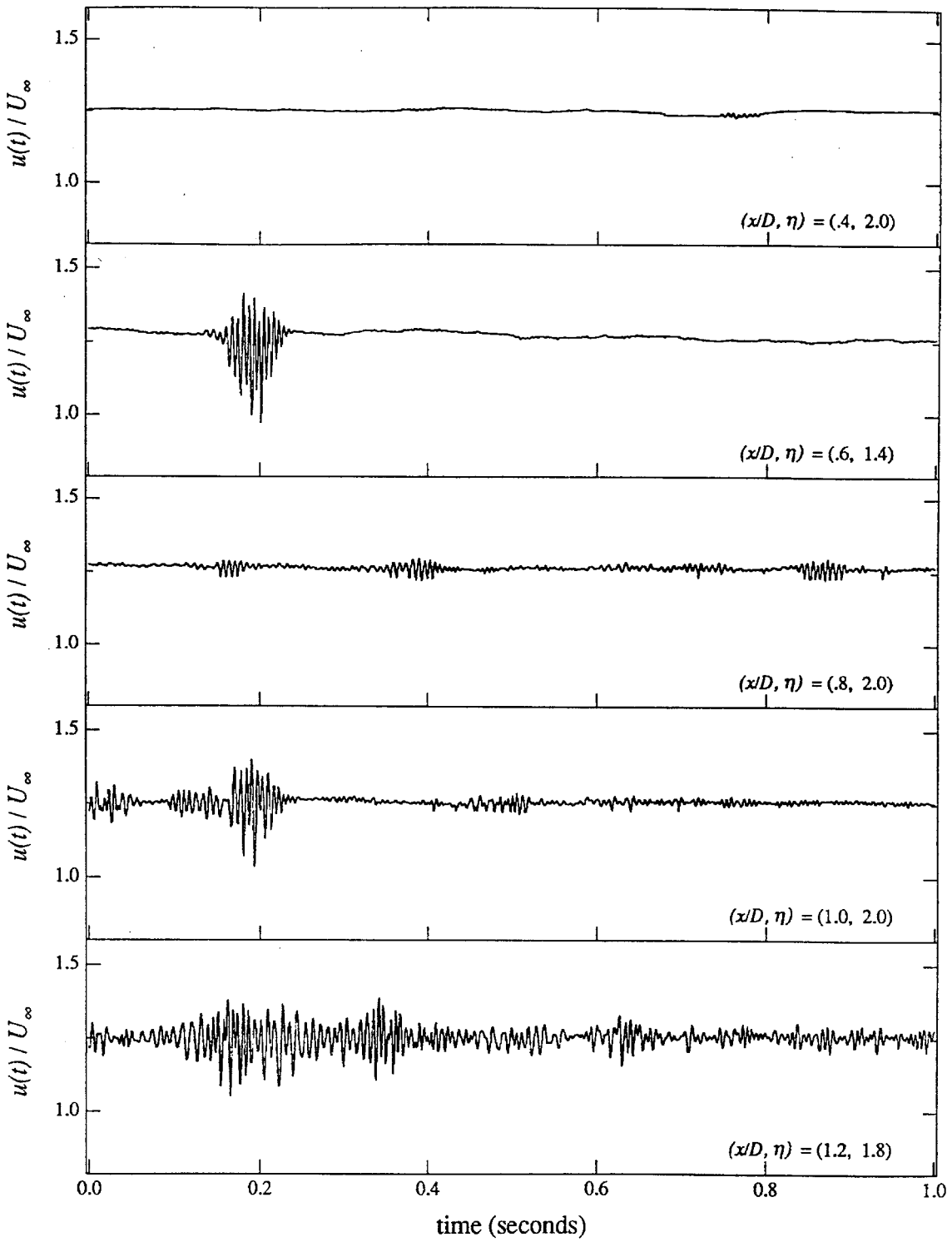

FIG. 5.6d $\sigma = 0.65$, Re = 5300 *(figure continues on next page).*

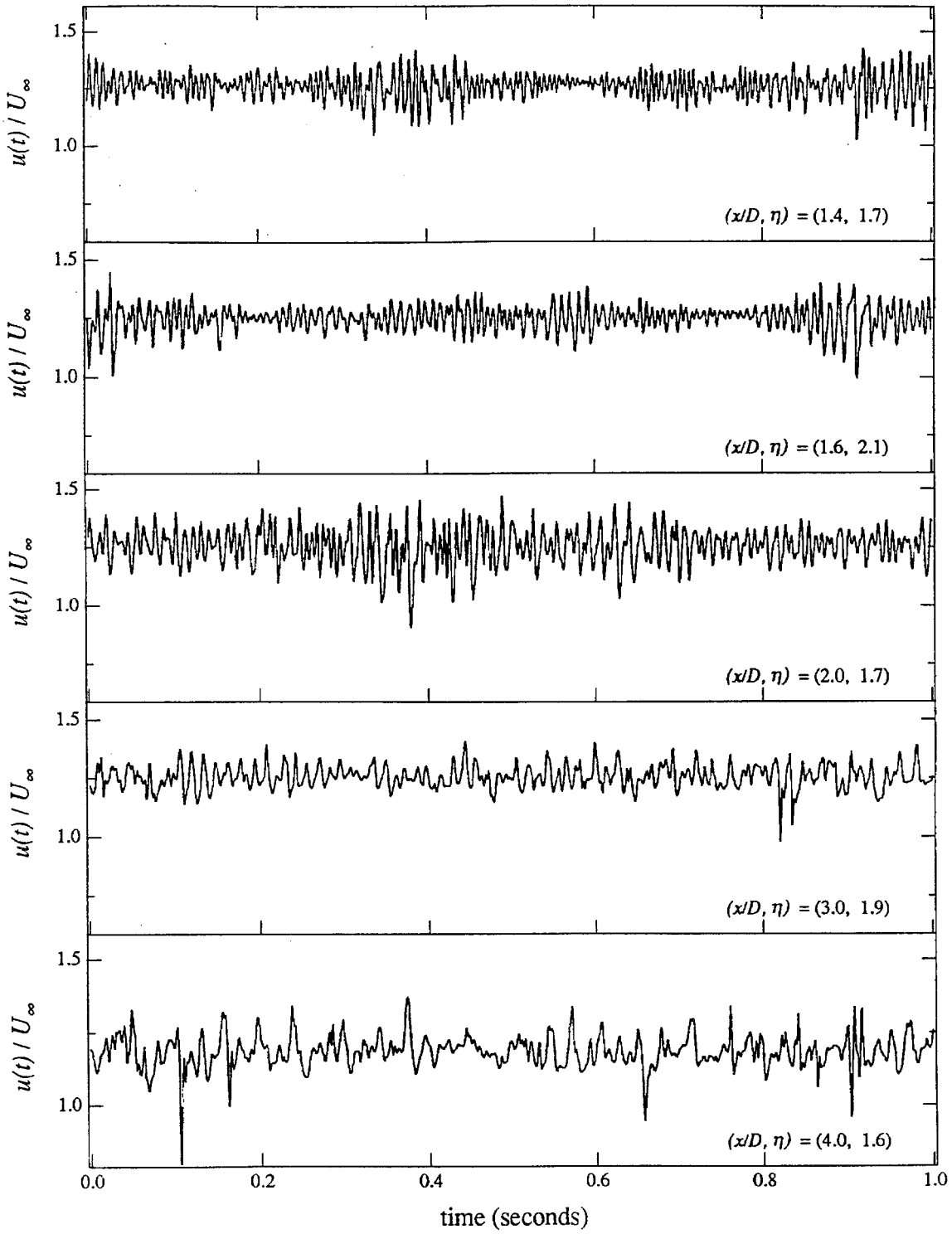

FIG. 5.6 Continuation of part **d.**

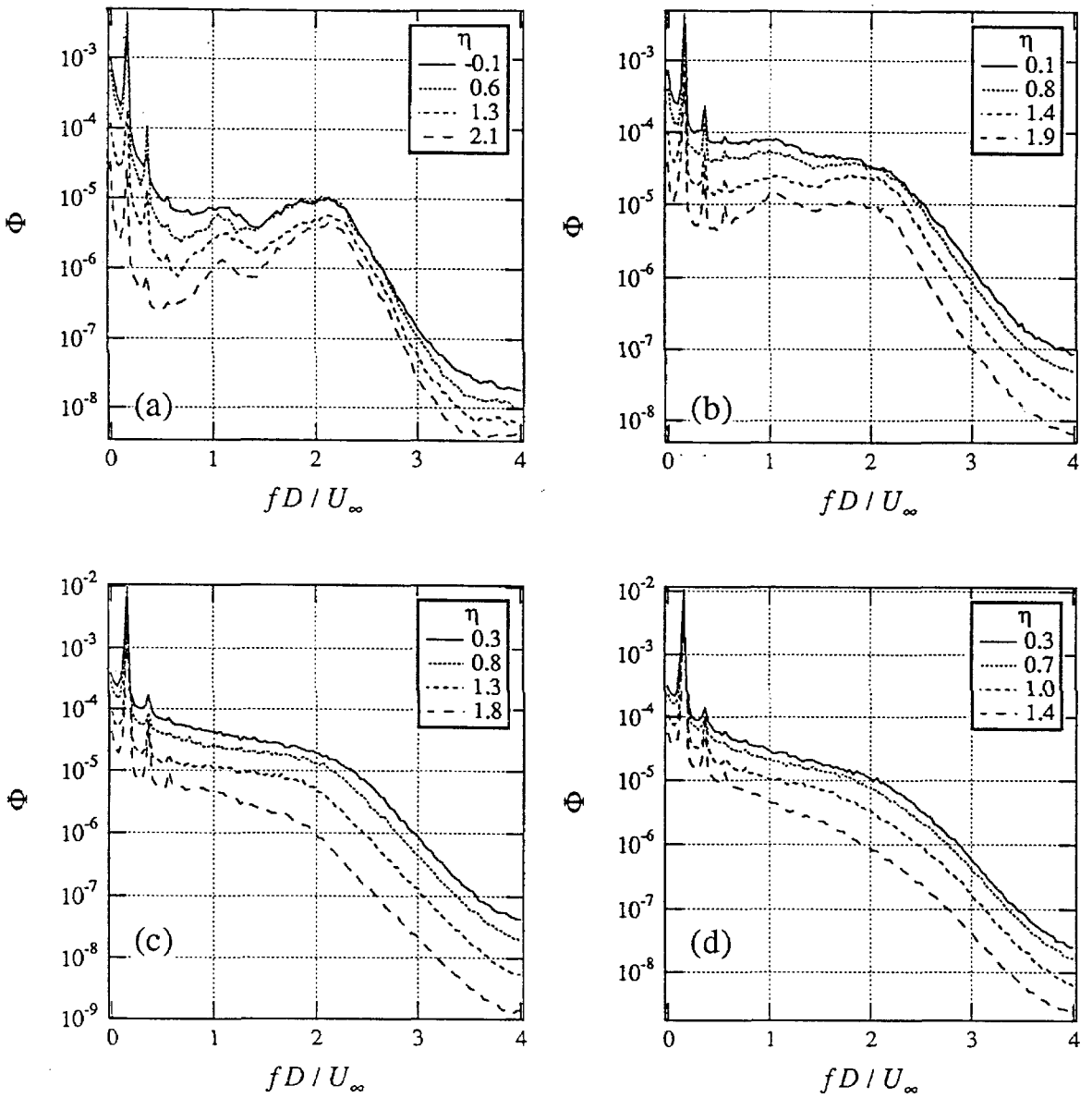

FIG. 5.7 Variation of shear layer spectra with transverse shear layer coordinate near the outer (high speed) side of the shear layer, $\sigma = 0.65$, Re = 9300. The transverse locations from which the data were taken that were used to compute the spectra are shown by the solid symbols in Fig. 5.1: (**a**) $x/D = 0.7$, (**b**) $x/D = 1.3$, (**c**) $x/D = 1.7$, (**d**) $x/D = 2.0$.

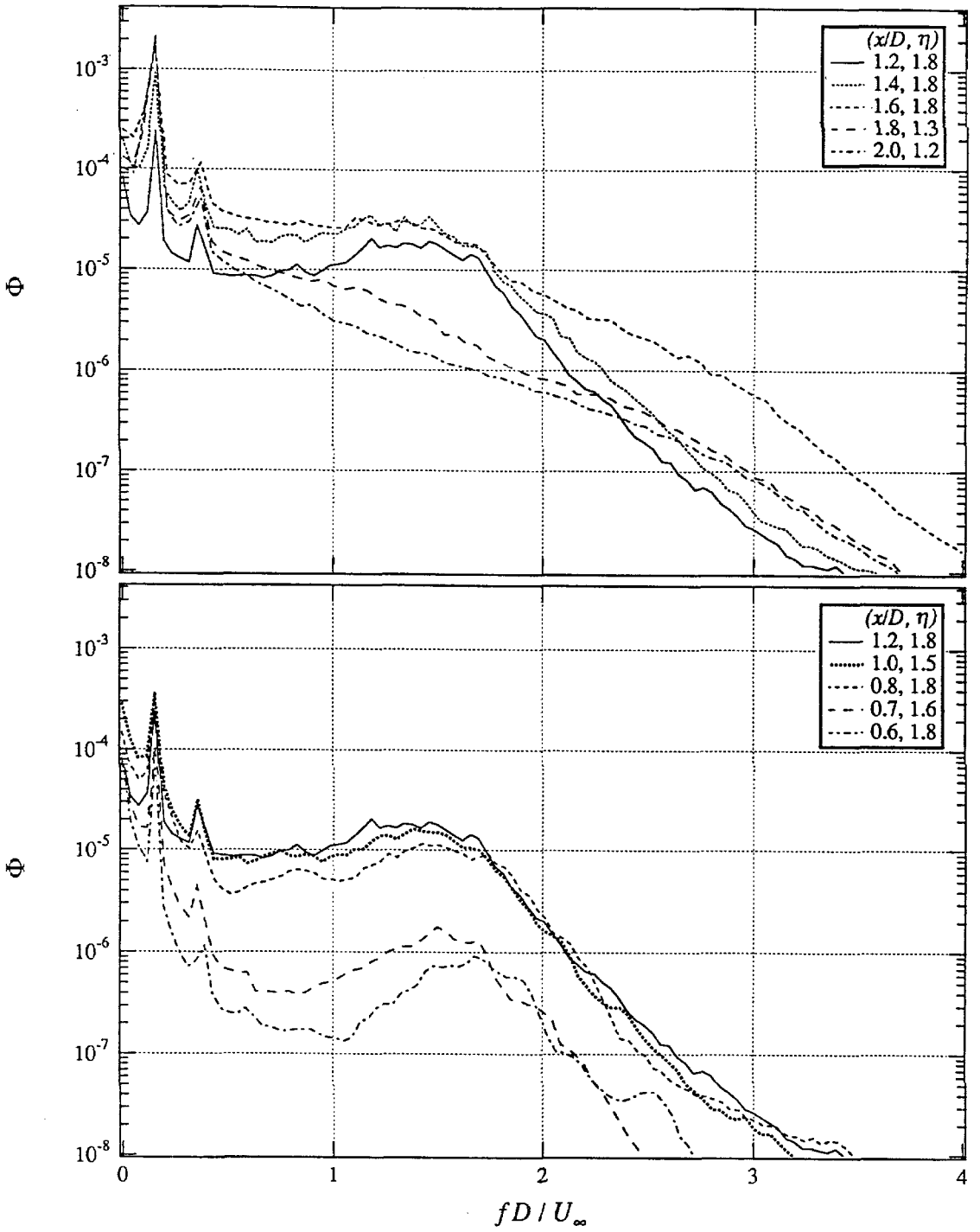

(a) $\sigma = 0$, Re = 4800

FIG. 5.8 Shear layer power spectral density for each of the nine flow conditions surveyed, computed from data obtained at different downstream locations to show the development of the shear layer instability frequencies *(figure continues on next page)*.

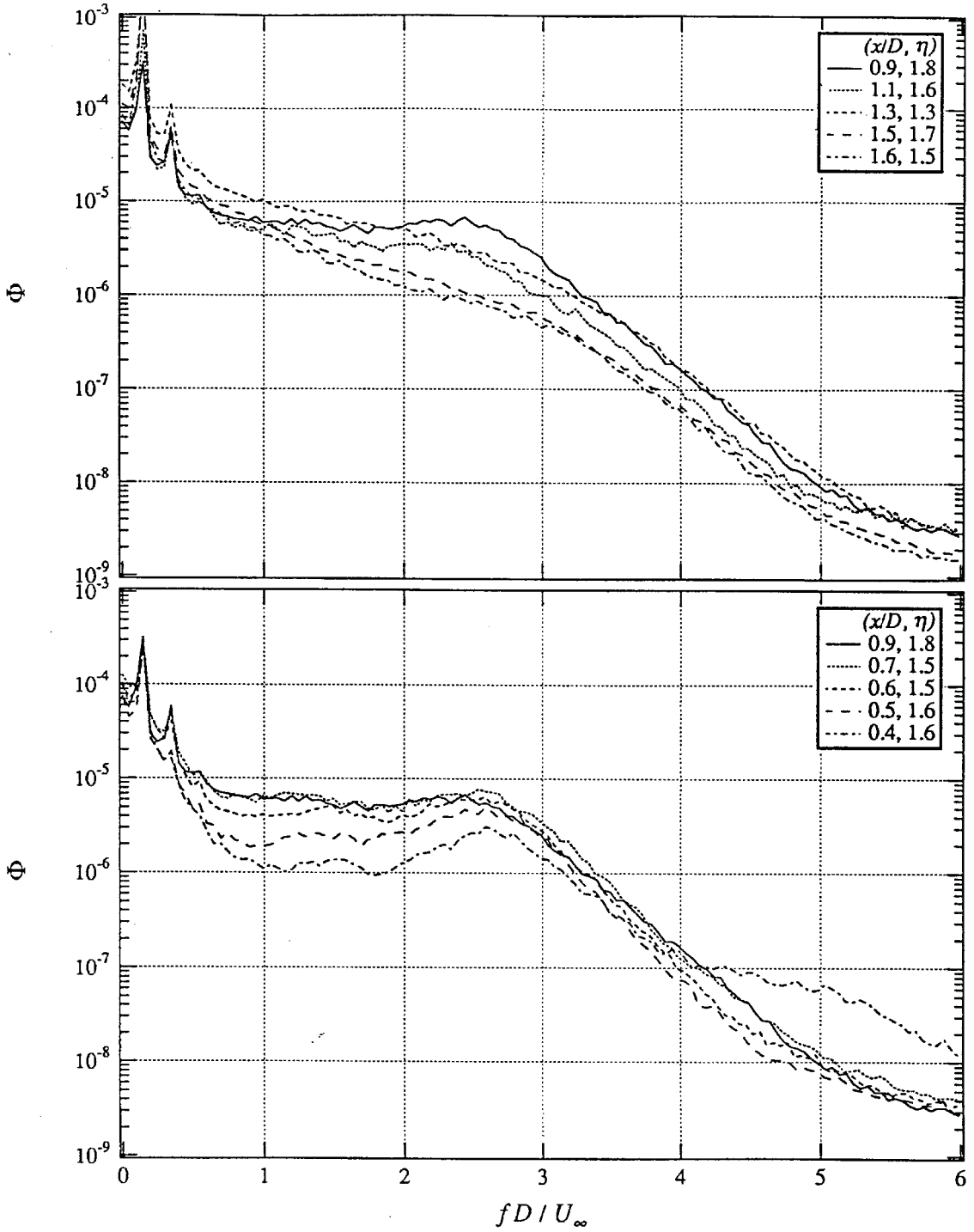

FIG. 5.8**b** $\sigma = 0$, Re = 9500 *(figure continues on next page).*

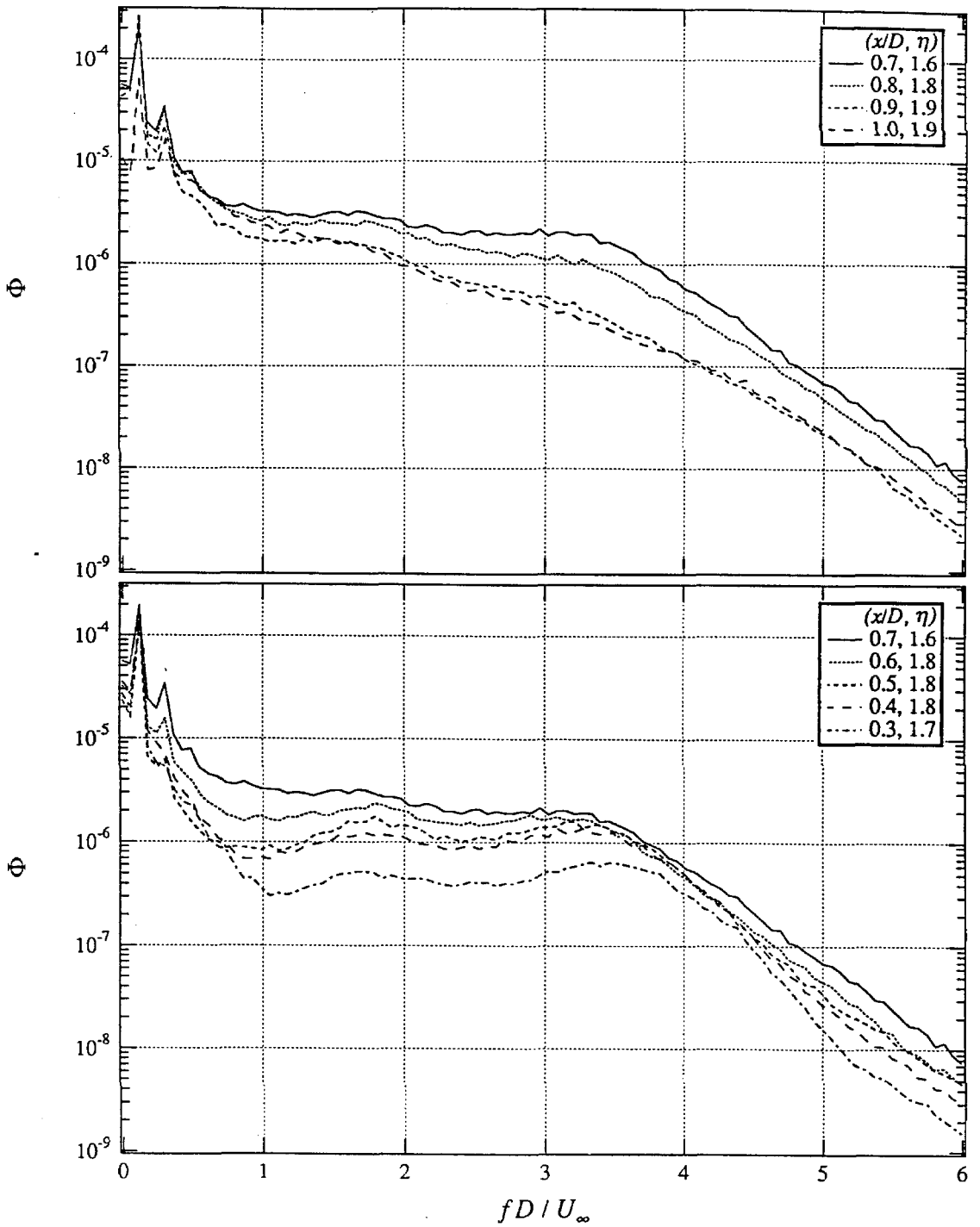

FIG. 5.8c $\sigma = 0$, Re = 15200 *(figure continues on next page).*

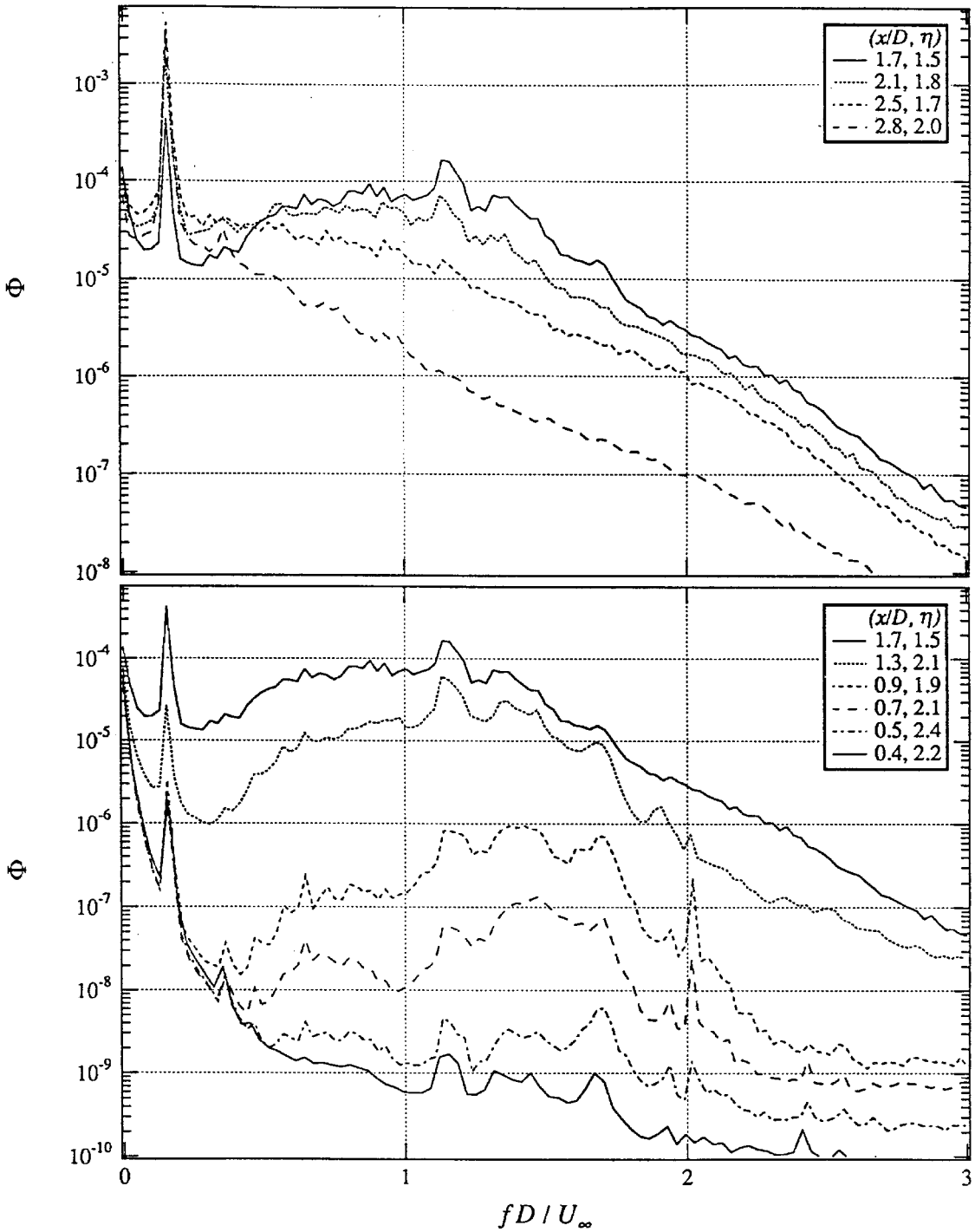

FIG. 5.8d $\sigma = 0.22$, Re = 4800 *(figure continues on next page).*

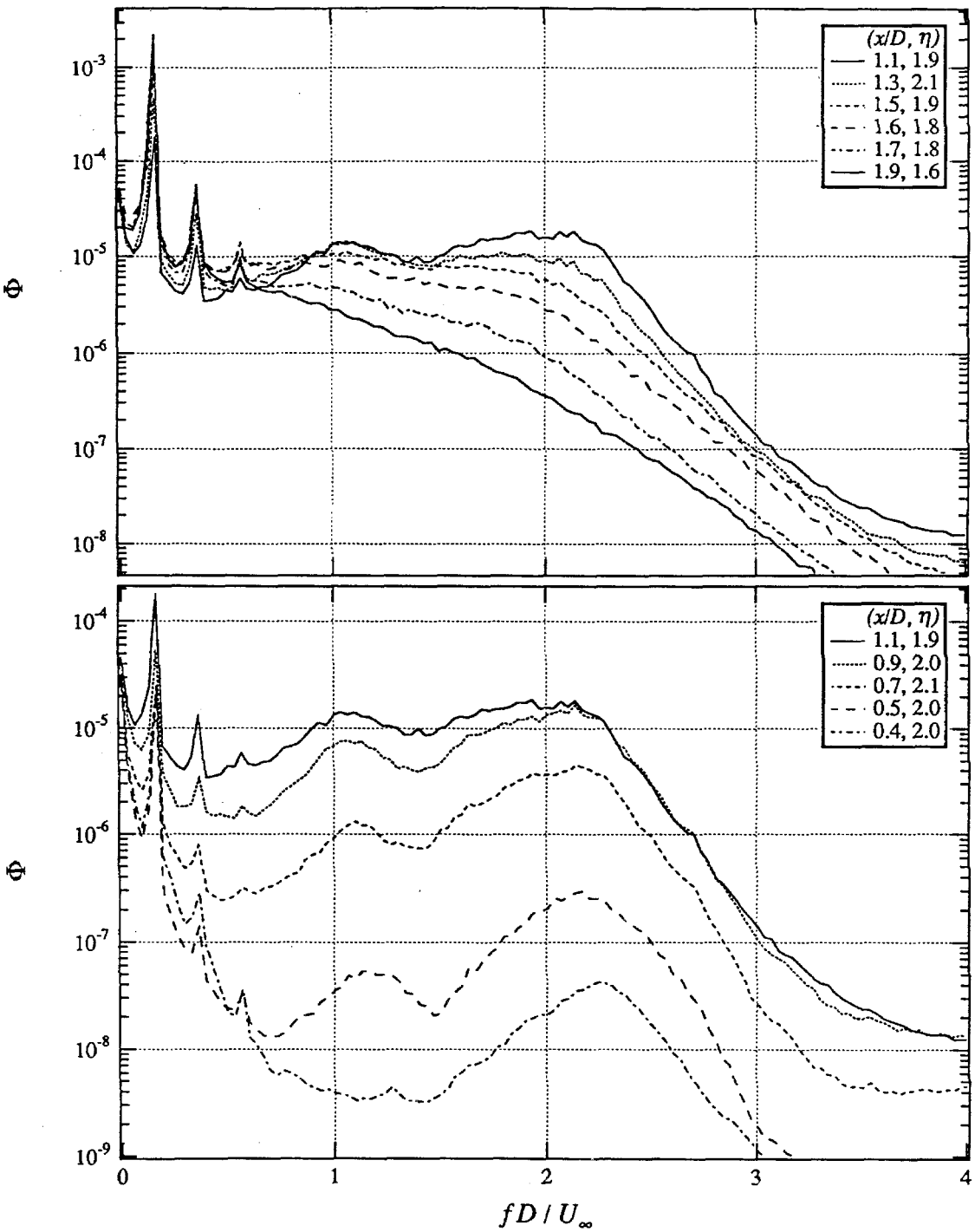

FIG. 5.8e $\sigma = 0.22$, Re = 9300 *(figure continues on next page).*

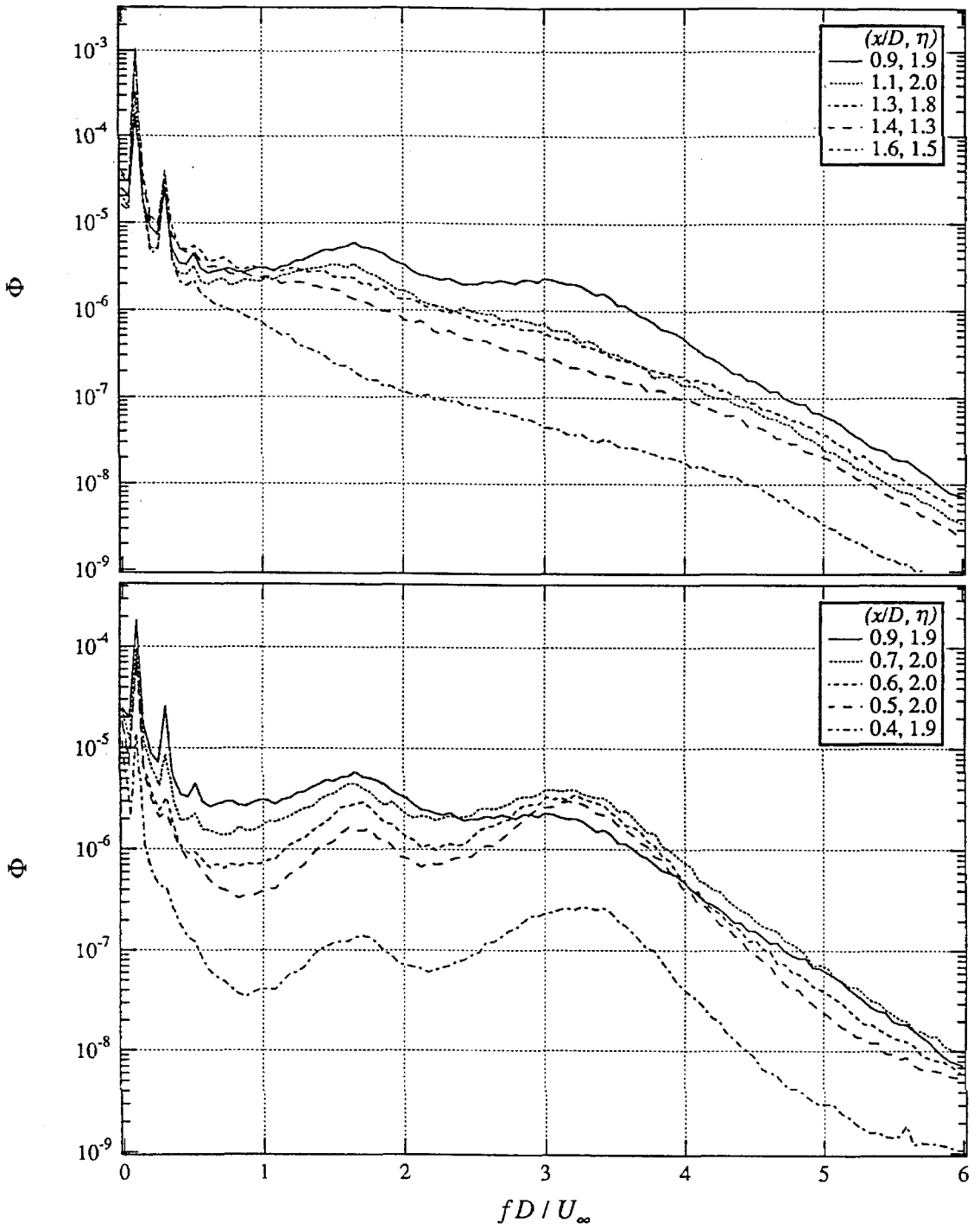

FIG. 5.8f $\sigma = 0.22$, Re = 15000 *(figure continues on next page).*

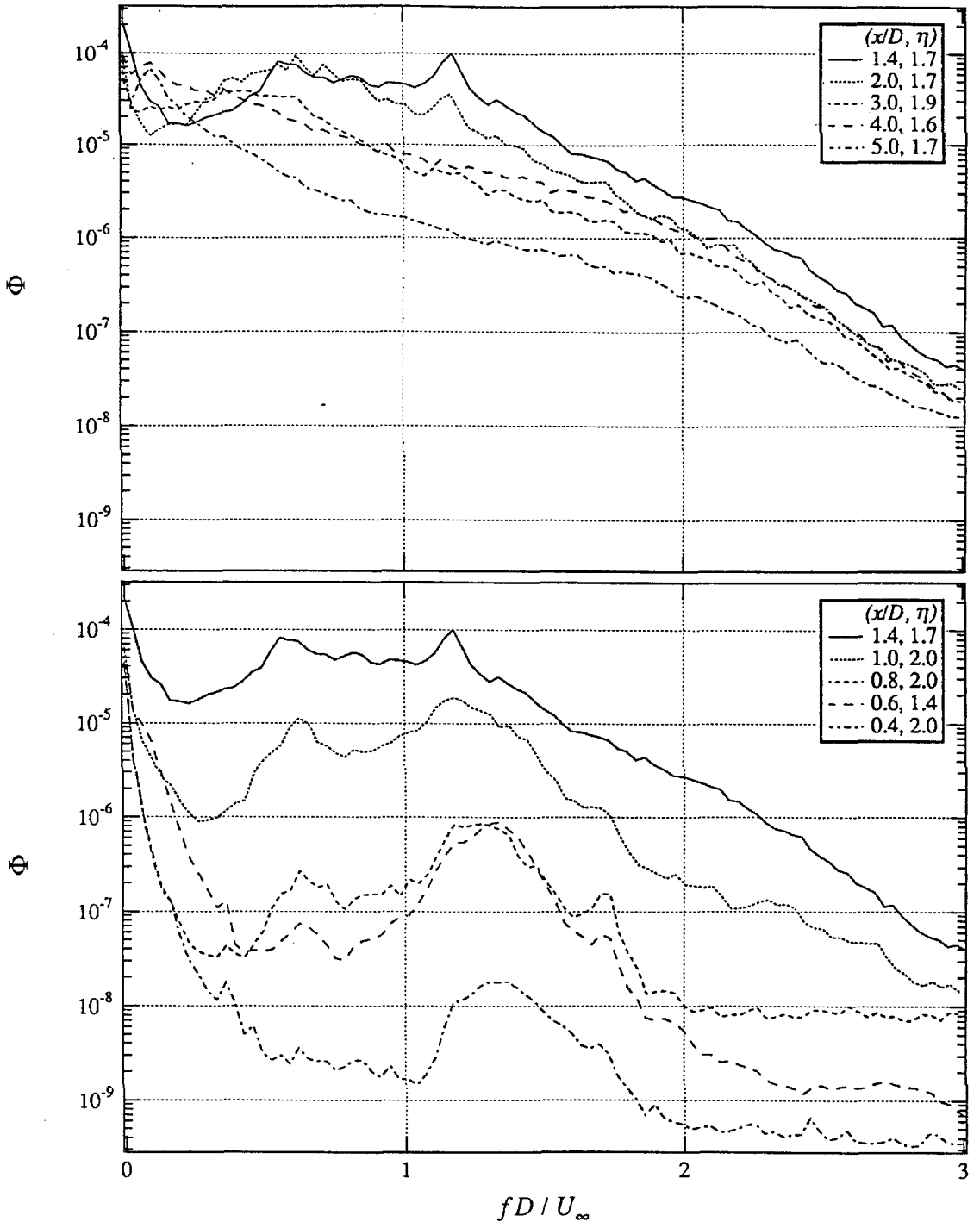

FIG. 5.8g $\sigma = 0.65$, $\mathrm{Re} = 4900$ *(figure continues on next page).*

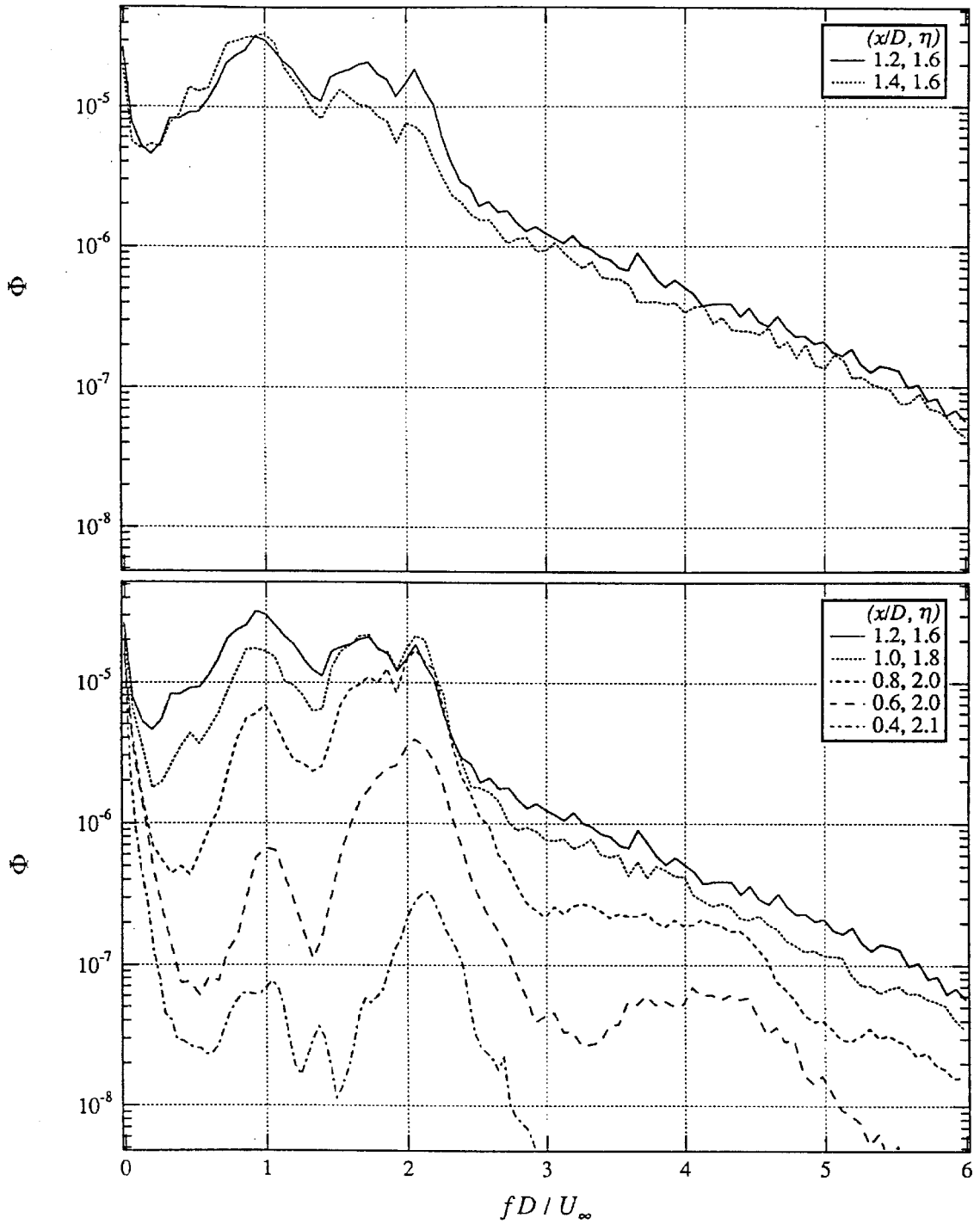

FIG. 5.8h $\sigma = 0.65$, Re = 9400 *(figure continues on next page).*

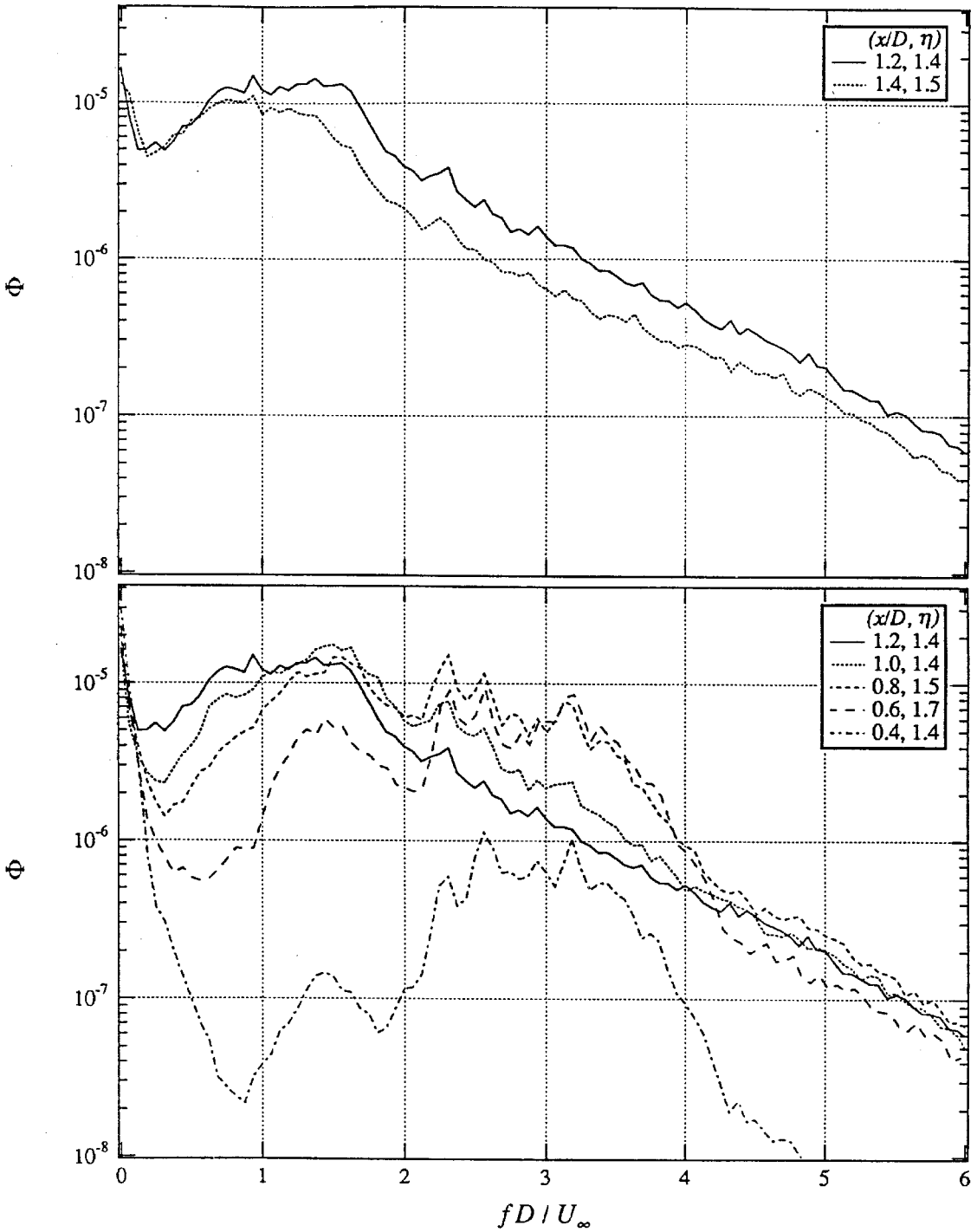

FIG. 5.8i $\sigma = 0.65$, Re = 15200.

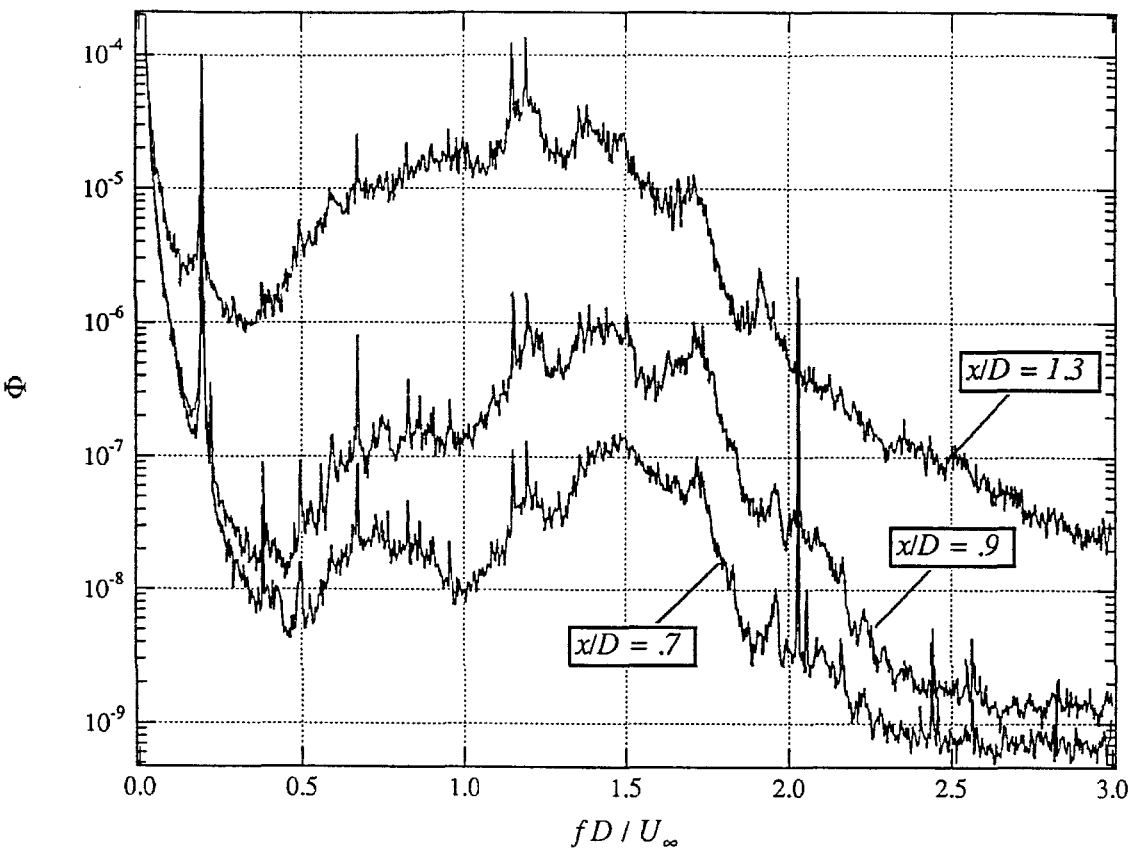

FIG. 5.9 Several of the spectra from Fig.5.8**d**, $\sigma = 0.22$, Re = 4800, shown at high resolution to resolve spectral features.

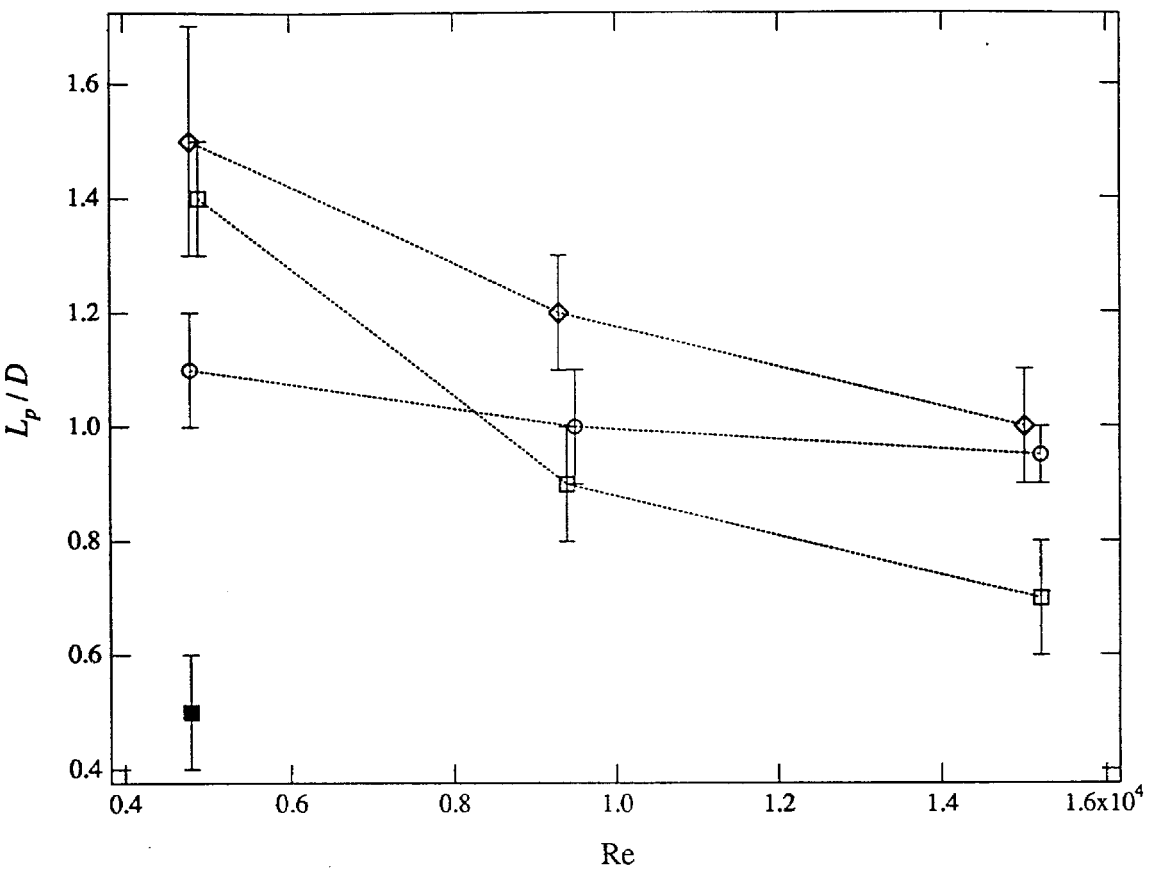

FIG. 5.10 Pairing length L_p versus Reynolds number, taken from Fig. 5.4. Symbols are; (○) $\sigma = 0$; (◇) $\sigma = 0.22$; (□) $\sigma = 0.65$; (■) $\sigma = 0.65$, with acoustic excitation of the separated shear layers (see Chapter 6).

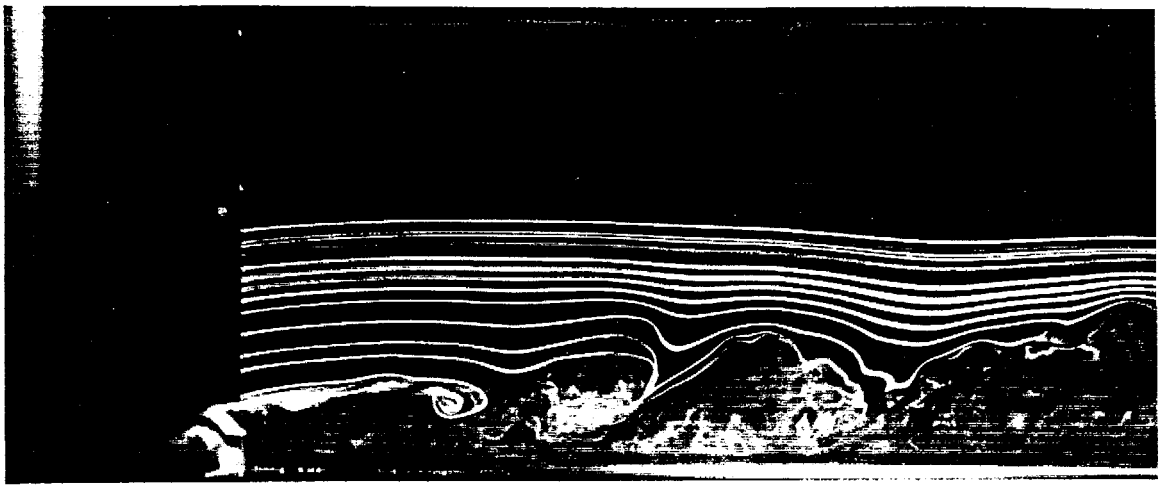

FIG. 5.11 Smoke wire flow visualization of shear layer vortices, $\sigma = 0.65$, $\mathrm{Re} = 2600$

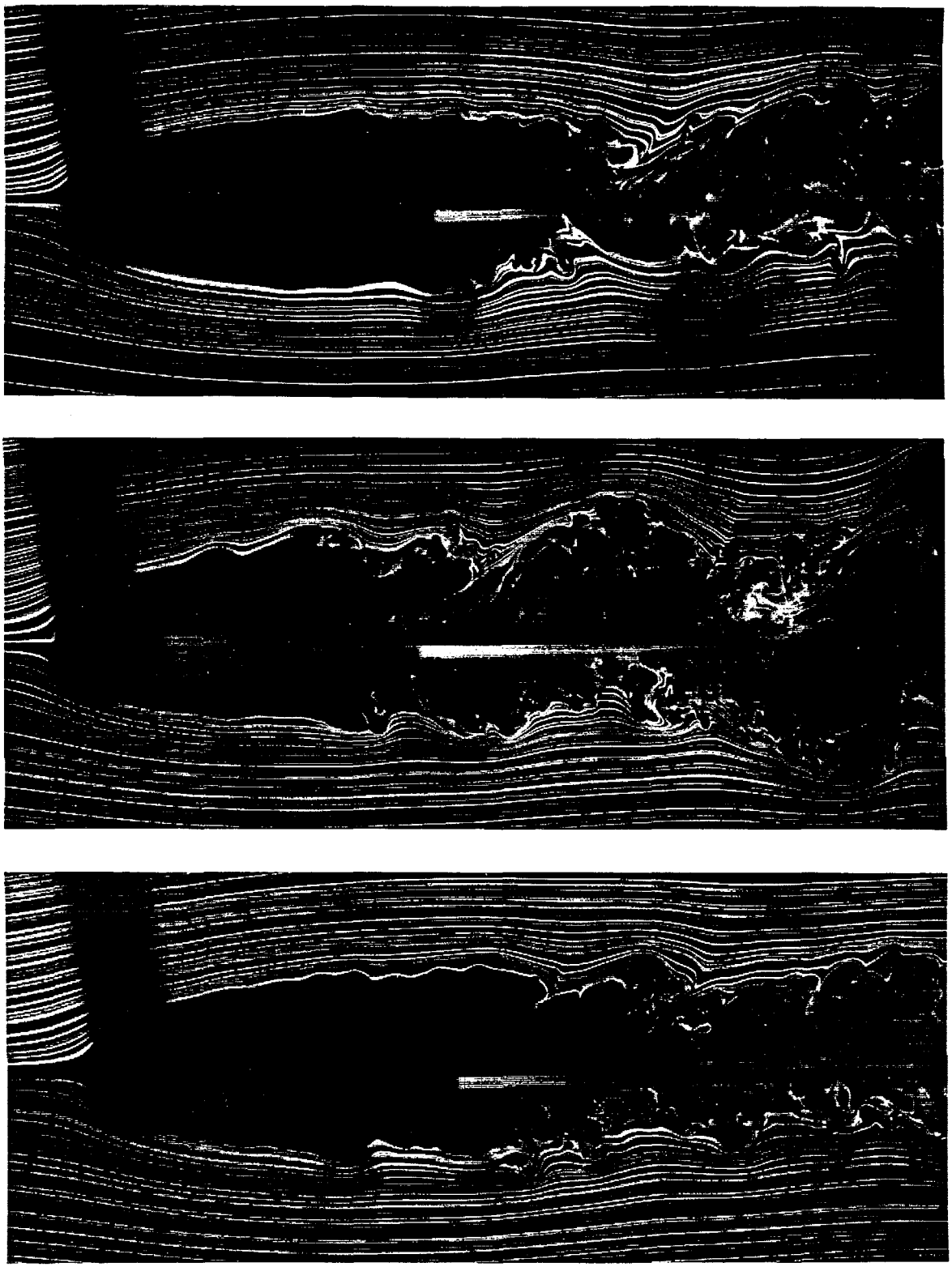

FIG. 6.1 Smoke wire flow visualization of the acoustically forced near wake, $\sigma = 0.65$, $\mathrm{Re} = 4900$: (**a**) no acoustic forcing, (**b**) acoustic forcing at $f_{a*} = 1.14$, (**c**) acoustic forcing at $f_{a*} = 1.18$.

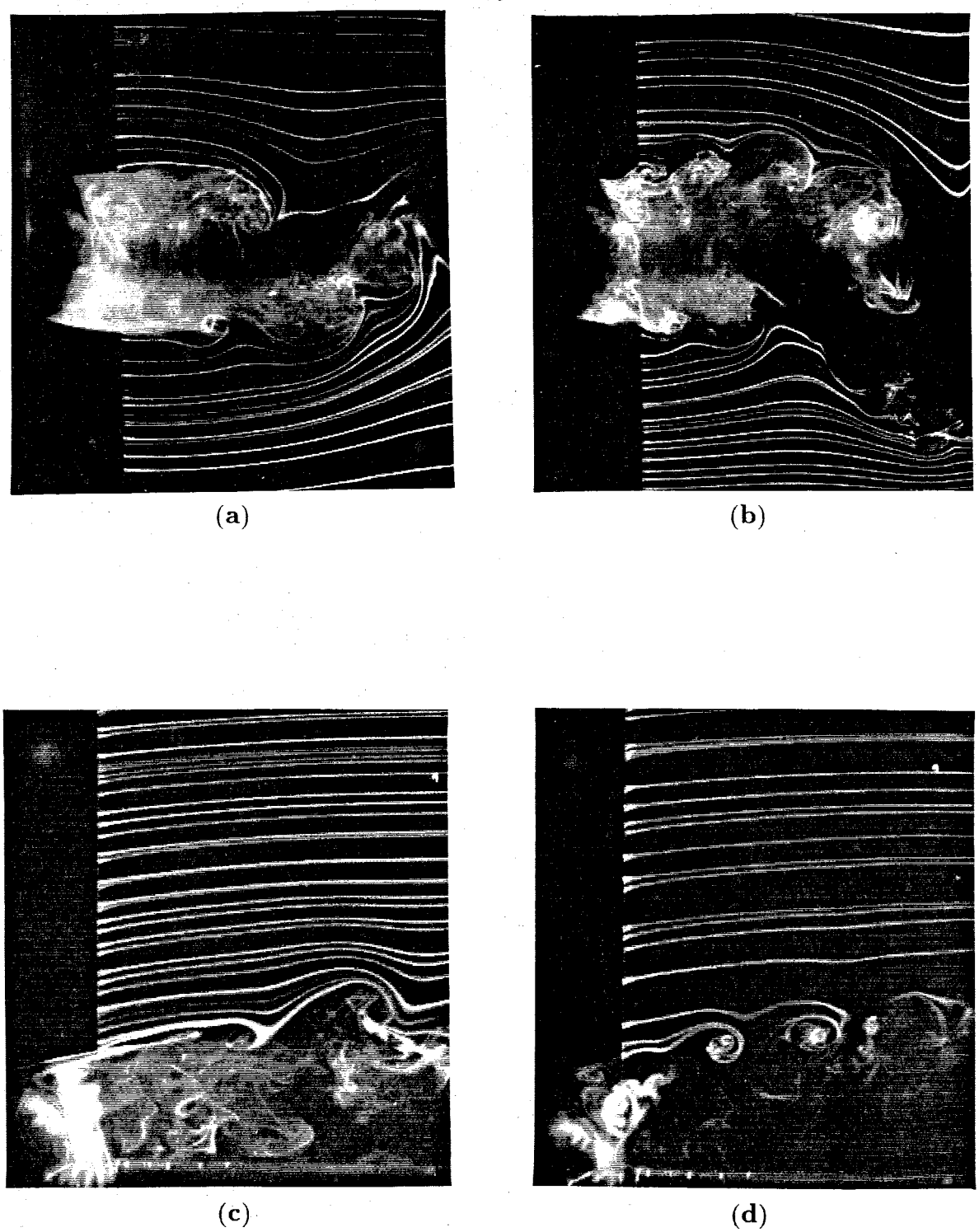

(a) (b)

(c) (d)

FIG. 6.2 Smoke wire flow visualization of the separated shear layers, with and without forcing. (**a**) $\sigma = 0$, Re = 5000, no forcing; (**b**) $\sigma = 0$, Re = 5000, forced at $f_{a*} = 1.68$; (**c**) $\sigma = 0.65$, Re = 5650, no forcing; (**d**) $\sigma = 0.65$, Re = 5600, forced at $f_{a*} = 1.39$.

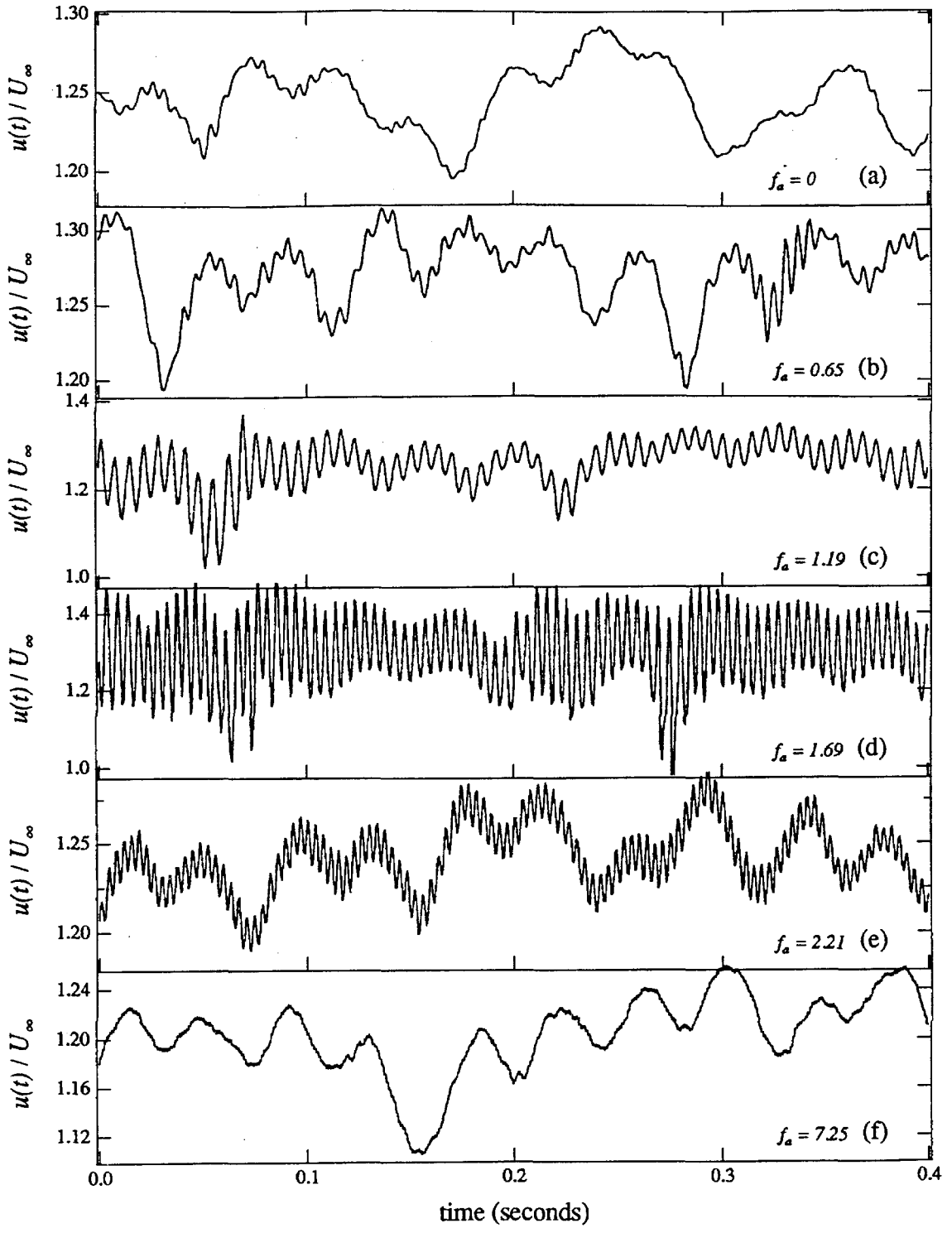

FIG. 6.3 Shear layer velocity traces showing the response of the shear layer to the acoustic forcing, $\sigma = 0.22$ Re $= 4900$. Each separate trace in the figure corresponds to a different forcing frequency, shown on each trace.

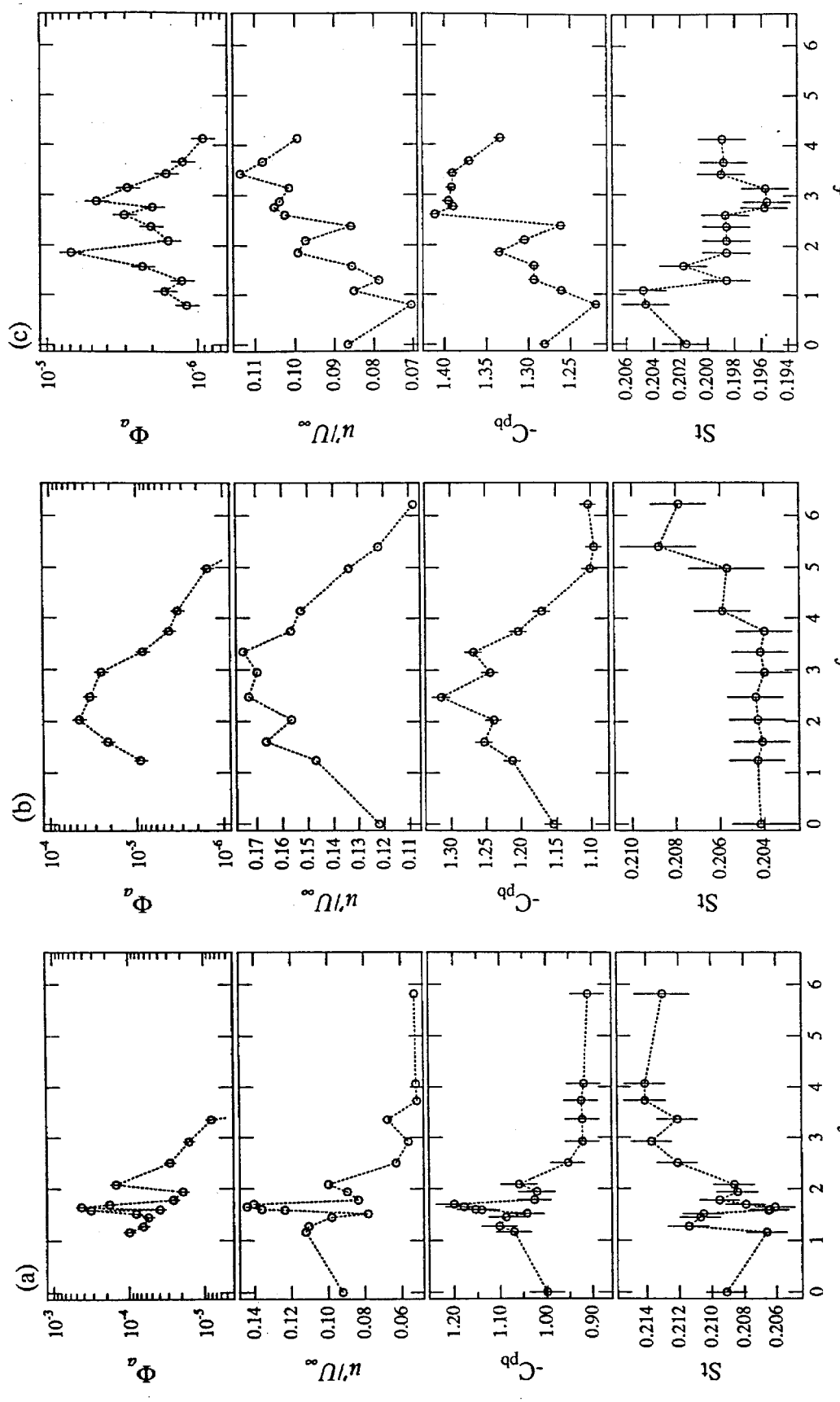

FIG. 6.4 Response of the shear layers to acoustic forcing. Hot wire located at $(x/D, y/D) = (0.6, 0.6)$, base pressure and hot-wire signals recorded simultaneously. The independent coordinate is the normalized forcing frequency $f_{a*} = f_a D/U_\infty$: (**a**) $\sigma = 0$, Re = 4900; (**b**) $\sigma = 0$, Re = 9500; (**c**) $\sigma = 0$, Re = 15100 *(figure continues on next page)*.

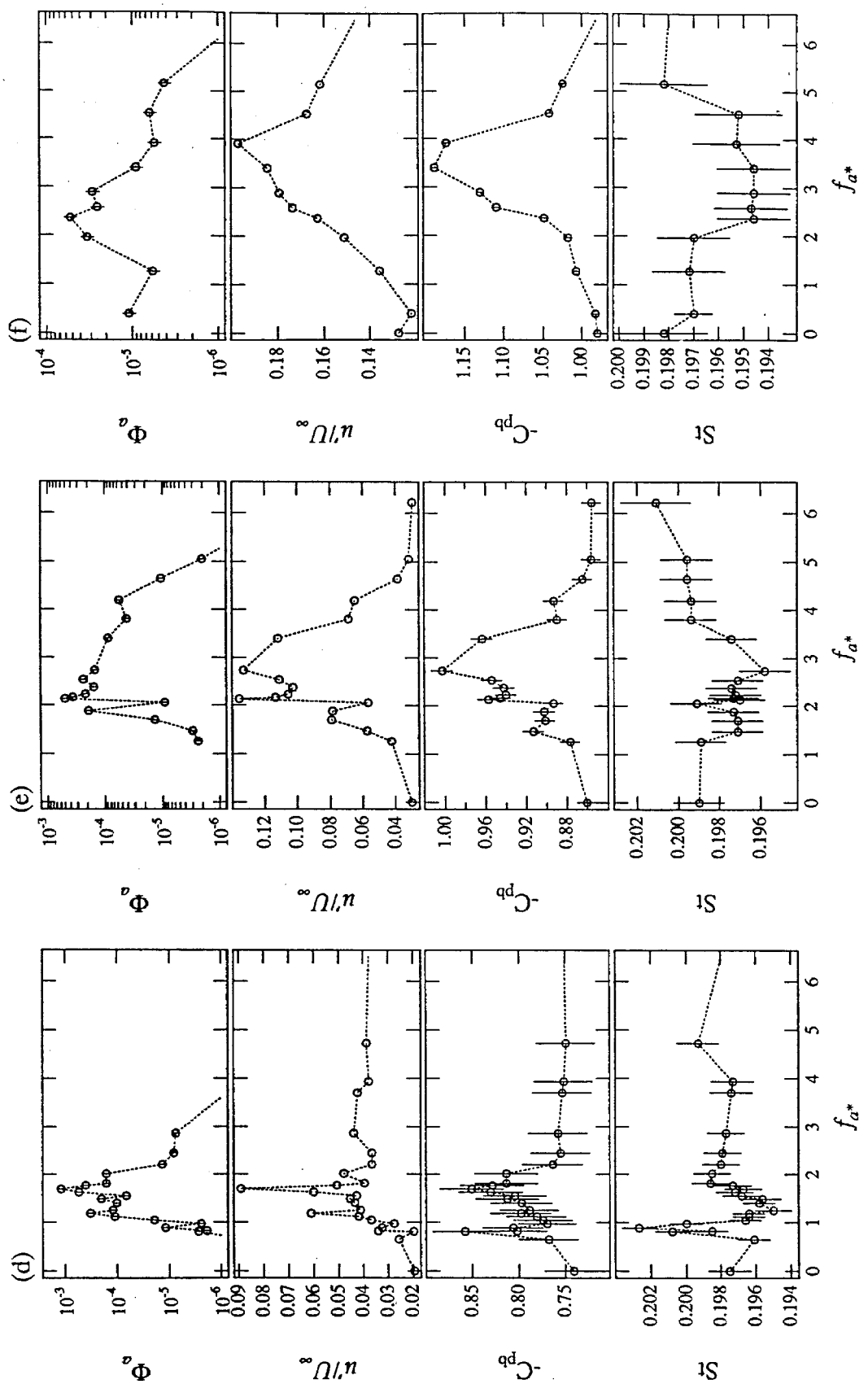

FIG.6.4 (**d**) $\sigma = 0.22$, $\mathrm{Re} = 4900$; (**e**) $\sigma = 0.22$, $\mathrm{Re} = 9500$; (**f**) $\sigma = 0.22$, $\mathrm{Re} = 15100$ *(figure continues on next page).*

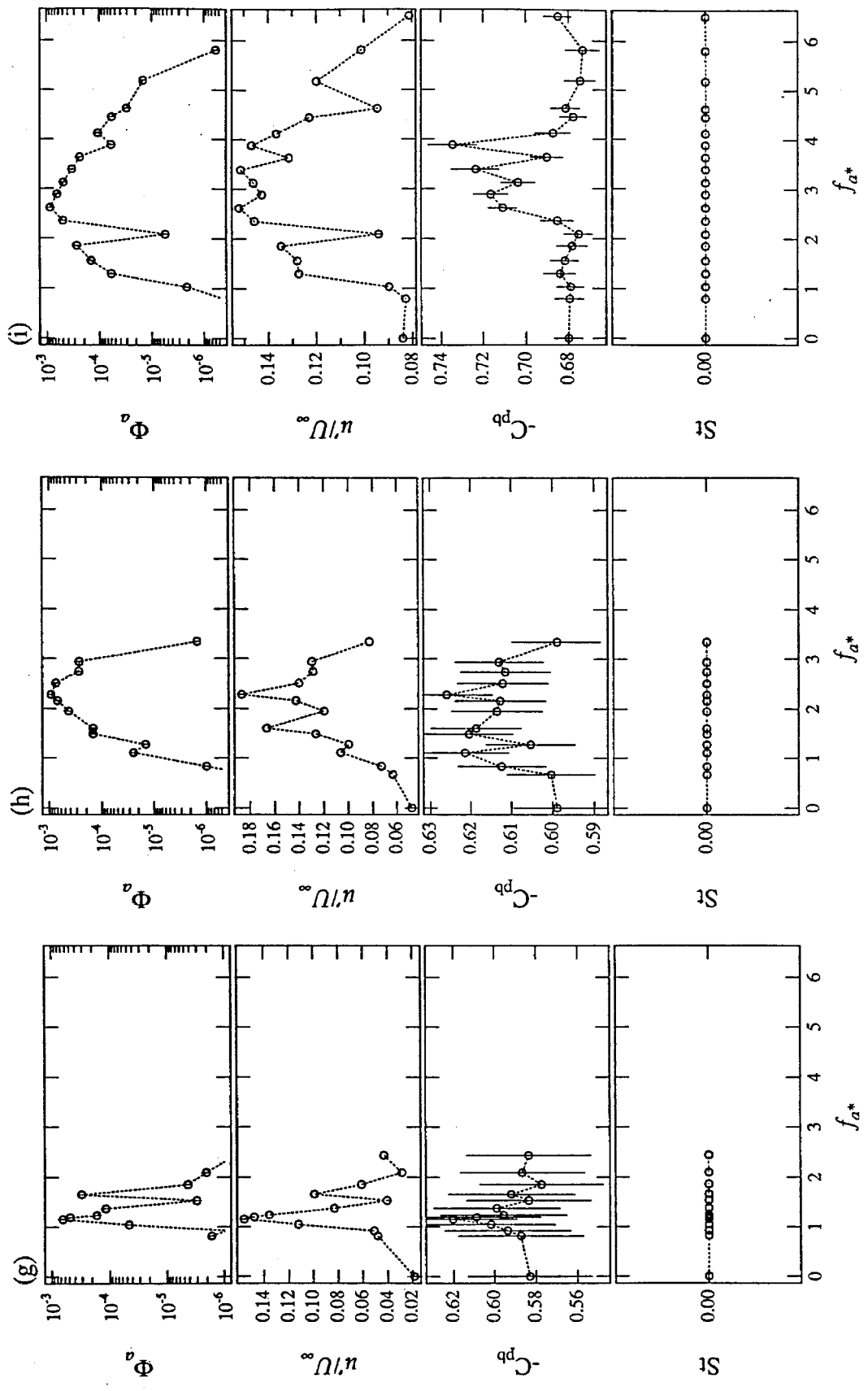

FIG. 6.4 (g) $\sigma = 0.65$, $\mathrm{Re} = 4900$; (h) $\sigma = 0.65$, $\mathrm{Re} = 9500$; (i) $\sigma = 0.65$, $\mathrm{Re} = 15200$.

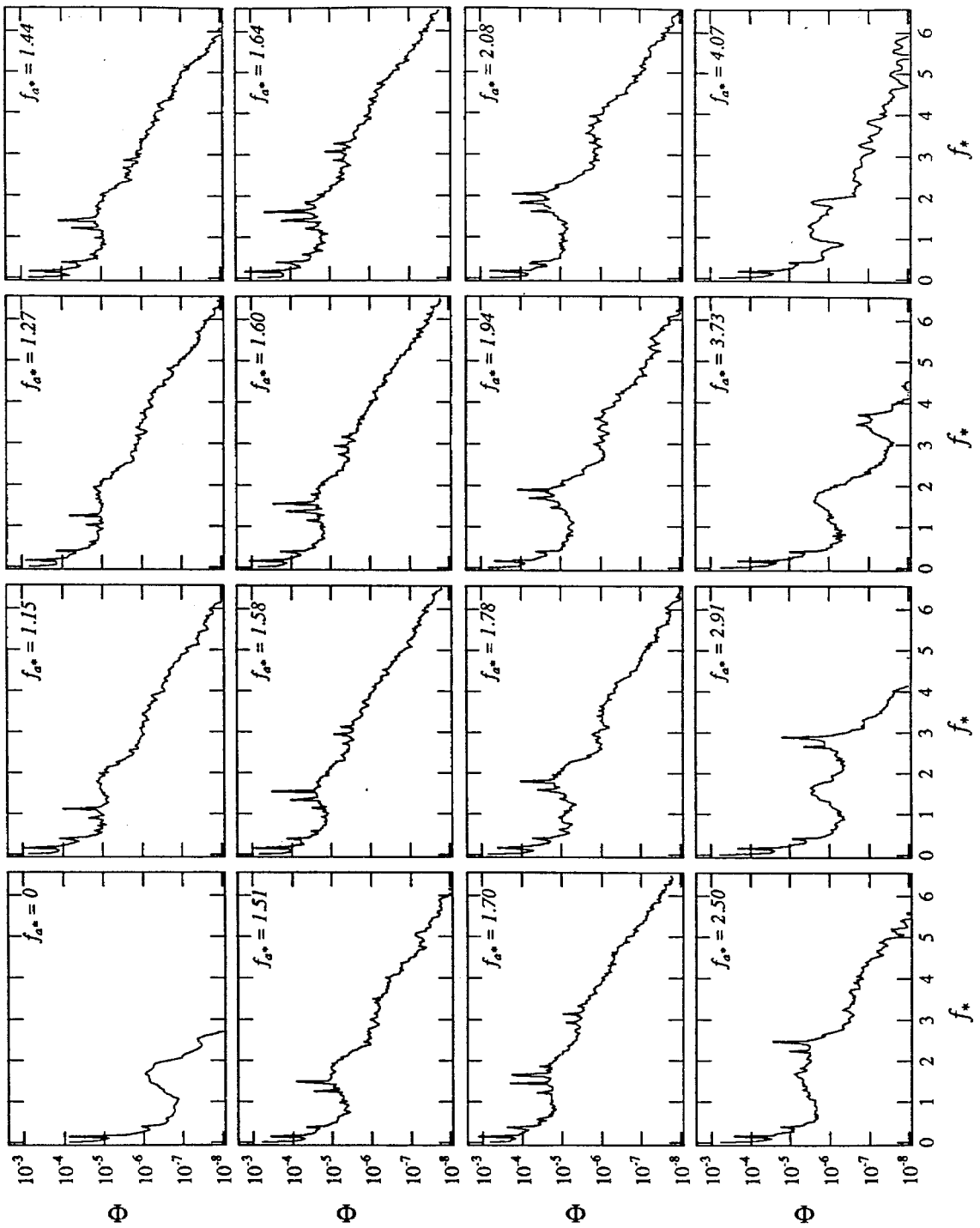

FIG. 6.5 Spectra computed from single point measurements in the forced shear layer, hot wire located at $(x/D, y/D) = (.6, .6)$; (a) $\sigma = 0$, Re = 4900 *(figure continues on next page).*

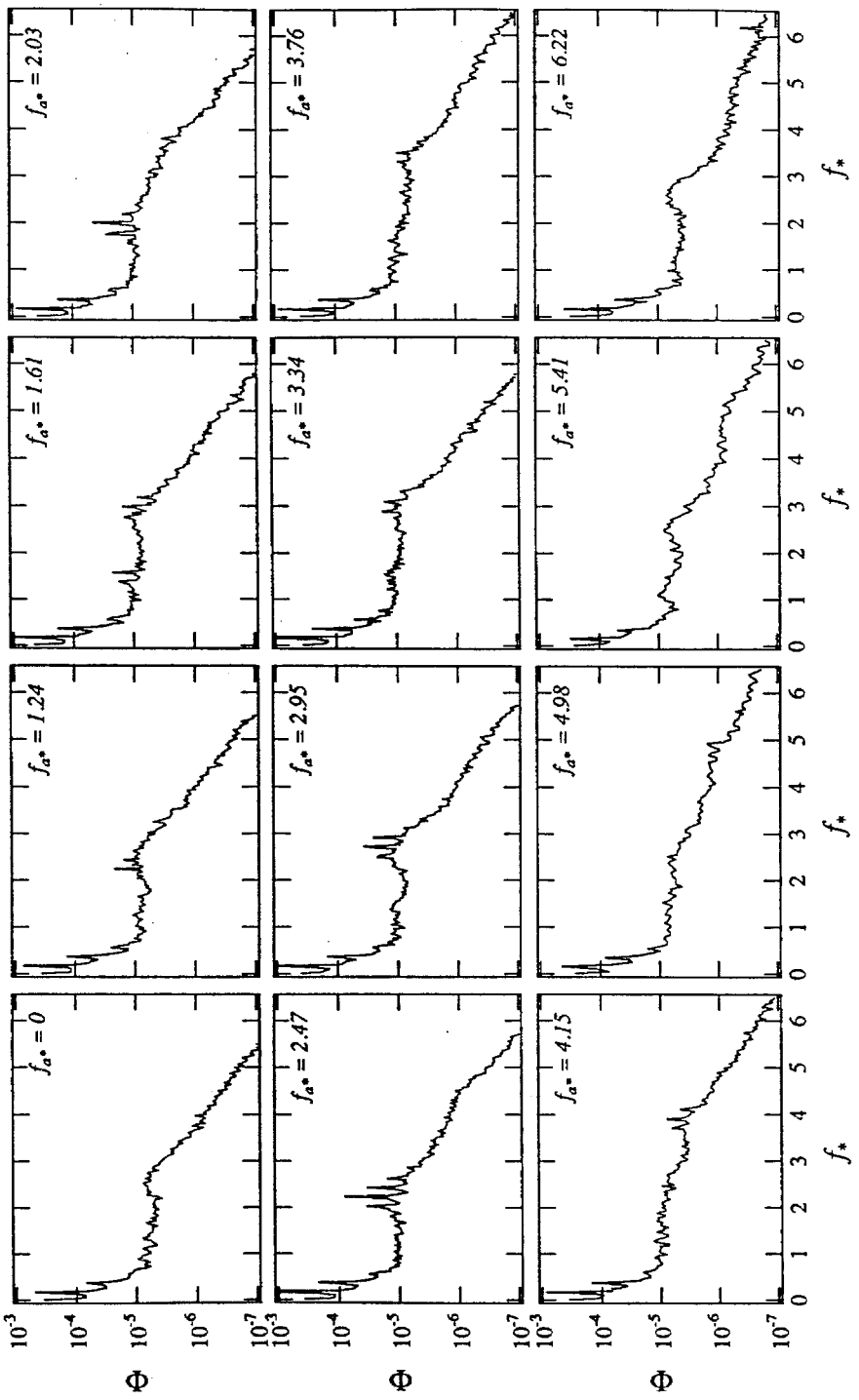

FIG. 6.5b $\sigma = 0$, Re = 9500 *(figure continues on next page).*

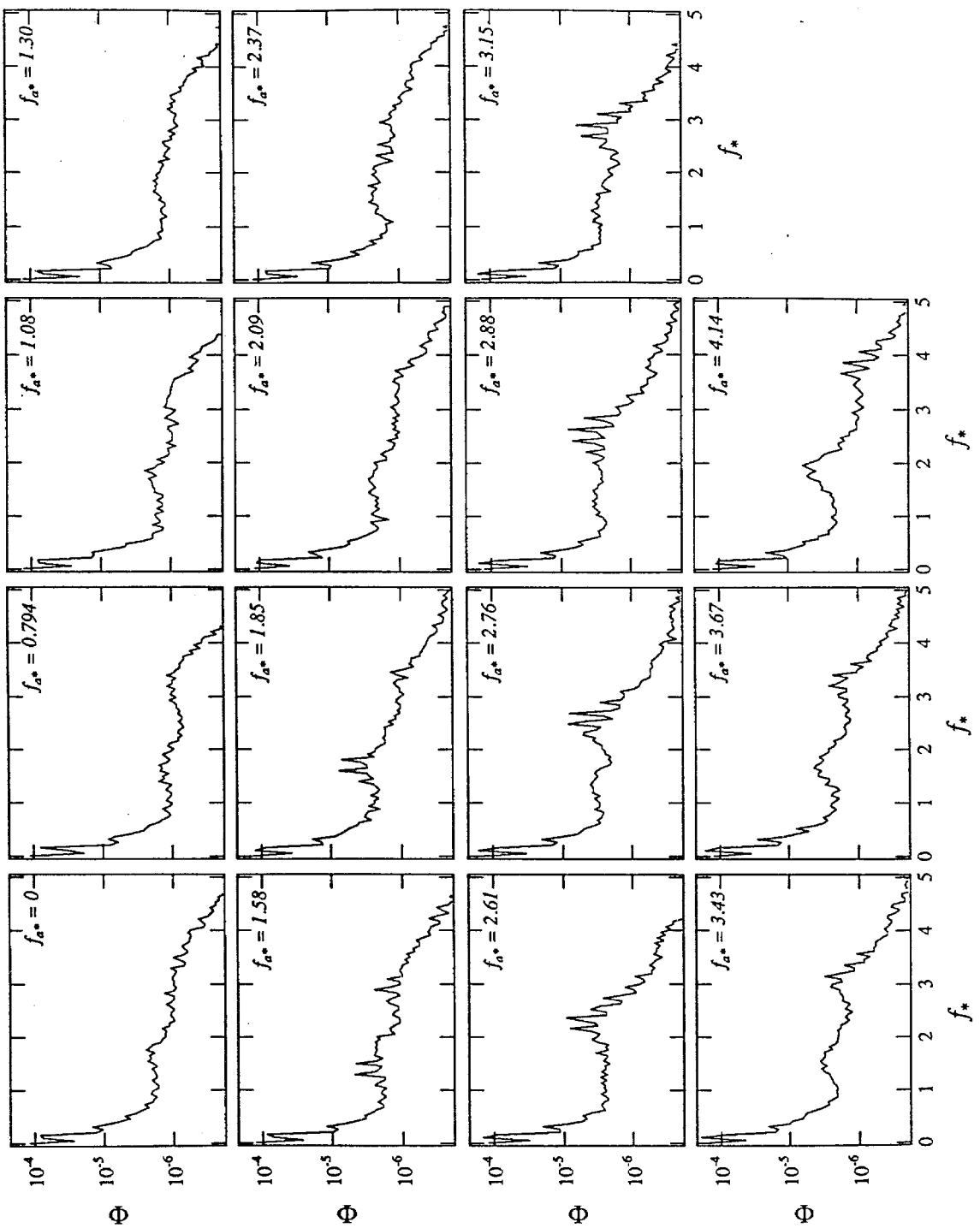

FIG. 6.5c $\sigma = 0$, Re = 15100 *(figure continues on next page).*

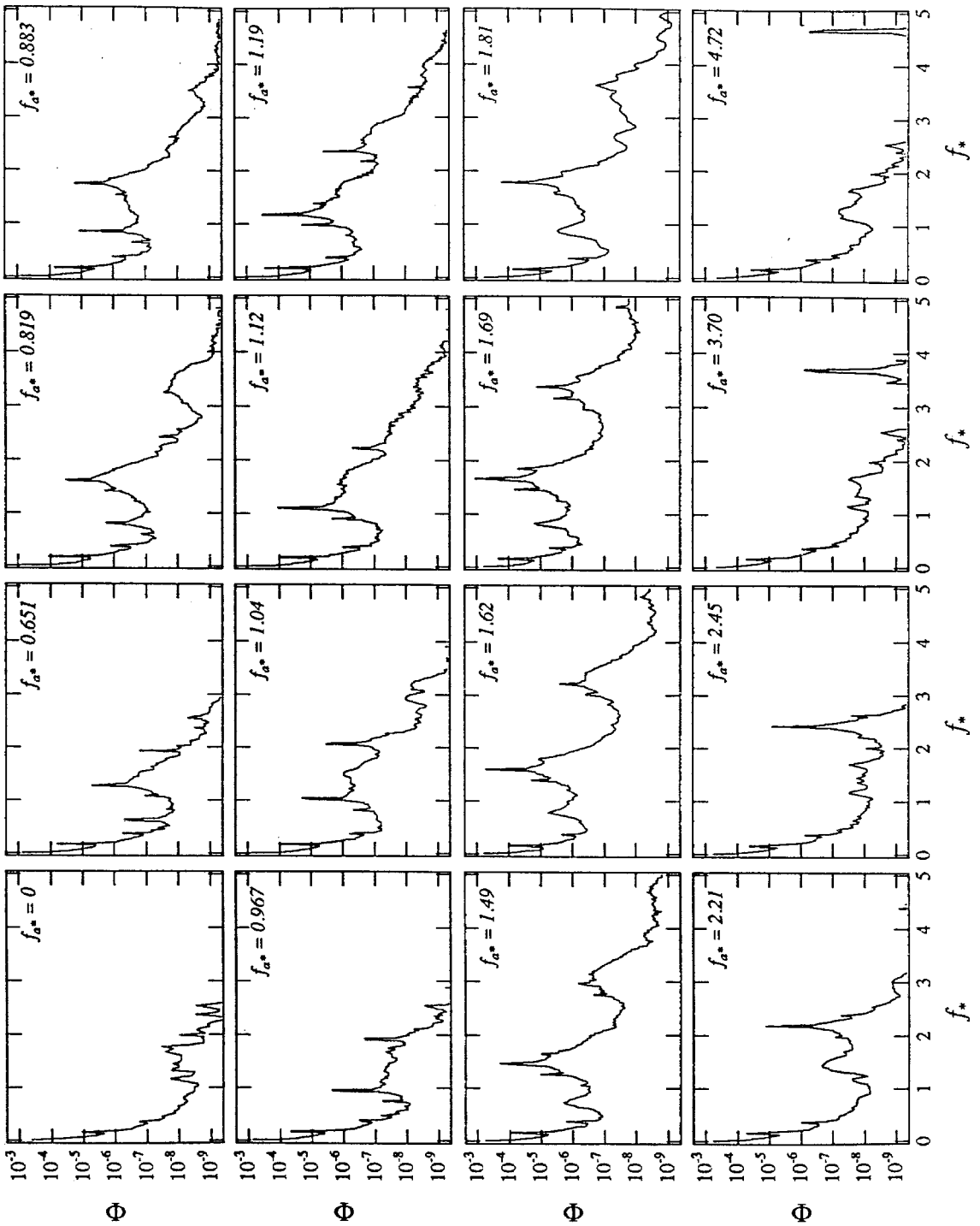

FIG. 6.5d $\sigma = 0.22$, Re = 4900 *(figure continues on next page).*

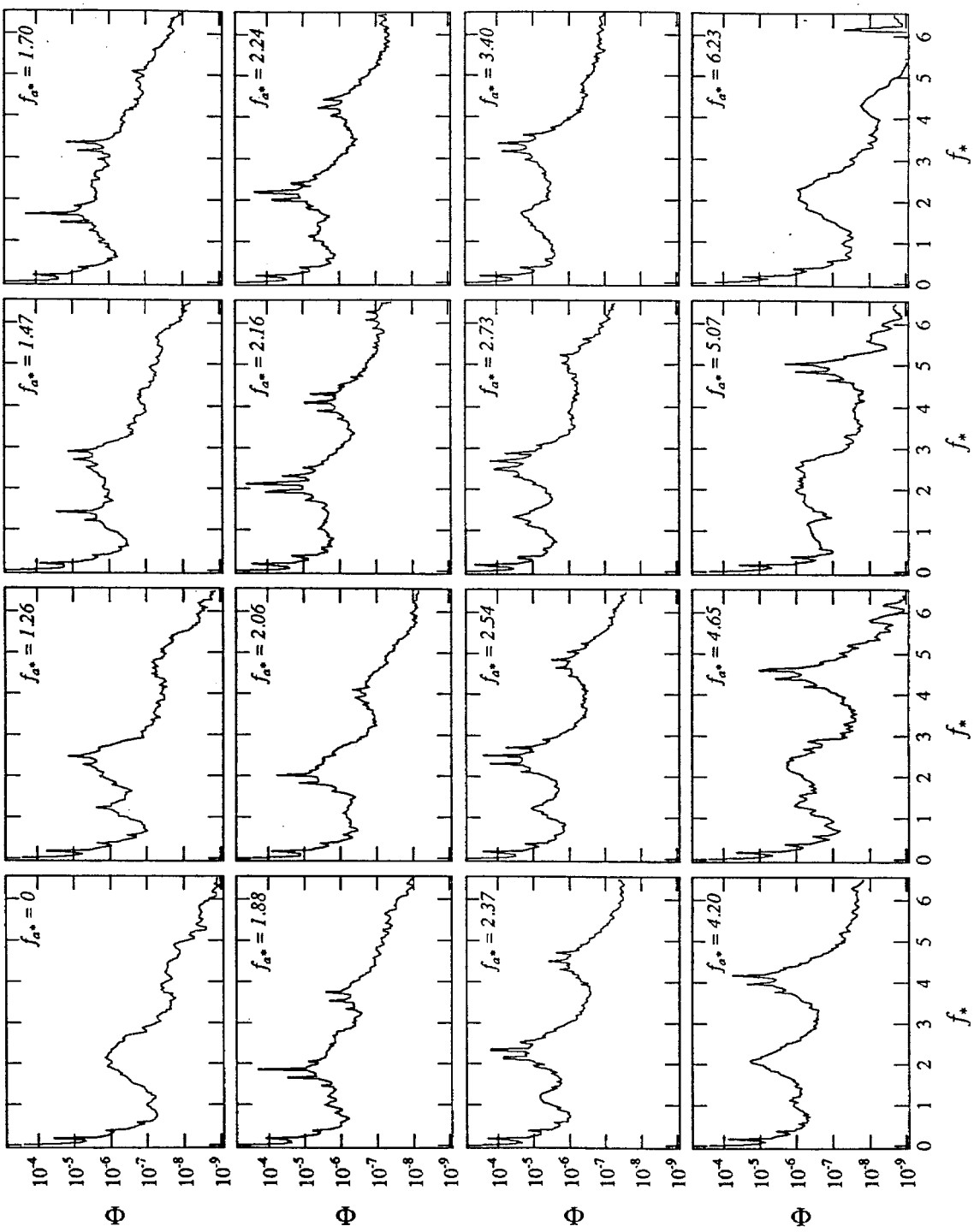

FIG. 6.5e $\sigma = 0.22$, Re = 9500 *(figure continues on next page).*

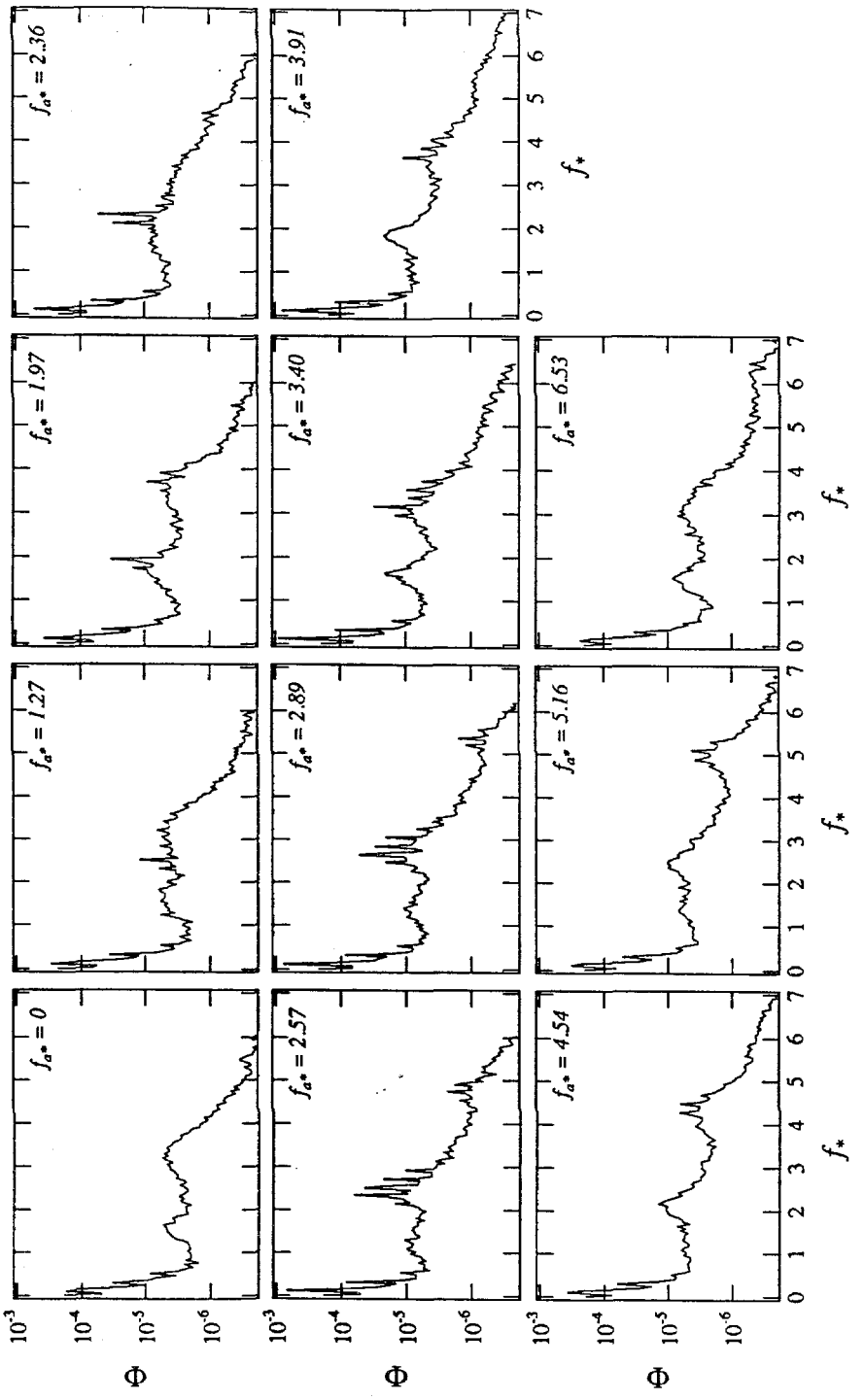

FIG. 6.5f $\sigma = 0.22$, Re = 15100 *(figure continues on next page).*

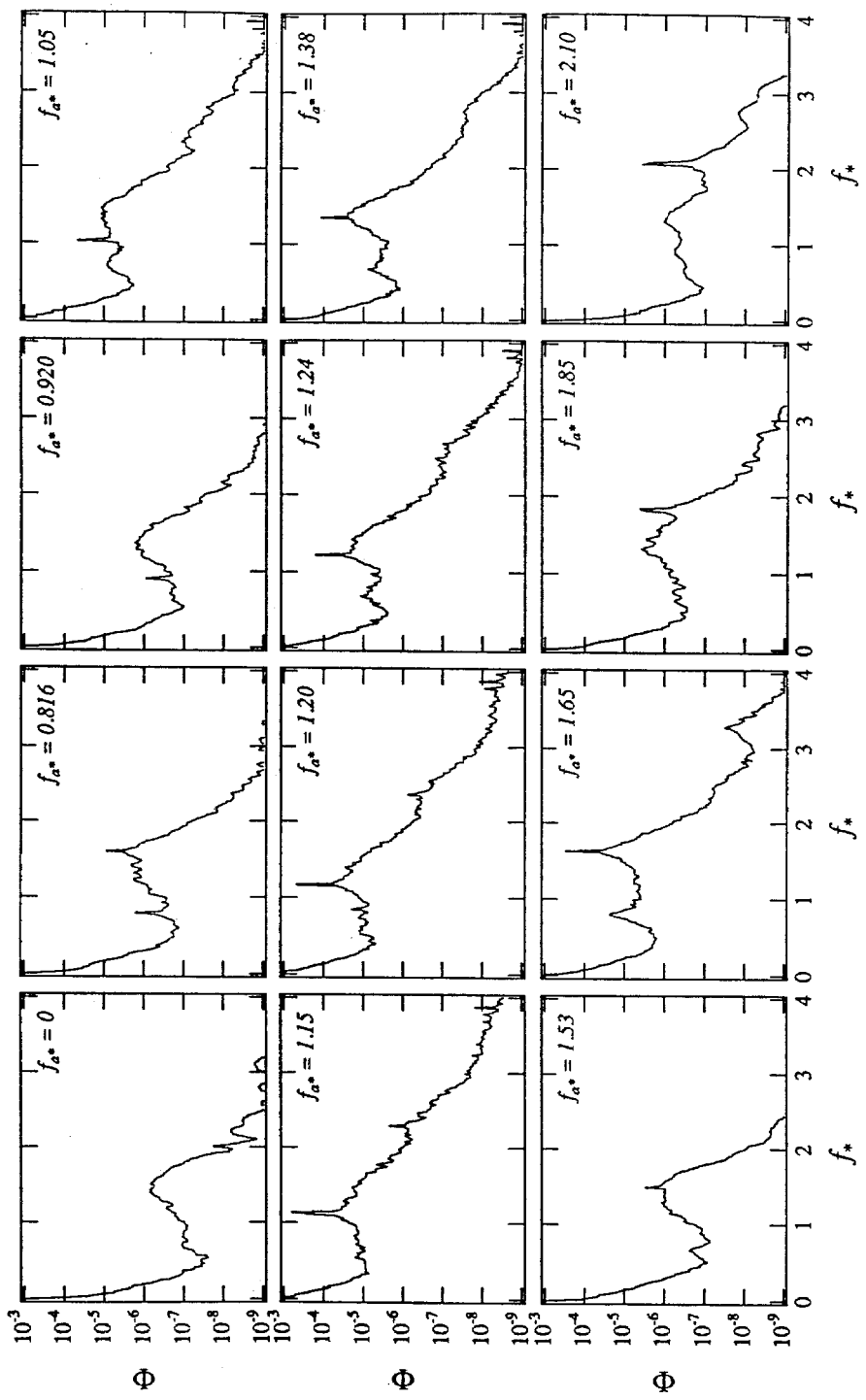

FIG. 6.5g $\sigma = 0.65$, Re = 4900 *(figure continues on next page).*

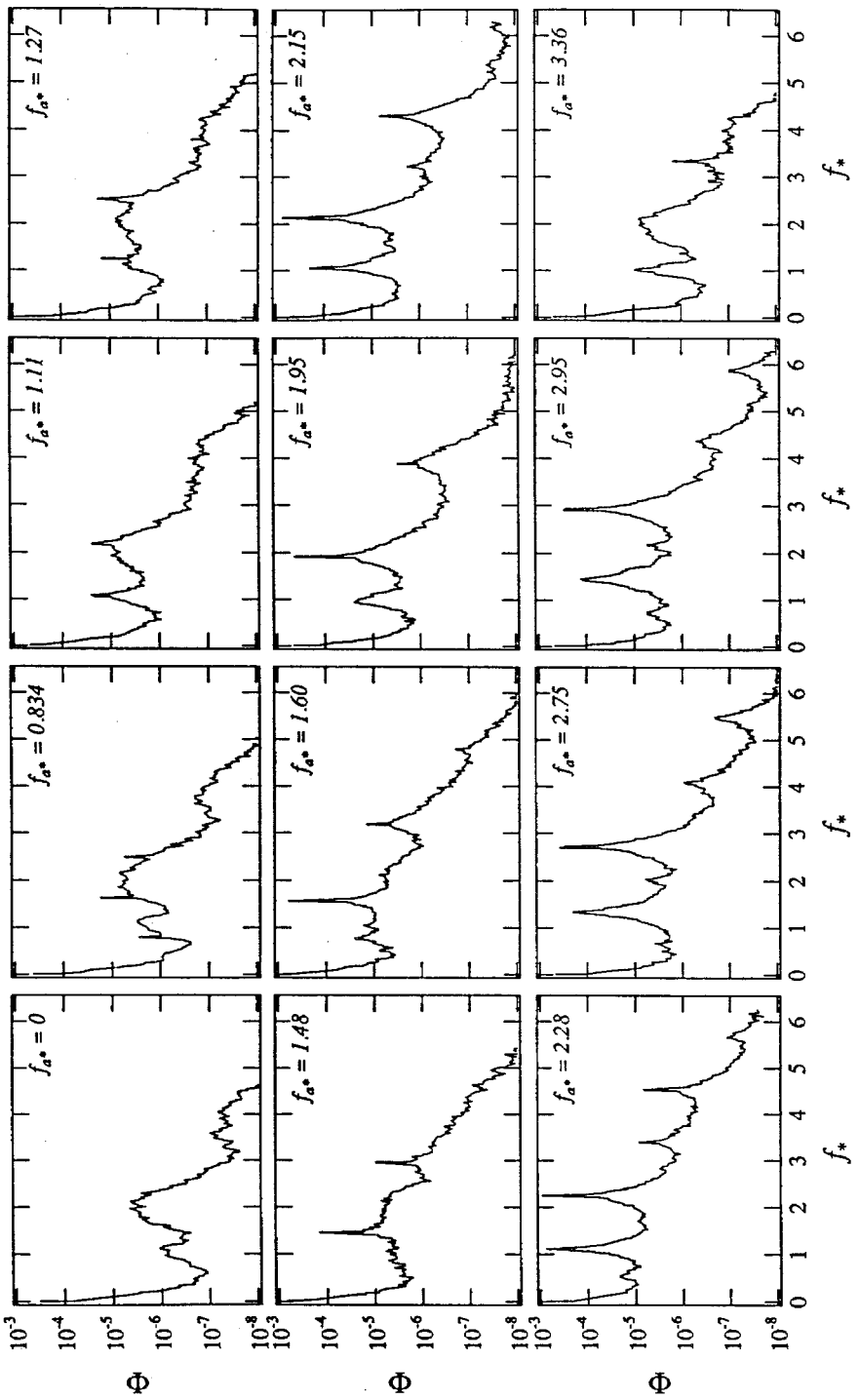

FIG. 6.5h $\sigma = 0.65$, Re = 9500 *(figure continues on next page).*

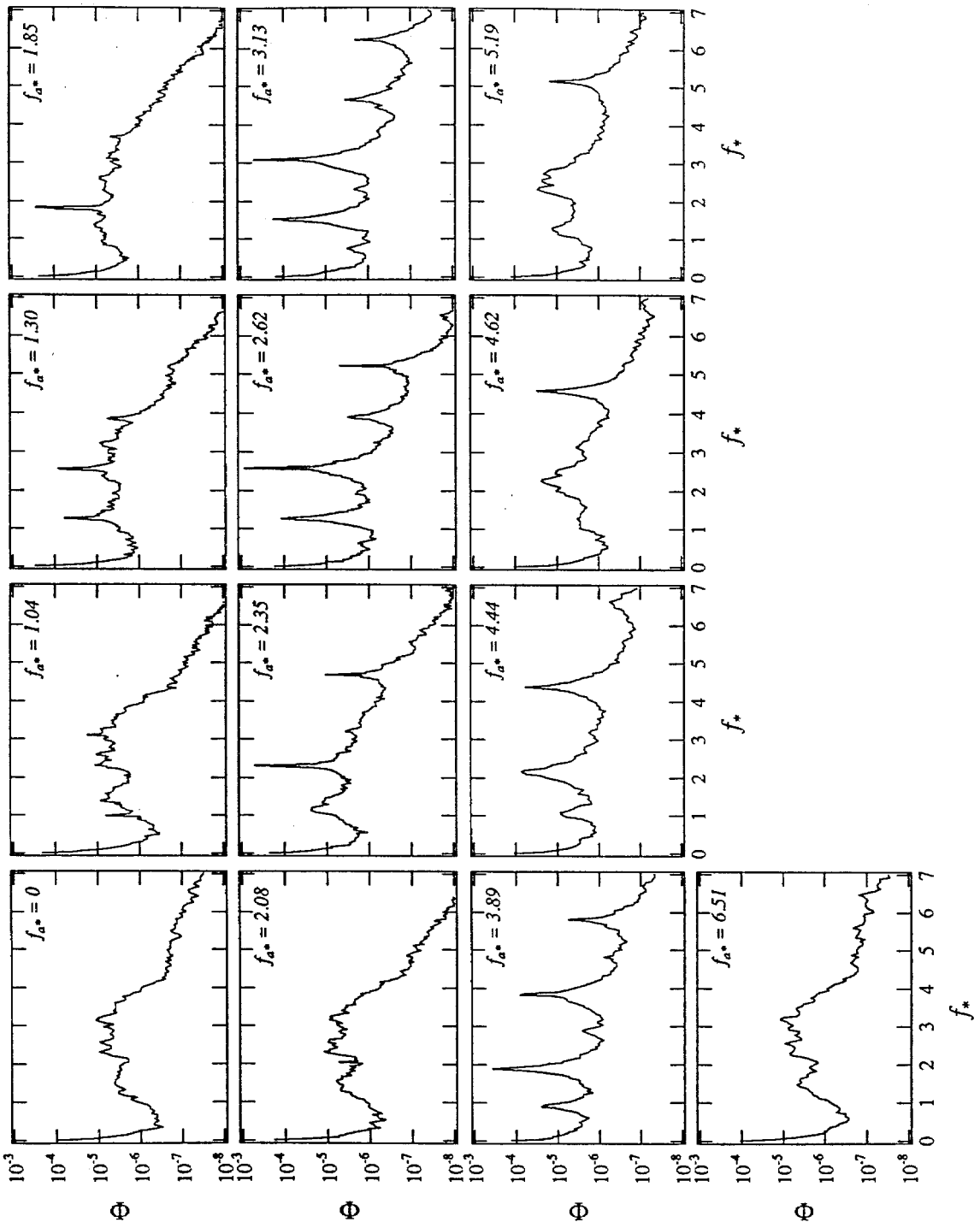

FIG. 6.5i $\sigma = 0.65$, Re = 15200.

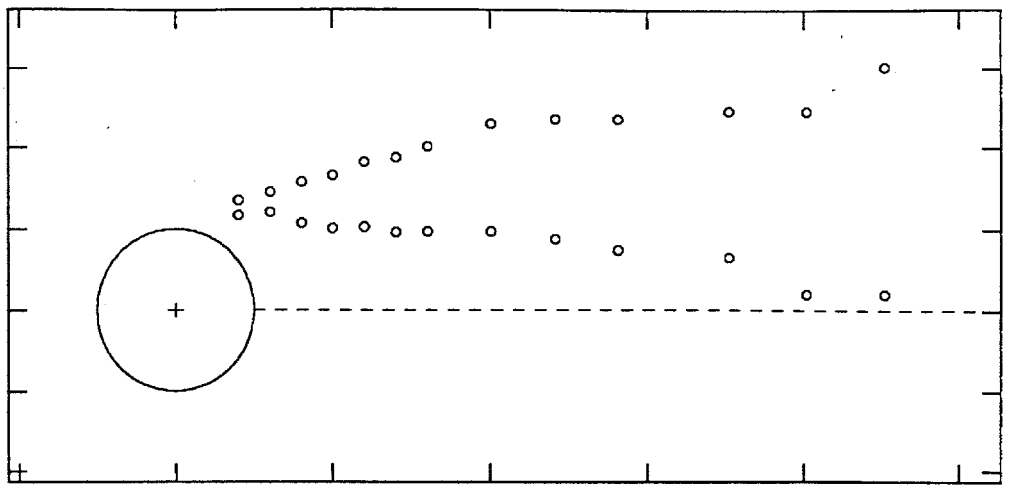

FIG. 6.6 Plot of approximate locations in the shear layers where the velocity reaches 1% and 99% of the local velocity difference across the layers, for the acoustically forced shear layer , Re = 4800, $\sigma = 0.65$, forced at $f_{a*} = 1.25$.

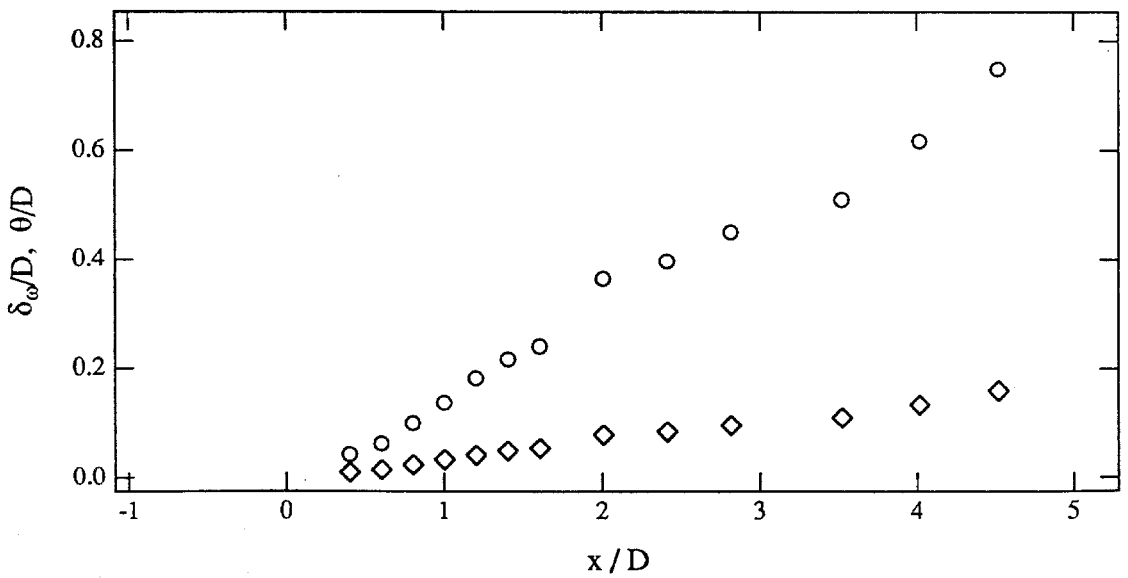

FIG. 6.7 Plot of the vorticity and momentum thickness with downstream position for the acoustically forced shear layer , Re = 4800, $\sigma = 0.65$, forced at $f_{a*} = 1.25$. Symbols are (◇) θ; (○) δ_ω.

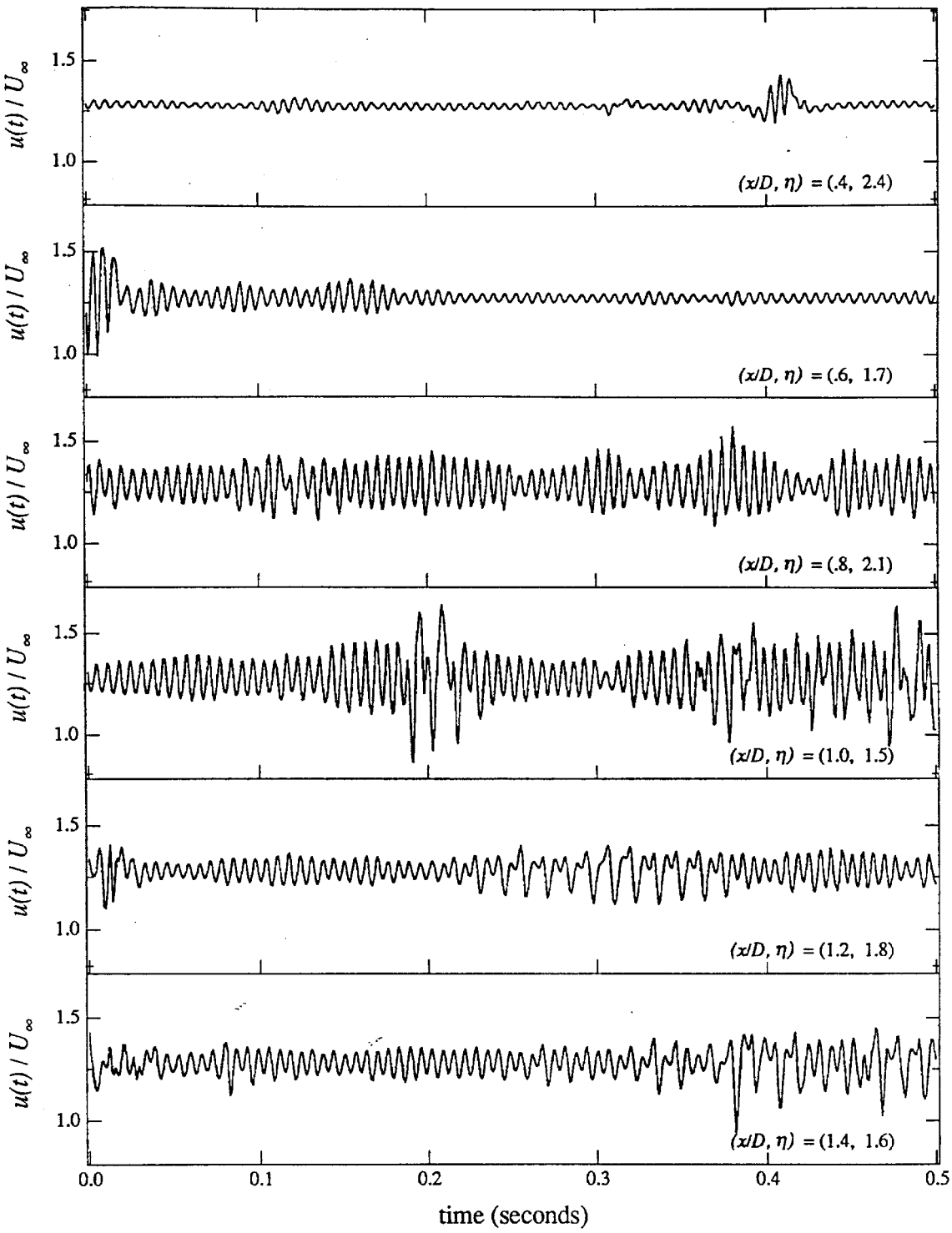

FIG. 6.8 Shear layer velocity traces showing the development of the shear layer instability in the presence of forcing. Re = 4800, $\sigma = 0.65$, forced at $f_{a*} = 1.25$. Each separate trace in the figure corresponds to a different downstream location, and the downstream location x/D and the transverse location in normalized shear layer coordinates are shown with each trace *(figure continues on next page)*.

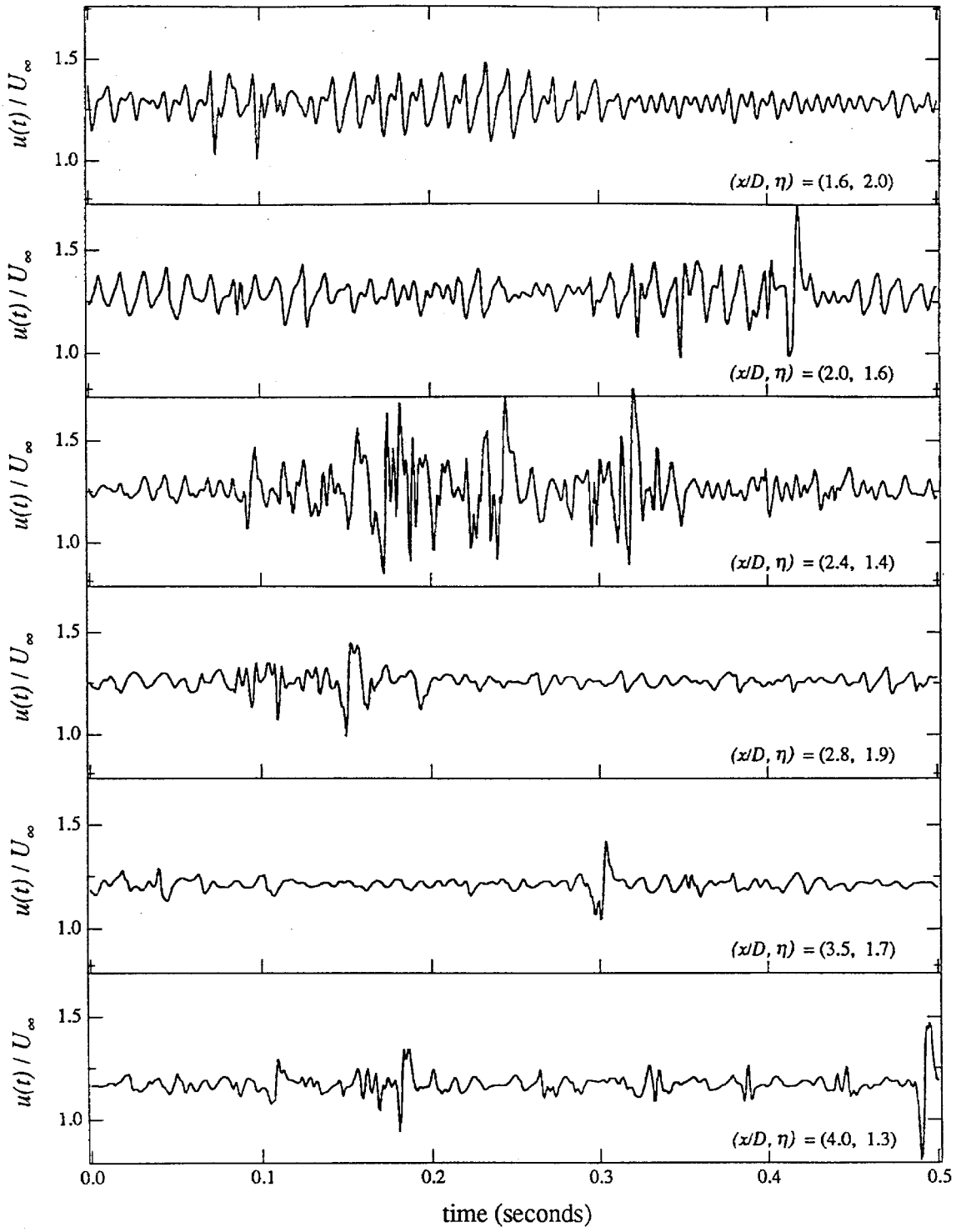

FIG. 6.8 *cont.* See the preceding page for caption.

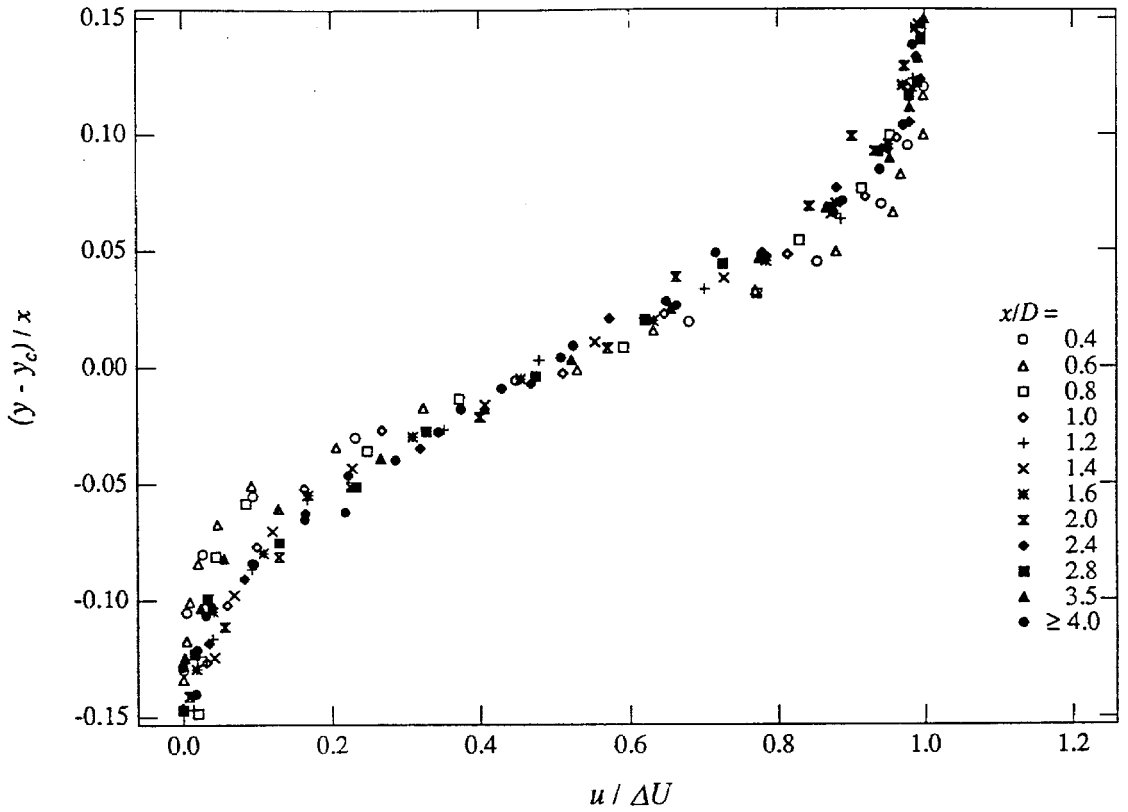

FIG. 6.9 Forced shear layer profile data plotted using similarity coordinates $u/\Delta U$ versus $(y - y_c)/x$; $\sigma = 0.65$, Re $= 4800$, $f_{a*} = 1.25$.

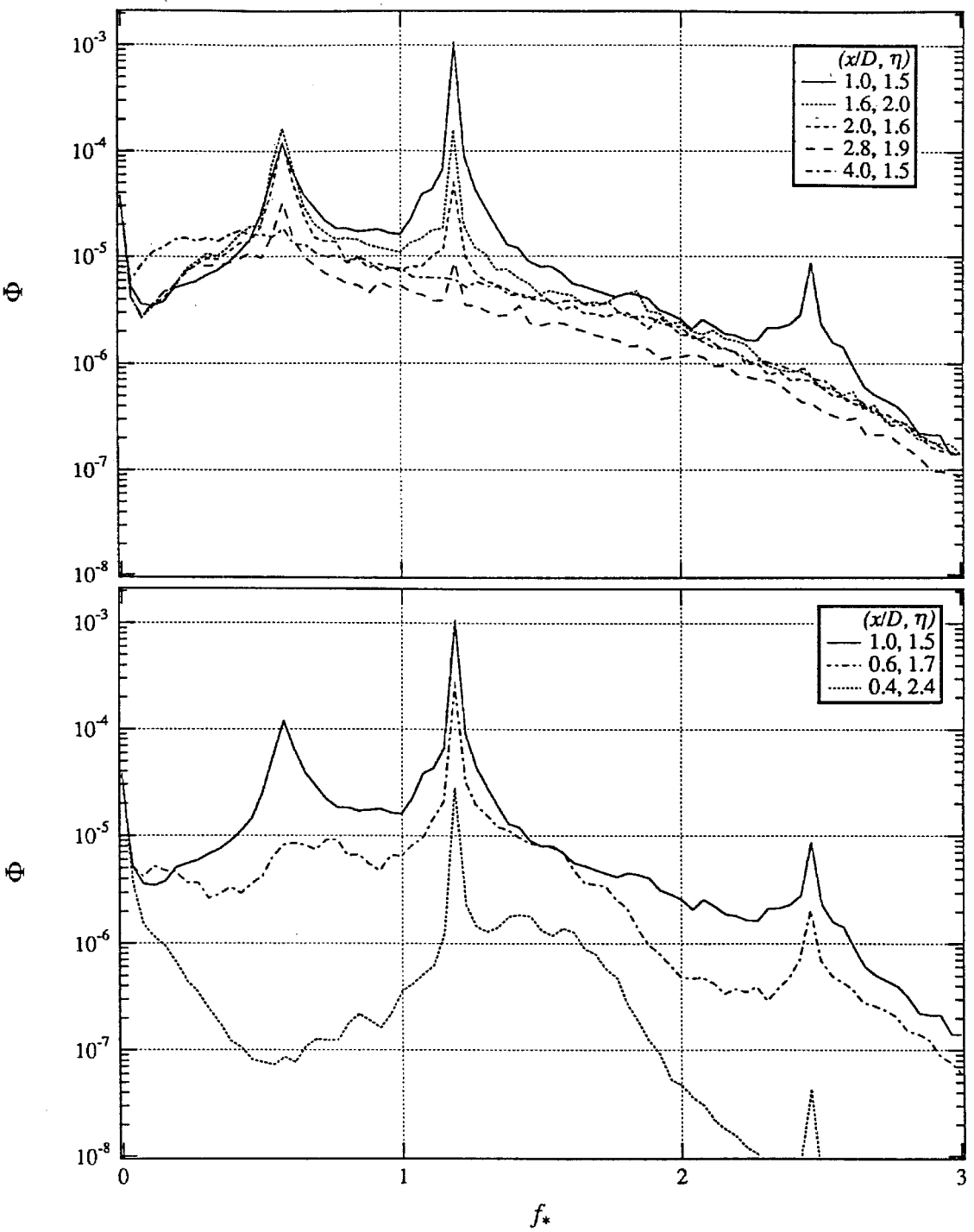

FIG. 6.10 Spectral evolution of the acoustically forced shear layer, , $\sigma = 0.65$, Re = 4800, forced at $f_{a*} = 1.25$. Spectra computed from data taken near the outside edge of the shear layer at different downstream positions, showing the development of the shear layer instability frequencies with increasing downstream position.

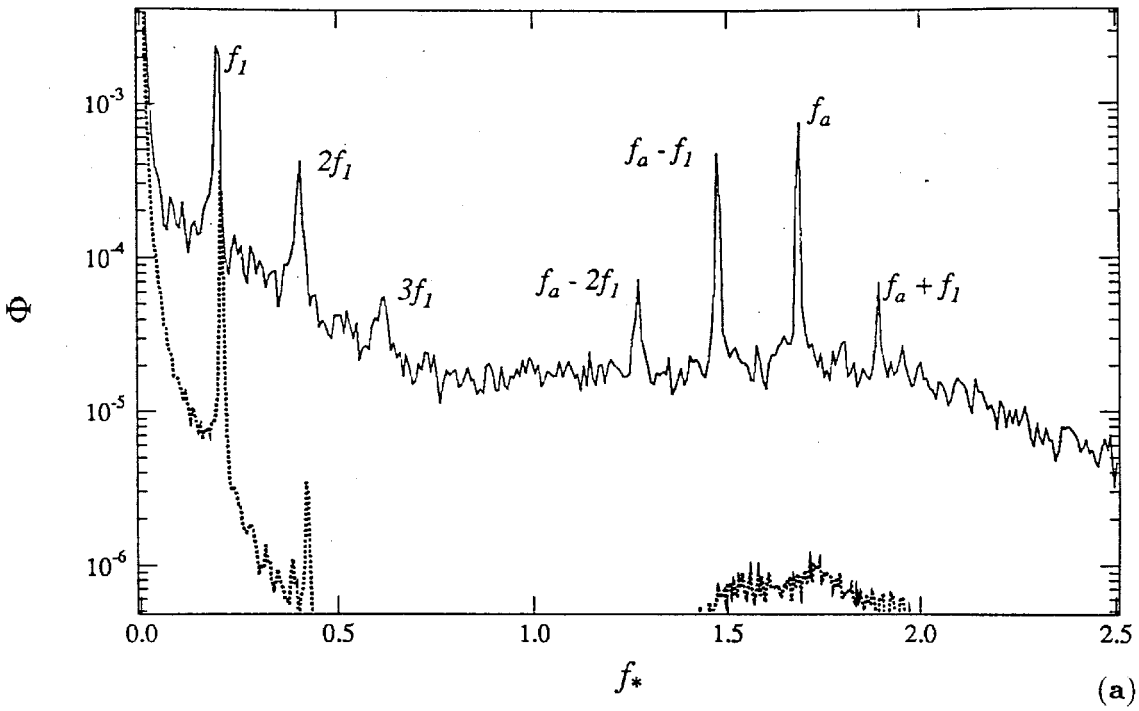

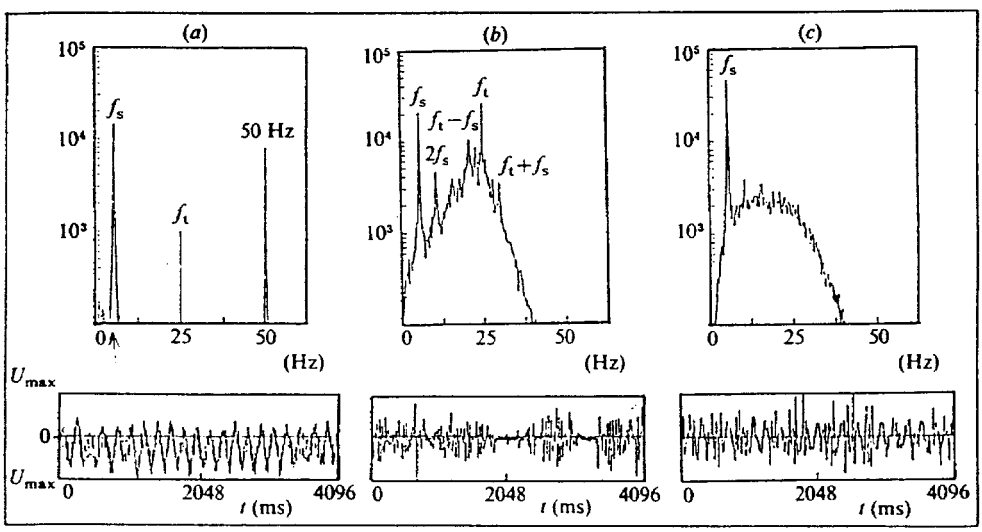

FIGURE 8. Power spectra and traces in the shear layer; $Y/D = 0.625$, $R = 2660$. (*a*) $X/D = 0.125$; (*b*) 1.375; (*c*) 3.525 (arbitrary scales).

FIG. 6.11 Spectra from single point measurements showing beat frequencies between the primary wake frequency and a forcing frequency, (**a**) Present experiments, $\sigma = 0$, Re = 4800, acoustic forcing imposed at $f_{a*} = 1.70$; (**b**) Figure 8 from Kourta *et al.*, $\sigma = 0$, Re = 2660, $f_{a*} \approx 1.1$ (estimated from the figure).

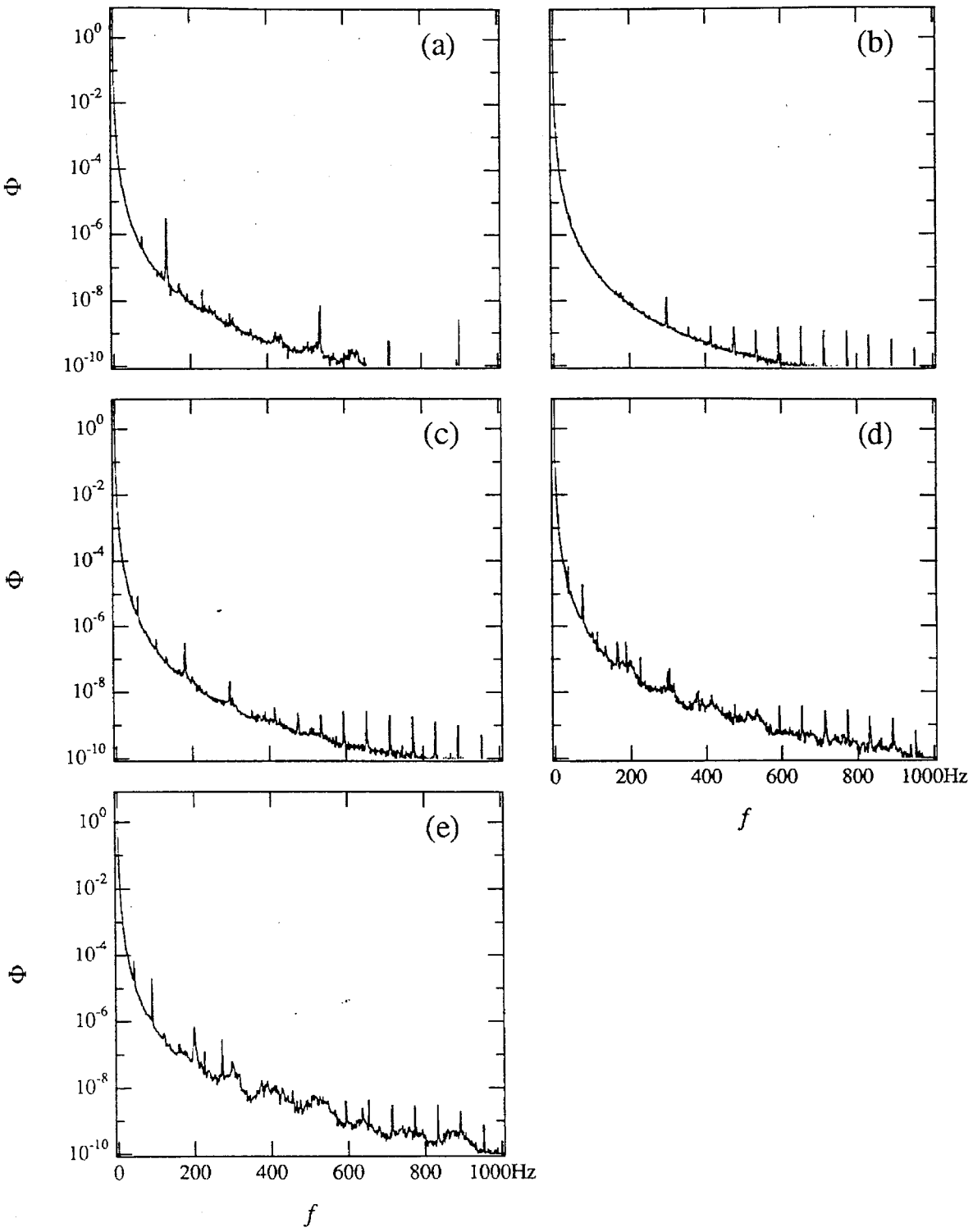

FIG. A.1 Power spectral density computed from measurements of the free-stream turbulence in the wind tunnel at different values of U_∞. The hot-wire output was converted to velocity. Spectra computed from 32 blocks of 2048 samples, signal gain $G = 1000$, $f_C = 1$ kHz, $f_N = 1.5$ kHz.

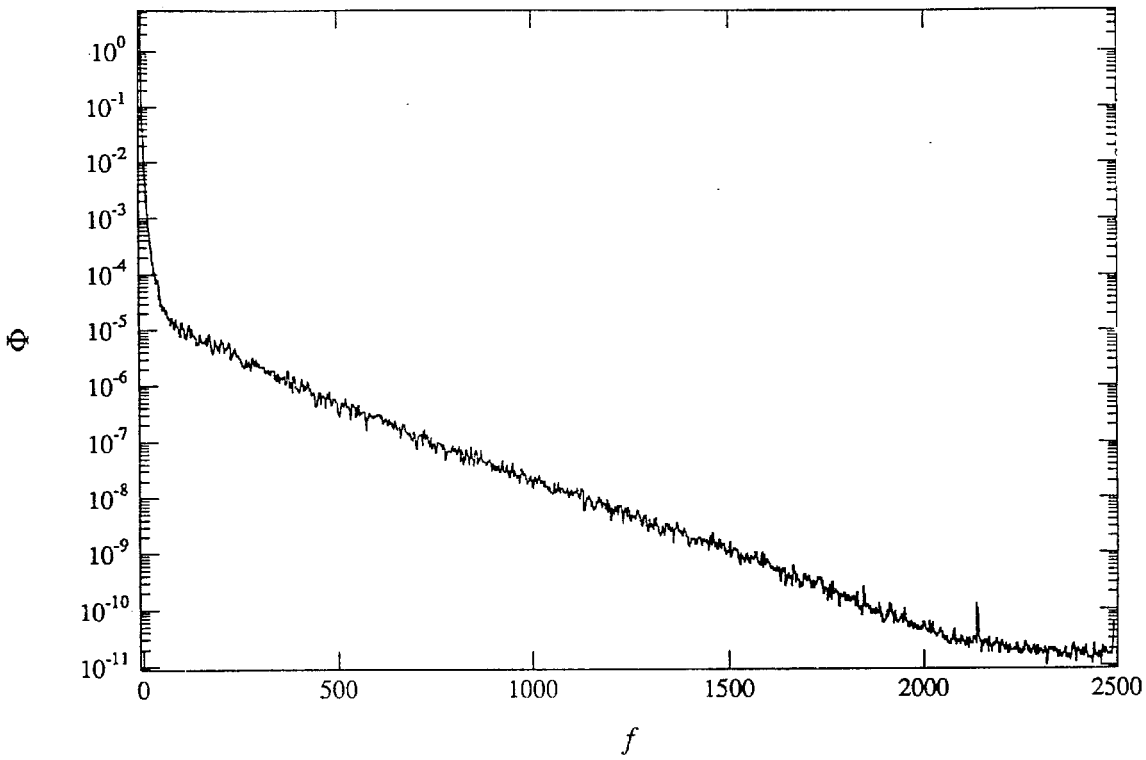

FIG. A.2 Power spectral density computed from hot-wire measurements behind a turbulence generating screen. The hot-wire output was converted to velocity. Spectra computed from 32 blocks of 2048 samples, signal gain $G = 200$, $f_C = 2$ kHz, $f_N = 2.5$ kHz.

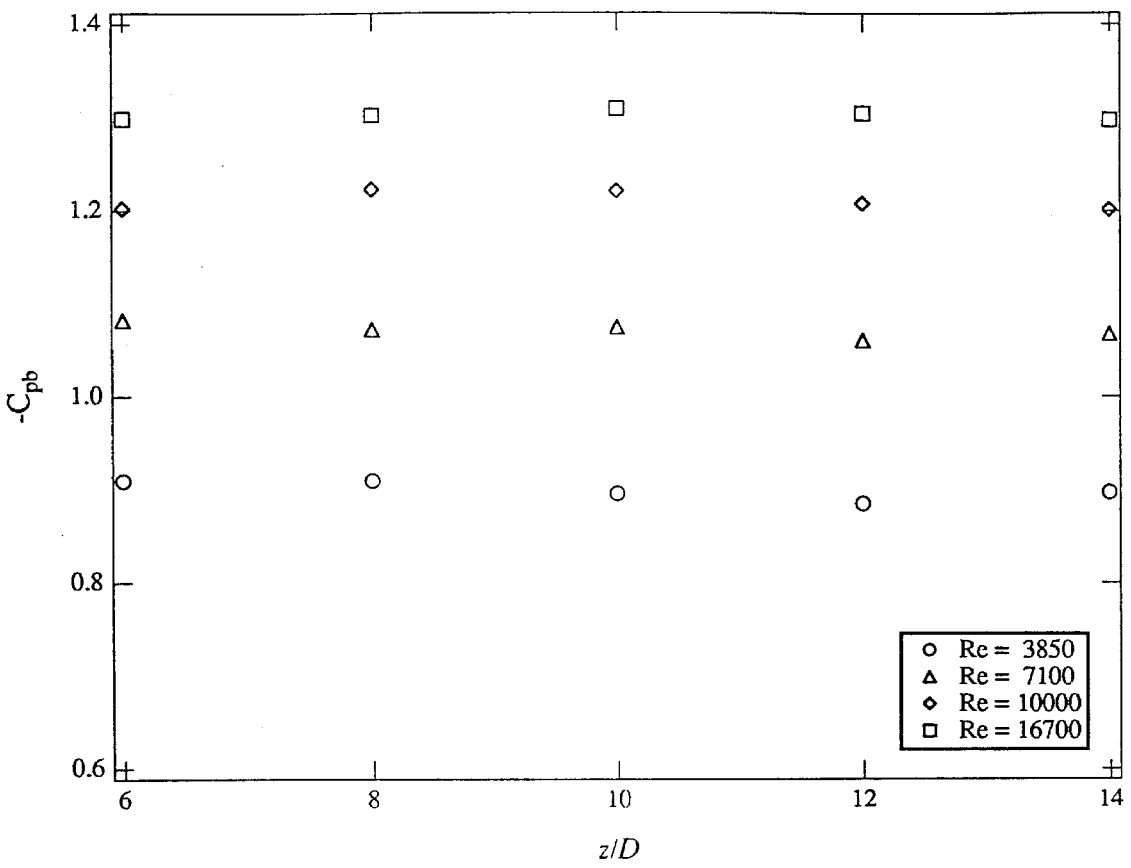

FIG. A.3 Cylinder base pressure measured at different spanwise locations.

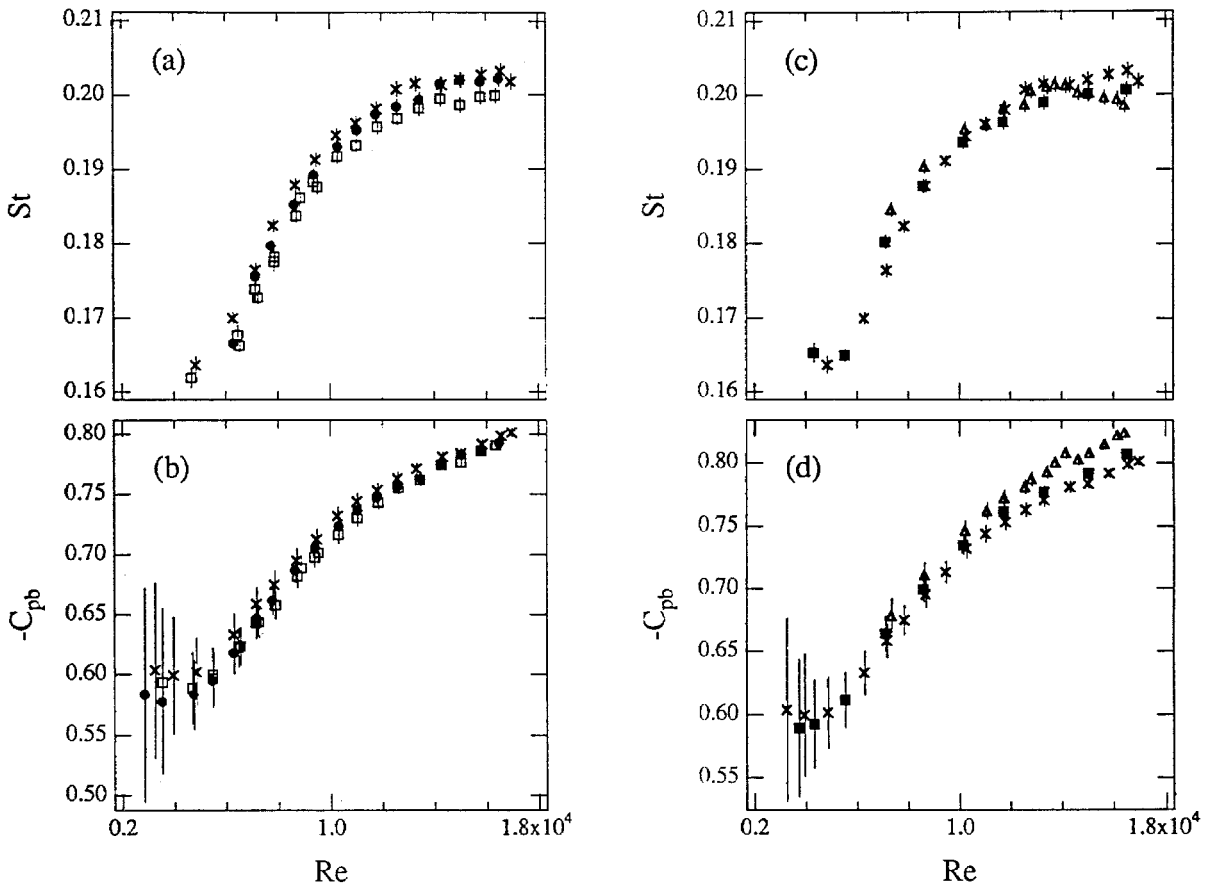

FIG. A.4 Global measurements using permeable splitter plates of different streamwise length ℓ and leading edge gap g. For all data, $\sigma = 0.35$. (**a**) St vs. Re, different ℓ, $g = 0$; (**b**) $-C_{pb}$ vs. Re, different ℓ, $g = 0$; Symbols are: (×) $L = 8D$, (•) $L = 12D$, (□) $L = 16D$. (**c**) St vs. Re, different g, $\ell = 8D$; (**d**) -Cpb vs. Re, different g, $\ell = 8D$. Symbols are: (×) $g = 0$, (■) $g = 0.25D$, (△) $g = 0.75D$.

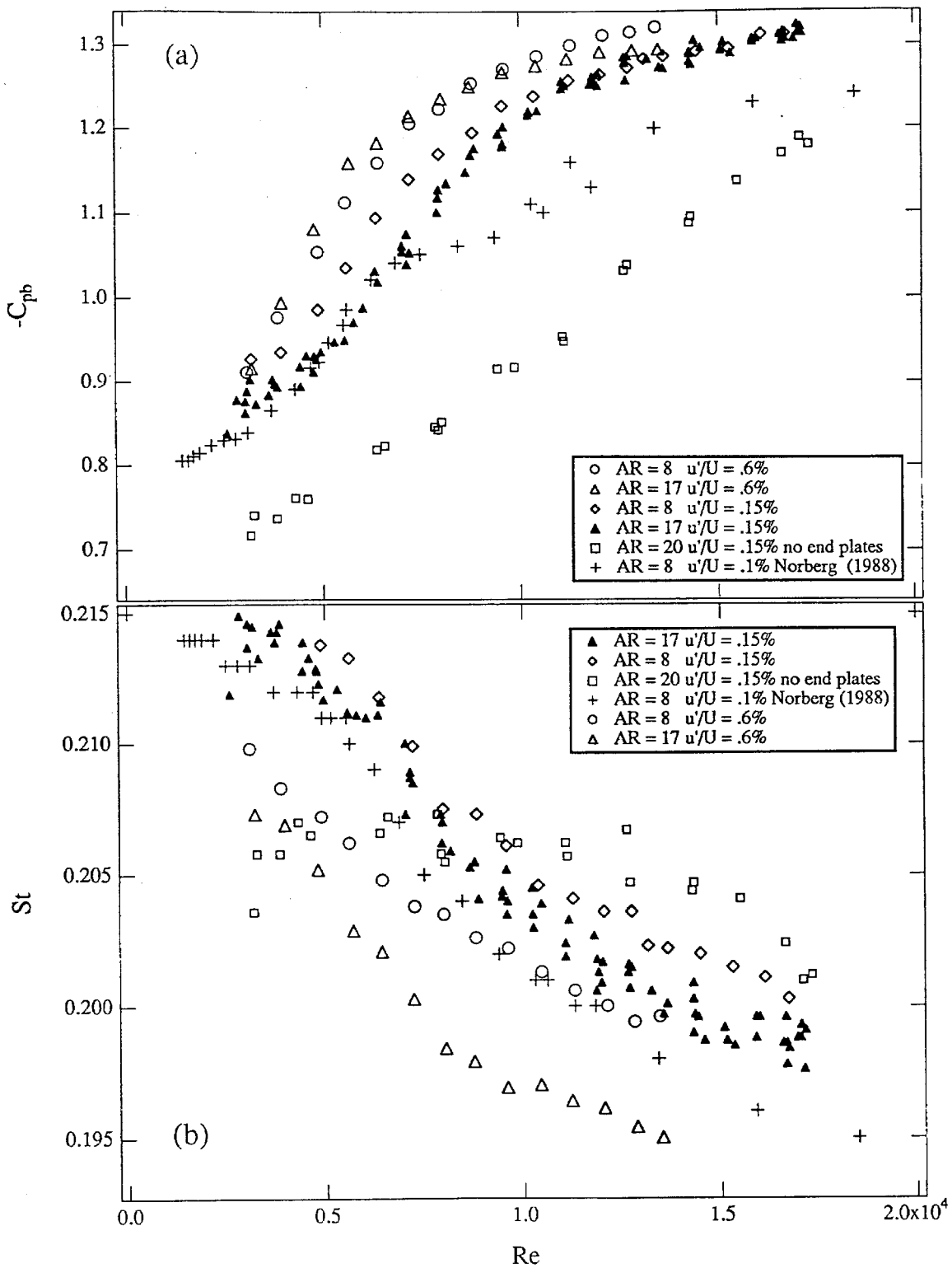

FIG. A.5 Base suction coefficient and Strouhal number measured under different experimental conditions.

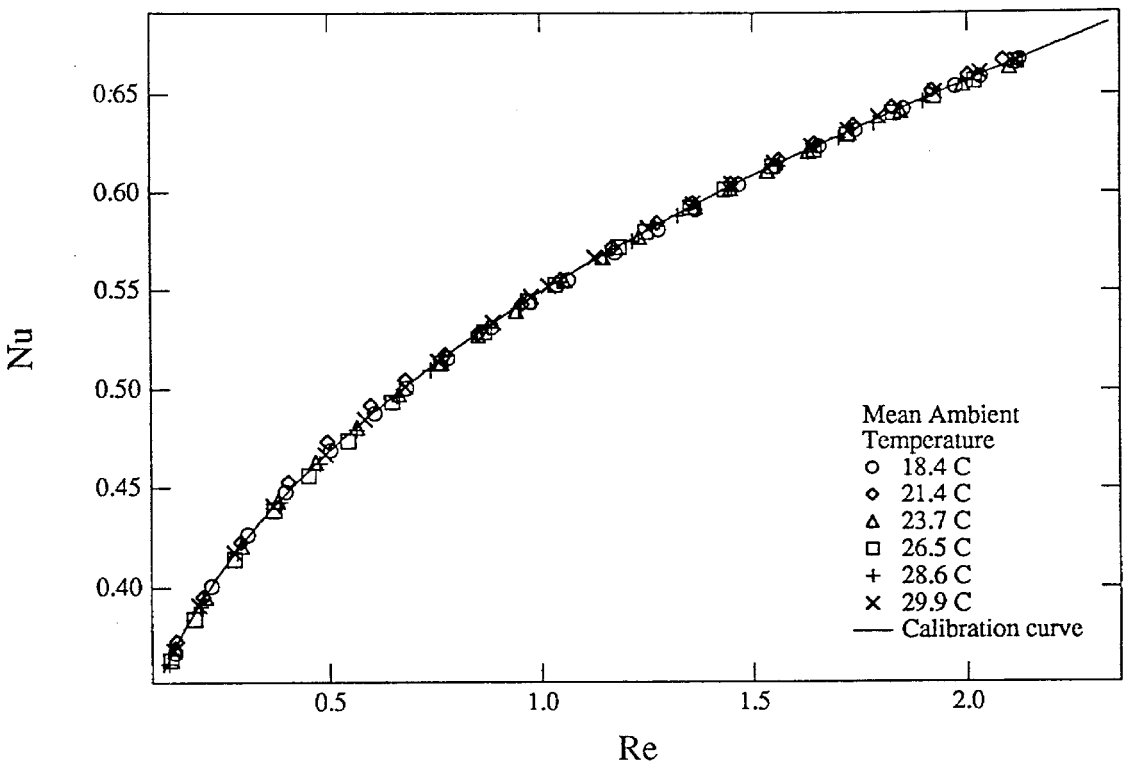

FIG. B.1 Example hot-wire calibration data used for finding the coefficients in Eqn. B.1, plotted in the form of Eqn. B.1 as Nu_w vs. Re_w . The data cover a temperature range of 18–30 C. The solid line is a plot of Eqn. B.1 evaluated using the coefficients in Table B.1.

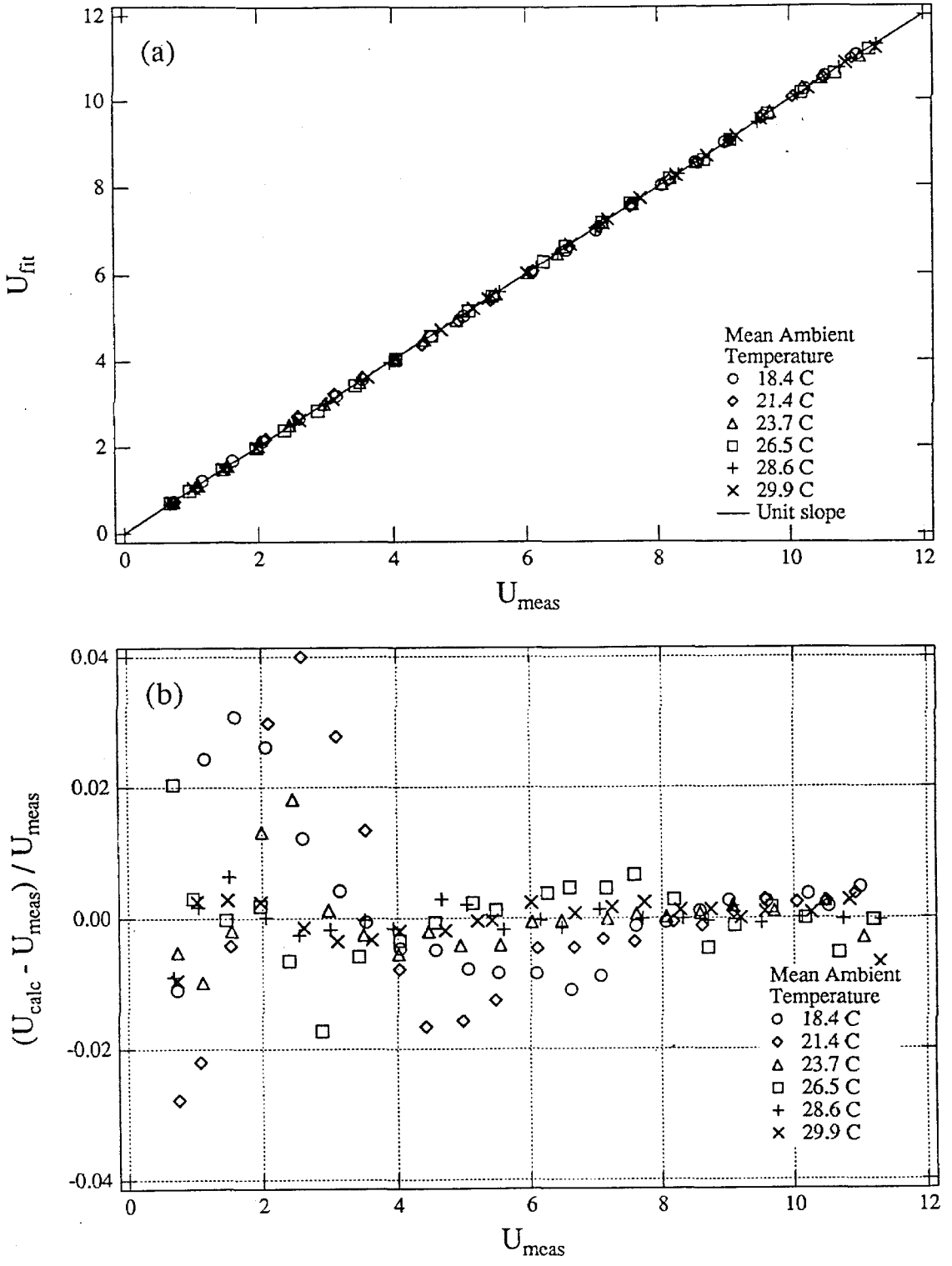

FIG. B.2 Velocities computed using the measured hot-wire voltages from the example calibration data; (**a**) U_c vs. U_m (the solid line has slope 1), (**b**) $(U_c - U_m)/U_m$ vs. U_m.

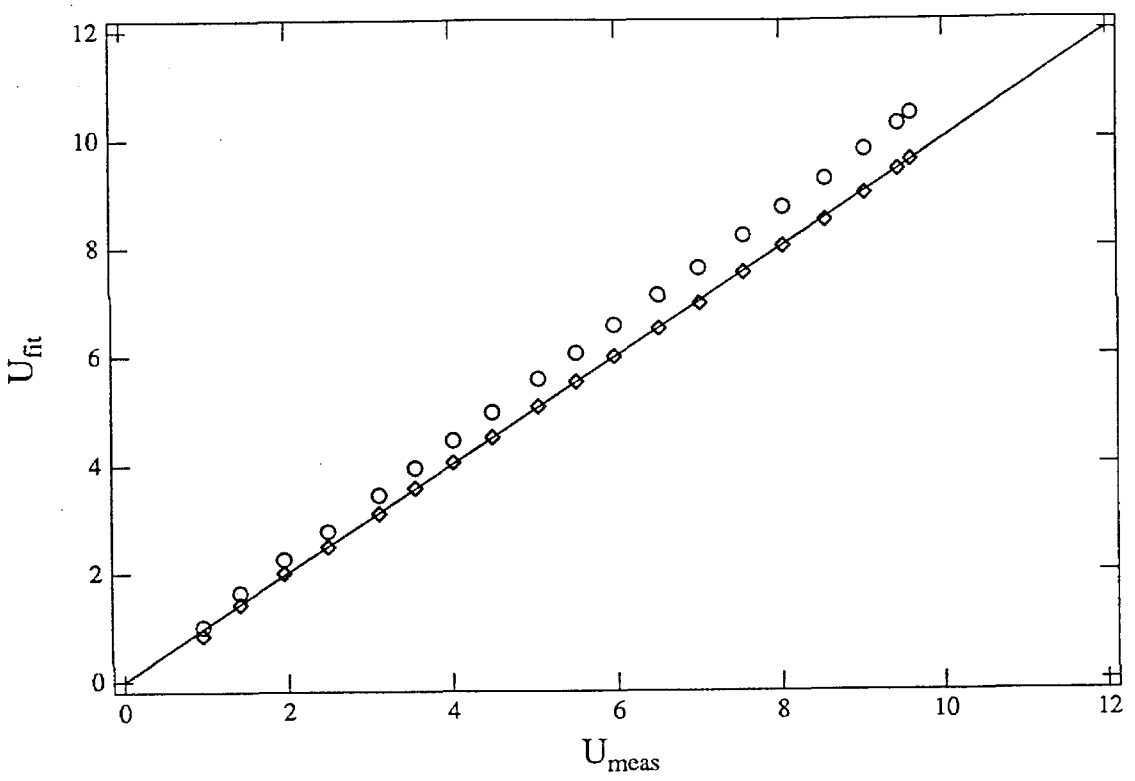

FIG. B.3 Hot-wire drift illustrated by taking calibration data on a different day using the same hot wire as was used for Fig.B.1, and linearizing using the coefficients from Table B.1; (o) linearized data before linear correction, (◇) data after being linearly corrected. The solid line has slope 1.

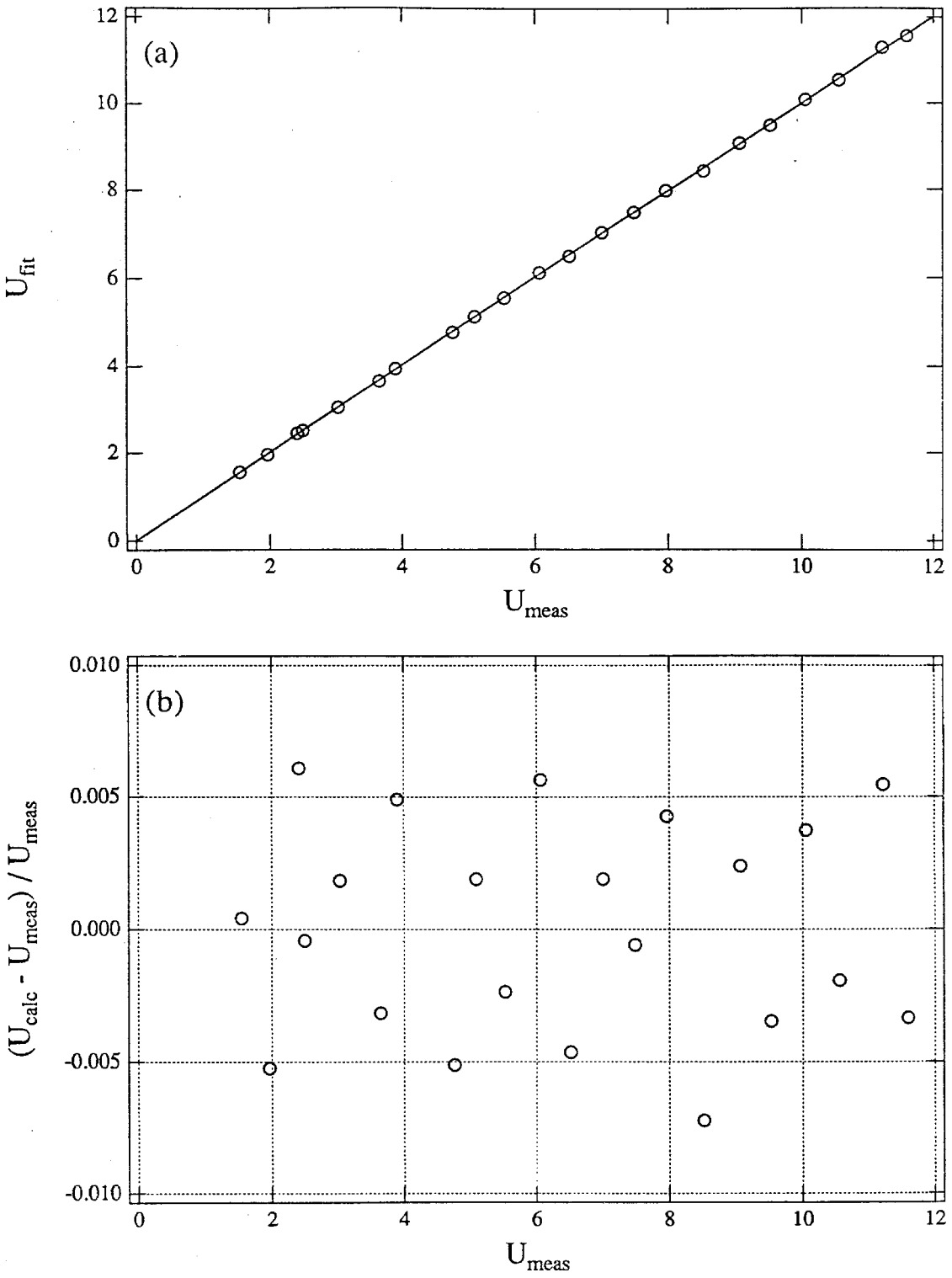

FIG. B.4 Velocities computed using measured hot-wire voltages, from data taken at constant temperature; (**a**) U_c vs. U_m (the solid line has slope 1), (**b**) $(U_c - U_m)/U_m$ vs. U_m.

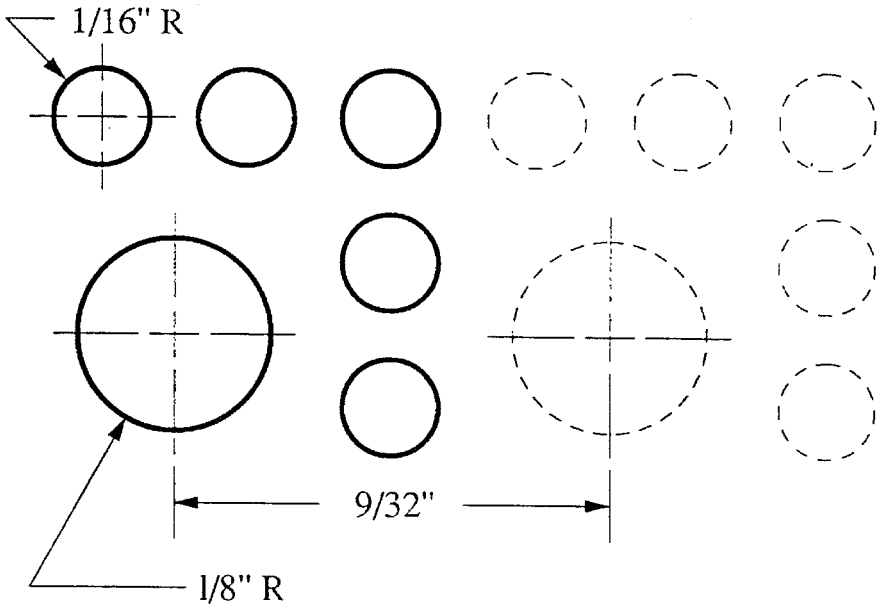

FIG. C.1 Sketch of the perforation pattern on the perforated aluminum plate.

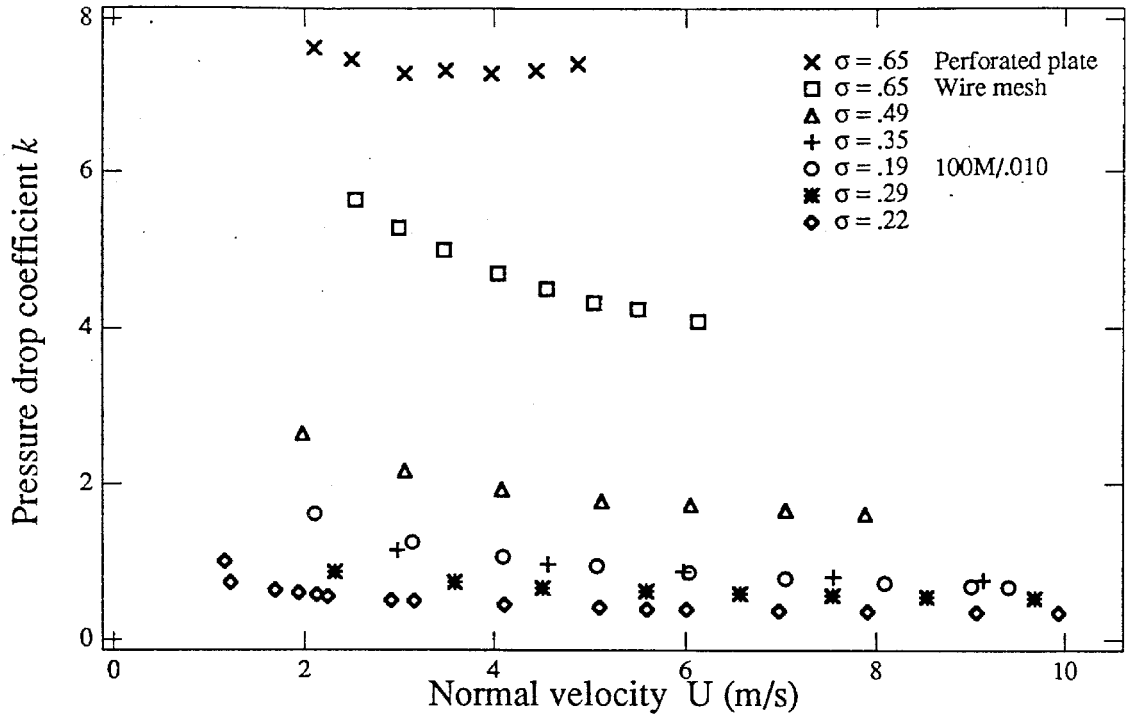

FIG. C.2 Screen pressure drop coefficient k plotted against the free-stream velocity U_∞, all plates.

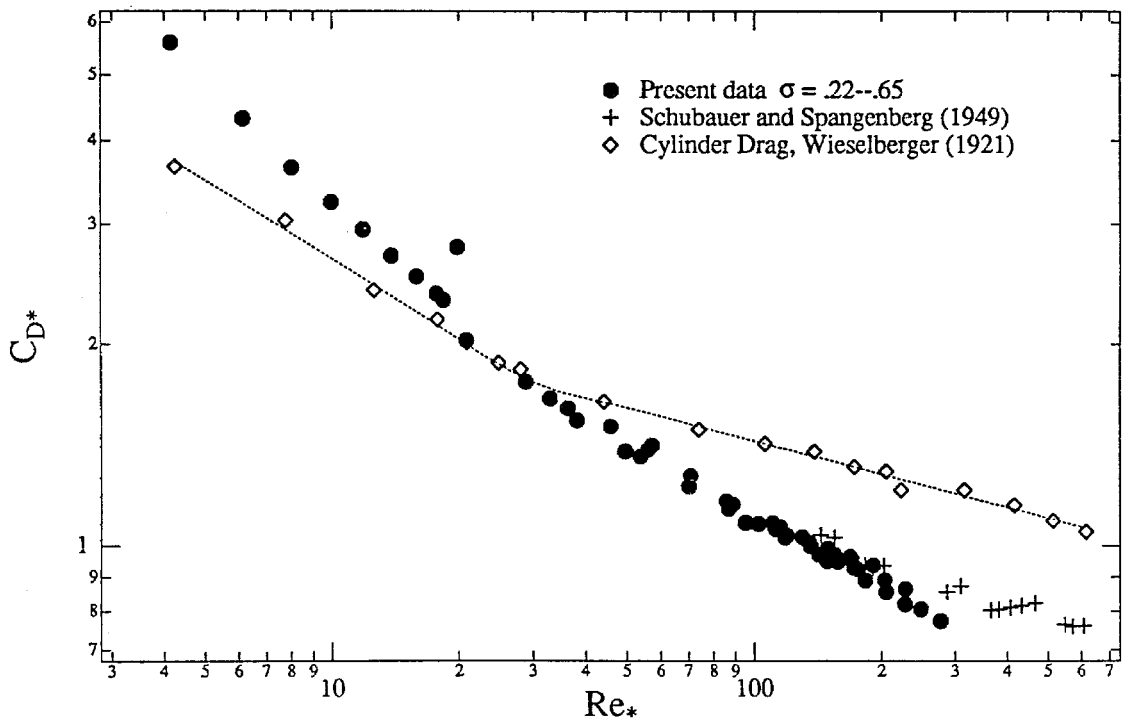

FIG. C.3 Scaled plate drag coefficient C_{D*} plotted against the scaled plate Reynolds number Re_*.

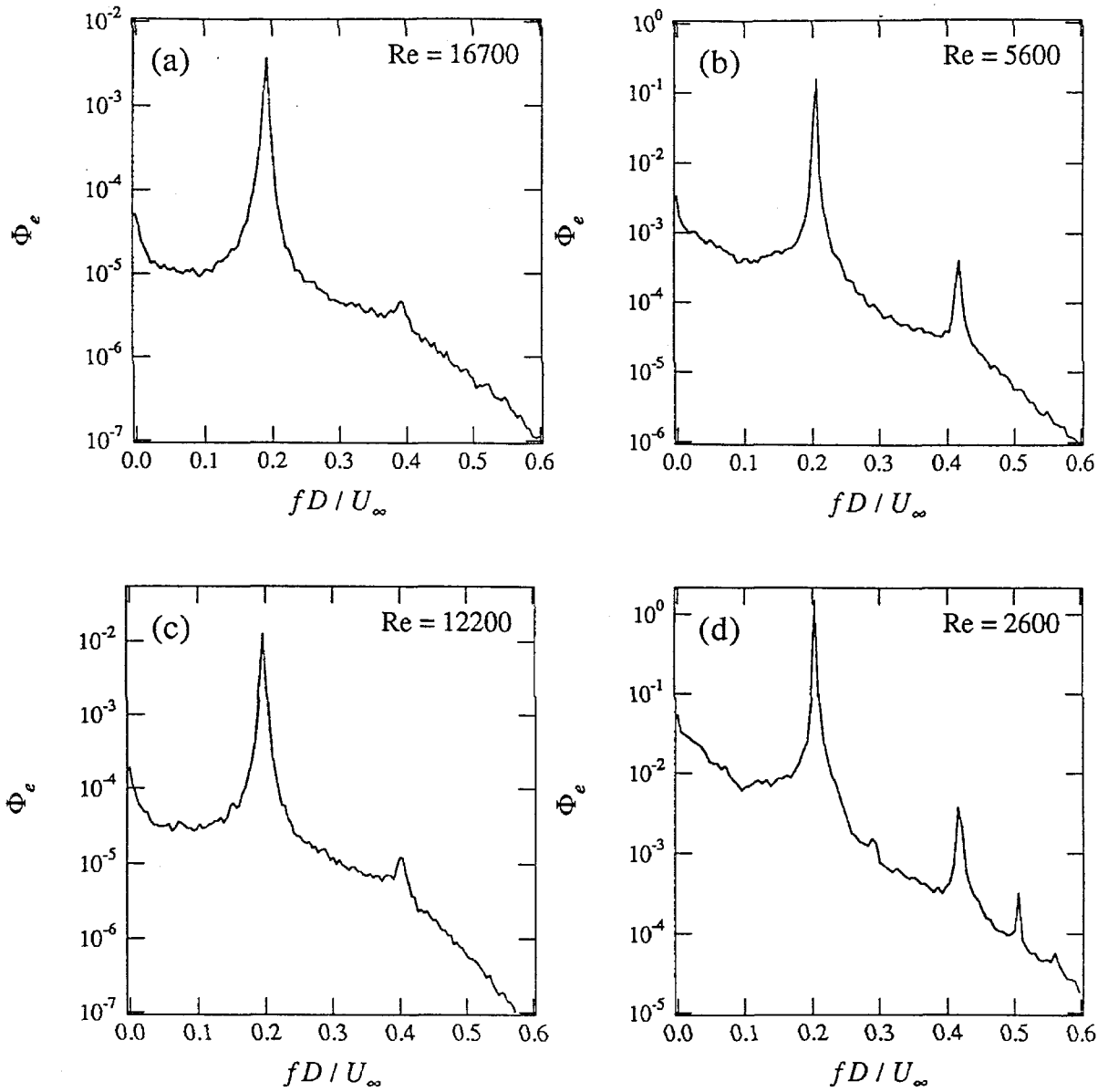

FIG. D.1 Example power spectra showing the primary wake frequency for flow past a circular cylinder with no splitter plate. Power spectra were computed directly from the hot-wire voltage data.

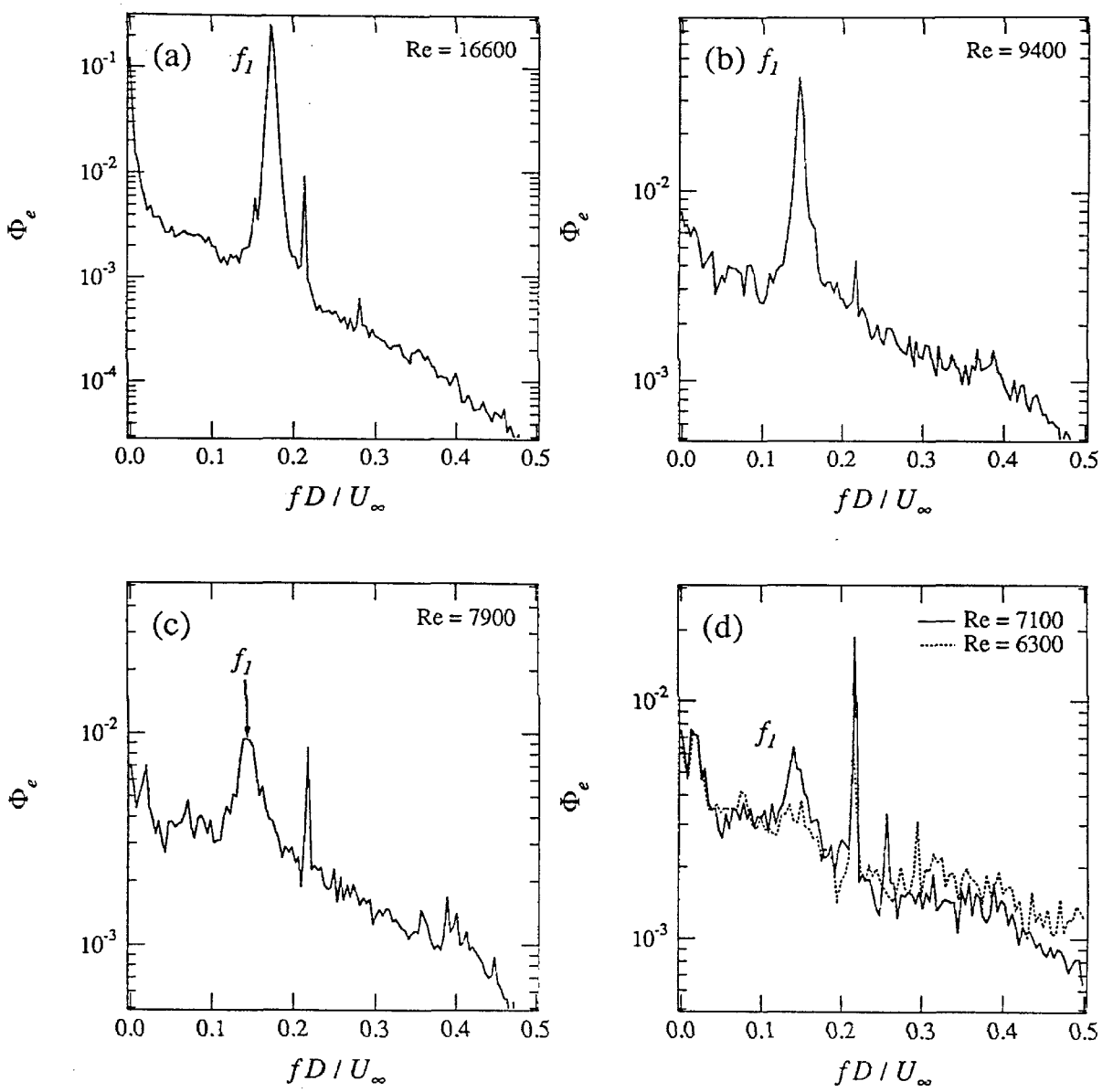

FIG. D.2 Example power spectra showing the primary wake frequency for flow past a circular cylinder with a permeable splitter plate of solidity $\sigma = 0.65$. Power spectra were computed directly from the hot-wire voltage data.

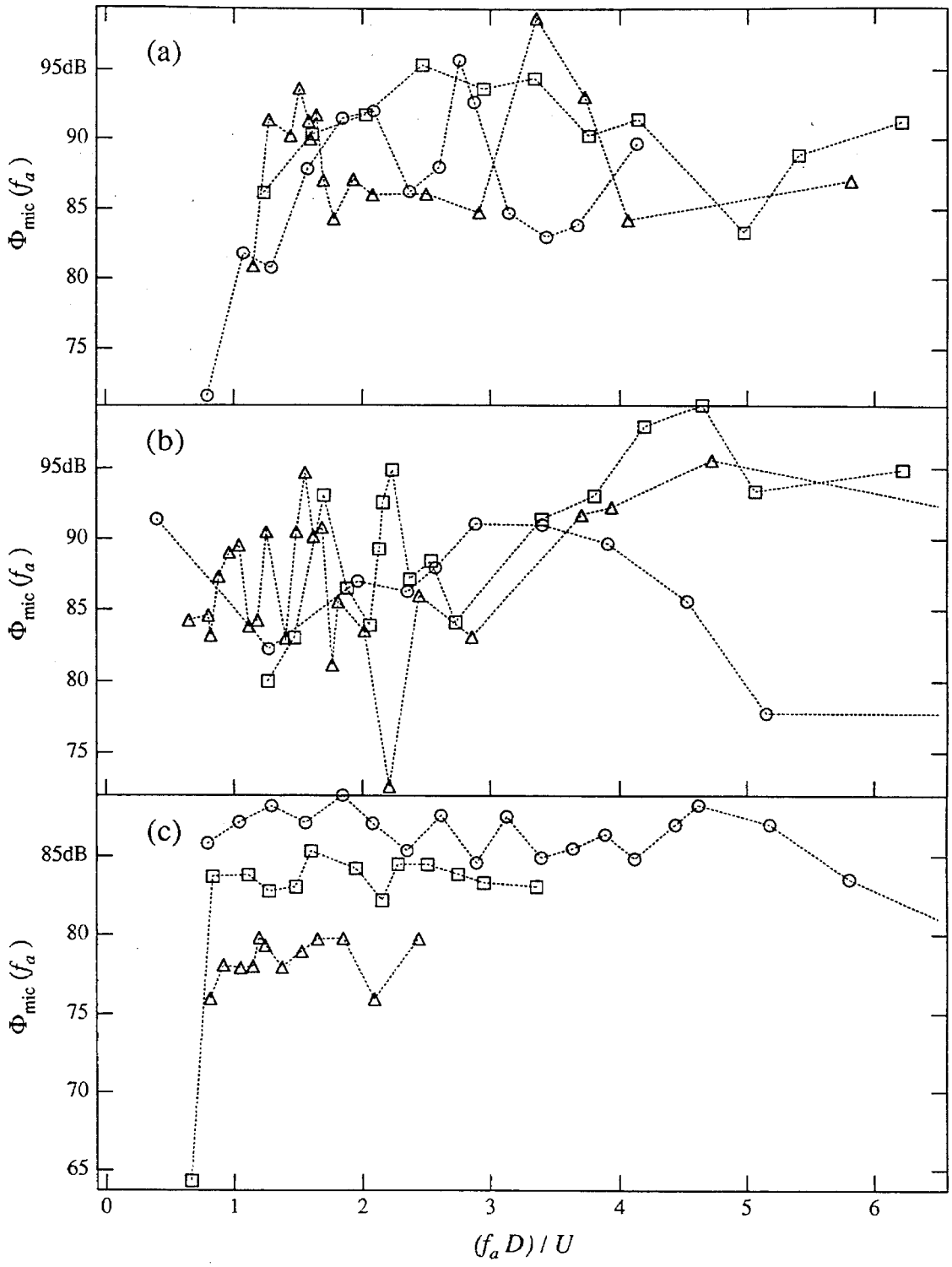

FIG. E.1 Amplitude of the power spectral density at the forcing frequency, as measured by the microphone installed in the wind tunnel during the experiments reported in Sec. 6.2.1 . Symbols correspond to different parts of Fig. 6.4 as follows:

a (△) Fig. 6.4**a** (□) Fig. 6.4**b** (◇) Fig. 6.4**c**
b (△) Fig. 6.4**d** (□) Fig. 6.4**e** (◇) Fig. 6.4**f**
c (△) Fig. 6.4**g** (□) Fig. 6.4**h** (◇) Fig. 6.4**i**